Fiber Optic Sensors and Self-reference Techniques for Temperature Measurements in Different Industrial Sectors

A thesis presented for the Degree of

Doctor of Philosophy

by

Alberto Tapetado Moraleda

Supervisor: Prof. Dr. Carmen Vázquez García

Electronics Technology Department

Escuela Politécnica Superior

Carlos III University of Madrid

Leganés, July 2,015

— Thesis —

Fiber Optic Sensors and Self-reference Techniques for Temperature Measurements in Different Industrial Sectors

Author: Alberto Tapetado Moraleda

Supervisor: Prof. Dr. Carmen Vázquez García

President	(Full name)	(Signature)
	---	---
Vocal	(Full name)	(Signature)
	---	---
Secretary	(Full name)	(Signature)
	---	---

Mark:

Leganés, 23rd July 2,015

Dedicado a todos los abuelos/as

que sacrificaron su bienestar por el futuro de sus hijos.

Sin su grandiosa dedicación

nunca podríamos haber alcanzado nuestros sueños.

Acknowledgements

Las ideas que tenemos sobre el éxito y el fracaso son sumamente importantes en la sociedad actual. Nos juzgamos a nosotros mismos según nuestras ideas de lo que constituye el éxito y el fracaso. Cuando decidimos que alguien ha triunfado, lo aplaudimos y lo envidiamos. Cuando ha fracasado, lo evitamos y lo repudiamos. Sin embargo, nuestras ideas sobre el éxito y el fracaso son muy limitadas, ligadas fuertemente al ámbito profesional. En la sociedad actual, un hombre o una mujer que ostenta gran poder sobre los demás son considerados como triunfadores, al margen de la felicidad que hayan podido conseguir en el camino. Sin embargo, personas satisfechas con pequeños objetivos compartidos, en ocasiones, son juzgadas y apartadas.

El secreto del éxito es aceptar incondicionalmente la vida y lo que te trae cada día. Una persona debe de aceptar cualquier situación que se presente, tanto buena como mala, fácil o difícil, con la misma actitud serena y positiva en todas las situaciones. Muchas personas se rinden antes de alcanzar lo que se habían propuesto. Pierden la esperanza y no creen poder conseguirlo. Muchas de esas personas no saben lo cerca que habían estado de triunfar cuando decidieron rendirse. En este sentido, arroparte de las personas que más te quieren sirve para identificar cada callejón sin salida, ayudándote a evitar futuros errores que te hagan retroceder en la consecución de tus metas. Porque la consecución de un objetivo no es lo mismo si se comparte con las personas que lo han hecho realidad.

Es por este motivo por el cual quiero expresar mi agradecimiento a todas aquellas personas que directa o indirectamente me han ayudado a la consecución de este objetivo.

A mi madre y a mi padre; *María Zoila* y *Pablo*, y a mi hermano, *Pablo*, porque sin su apoyo no podría haber conseguido todas y cada una de las metas que siempre me he propuesto alcanzar. Sin lugar a dudas, la educación recibida basada en el esfuerzo y en el espíritu de superación se ve recompensada con el paso del tiempo.

A mis abuelas y abuelos; *María Felipa*, *Aurelio*, *Benita* y *Pablo*, porque a pesar de sus dificultades, siempre se han preocupado porque nunca me faltase de nada. Nunca podré devolverles todo lo que me han aportado durante todos esos años que compartimos juntos. Espero disfrutar por mucho tiempo de aquellos que todavía están a mi lado. Para todos aquellos que nos dejaron, decirles que siempre os estaré agradecido por haber hecho de mí la persona que soy.

A *Ángela*, la persona que desde hace un año comparte conmigo la ilusión por aprender y progresar juntos. No existen las palabras para agradecerle lo vivido en este último año. Sin lugar a dudas, has sido una pieza clave en la consecución de esta meta.

A todos mis amigos de Consuegra, por haber estado todos estos años a mi lado compartiendo alegrías y tristezas. Hoy en día resulta difícil encontrar a personas a las que puedas calificar de amigos, no me cabe la menor duda, que ellos sí lo son. Gracias por todo lo que me aportáis.

A todos mis amigos de Ciudad Real, por compartir momentos inolvidables durante mi etapa como estudiante. Han transcurrido muchos años desde que nos graduamos, pero esto no ha hecho nada más que alimentar las ganas de vernos año tras años para comentar nuestras vivencias dentro y fuera de nuestras fronteras.

A todos las personas que durante mis estancias en Margate, Birmingham y Cambridge han querido compartir parte de su tiempo conmigo. Sin lugar a dudas, nunca olvidaré los buenos momentos vividos. Espero que nuestra amistad permanezca para siempre.

A todos los tutores y compañeros con los que tuve el privilegio de trabajar durante mis estancias doctorales en Aston University y el Massachusetts Institute of Technology. Gracias por vuestras valiosas sugerencias durante mi estancia.

A todos los miembros del Departamento de Tecnología Electrónica de la Universidad Carlos III de Madrid por ayudarme en la difícil tarea de formarme como profesional. En especial, a todos los integrantes del Grupo de Displays y Aplicaciones Fotónicas por brindarme la posibilidad de trabajar con un excelente grupo de profesionales, pero sobre todo, personas con una excelente calidad humana.

A Carmen Vázquez García, por ser la persona que confió en mí para llevar a cabo esta tesis doctoral. Sin lugar a duda, durante todos estos años de trabajo he aprendido que con esfuerzo y dedicación se obtienen buenos resultados.

A todos ellos mi mayor reconocimiento y admiración.

Contents

List of Figures

List of Tables

Acronyms List

Acronym	Term
HDTV	High-definition TV
P2P	Peer-to Peer
VOD	Video on Demand
RTDs	Resistance Temperature Detectors
MRI	Magnetic Resonance Imaging
EMI	Electromagnetic Disturbances
WDM	Wavelength Division Multiplexing
PON	Passive Optical Network
POF	Polymer Optical Fiber
CWDM	Coarse WDM
DWDM	Dense WDM
FBG	Fiber Bragg Gratings
WDM-PON	Wavelength Division Multiplexing-Passive Optical Networks
GDAF	Displays and Photonics Application Group
MPOF	Microstructured Polymer Optical Fibers
ONU	Optical Network Unit
MMI	Multimode Interference
CICYT	Spanish Interministerial Commission of Science and Technology
OFSESA	Optical Fiber Sensor Systems for Future Security and Safety Applications
MPOFBG	Microstructured Polymer Optical Fiber Bragg Gratings
FOS	Fiber-Optic Sensors
GOF	Glass Optical Fiber
PMMA	Polymethacrylate
SI	Step-Index
GI	Graded-Index

GI PF POF	Graded-index Perfluorinated Polymer Optical Fiber
CYTOP	Cyclic Transparent Optic Polymer
SMEs	Medium-size Enterprises
LANs	Local Area Networks
TO	Thermo-optic
LED	Light- Emitting Diode
DAQ	Data Acquisition Card
GFBGs	Glass Fiber Bragg Gratings
POFBGs	Polymer Fiber Bragg Gratings
ICP	Intracranial Pressure
HDPE	High Density Polyethylene
GI-POF	Graded-index Polymer Optical Fiber
PCF	Photonics Crystal Fibers
COC	Cyclo-olefin Co-polymer
MGOF	Microstructural Glass Optical Fiber
LPG	Long Period Gratings
GI-MPOF	Gradual-index Microstructured Polymer Optical Fiber
UV	Ultraviolet
He-Cd	Helium-cadmium
CW	Continuous Wave
OSA	Optical Spectrum Analyser
FC/APC	Ferrule Contact / Angle Physical Contact
MOF	Microstructured Optical Fiber
FWHM	Full Width at Half-maximum
SNR	Signal-to-noise Ratio
FC/PC	Ferrule of the Contact/Physical Contact
BLS	Broadband Light Source
AOM	Acousto-optic Modulator
PD	Photodetectors
BPF	Band-pass Filter

FIR	Finite Impulse Response
VOA	Variable Optical Attenuator
NEP	Noise-equivalent Power
ESNR	Electrical Signal-to-noise Ratio
IR	Infrared
ADC	Analog-to-digital Converter
NA	Numerical Aperture
Ge	Germanium
NIR	Near-infrared
SWIR	Short-wavelength Infrared
MWIR	Mid-wavelength Infrared
Si	Silica
InGaAs	Indium Gallium Arsenide
GaP	Gallium Phosphide
GeSn	Germanium Tin
PONs	Passive Optical Networks
FTTH	Fiber to the Home
WR-ODN	Wavelength Routed Optical Distribution Networks
SLA	Service Level Agreement
CPE	Customer Premises Equipment
T-OTDR	Tunable Optical Time Domain Reflectometers
OLT	Optical Line Termination
OMM	Optical Monitoring Module
AWG	Arrayed Waveguide Grating
RF	Radio-frequency
BER	Bit Error Rate
SMF	Singlemode fiber
PIC	Photonics Integrated Circuits
CPU	Central Processing Unit

Chapter 1

Introduction

1.1. Motivation of this Work

Growing research interests are focused on the high-speed telecommunication and data communication networks with increasing demand for accessing to the Internet even from home. This increasing demand for high-speed information transmission has been driven by the huge successes during the last decade of new multimedia services such as High-Definition TV (HDTV), Peer-to Peer (P2P), cloud storage and Video on Demand (VOD), among others. These services required the increment of the access network capacity. To overcome this problem, a growing number of service providers are turning to solutions capable of exploiting the full potential of optical fiber communication networks, the copper lines infrastructures being progressively replaced by a high capacity fiber-based topologies.

The limited cost of the fiber technology and the advanced methods for manufacturing devices in the optical communication area, along with the current demand of the automation and process controls, has stimulated the development and the standardization of different optical fiber applications. Among them stands out the development of sensors for the measure of diverse physical and chemical magnitudes, such as the temperature, pressure, humidity, deformation, chemical substances concentration, among others.

The field of temperature sensors covers a high percentage of today's world sensor market due to the large number of applications in which it is necessary to measure temperature for instance: the automotive and aircraft industry, air-conditioning control, chemical industry, medical applications, materials machining, alimentary industry, power transformer applications , among others. Nevertheless, traditional temperature sensor schemes such as thermocouples, thermistors, resistance temperature detectors (RTDs), among others are not well suited for use whenever specific needs are required.

An example of this situation is the temperature measurement in power transformers. The size of these transformers ranges is increasing according with the demand, with replacement costs ranging from a few hundred dollars to millions of dollars. Power transformers are usually very

reliable. However, the in-service failure of a transformer is potentially dangerous to utility personnel through explosions and fire, potentially damaging to the environment through oil leakage, is costly to repairs or replace, and may result in significant loss of revenue. To prevent these failures and to maintain transformers in good operating condition is very important to monitor the temperature of the cooling oil. The reliability of conventional electrical sensors decreases under the presence of electromagnetic disturbances (EMI), and the electrical sensors may even increase the possibility of explosion inside the coolant oil in the transformer tank. On the other hand, a link between the substation and the control center is required. A possible solution is the use of a wireless portable interrogators, but continuous monitoring of critical parameters in day-to-day activities requires more stable and safer communication links.

Another field where traditional temperature sensors are not well suited is the biomedical instrumentation to enable more efficient patient diagnosis, monitoring and treatment. In this context, biomedical sensing applications are of growing importance. Recent advances in minimally surgery demand smaller disposable sensing elements. The use of sensors in biomedical applications presents unique design challenges and particular problems related to their interface with a biological organism. Sensors must be safe, reliable, highly stable, biocompatible, amenable to sterilization and autoclaving, not prone to biologic rejection. Sensor packaging is an especially critical aspect since the devices must be very small, particularly those for implanting or indwelling purposes. On the other hand, over the last decades, magnetic resonance imaging (MRI) compatible sensors are required to monitor patients in the presence of EMI. This is the case in the temperature measurement of patients undergoing MRI-guided hyperthermic procedures. The material used to manufacture the biomedical sensors should not perturb the magnetic field inside the scanner.

Another important application where traditional temperature sensors have not been effective is temperature measurement during cutting processes in the aerospace industry. Heat resistant alloys are used to manufacture aero-engine components. The energy consumed in a machining process is largely converted into heat during the cutting process. An uncontrolled temperature generated by the cutting tool is the main cause of surface degradation and tool wear, increasing the production costs. Temperature measurement in exactly defined locations is a key challenge in order to overcome these problems. The use of traditional sensors to measure temperature in machining process was demonstrated but the main disadvantage is that these sensors required contact for heat transfer in order to work. This type of sensors in fact measure its own temperature, thus requiring enough time for the temperature equilibrium between the workpiece and the sensors to occur. The fast response of the cutting process reduces the use of these sensors in machining applications. In order to overcome these problems, from the 1930's

and onward infrared radiation thermography have been investigated. In general such techniques enable higher sampling rates since the principle of operation depends on heat radiation rather than equilibrium, although the accuracy is somewhat less than that of the thermocouples due to the complexities of emissivity. These techniques also require a free line of sight the work piece to the sensors.

Advance in optical technology have led to the development of a number of different sensors systems suitable to overcome some of these problems. The traditional temperature sensor systems have been well established for a long time, and they have been proven to have good reliability records and reasonable manufacturing cost; therefore, fiber-based sensors systems have to exhibit superior advantages in order to penetrate into the market to replace the existing conventional sensors in many applications. In particular, intensity modulation temperature sensing is a technique widely used in fiber-optic temperature measures. This technique uses variation of light intensity induced by temperature changes in the optical fiber. This approach is by far the easiest to carry out since there are numerous configurations to make an intensity modulation. Compared to interferometric techniques, this technique leads by lower sensitivity sensing solutions but with cheaper and simpler signal processing schemes. This technique also keeps the advantages of the optical fiber sensors including electromagnetic interference immunity, lightweight, small size, and environmental ruggedness.

Nonetheless, the main drawback of the intensity-based topology is the need for a self-referencing scheme in order to avoid undesirable optical power fluctuations, for example, the presence of dirt during temperature measurements in machining processes, patient movements during a temperature measurement in a medical surgery, among others. Other benefits of these self-referencing techniques are the possibility to improve resolution and simultaneously multiplex a large number of optical fiber sensors. These improvements are achieved at the expense of using complex schemes that increase the cost of the system.

The motivation for multiplexing fiber optic sensors depends on the application but the most fundamental reason being reduced cost and increased simplicity as fewer components are used. Multiplexing allows the cost of the more expensive components to be amortized over an array of sensors, reducing the cost per sensor of the system, as long as the transducers themselves are inexpensive, which is typically the case in intensity-based fiber optic sensors. Reducing the number of optical fiber leads is another fundamental reason for multiplexing.

A wide range of enabling techniques for implementing multiplexed intensity fiber-optic sensor networks have been developed. The choice of the multiplexing approach depends on the

requirements of the sensor network and the applications. The tendency of the optical sensor market is to use specialized schemes developed for optical communication systems. In this framework, the current generation of access networks permits to use Wavelength Division Multiplexing (WDM) components in Passive Optical Network (PON) infrastructures. The wider adoption of WDM-PON lies in the development of sufficiently low cost technology to be used at the users' premises. Self-seeded WDM-PON has been actively investigated in recent years as potentially the lowest cost solution for next-generation access networks. The primary attraction of this architecture is its simplicity, lower power consumption, and cost advantage. Similar principles can be applied to multiplexing and interrogation systems for fiber optic sensors; with the aim to develop, analyse and demonstrate sustainable all-optical infrastructure to provide a physical layer for both, access communication and sensor networks.

1.2. Objectives of the Work

As a general aim, this work specifically focuses on the development of temperature sensors and self-reference techniques for temperature measurement in different industrial sectors.

The first objective of this work is the design and development of a low-cost fiber optic sensor for measuring temperature in power transformers and biomedical applications where the presence of EMI prohibits the use of traditional sensors. Compatibility with the human being is a requirement when the temperature sensors are used in medical applications. Following simple fiber optic configurations, intensity sensors modulate the optical power loss as the temperature changes, thus providing the measurement as an optical intensity modulation signal. Polymer Optical Fiber (POF) technology, with very low-cost components, enables temperature sensing using a low precision connectors and lenses as well as simple multiplexing and demultiplexing devices, especially if compared with glass optical fibers.

However, intensity sensors need a self-referencing method to minimize the influences of long-term aging of source and receptor characteristics, as well as undesirable random short-term fluctuations of optical power loss in the fiber link connecting the control unit, where the measurements are taken, to the remote sensing point, where the optical sensor is located.

The second objective of this work is to promote, study and develop a multiplexing strategy to implement and scale POF sensor networks using low cost off-the-shelf devices, enhancing the power budget and keeping the self-reference of the measurements.

This work focuses on low-cost Coarse WDM (CWDM) technology, where a grid of wavelengths with a 20nm channel spacing for target distance of up to tens of kilometres is

specified. CWDM technology have lately been promoted in the field of telecommunication as standard for metro applications with shorter distances, lower network capacity and cost than Dense WDM (DWDM). This topology requires simpler, wider tolerance laser manufacturing, less laser accurate temperature control and reduced design complexity and cost of optical filters. These relaxed requirements make the CWDM technology an interesting approach for building low-cost self-referencing sensors networks. The development of this technology, adapted to the use of POF, can be carried out with the development of fiber Bragg gratings (FBG) in POF, providing an effective and compact strategy for exploiting fiber links for both propagating directions of the light with a single fiber lead.

The third objective is to develop a non-contact two-colour fiber-optic pyrometer for temperature measures in the aerospace machining industry, enhancing the location measurement area, reducing the surface emissivity effect and keeping the self-reference of the measurement. This work also focuses on the reduction of the pyrometer temperature errors, analysing the wavelength dependence losses of the optoelectronics devices used in the pyrometer set-up and its influence on the temperature measurements. The fulfilment of these requirements promote the use of simple and robust configurations, making the use of low-loss fiber-optic components compatible with commercial off-the-shelf optoelectronics well established in WDM-based optical communication networks an interesting approach.

As a complementary studies related to the techniques used to develop the fiber-optic sensor networks presented in this work, two secondary objectives are proposed:

The adaptation of self-referencing sensor techniques to the development of a low-cost in-service preventive monitoring system for Wavelength Division Multiplexing-Passive Optical Networks (WDM-PON). In this scenario, the use of a self-referencing technique with the possibility to address multiple connections or subscribers is needed in order to reduce operating cost of the optical distribution network and to guarantee high service level agreements.

Promoting the integration of photonics functions in the next generation of microprocessors. The possibility to integrate sensing and communication functions using WDM topologies in the next generations of microprocessors, gives the possibility to develop more efficient, powerful and smaller electronics devices.

The work comprised in this document has been developed in the framework of the activities carried out in the Displays and Photonics Application Group (GDAF) at Carlos III University of Madrid.

1.3. Contents of the Work

This work is divided into seven chapters and three short appendixes and is organized as follows:

In Chapter 2 of this document, a brief state-of-art of temperature fiber-optic sensors is further described, focusing on the advantages and disadvantages of using intensity fiber optic sensors. A novel temperature sensor based on POF macro-bend is also developed for use in power transformers and biomedical applications. Two different topologies are analysed in order to implement a self-reference technique to avoid false readings caused by fluctuations of the power of the light source. The first configuration uses a dummy fiber-optic sensor for referencing purposes. The second configuration uses the optical power ratio between two wavelengths traveling along a single macro-bend loop to implement a WDM self-referencing technique. A complete analysis of the optimum wavelength has been carried out to optimize the sensor response. In both cases, experimental results are compared with mathematical models based on geometric approaches. Finally, the proposed temperature sensors are compared with other proposals reported in the literature.

In Chapter 3 of this document, a brief state-of-art of intensity fiber-optic sensors for medical purposes is described. Features like sensitivity, robustness and materials used to manufacture optical sensors are compared for the different alternatives reported. Using the advantages of inscription of FBGs in microstructured polymer optical fibers (MPOF), a WDM approach is described as FBG-based self-referencing sensor network. This topology uses the compatibility of the polymer fiber with the human being to extend its application to the medical field. This scheme also takes advantage of the passive wavelength splitting feature provided by the FBG device. Finally, the self-referencing FBG-based fiber-optic intensity sensor network with virtual delays at the reception stage is demonstrated in a CWDM topology. It is shown the performance of the measurement parameters in terms of their self-reference property, crosstalk, sensitivity, linear response and resolution. Computer software based on a graphical code is developed to obtain the measurements. Additionally, the self-referencing system for monitoring intensity fiber-optic sensors in WDM-PON networks is also evaluated to provide a remote monitoring service unit fully compliant with short-reach or medium-reach networks.

In Chapter 4 of this document, a brief state-of-art of different techniques used to measure temperature in material removal processes is reported. Advantages and disadvantages of conventional temperature sensors are used to justify the development of a fiber-optic two-colour pyrometer. The sensor uses the ratio of optical power at two wavelengths to implement a self-

referencing technique to avoid the influence of the surface emissivity. A theoretical model of the pyrometer behaviour has been carried out to understand the measuring mechanism and identify which factors are related to the system temperature error and the minimum measureable temperate. The influence of those characteristics over different wavelength configurations is addressed by means of a set of theoretical simulations.

In Chapter 5 of this document, the possibility of using a non-conventional sensor for localized temperature measures during superalloys machining is analysed in order to increase the productivity while reducing costs. The use of a two-colour fiber-optic pyrometer using low-loss fiber-optic components compatible with commercial off-the-shelf optoelectronics well established on WDM-based optical communication networks is demonstrated. The sensor uses the power ratio of two different wavelengths to implement a self-reference technique to avoid the influence of the emissivity changes while reduce the temperature error. An analysis of the losses at each wavelength has been carried out to analyse the system temperature errors. The theoretical model, presented in Chapter 4 is used to justify the pyrometer response. A study of the influence of different factors on the temperature measurement has been performed in order to identify the sensor limitations of the implemented prototype. Finally, the two-colour pyrometer is tested in a real scenario with the aim of verifying its correct operation.

In Chapter 6 of this document, the main conclusion of this work and future research directions are reported.

In Chapter 7 of this document; the motivation, objectives, conclusions and future research of this work are written in Spanish.

Appendixes to this work are included for a better understanding of the document and also offering the possibility to briefly describe some aspects on the secondary objectives of this work. Their contents are:

- In Appendix A, a short description of the analytical expressions for the self-referencing parameters described in Chapter 3.
- In Appendix B, measurements of a new low-cost in service preventive monitoring system for remote measurement of fiber attenuation in DWDM-PONs using single colourless reflector at Optical Network Unit (ONU) side is presented.

- In Appendix C, measurements of multimode interference (MMI) devices to be used in photonics integrated circuits for communication and sensing purposes are presented.

Finally, related publications of the author are attached together with an acronyms list used within this document.

1.4. Acknowledgements

The research work of this dissertation has been supported by the following Spanish projects: TEC2009-14718-C03-03 (DEDOS), and TEC2012-37983-C03-02 (CFOOT-TIC) of the Spanish Interministerial Commission of Science and Technology (CICYT); BES-2010-033348, EEBB-I-12-05434 and EEBB-1-13-07511 of the Spanish Ministry of Economy and Competitiveness; PRX12/00007 of Spanish Ministry of Education; P2013/MIT-2790, FACTOTEM-2/2010/00068/001 and S2013/MIT-2790 (SINFOTON-CM) of Autonomous Community of Madrid.

Additional financial support was obtained from ICT COST Action TD1001: Novel and Reliable Optical Fiber Sensor Systems for Future Security and Safety Applications (OFSESA) of the European Union.

Simulations used in Chapter 2 were done in collaboration with Applied Photonics Group at Universidad del País Vasco leaded by Prof. Dr. Joseba Zubia Zaballa. I also want to thanks Dr. Jon Arrue for the help given to simulate the behaviour of the macro-bend POF sensor.

Microstructured Polymer optical fiber Bragg gratings (MPOFBGs) used in Chapter 3 were fabricated by Alberto Tapetado Moraleda during a five-month research stay in the Institute of Photonics Technologies at Aston University, Birmingham, United Kingdom, under the supervision of Prof. Dr. David J. Webb. I also want to thanks Dr. Lutful Khan and Eng. Ada Abang for the help given to fabricate the MPOFBGs.

The calibrated metallic holder used in Chapter 5 was fabricated by Eng. Ernesto Garcia Ares in the Technical Department at Carlos III University of Madrid.

Part of the work comprised in Chapter 5 was done in collaboration with the Mechanical Department at Carlos III University of Madrid leaded by Prof. Dr. María Henar Miguélez Garrido. I also want to thank Dr. José Díaz Álvarez for the help in the machining process measurements.

Part of the work comprised in Appendix B was done in collaboration with the Fixed Access and Home Network Direction at Telefónica Investigación y Desarrollo. The scientific supervisor of this collaboration in Telefónica Investigación y Desarrollo was Dr. Julio Montalvo García.

Part of the work comprised in Appendix C was done by Alberto Tapetado Moraleda during a two-month research stay in the Physical Optics and Electronics Group at Massachusetts Institute of Technology under the supervision of Prof. Dr. Rajeev Ram and Prof. Dr. Carmen Vázquez Garcia. I also want to thanks Dr. Jason Orcutt, Eng. Huaiyu Meng and Eng. Karan Mehta for the help given to characterise the MMI devices.

Chapter 2

Chapter 2

A Temperature Sensor Based on Polymer Optical Fiber Macro-bend

In this chapter, the design and development of a polymer optical fiber (POF) macro-bend temperature sensor is presented. The fiber-optic sensor can operate in a temperature range from -55 to 70ºC. The proposed temperature sensor can be used in power transformers and biomedical applications. Two different self-referencing topologies are analysed in order to avoid false reading caused by fluctuations of the light source, optical fiber attenuation and other undesired losses. The first configuration uses a dummy fiber-optic sensor for referencing purposes. The sensor requires only a few and relative low-cost components to measure temperature but the main disadvantage is the repeatability of the manufacturing process which limits the robustness of the system. In contrast, the second self-referencing configuration uses the optical power ratio between two wavelengths traveling along a single macro-bend loop. The use of this technique reduces the error related to the repeatability of the manufacturing process despite an increase in the cost of the equipment. A complete analysis of the optimum wavelength has been carried out to optimize the sensor response. Experimental results are successfully compared with mathematical model based on geometric approaches.

2.1. Introduction

The field of temperature sensors covers a high percentage of today's World sensors market [1] due to the large number of application in which it is necessary to measure temperature, for instance: the automotive industry, air-conditioning control, chemical industry, medical applications, alimentary industry, power transformer applications, among others. Nevertheless, traditional temperature sensor schemes such as thermocouples, thermistors and resistance temperature detectors (RTDs) are not well suited for use whenever specific needs are required. This is the case of temperature measurements in low-cost industrial processes in the presence of

electromagnetic interferences (EMI) generated, for example, by high-current and high-voltage devices [2]. Other important scenario where traditional sensors have a limited place is the medical applications. Minimally invasive tools and sensors have become essential for medical diagnosis and surgery with the desire of not only serving at the same time to sense physical parameters, but also being able to overcome biocompatibility concerns. In addition the use of Magnetic Resonance Imaging (MRI) for monitoring patients limits the use of conventional sensors due to the presence of strong electromagnetic fields.

To overcome these problems, new optical fiber based sensors have been developed. Optical fiber sensors advantageous features include small size, light weight, geometrical flexibility, chemical inertness, electric and thermal isolation and potential multiplexing. As the principle of operation is based on an optical signal, optical fiber sensors also exhibit immunity to electromagnetic fields [3]. Different fiber-optic techniques have been developed including the use of optical interferometers in multiple configurations (Sagnac, Michelson, Mach-Zehnder or Fabry-Perot), intensity-based fiber-optic sensors (FOS) and fiber Bragg gratings (FBGs). The first approach usually leads to extremely high sensitivity sensing solutions, but at the cost of very complex signal processing schemes. In contrast, potentially low-cost intensity-based optical sensors modulate the power loss in response to change in measurand. Nonetheless, the main drawback of the intensity-based topology is the need for a self-referencing scheme in order to avoid undesirable optical power fluctuations, for example, in bends in fibers or because of slightly variable mechanical misalignments or background light fluctuations on free-space systems. A wide range of self-referencing techniques [4] have been proposed including frequency [5-9] and wavelength [10] modulated topologies. Many of these techniques offer the possibility to improve resolution, self-referencing, and simultaneously multiplexing a large number of optical fiber sensor [7, 11, 12]. These improvements are achieved despite of using complex schemes that increase the cost of the system.

In parallel with the development of self-referencing techniques, intensity sensors based on glass optical fiber (GOF) have been developed for monitoring temperature. Different techniques to measure temperature with macro-bend sensors have been developed using singlemode [13-20], multimode [19, 21] and doped [22] singlemode GOF. However, the expectation for the production of optical fiber sensors at low or competitive cost compared to the well-stablished conventional technologies are not satisfied with glass-based technology. For this reason, POFs are seen as a lower cost alternative solution to glass-based sensors. POFs have the intrinsic advantages of any optical fiber and in addition they have a larger core diameter and a smaller Young modulus [23], making them less fragile and easier to handle; reducing development and maintenance costs associated with the complete system. POF dimensions allow the use of low precision connectors

and lenses as well as simple multiplexing and demultiplexing devices, especially if compared with GOF-based sensors, which can make possible the implementation of low cost sensing systems. Although polymer based sensors have a smaller temperature range [23]. POFs are also very attractive for exploitation in medical or alimentary industry because they are inherently more biocompatible compare to their glass counterparts. Moreover the use of glass fiber is sometimes inappropriate due to the risks from breakages.

In this chapter, it is developed a low-cost intensity macro-bend temperature sensor based on POF. In a first approach, a self-reference property is achieved by a dual-beam technique [24], using a dummy fiber-optic sensor, and then computing the optical power ratio of both signals. The main disadvantage of using a dummy fiber-optic sensor is the repeatability of the manufacturing process which limits the robustness of the system. To overcome this problem, the temperature sensor is improved in a second approach, by using a single macro-bend loop. The sensor system used the ratio of transmittance at two wavelengths to implement the self-referencing technique [25]. An analysis has been developed to find the two wavelengths which ratio offers the highest linearity and sensitivity response. In both schemes, experimental results are successfully compared with mathematical models based on geometric approaches [26]. Another important attribute that will be discussed in this chapter is a comparison between other intensity temperature sensors and self-referencing techniques reported on the literature. Finally, the highly multimode nature of POF sensors implies special features as the influence of external surrounding media that have to be analysed in practical implementations.

2.2. Multimode Step-Index Polymer Optical Fiber

2.2.1. History of Multimode Polymer Optical Fiber

The first multimode POF based on polymethacrylate (PMMA) was manufactured by DuPont as early as the late sixties. This fiber-optic had a step-index (SI) profile and could be enlarged to about 980μm in diameter without losing its flexibility or ease of fiber alignment. SI POF was also advantageous in terms of mass production. Such fiber was not only inexpensive to fabricate, but it was also easy to mold and manufacture. Due to the incomplete purification of the monomer material used, attenuation was still in the vicinity of 1,000dB/km [27].

The first commercialized SI POF was introduced by Mitsubishi Rayon during the seventies. The high attenuation of the first fibers could be reduced nearly to 300dB/km at a wavelength of 650nm [28, 29]. Comparatively, GOF presented attenuation in the order of 1dB/km at 1,300nm and were already available commercially at relative low prices [23].

In spite of this breakthrough, SI POF were not transparent enough to be used in the last hundred meters. Over the next few years, different research were able to reduce the loss of PMMA fibers to close to the theoretical limit of 150dB/km at 650nm [30]. However, despite innumerous developments, improvement of the bandwidth of SI POF has its limitations. For transmission, it must excite several tens of thousands of mode, more modes than those found in multimode GOF. The large core increases modal dispersion, drastically degrading its bandwidth to about several hundred megahertz over 100m [31].

The forecast of a fast increase in demand for high-speed information transmission conducted to improve the bandwidth of SI POF. The modal dispersion could be reduced drastically by adopting and appropriate refractive index profile in the core region, as in multimode GOF. Prof. Koike and colleagues at Keio University developed a process to manufacture graded-index (GI) POFs using PMMA material to reducing the modal dispersion. The development of GI PMMA POF solved the bandwidth problem of the SI PMMA POFs, reported a bandwidth of 2GHz·km with losses of 150dB/km at 650nm [32]. Despite the high development of the manufacturing technique to improve the bandwidth, the losses were still high. The next major development was a graded-index perfluorinated polymer optical fiber (GI PF POF). GI PF POF is considered feasible for wavelengths from 650 to 1,300nm, with attenuation coefficient lower than 50dB/km [23]. To date, the best results in the production of low attenuation POF with PF material were obtained with cyclic transparent optic polymer (CYTOP). The attenuation coefficient was 10dB/km for 1,300nm [23].

2.2.2. Mechanical Properties

The great interest of POF based on PMMA has been due to the wide range of applications and the good mechanical characteristics with respect to GOFs.

Several authors have studied the mechanical properties of POFs. The majority of these studies have been focused on the attenuation induced by bends and tensile or torsion stresses. The Young's modulus of a POF based on PMMA is around 2.7GPa [33]. This value is twenty times lower than the one at GOF [34]. For this reason, POFs offer high flexibility allowing rough handling of the fiber without causing permanent damages. In addition, the minimum bend radius for POFs is smaller, since plastic is more ductile and much less stiff than glass. The transmission rate through a POF depends on some mechanical properties. An important factor is the cycling bendings that can cause variation in the attenuation and limit the bandwidth. It has been demonstrated that more than 20 bends at 90º with a radius of 14mm can cause a loss over 5dB for a 50m length Gigabit Ethernet link [35].

2.2.3. Thermal Properties

POF based on PMMA can operate at temperatures around 80ºC. Above this limit, POF begin to lose their rigidity and transparency. Fibers with high resistance to heat have been developed for use in certain applications where temperature can go up to over 100°C, for instance the sensor communication network in the automobile engine compartment. PMMA POF can easily be used with such temperatures. The majority of these fibers are based on partially fluorinated polycarbonate [36], thermoplastic resin [37] and silicon elastomer [38]. In general, POFs can also withstand temperature as low as -70ºC.

An important factor to characterize the thermal behaviour of a POF is the thermal stability. The thermal stability is determined by measuring the maximum increase in the attenuation over a maximum period of aging. In case the aging procedures are thermally activated, then the permissible operating period decreases almost logarithmically with the temperature. For a POF based on PMMA, with an approximate 10ºC increase in temperature the fiber optic loss increases about one order of magnitude after 1,000 hours [23].

Other important factor to determine the thermal behaviour of POFs is the degree of humidity. Different experiments have demonstrated that if the POF is maintained at 85ºC with 85% of relative humidity for 1,000 hours, the attenuation will increase in 0.02dB/km [39]. On the other hand, if the relative humidity level is around 90%, the attenuation increases more than 0.03dB/m [39]. To overcome this problem, TOPAS fiber [40] has been developed displaying lower water absorption than PMMA based optical fiber.

2.2.4. Multimode Polymer Optical Fiber Connectors

Transmission and sensor systems require connectors for coupling fibers to active equipment (light sources, power meters, couplers, among others). The connector design must allow for repeated connection and disconnection, have good loss performance, and also protect the fiber from damage.

The steps for assembling a POF connector by polishing technique are shown in Figure 2.1. The simplest optical fiber connector are based on a ferrule (ST, SC, FC, V-Pin or SMA types), which can also be made of metal, ceramic or plastic. A short piece of fiber cladding is stripped off. The fiber to be connected is permanently bonded with epoxy inside the ferrule. Different systems with crimped fiber using a metal ring or mechanical splice inside the connector also exist [23]. After cutting off the excess fiber, except for a little bit left over, cutting and polishing take place using sandpapers in several steps.

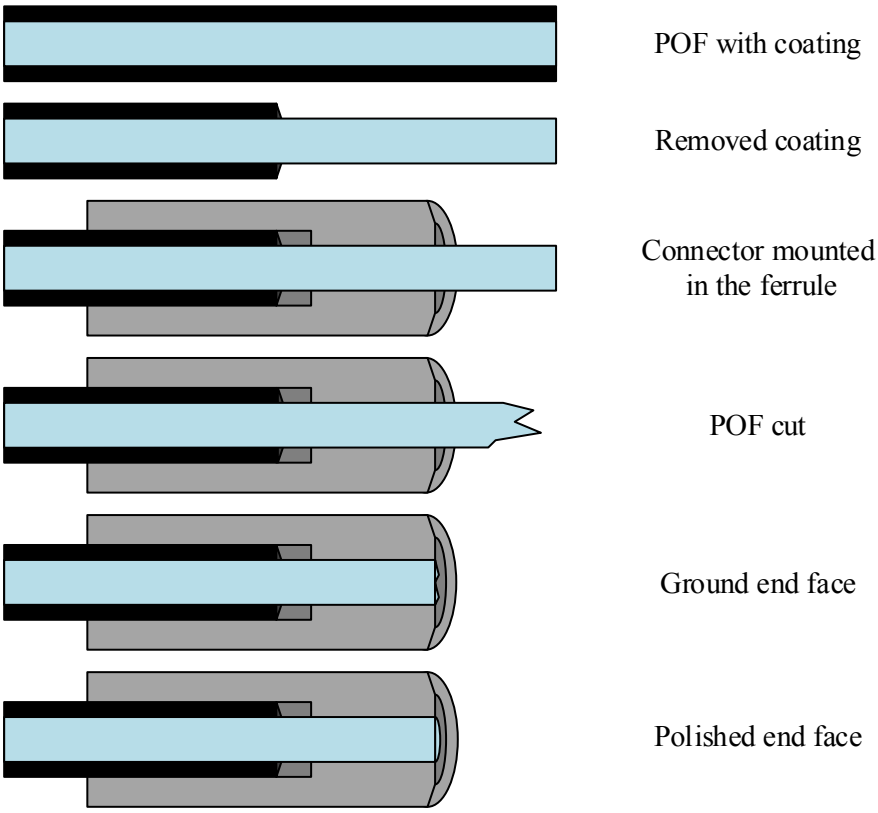

Figure 2.1. Surface preparation by polishing technique.

The major advance of POF is the fiber diameter. POF requires less precise parts to align the fiber. This make it possible to have a low-cost, quick and easy to assemble connector compared to GOF.

2.2.5. Applications of Step-index Polymer Optical Fiber

Although SI POFs have been available for some time, only GOF found applications as a high capacity transmission medium. The recent improvements in the transparency and bandwidth of SI POF have led to their use in the telecommunications field. At present, SI POF are advantageously replacing copper cables in local communications networks by offering the advantages intrinsic to any optical fiber in relation to transmission capacity, immunity to interference and small weight. In addition, SI POFs offer a complement for glass fiber in short-reach communication links because they are easy to handle, flexible, small weight, economical and relative low-loss at short distances. These characteristics make them suitable as a means of connection between a large net of GOF and residential area, medium-size enterprises (SMEs) and local area networks (LANs). Fast Ethernet LANs (100Mbps) or Gigabit Ethernet LANs (1Gbps) over SI POF are now considered for small business and homes due to the announce of several POF companies to commercialize low-cost transceivers [41].

An important field where the use of POF has led a significant progress is the automotive industry. Automobile manufactures recognize that the increasing use of digital devices in automobiles increased the weigh, susceptibility to EMI, and complexity of wiring harnesses. As automobiles become more and more complicated, the weight and volume of copper-based networks create limitations for new automobiles designs. To overcome those limitations, cost-conscious automotive engineers are finally turning to SI POF developing several optical buses [42-44] . SI POF can replace many individual copper wires, resulting in major weight and space savings. The current copper cable inevitably generate electromagnetic noise problem limiting the data transmission speed. SI POF offers a high operation bandwidth, increased transmission security and reliability, immunity to EMI and anti-shock, ease of handling, connection and installation, flexibility, long shelf life and low-cost solution.

Due to successful growth of SI POF in the automotive industry, such fibers are now seriously being considered for applications in the aerospace industry. A viable solution to implement the use of optical fibers in the aerospace industry is using fly-by-light hardware [45, 46]. In general, fly-by-light refer to the applications of fiber optic to aircraft control and avionics systems. Different studies advocate the use of SI POF to replace their conventional electronic counterparts [47]. As success with automobile industry, there are a wide variety of potential benefits that can be realized with the use of optical fibers. The light weight of fiber optic cables represents an important benefit on aircraft. For the flight and engine control systems of a commercial widebody, over 450Kg can be saved by replacing today's fly-by-wire systems with their fly-by-light counterpart, and over 900Kg of weight saving over conventional mechanical control systems [48]. This weight reduction represents a considerable fuel efficiency improvement.

Historically, the main application of the SI POF was the transmission of optical signals, developing short reach low-cost telecommunication networks [39]. The advances in fabrication of low-loss POF and in components for optical fiber communications have encouraged the development of a new range of highly versatile optical sensors based on POF technology. There are many strong arguments for the use of SI POFs as sensors. In addition to their easiness to handle, small size and low prices, SI POF present the advantages common to all multimode optical fibers. SI POFs have important characteristics particularly associated to all fiber optic sensors, such as: extremely good electromagnetic interference immunity and a risk reduction of electric sparks in explosive environments. On the other hand, SI POF offers the possibility to develop medical sensors due to its high biocompatibility with the human being [49]. These good characteristics have been used to develop a large variety of SI POF sensor configurations which are able to collect information for remotely located monitoring centers. These include pressure

[50], humidity [51], temperature [52], wind speed [53], liquid level [54], liquid detection [24], among others.

2.3. Principle of Operation

A SI multimode optical fiber curved with a bend radius R and a core diameter $2\rho_{Core}$ is shown in Figure 2.2.(a) and Figure 2.2.(b). The core and cladding refractive indices are n_{Core} and $n_{Cladding}$, respectively. The geometrical approach used to describe the core rays in a planar waveguide [55] is adapted to the bent optical fiber, due to the presence of the skew rays [56].

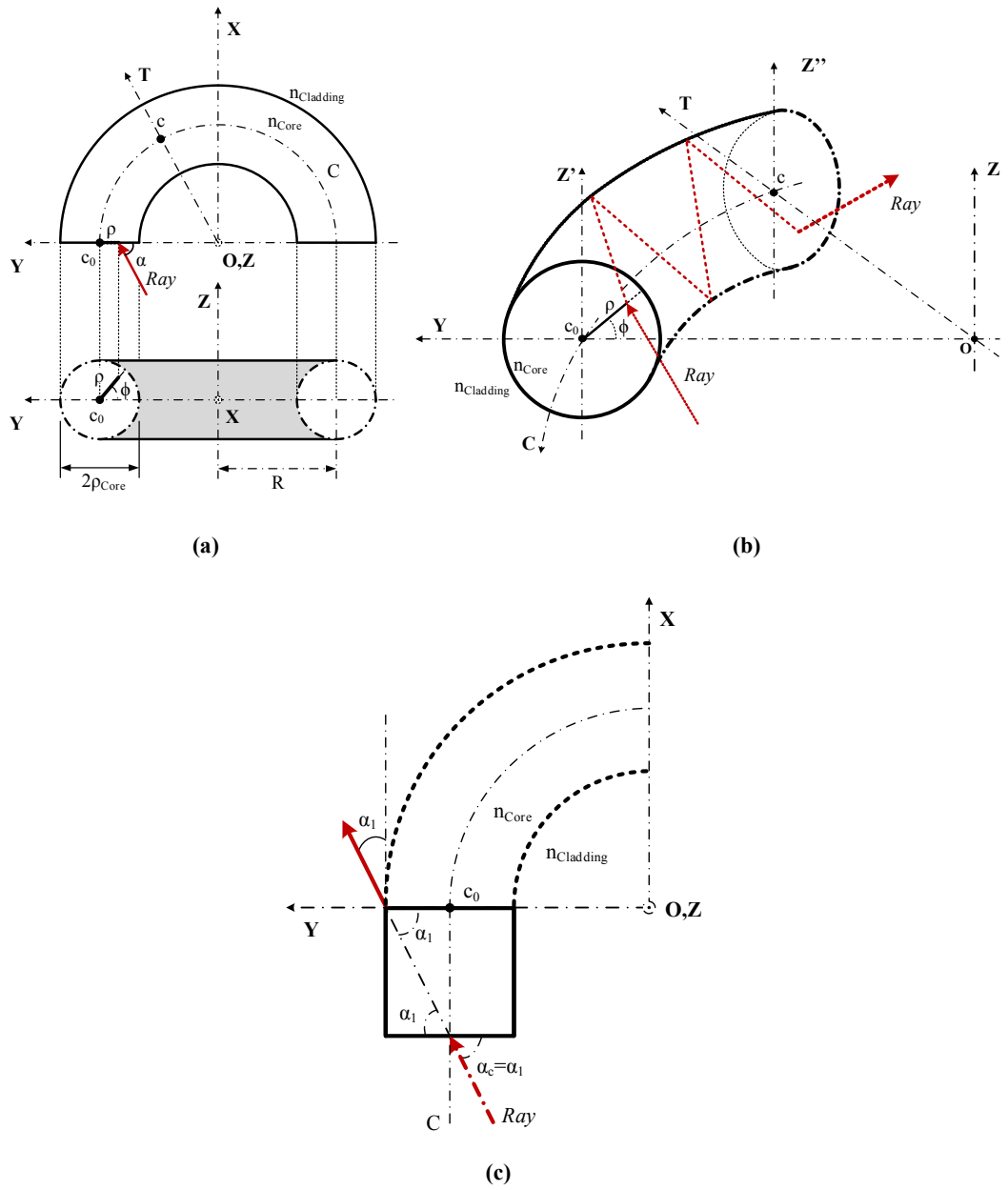

Figure 2.2. Schematic of a bend fiber section curved with a radius of curvature R. (a) Top view (b) 3-D section. (c) Rectilinear fiber interface.

The guidance of the core rays is achieved by ensuring that the propagation angle, α, satisfies the condition: $0 \leq \alpha \leq \alpha_c$, see Figure 2.2.(c), where the critical angle (α_c) is given by:

$$\alpha_c = \sin^{-1}\left(\frac{n_{Cladding}}{n_{Core}}\right) \quad (2.1)$$

The expression of the numerical aperture (NA) for the rectilinear region is given by:

$$NA = n_{Core} \cdot \sin(\alpha) \leq \left(n_{Core}^2 - n_{Cladding}^2\right)^{1/2} \quad (2.2)$$

However, in the bend optical fiber, the guidance of the core rays can follow two ways. Only the rays entering the bent part of the fiber in the meridional plane remain with the same angle of incidence along a given ray path. On the other hand, the skew rays entering this plane, after the successive reflections within the core, do not follow a simple repeatable pattern because of the asymmetry introduced by bending the fiber. So when the optical fiber is bent, the local NA changes at a given location of the bent optical fiber. The dependence of the NA with the bend is given by [55]:

$$NA(R,\rho,\phi) = n_{Core} \cdot \left[1 - \frac{n_{Cladding}^2}{n_{Core}^2} \cdot \left(\frac{R + \rho_{Core}}{R - \rho \cdot \cos(\phi)}\right)^2\right]^{1/2} \quad (2.3)$$

where ϕ is the ray angle at the beginning of the bend, which varies from 0º to 180º, ρ_{Core} is the fiber core radius and ρ is the radial position in the core satisfying the relation $0 \leq \rho \leq \rho_{Core}$.

The optical fiber sensor proposed in this chapter is based on a macro-bend POF. In this intensity sensor, the losses induced by the bending effect depend on the NA, that changes with temperature. The refractive index of the core and cladding POF depend on the temperature. The optical fiber used in this experiment is a SI POF [57] with polymethylmethacrylate (PMMA) 980μm core diameter and 1mm cladding diameter of fluorinated polymer. The temperature dependence of the core refractive index can be expressed as [58]:

$$n_{Core}(T) = K_2 \cdot T^2 + K_1 \cdot T + n_0 \quad (2.4)$$

where K_1=-1.15·10^{-4} ºC^{-1} is the thermo-optic (TO) coefficient of the core, K_2=-5.173·10^{-7} ºC^{-2} is the second order temperature dependence term of the core and n_0=1.49538 is the core refractive index at 0°C. On the other hand, the temperature dependence of the cladding refractive index is given by [59]:

$$n_{Cladding}(T) = n_{Cladding}(T_0) + K_3 \cdot (T - T_0) \quad (2.5)$$

where K_3=-3.5·10^{-4} ºC^{-1} is the TO coefficient of the cladding and $n_{Cladding}(T_0)$=1.403 is the cladding refractive index at the reference temperature (T_0=25°C). It can be seen that $|K_3|>|K_1|$. Finally, from Equation (2.3), the local NA in the bent section of the fiber versus the temperature can be expressed as:

$$NA(T,R,\rho,\phi) = n_{Core}(T) \cdot \left[1 - \frac{n^2_{Cladding}(T)}{n^2_{Core}(T)} \cdot \left(\frac{R + \rho_{Core}}{R - \rho \cdot \cos(\phi)} \right)^2 \right]^{1/2} \quad (2.6)$$

Using Equations (2.4) to Equation (2.6), the temperature dependence of the NA for different ray radial positions in the core has been plotted in Figure 2.3.

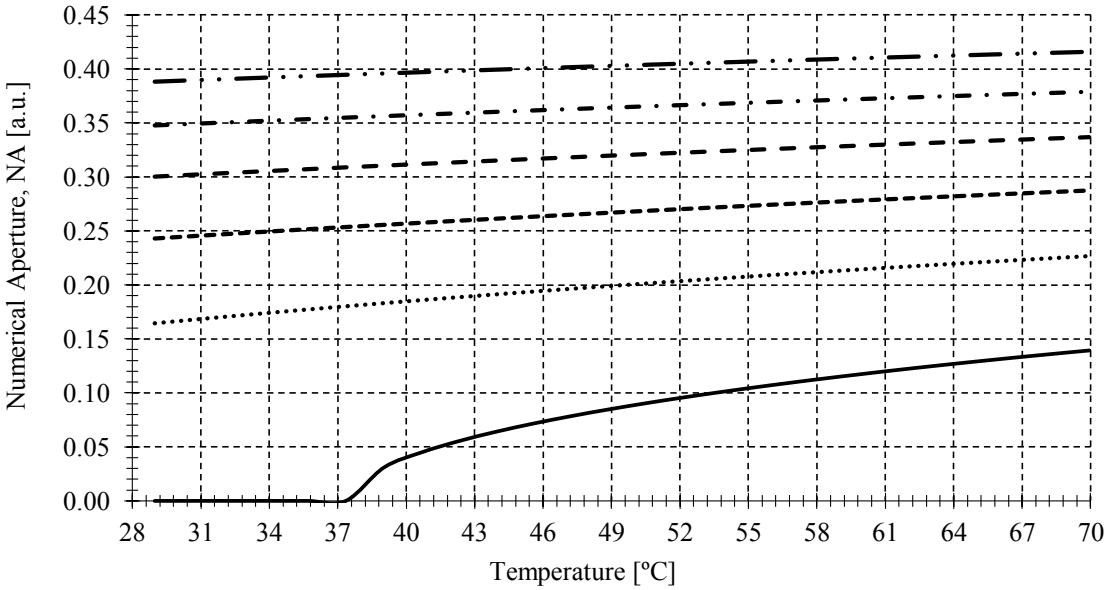

Figure 2.3. Local numerical aperture versus temperature, 2·ρ_{Core}=980µm, R=2mm and ϕ=150º: — ρ=390µm, · · ρ=410µm, -- ρ=430µm, – – ρ=450µm, –·– ρ=470µm, –··– ρ=490µm.

Analysing the positive slope of the curves for each radial position, it can be seen that the local NA increases when the applied temperature increases. This increment happens because an optical ray that is unguided at the reference temperature becomes guided at temperatures greater than the reference temperature. Figure 2.4 shows the local NA as a function of the bend radius at T_0=25°C. The local NA increases as the bend radius increases up to the local NA for a straight fiber (R=∞) with a value around 0.5.

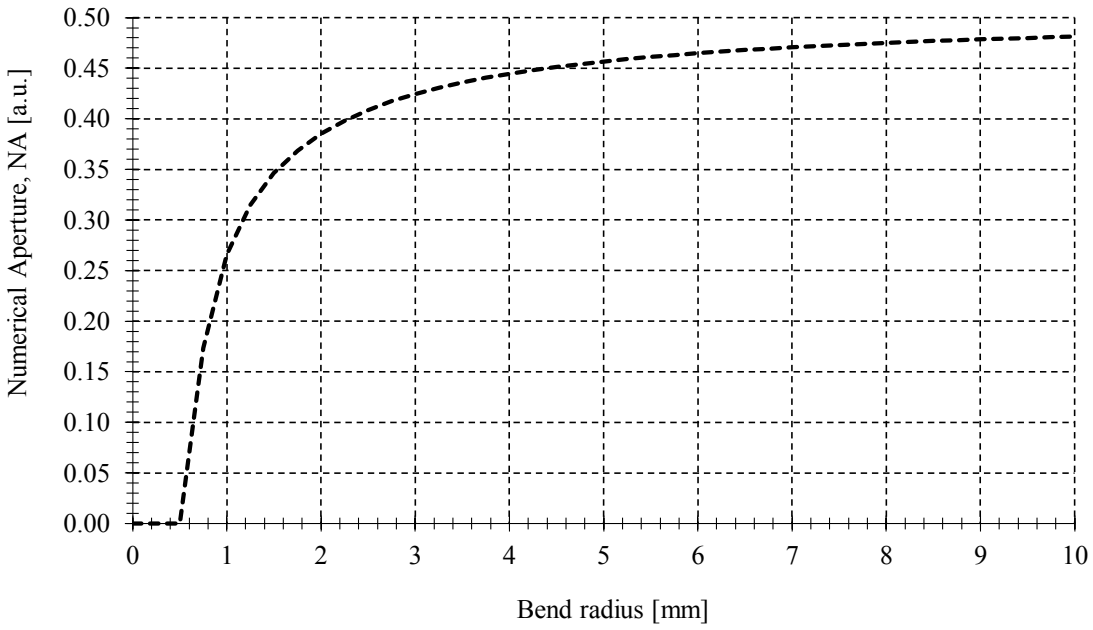

Figure 2.4. Local numerical aperture versus bend radius, ρ=490μm and ϕ=150º.

The insertion losses of the sensor at a specific temperature increase as the bend radius decreases. The POF used in the experiments has a critical radius of curvature of 25mm, so the manufactured sensor is always operating at a lower *R* value as it is shown below.

For small amplitude variations in the core radius, the ratio of output to input power at the bent sensor (η) is given by [39]:

$$\eta_{Sensor} = \left.\frac{P_{Out}}{P_{In}}\right|_{Sensor} = \frac{\left[n^2_{Core}(T) - n^2_{Cladding}(T)\right]\Big|_{Bent\ region}}{\left[n^2_{Core}(T) - n^2_{Cladding}(T)\right]\Big|_{Straight\ region}} \qquad (2.7)$$

where P_{Out} is the output optical power in the bent region and P_{In} is the input power, corresponding to the output of a straight region at c_0, see Figure 2.2. Insertion losses, fiber attenuation and other parameters of the system are not included.

The output power ratio temperature sensitivity increases as the bend radius, *R*, increases as demonstrated in [26]. In addition, the linearity of the sensor output power ratio decreases as the bend radius increase. For these reasons, a sensor bend radius of 2mm is selected to achieve low insertion losses, and higher linearity and sensitivity of the calibration curve.

On the other hand, in this intensity sensor, the losses depend on the NA change with the core and cladding refractive index variations. Those refractive indexes depend on the temperature

and the wavelength. The refractive index of the core and cladding can be fitted to a three-term Sellmeier dispersion relation of the form [60]:

$$n(\lambda)=\left[1+\sum_{i=1}^{3}\frac{A_i\cdot\lambda^2}{\lambda^2-l_i^2}\right]^{1/2} \qquad (2.8)$$

where n is the core or cladding refractive index, A_i is the oscillator strength, l_i is the oscillator wavelength, and λ is the wavelength of light.

The Sellmeier equation coefficients for a PMMA and a fluorinated polymer as a function of temperature are reported in [61, 62]. From Equation (2.8), the first term of the Sellmeier coefficients for a fluorinated polymer have been adjusted to obtain the cladding refractive index of the fiber at the conditions given by the manufacturer. The fiber used in this experiment has a cladding refractive index of 1.4 at 25ºC and 650nm [63]. Using the Sellmeier coefficients for the core and cladding material (see Table 2.1) and considering T_1=27ºC, the NA for the fiber at 25ºC and 650nm is 0.511. This value is in good agreement with the NA given by the manufacturer, NA=0.485±0.045 at 25ºC and 650nm [63].

Coefficient	**Units**	**PMMA**	**Original fluorinated polymer**	**Adjusted fluorinated polymer**
A_1	a.u.	0.4963	0.2680	0.34
l_1	nm^2	$71.8\cdot(T/T_1)^2$	$79.13\cdot(T/T_1)^2$	$79.1\cdot(T/T_1)^2$
A_2	a.u.	0.6965	0.3513	0.351
l_2	nm^2	$117.4\cdot(T/T_1)^2$	$83.81\cdot(T/T_1)^2$	$83.81\cdot(T/T_1)^2$
A_3	a.u.	0.3223	0.2498	0.25
l_3	nm^2	$9237\cdot(T/T_1)^2$	$106.2\cdot(T/T_1)^2$	$106\cdot(T/T_1)^2$

Table 2.1. Coefficient of the Sellmeier equation for different polymers. Note: T is the temperature and T_1 is a reference temperature in ºC.

From Equation (2.2) and (2.8), and using the core and cladding Sellmeier coefficients, the NA in a POF rectilinear region is plotted against wavelength for different temperatures in Figure 2.5.

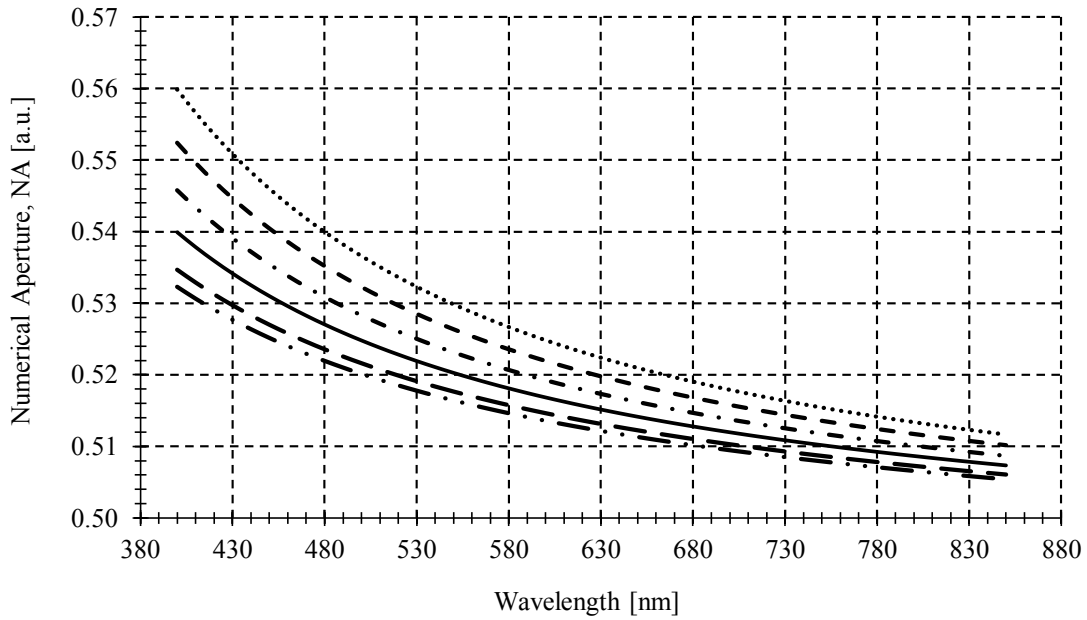

Figure 2.5. Local numerical aperture versus wavelength in a POF rectilinear region: −··− 25ºC, − − 30ºC, — 40ºC, −·− 50ºC, -- 60ºC, · · 70ºC

On the other hand, when the optical fiber is bent, the temperature and wavelength dependence of the NA changes at a given location of the bent optical fiber. Using Equations (2.3) and (2.8), and the core and cladding Sellmeier coefficients, the temperature and wavelength dependence of the NA for a bend fiber can be expressed as:

$$NA(T,\lambda,R,\rho,\phi) = n_{Core}(T,\lambda)\cdot\left[1-\left(\frac{n^2_{Cladding}(T,\lambda)}{n^2_{Core}(T,\lambda)}\right)\cdot\left(\frac{R+\rho_{Core}}{R-\rho\cdot\cos(\phi)}\right)^2\right]^{1/2} \qquad (2.9)$$

NA in a bend region is plotted against wavelength for different temperatures in Figure 2.6. A bend radius of 2mm is considered.

It can be seen that the local NA decreases when the wavelength of light increases. In addition, the local NA increases when temperature increases. This happens because an optical ray that is unguided at the reference temperature becomes guided at greater temperatures. On the other hand, the NA temperature sensitivity increases when a bend is applied to the optical fiber, as shown in Figure 2.5 and Figure 2.6, with maximum NA temperature sensitivity of $1.3\cdot10^{-3}$ ºC^{-1} and $6.1\cdot10^{-4}$ ºC^{-1} for an unbent and bent fiber illuminated with a 400nm light source, respectively.

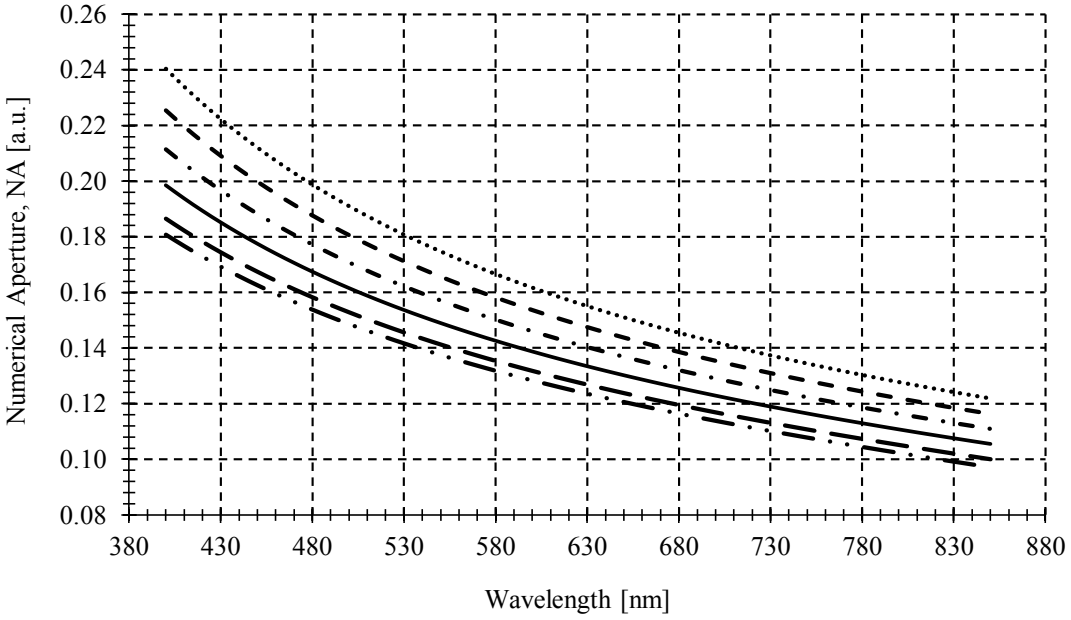

Figure 2.6. Local numerical aperture versus wavelength for a bent POF, R=2mm, ϕ=135º and ρ=490μm: −··− 25ºC, − − 30ºC, — 40ºC, −·− 50ºC, -- 60ºC, · · 70ºC

The output optical power in the bent region can be calculated using Equation (2.8) and (2.9). On the other hand, the input power of the sensor corresponds to the output power of a straight fiber, as shown in Figure 2.2.(c). This value is obtained using the Equations (2.2) and (2.8). In both cases, the Sellmeier coefficient of the cladding and core is used. The output power ratio versus temperature for different wavelengths is plotted in Figure 2.7. The power ratio increases when temperature increases as demonstrated in [52].

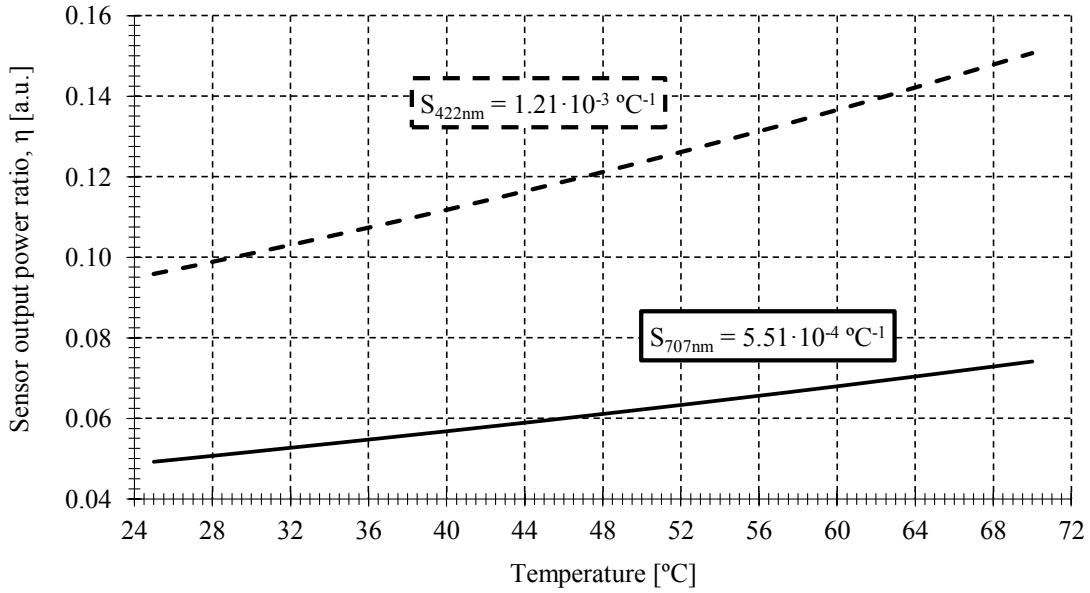

Figure 2.7. Power ratio versus temperature in a bent fiber, ρ=490μm, R=2mm and ϕ=135º: − − λ=422nm, — λ=707nm.

2.4. Design and Manufactured Sensor

In this section, some aspects of the manufacturing process and the sensor dimensions are reported. The Figure 2.8. describes a photograph of the manufactured fiber-optic temperature sensor. A bend radius of 1.5 and 2mm are selected to achieve a linear response of the output power ratio versus temperature as described in [26].

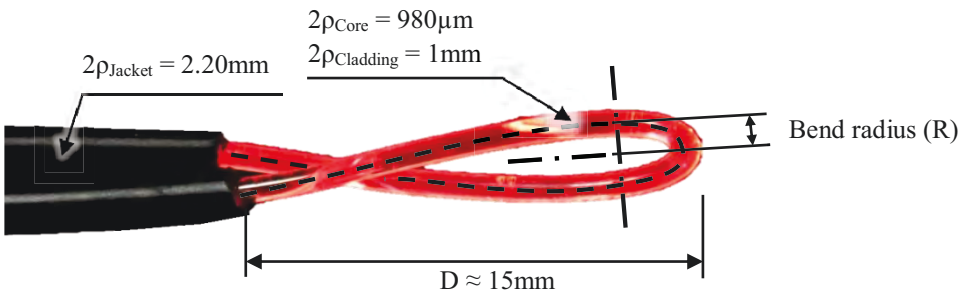

Figure 2.8. Schematic and photograph of the macro-bend POF sensor

The PMMA-based POF used in the experiment allows a minimum bend radius of 25mm [57]. This means that the losses are negligible when the fiber is bent with a radius above 25mm. The tensile strength and the Young's modulus are 70N and 2.7GPa, [57], [33], respectively. These characteristics provide good mechanical properties at the time of manufacturing the sensor and permit to bend the fiber below the minimum bend radius without break, despite of the attenuation increments. From the middle section of the fiber length, the buffer coating is partially stripped. The length of this stripped section is around 30mm. The fiber sensor is formed by creating a single 180º loop with a specific bend radius, as shown in Figure 2.8. To fix the radius, a cylinder is used to facilitate and give more precision to the bending process. Then, the buffer coating in the junction of the two branches is fixed by cyanoacrylate adhesive.

2.5. Self-referenced Technique Using a Dummy Fiber-optic Sensor

For avoiding errors related to undesired intensity fluctuations, an additional macro-bend fiber loop, identical to the proposed fiber-optic sensor is used for reference purposes, as shown in Figure 2.9. This fiber-optic reference or dummy sensor, placed outside of the heating unit, monitors the optical power fluctuations not related to the sensing magnitude. The output voltage at the reference ($V_{Reference}$) and sensing (V_{Sensor}) branch can be expressed as:

$$V_{Reference} = L_{Reference} \cdot \Re_{\lambda} \cdot \delta \cdot G_{Reference} \cdot F'(T_0) \cdot P_{LightSource} \qquad (2.10)$$

$$V_{Sensor} = L_{Sensor} \cdot \Re_{\lambda} \cdot \delta \cdot G_{Sensor} \cdot F(T) \cdot P_{LightSource} \quad (2.11)$$

where L_{Sensor} and $L_{Reference}$ are factors including the attenuation of the fiber leads, coupler insertion losses and connectors losses, of the sensing and reference branch respectively. $\Re_{\lambda}$ is the photodiode responsivity at the operating wavelength (λ=660nm), considering identical photodiodes. δ is the scale factor of the receivers for a specific output impedance. $G_{Reference}$ and G_{Sensor} are the transimpedance amplifier gains for the reference and sensor branch, respectively. $F(T)$ is the optical power modulation function versus temperature at the fiber-optic sensor and $F'(T_0)$ is the insertion loss at the reference temperature (T_0) of the dummy sensor. Finally, $P_{LightSource}$ is the optical power of the light source.

In order to compare the calibration curve with mathematical models and other intensity fiber optic sensors, the output voltage at the reference and sensing branch is expressed in optical power units. The output optical power at the reference ($P_{Reference}$) and sensing (P_{Sensor}) branch can be expressed as:

$$P_{Reference} = L_{Reference} \cdot F'(T_0) \cdot P_{LightSource} \quad (2.12)$$

$$P_{Sensor} = L_{Sensor} \cdot F(T) \cdot P_{LightSource} \quad (2.13)$$

From both equations, the self-reference output power ratio γ_{SR} is defined as:

$$\gamma_{SR} = \frac{P_{Sensor}}{P_{Reference}} = \frac{L_{Sensor} \cdot F(T) \cdot P_{LightSource}}{L_{Reference} \cdot F'(T_0) \cdot P_{LightSource}} = \frac{L_{Sensor}}{L_{Reference} \cdot F'(T_0)} \cdot F(T) \quad (2.14)$$

Therefore the ratio of the output optical powers depends on the power sensor variations with temperature and on a constant ratio between the insertion losses of the sensing and reference branch.

2.5.1. Experimental Set-up

The schematic and a photograph of the experimental set-up is shown in Figure 2.9. The light source is a 660nm Light-Emitting Diode (LED) [64]. The fiber-optic sensor is fixed close to the rectangular highly conductive metal base plate of a heating unit [65]. The temperature of the hot plate is controlled with a controller unit [66]. For measuring the real temperature of the optical fiber sensor, an independent electronic temperature sensor [67] is used in the measurements. Temperature measurements are taken on the hot plate and at a 1mm distance from the hot plate.

A thermal isolated stage is performed for supporting the fiber sensor when it is placed at a 1mm distance from the plate. A calliper is used to measure the position.

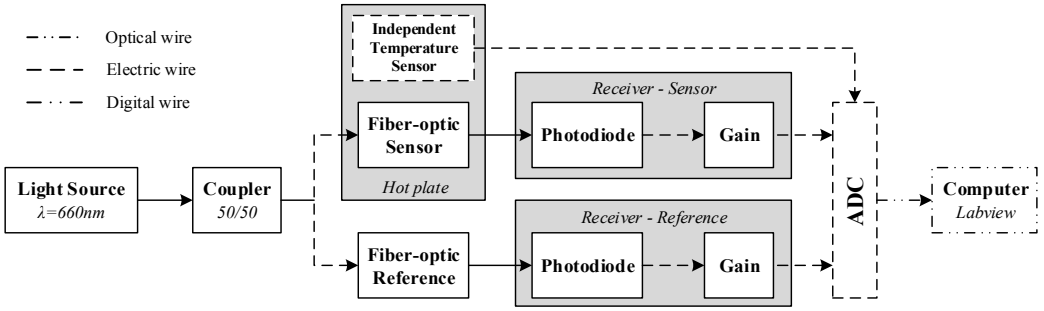

(a)

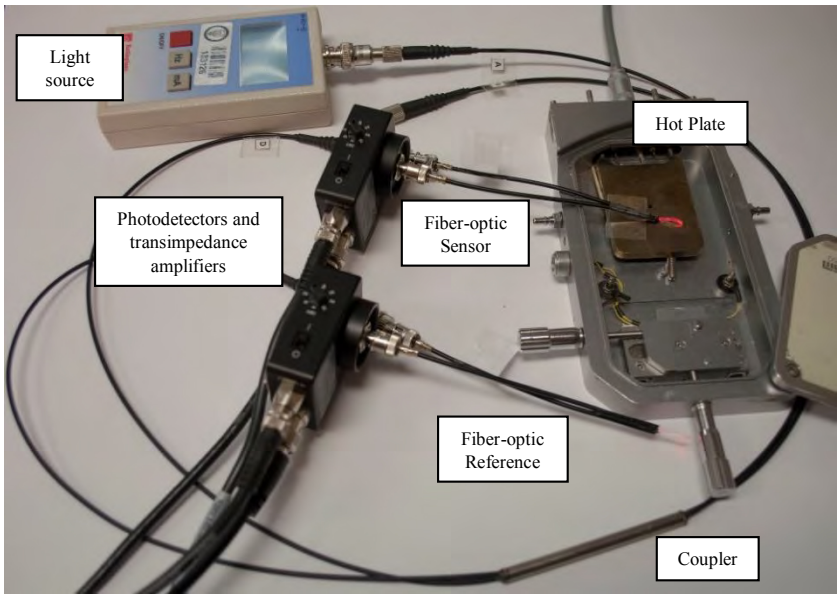

(b)

Figure 2.9. (a) Schematic of the experimental set-up characterizing the POF temperature sensor. (b) Photograph of the experimental set-up with the sensing and referencing branch.

In the experiments, the self-reference output power ratio (γ_{SR}) is measured from 29 to 70ºC at 2ºC intervals. The minimum temperature is limited by the cooling capabilities of the heating unit and the maximum temperature is limited by the capabilities of the POF. A time interval of 2min is set, between each temperature measurement, to ensure the stabilization of the voltage values. The amplifier gain of the transimpedance amplifier is fixed at 10dB for all measurements. The sample rate and the number of samples of the output power ratio at each temperature are fixed at 5Hz and 10 samples, respectively. A total of six sets of measurements of the calibration curve are carried out to perform a complete statistical analysis of the sensor parameters. Software based on a graphical code is developed to acquire the voltage from the receivers, to calculate the optical power of each branch and to post-process the data.

2.5.2. Temperature Sensor Characterization for Different Bend Radii

Figure 2.10 shows the measured calibration curves for a bend radii of 1.5 and 2mm. The distance between the sensor and the hot plate is fixed at 1mm. Setting a distance between the sensor and the hot plate prevents possible changes in the refractive index of the cladding due to the contact with other materials as it is discussed in the next section. At a 1mm distance, the temperature of the sensor varies from 27.2 to 50.2°C.

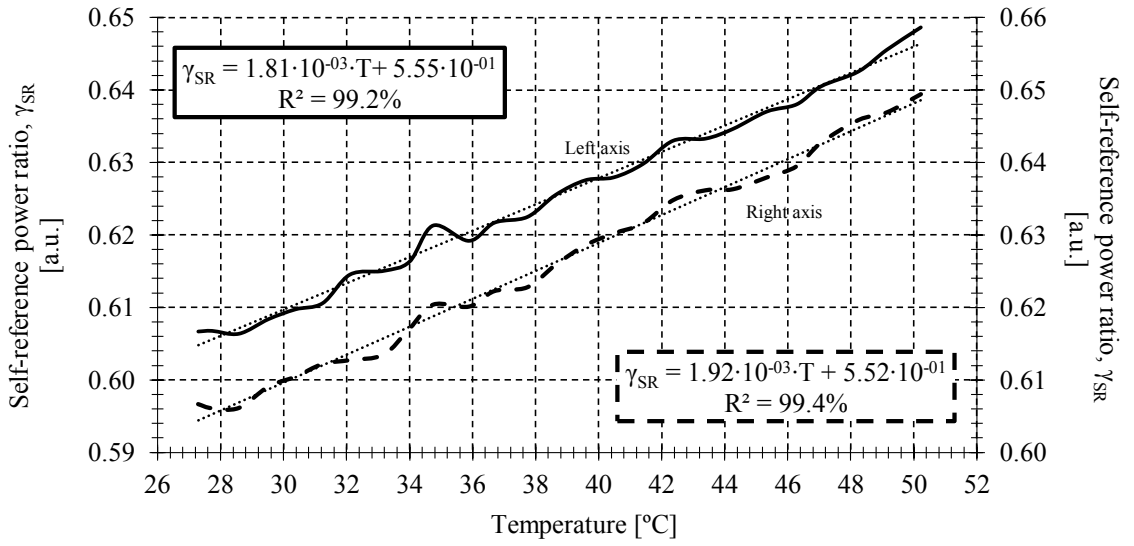

Figure 2.10. Self-reference output power ratio versus temperature: — R=1.5mm, − − R=2mm.

The measurements show a good linearity response. The sensitivity obtained for the two bend radii is $1.81 \cdot 10^{-3}$ and $1.92 \cdot 10^{-3}$ ºC^{-1} for bend radii of 1.5 and 2mm, respectively. These values can be expressed as $1.27 \cdot 10^{-2}$dB/ºC and $1.29 \cdot 10^{-2}$dB/ºC. From these values, it is observed that the sensor temperature sensitivity is clearly higher than the temperature coefficient of the fiber attenuation $\beta_R = 1.5 \cdot 10^{-6}$dB/ºC, for a 3cm long POF sensor [63]. Linear regression coefficients greater than 99% are obtained.

The experimental results are compared with simulations using a mathematical model based on geometric approaches. The model is based on treating light as individual rays that propagate in a zigzag path, taking into account the changes in ray directions and probable radiation losses that take place at the reflection points on the core-cladding interface. A detailed description of the model can be seen in [26]. The simulations are done in collaboration with Applied Photonics Group[1] at Universidad del País Vasco leaded by Prof. Joseba Zubia, and they show the input to

[1] Applied Photonics Group. Communication Engineering Department. Escuela Técnica Superior de Ingenieros de Bilbao. Universidad del País Vasco. Spain.

output power ratio at the sensor (η) for 50,000 rays and an infinite cladding interface using the model reported in [26].

In order to compare the measured calibration curves with the simulations, it is derived the measured input and output optical power at the sensor curve. The simulations and measurements for bend radii of 1.5 and 2mm can be seen on Figure 2.11. Four temperatures from 29 to 52ºC are evaluated to get the theoretical calibration curve of the sensor in both cases.

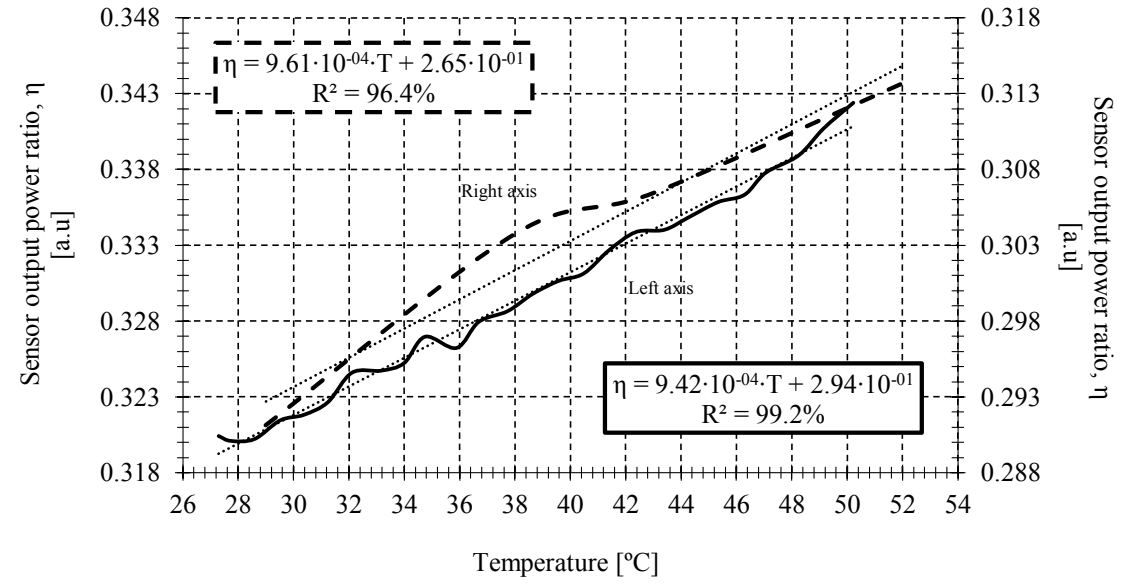

(a)

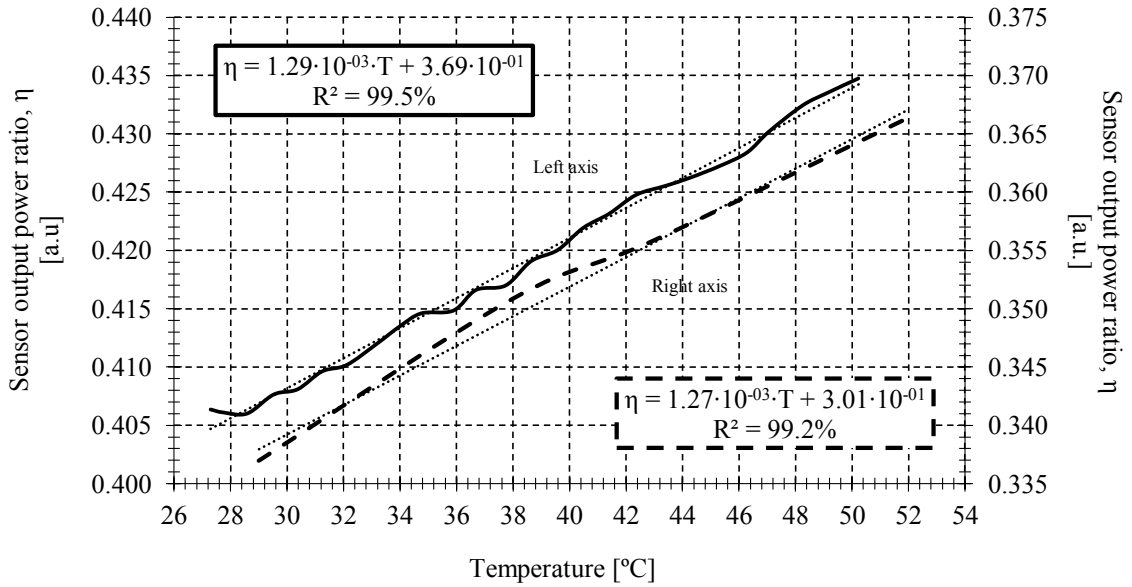

(b)

Figure 2.11. Experimental (—) and simulation (− −) sensor output power ratio versus temperature for several bend radii: (a) 1.5mm; (b) 2mm.

Figure 2.11.(a) shows the theoretical and experimental sensitivity for a bend radius of 1.5 and 2mm. The values obtained are $9.61 \cdot 10^{-4}$ ºC^{-1} and $9.41 \cdot 10^{-4}$ ºC^{-1}, respectively. The linear regression coefficients are 96.4% and 99.2%, respectively. On the other hand, Figure 2.11.(b) shows the theoretical and experimental sensitivity for a bend radius of 2mm, with values of $1.27 \cdot 10^{-3}$ ºC^{-1} and $1.29 \cdot 10^{-3}$ °C^{-1}, respectively. The linear regression coefficients are higher than 99%, in both cases. The insertion losses of the macro-bend sensor without connectors for bend radii of 1.5 and 2mm are 4.94 and 3.91dB, respectively. As expected, the insertion losses for a bend radius of 1.5mm are greater than those for a bend radius of 2mm. It can be concluded that measurements are in good agreement with simulations, with better results for a 2mm bend radius. Analysing the sensitivity for the proposed bend radii, it can be seen that it increases when bend radius increases, due to the increment of the NA with bend radius, as previously shown in Figure 2.4.

2.5.3. Temperature Sensor Characterization on Different Surrounding Media.

The SI POF fiber is highly multimode, so part of the light propagates through the cladding, but the cladding is only around 20µm thin, so the external medium with a specific refractive index can influence the propagation through the fiber. The practical implementation of the sensor implies different manufacturing procedures and testing, and different surrounding media related to them.

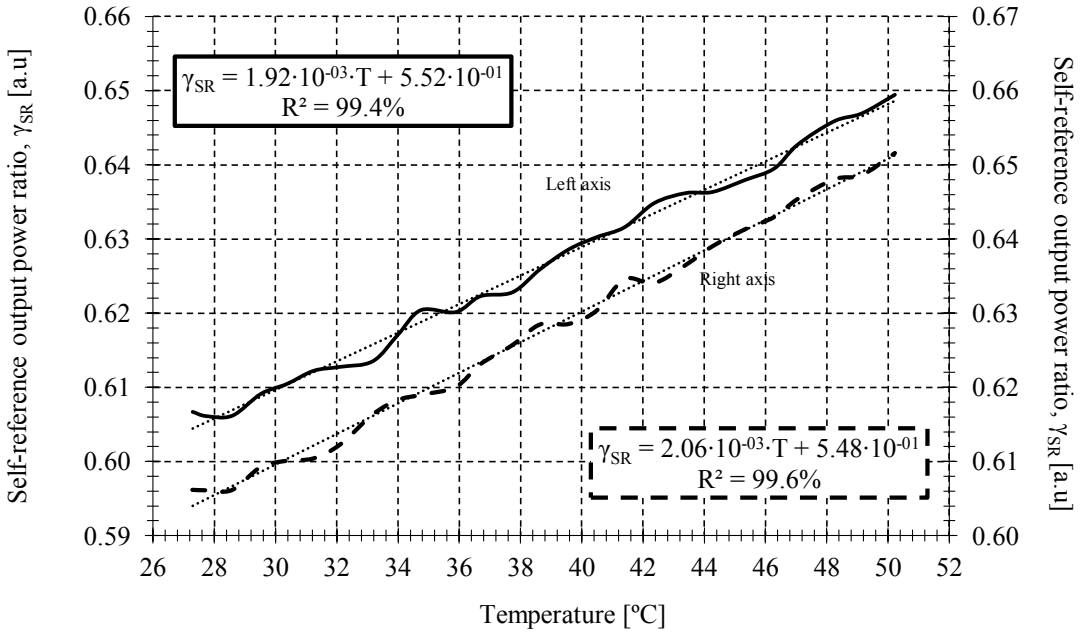

Figure 2.12. Calibration curves for a sensor with different coatings: — Without polypropylene, − − With polypropylene

One possible disturbance of the refractive index is the use of adhesives on the probe to fix the temperature sensor on the sensing point. These adhesives typically are manufactured with polymeric materials and have a different refractive index to that of the fiber cladding. In these experiments, the adhesive used to cover the fiber cladding of the sensing area is a polypropylene tape whose refractive index ($n_{Polypropylene}$=1.515) [68] is higher than the refractive index of the cladding. Figure 2.12 shows the calibration curves for a sensor with and without the tape. In these measurements, the distance between the optical sensor and the hot plate is fixed at 1mm to avoid any possible contact with the copper plate. The bend radius of the optical sensor is fixed at 2mm. The sensitivity obtained with and without the tape is $2.06 \cdot 10^{-3}$ ºC^{-1} and $1.92 \cdot 10^{-3}$(°C)$^{-1}$, respectively. In both cases, the linear regression coefficient is greater than 99%. It can be inferred that with and without the tape the results can be considered the same within the sensor error.

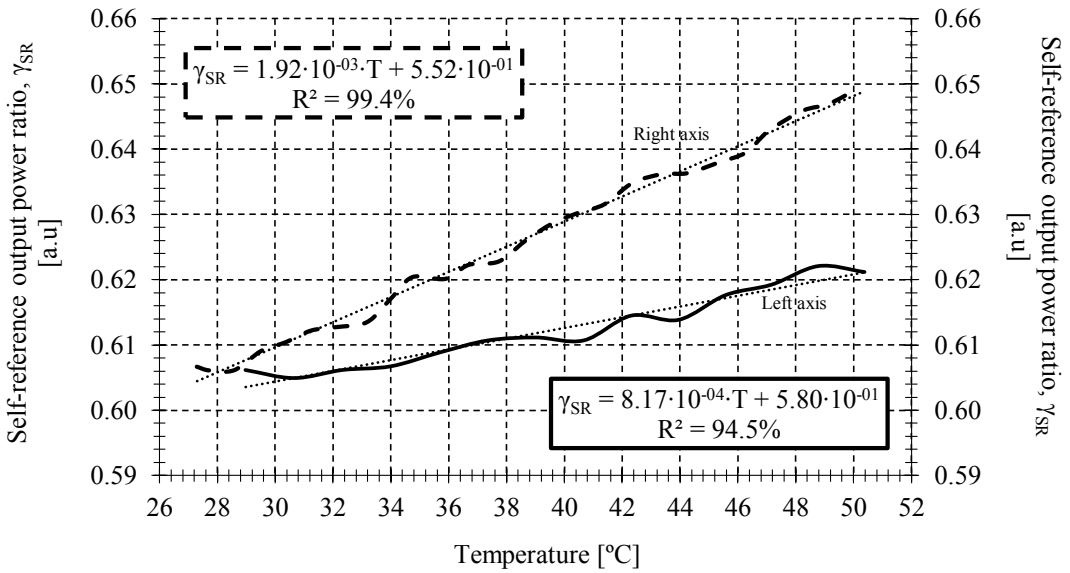

Figure 2.13. Calibration curves for a sensor with different distances to the metallic surface of the hot place: — D=0mm (contact), − − D=1mm (non-contact).

Another important parameter to consider is the possible influence of the hot plate metal surface. Placing the sensor on the surface can cause changes of the refractive index surrounding the cladding. In our experiments, the heater for measuring the calibration curves is a hot plate made of copper. The refractive index of the copper (n_{Copper}=0.23) [69] is much lower than the refractive index of the cladding. To analyse its influence, it is measured the output voltage ratio in two scenarios: non-contact and in contact with the hot plate. The distance to ensure non-contact between the sensor and the hot plate is fixed at 1mm. On other hand, for this experiment, no tape is used in order to isolate the phenomenon to be analysed. The bend radius of the optical sensor is 2mm. Measurements are shown on Figure 2.13, it can be seen that the sensitivity at both

scenarios is $8.17 \cdot 10^{-4}(°C)^{-1}$ and $1.92 \cdot 10^{-3}(°C)^{-1}$, for in contact and at a 1mm distance respectively. The sensitivity is reduced by a factor of around 2.4 when the POF is in contact with copper, a metal with an imaginary refractive index. The linear regression coefficients for the two measured distances are 99.4 and 94.5%, respectively. The contact with the metal surface is the responsible of the additional loss, having in mind that the cladding thickness is sufficiently small that the evanescent field of the core modes may extend through the cladding into the jacket. If the cladding is lossless, all the attenuation takes place in the lossy metal jacket. The power distribution ratio of the cladding to the total power changes with the cladding thickness and the temperature [70].

2.5.4. Discussion

Different experiments are carried out for measuring the calibration curves at different conditions. To ensure the stability of the sensor over time, six sets of measurements are carried out with a time interval between them of about 2hours. The sensor can operate in a temperature range from -55 to 70ºC. Meanwhile the measured calibration curve from 27.2 to 50.2ºC, shows a sensitivity of $1.92 \cdot 10^{-3}(°C)^{-1}$ for a bend radius of 2mm. A statistical analysis of the calibration curve shows that the sensor has a linear response with a non-linearity full scale error of 3.9%. The designed system allows a resolution of 0.3ºC.

The most limiting component in the system resolution is the data acquisition card (DAQ) [71]. The acquisition card in this experiment has a noise value of $0.5mV_{RMS}$ at a voltage range of ±1.0V. Using another acquisition card, the resolution of the system can be reduced to obtain a value of 0.1°C being limited by the noise generated by the transimpedance amplifier gain [72].

The optical input and output power measured at the sensor curve are compared with the simulations. Those values are obtained from measuring the optical power at the input and output of the sensor and estimating the connector, adaptor and straight section fiber losses. In the measurements, two types of connectors are used from different manufacturers and with different losses. For a bend radius of 1.5mm and 2mm, the connector losses are measured to be 1.2 and 2.2dB, respectively. These values are below the maximum limits (≤2.5dB) set by the two manufacturers. The self-reference topology proposed avoid the sensor response dependence of these connector losses and of other losses that can be present under the sensor operation.

The self-referencing technique uses a dummy sensor for referencing purposes. This sensor is identical to the one used in the sensing branch and is placed outside of the heating unit. The main drawback of this technique is the use of two identical sensors. The optical power at those two paths could be affected by different short and long term perturbations. In addition, possible

errors related to the tolerance of the sensor manufacturing process can make difficult to manufacture two identical sensors in a repetitive way. During the manufacturing process, bend radius tolerance of ±0.05mm is measured for the two proposed radii.

The experimental results show the effect of the external environment on the temperature measurement. As described previously, changes in the refractive index of the surrounding media in contact with the cladding, especially metals, produce a reduction in a factor of more than two in the sensor sensitivity. For the proper operation of the proposed temperature sensor, it is very important to carry out a characterization of the sensor under real working conditions. This property can also be used to improve the system but at the expense of increasing its complexity.

The intensity sensors are usually used at non-critical and low-cost systems when high precision and resolution are not required.

2.6. Self-referenced Technique Using a Pair of Wavelengths

In order to avoid false reading caused by fluctuations of the light source or other undesired losses, a relation between transmittances at two different wavelengths (λ_1, λ_2) is measured to implement a self-referencing technique. The output transmittance at the two selected wavelengths ($\tau_{\lambda 1}$, $\tau_{\lambda 2}$) can be expressed as:

$$\tau_{\lambda 1} = \frac{P_{\lambda 1}(T)}{P_{Ref,\lambda 1}} = \frac{L_{Dev,\lambda 1} \cdot L_{Sensor,\lambda 1}(T_0) \cdot F_{\lambda 1}(T) \cdot P_{Source,\lambda 1}}{L_{Dev,\lambda 1} \cdot P_{Source,\lambda 1}} = L_{Sensor,\lambda 1}(T_0) \cdot F_{\lambda 1}(T) \qquad (2.15)$$

$$\tau_{\lambda 2} = \frac{P_{\lambda 2}(T)}{P_{Ref,\lambda 2}} = \frac{L_{Dev,\lambda 2} \cdot L_{Sensor,\lambda 2}(T_0) \cdot F_{\lambda 2}(T) \cdot P_{Source,\lambda 2}}{L_{Dev,\lambda 2} \cdot P_{Source,\lambda 2}} = L_{Sensor,\lambda 2}(T_0) \cdot F_{\lambda 2}(T) \qquad (2.16)$$

where $P_{\lambda 1}(T)$ and $P_{\lambda 2}(T)$ are the output optical power at each wavelength for a given temperature (T). $P_{Ref,\lambda 1}$ and $P_{Ref,\lambda 2}$ are the output reference power for each wavelength at reference temperature.

These values are obtained measuring the output power for each wavelength without the macro-bend optical fiber sensor in the calibration set-up. The integration time of the spectrometer is fixed at 300ms. The experiment is performed at reference temperature T_0 of 25ºC. $L_{Dev,\lambda 1}$ and $L_{Dev,\lambda 2}$ are factors including the attenuation of the fiber leads, collimation losses, connectors and adaptor losses and insertion losses of the coupler at each wavelength. $F_{\lambda 1}(T)$ and $F_{\lambda 2}(T)$ are the optical power modulation function versus temperature at the fiber-optic sensor for each wavelength. $L_{Sensor,\lambda 1}(T_0)$ and $L_{Sensor,\lambda 2}(T_0)$ are the insertion losses at the reference temperature of

the macro-bend sensor for both wavelengths. Finally, $L_{Source,\lambda 1}$ and $L_{Source,\lambda 2}$ are the optical power of the light source at the two selected wavelengths, respectively. From Equation (2.15) and (2.16) the self-referencing output transmittance ratio (γ_{SR}) is defined as:

$$\gamma_{SR} = \frac{\tau_{\lambda 1}}{\tau_{\lambda 2}} = \frac{L_{Sensor,\lambda 1}(T_0)\cdot F_{\lambda 1}(T)}{L_{Sensor,\lambda 2}(T_0)\cdot F_{\lambda 2}(T)} = \frac{L_{Sensor,\lambda 1}(T_0)}{L_{Sensor,\lambda 2}(T_0)}\cdot F(T) \qquad (2.17)$$

The self-reference output transmittance ratio depends on the power sensor variations with temperature and on a constant ratio between the insertion losses of the macro-bend sensor at the different wavelengths.

2.6.1. Experimental Set-up

The schematic of the experimental set-up is shown in Figure 2.14. The light source is a 360 to 2,500nm stabilized tungsten halogen bulb [73]. In order to overcome the low power of the halogen light source at low wavelengths, a 400 to 460nm LED [74] is added to the main light source using collimating optics and a 50/50 POF splitter, as shown in Figure 2.15.

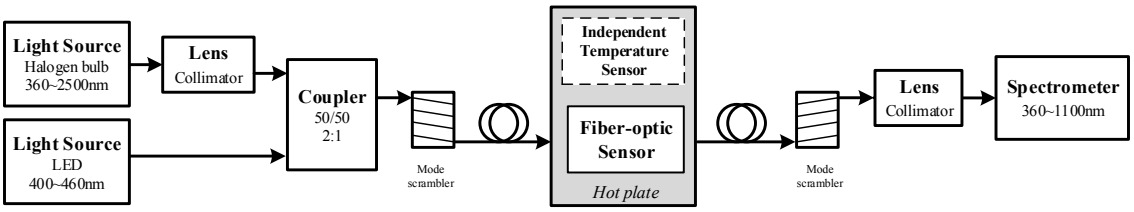

Figure 2.14. Schematic of the experimental set-up for characterizing the POF temperature sensor.

The fiber-optic sensor is fixed at a 1mm distance from a rectangular highly conductive metal base plate of the heating unit. A thermal isolated stage has been performed for supporting the fiber sensor. Setting a fixed distance between the sensor and the hot plate prevents possible changes in the refractive index of the cladding due to the contact with other materials, as it was discussed in Section 2.5.3. The temperature of the hot plate is controlled with a controller unit. For calibration purposes, an independent electronic temperature sensor is used in the measurements.

Two mode scramblers are placed before and after the fiber optic sensor to produce a stable mode distribution in the fiber regardless of the launch conditions.

All transmittance measurements are taken with a high speed diffraction grating based spectrometer with an array of 128 photodiodes (pixels), in the range from 360 to 886nm and

wavelength resolution of about 4nm [75]. The spectrometer sensitivity is controlled by the exposure time or integration time which can vary from 1ms to 60s [75]. The integration time of the spectrometer is initially fixed at 300ms. The experiment is performed at reference temperature T_0 of 25ºC.

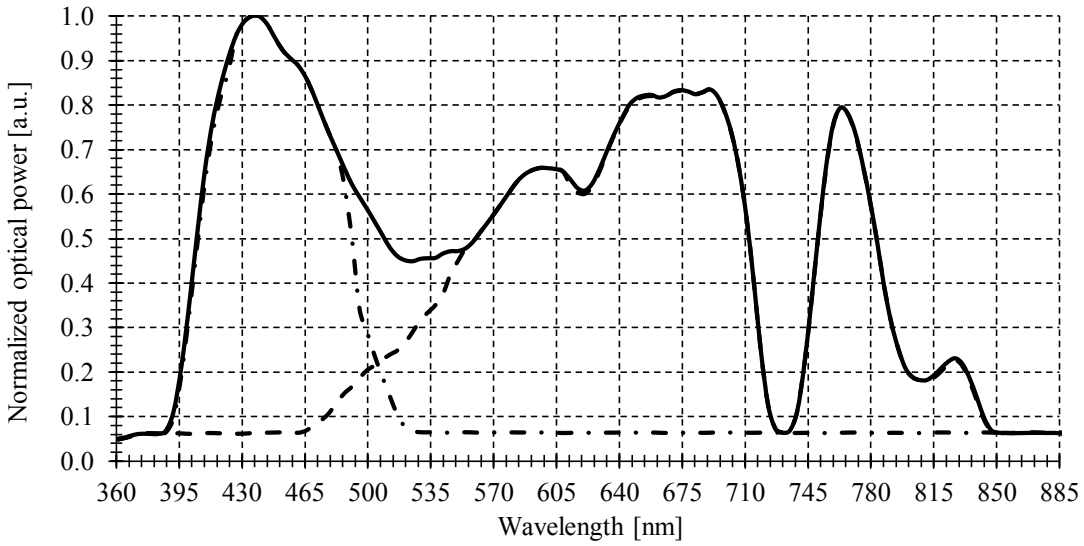

Figure 2.15. Normalized optical spectrum for the input light source at the output branch of the coupler: —— Halogen bulb and LED, – – – Halogen bulb, – · – LED.

In the experiment, the transmittance at different wavelengths is measured from 370 to 870nm with 4nm resolution using a spectrometer, in a temperature range from 27 to 70ºC at 2ºC intervals. A time interval of 2min is set, between each temperature measurement, to ensure the stabilization of the transmittance values. In those measurements, the integration time of the spectrometer is adjusted from 300ms to 3s in order to compensate the sensor insertion loss, of 10dB including the ST connectors. It is recommended that the spectral measurements cover 90% of the spectrometer's full-scale [75]. A total of five samples for each wavelength and temperature are carried out to perform a complete statistical analysis of the sensor parameters. Software based on graphical code is developed to acquire transmittance from the spectrometer.

A searching algorithm based on numerical programming language is developed by Eng. Plinio Jesús Pinzón Castillo who has also collaborated in taking measurements and analysing the results. The algorithm is used to find the output transmittance ratios that offer the highest linearity and sensitivity for among all possible pair of wavelengths. The analysed wavelengths are located in spectral regions of low attenuation. For each temperature and wavelength, the algorithm calculates the mean of the transmittances for the five samples. The ratio between the average transmittance at two different wavelengths is calculated for each temperature. This value is

estimated for all pairs of wavelengths. The sensitivity and the linear regression coefficient are calculated for each transmittance ratio using a linear regression model to approach the relationship between transmittance and temperature.

Figure 2.16 shows the measurements of the calibration curves for the two pairs of wavelengths that offer the highest linear regression and sensitivity values. These sensitivities are $8.95 \cdot 10^{-4}$ ºC^{-1} for 707/779nm transmission ratio, and $1.15 \cdot 10^{-3}$ ºC^{-1} for 422/409nm transmission ratio. These values can be expressed as $3.82 \cdot 10^{-3}$ and $4.49 \cdot 10^{-3}$dB/ºC. The sensor temperature sensitivity is higher than the temperature coefficient of the fiber attenuation $\beta_R = 1.5 \cdot 10^{-6}$dB/ºC [63], for a 3cm long POF sensor. The linear regression coefficients are 99.6 and 97.9%, respectively. The full-scale self-reference transmittance ratio errors are 2.6 and 3.2%, respectively. The sensor precision is calculated from the maximum standard deviation of the five samples for each temperature. The self-reference transmittance ratio precision for 707/779nm and 422/409nm transmission ratio is 0.1 and 0.2%, respectively. The attenuation at 409, 422, 707 and 779nm is 0.19, 0.16, 0.83 and 0.87dB/km, respectively.

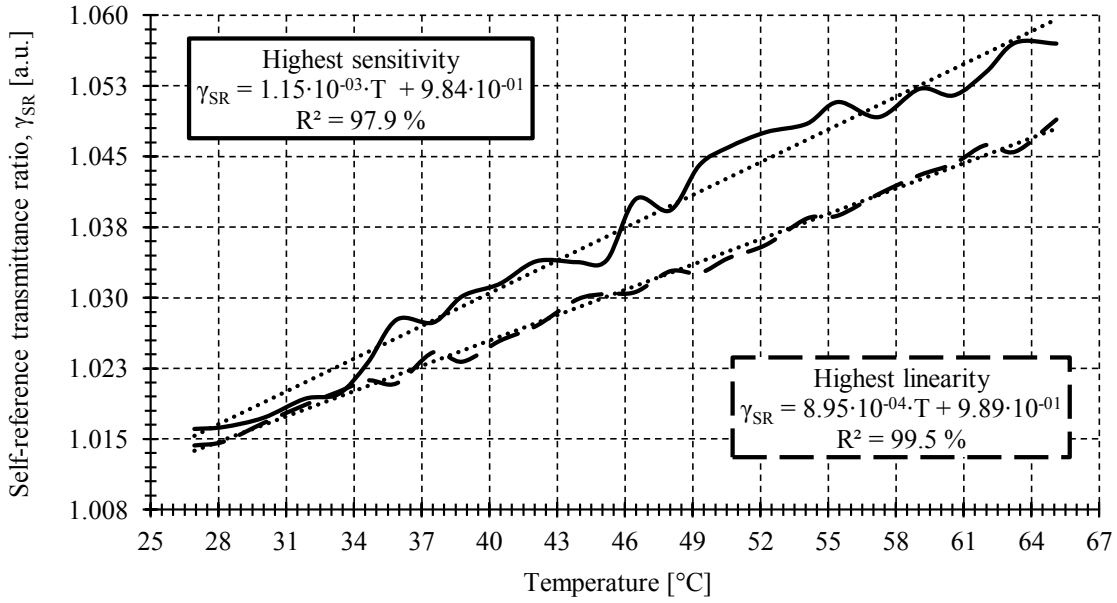

Figure 2.16. Self-reference transmittance ratio versus temperature: — 422/409 nm, – – 707/779 nm.

The sensitivity for the ratios of transmittance at the proposed two pairs of wavelengths increases at shorter wavelengths due to the decrement of the NA variation with temperature at longer wavelengths, as expected from simulations reported on Figure 2.6. This is shown in Figure 2.17, where output transmittance measurements are plotted against temperature for different wavelengths. Therefore, the measured wavelength dependence of the sensor is in good agreement with theory.

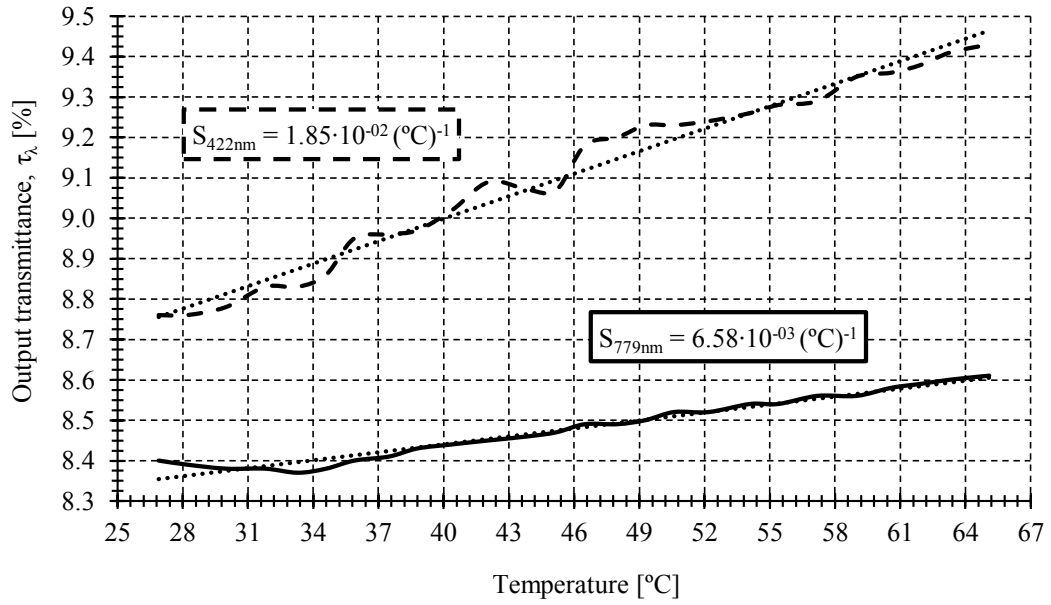

Figure 2.17. Output transmittance versus temperature: – – 422 nm, — 779 nm.

2.6.2. Self-referencing Test

The self-reference property is tested by inducing power fluctuation in the optical source through a mandrel. Measurements are taken for the highest linearity and sensitivity curves, see Figure 2.18.

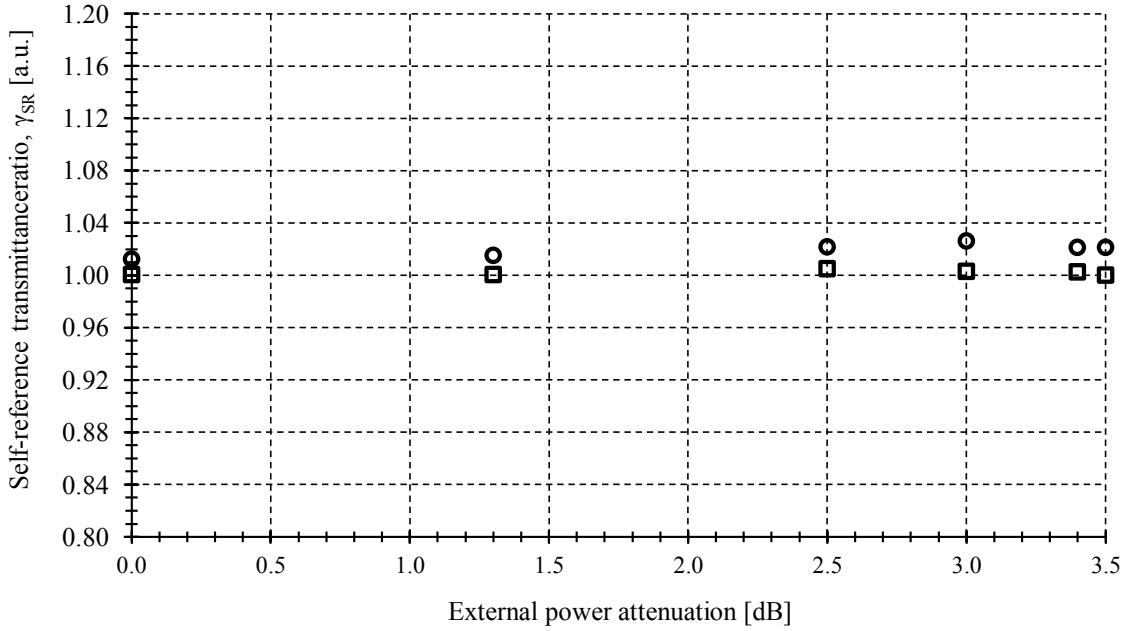

Figure 2.18. Output self-reference transmittance ratio γ_{SR}, self-reference test versus undesirable power fluctuations: ○ 422/409 (highest sensitivity) □ 707/779 (highest linearity).

The full scale self-reference transmittance ratio error from external power fluctuations at a fixed temperature is 0.2 and 0.5% for 707/779nm and 422/409nm, respectively. As expected, the self-reference transmittance ratio error for the sensor calibration curves are higher than those for the self-reference test. There are no significant changes in the measured ratio after inducing a power attenuation of 3.5dB.

2.6.3. Discussion

The proposed temperature sensor uses the ratio of transmittance at two different wavelengths to provide a robust wavelength division multiplexing (WDM) self-referencing technique. An experiment is carried out for measuring the transmittance at a range of wavelengths from 370 to 870nm. The output transmittance ratio measurements for all possible pair of wavelengths are calculated to find the ratio of wavelengths that offer the highest linearity and good sensitivity. Those are λ_1 = 707nm and λ_2 = 779nm. The sensor can operate in a temperature range from -55 to 70ºC. Meanwhile the measured calibration curve from 27 to 70°C, shows a sensitivity and linear regression coefficient of $8.95 \cdot 10^{-4}$ $ºC^{-1}$ and 99.5%, respectively. The self-reference transmission ratio accuracy and full-scale temperature error are 0.1 and 2.6%, respectively.

The most limiting component in the system error is the spectrometer. The spectrometer used in this experiment has a transmittance ratio repeatability error and resolution of 0.17 and 0.002% for 707/779nm, respectively. By using another spectrometer with higher intensity resolution and sensitivity, the system temperature error and the oscillations of the self-reference parameter can be reduced.

The sensor can be used under ambient lighting conditions, such as fluorescent ceiling lamps. Figure 2.19 shows the influence of the fluorescent light emission spectrum on the macro-bend sensor. Appreciable change on the sensor output power spectrum occurs at the maximum power peaks of fluorescent light emission spectrum but outside of the maximum sensitivity and linearity wavelength ranges. This analysis demonstrates no influence of fluorescent light in the measurement process.

Measurements presented in this work are performed using a stabilized halogen light source in combination with a LED, in order to compensate the low power of the halogen source in the violet-blue region (see Figure 2.15).

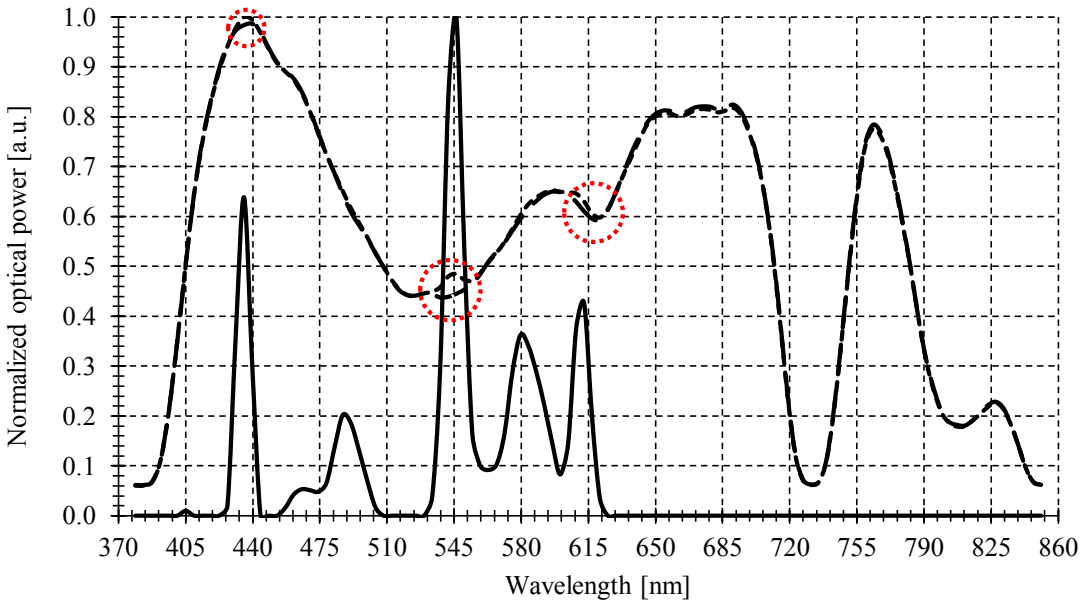

Figure 2.19. Normalized power spectrum: — Fluorescent light emission spectrum, – – Sensor output power without fluorescent light, · · · Sensor output power with fluorescent light.

The output power of the blue LED is not stabilized. Voltage changes in the DC power supply may present power drift with time. The calibration curve is measured 120min after turning on the sources and the measurements take 50min. An analysis of the output transmittance ratio is carried out to ensure the stability of the measurements, as shown in Figure 2.20.

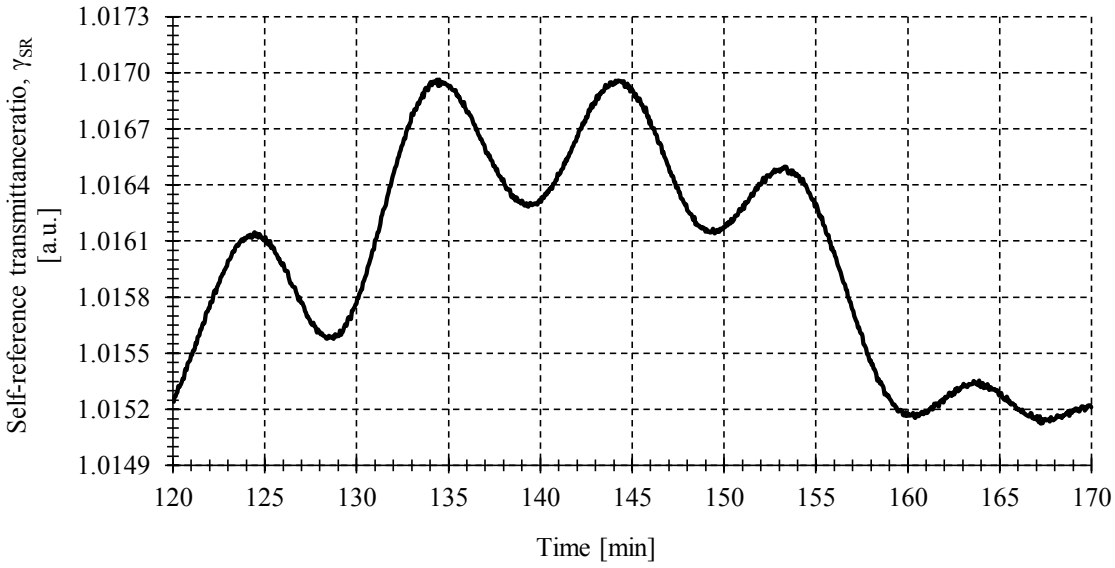

Figure 2.20. Blue LED light source stability for 422/409nm transmission ratio.

The blue LED has a power drift of 0.03% for 422/409nm transmission ratio during 50min test. To measure the power drift the blue LED was thermally stabilized using a thermal hot plate

at 25ºC. On the other hand, when measuring the sensor calibration curve, the blue LED is not thermally stabilized and may present a power drift with ambient temperature. During the measurement, the ambient temperature change between 25 and 26ºC. Considering these values, the power drift is 0.05% for 522/409nm transmission ratio. Using the calibration curve at the selected ratio of transmittances, this value can be expressed in term of full-scale temperature error as 1.7%. These results justify the higher temperature errors for the 422/409nm transmission ratio calibration curve. The use of a thermal and power stabilized halogen light source reduces the sensor temperature error. In a final application, it is possible to use other types of sources, e.g. a xenon light source (with a more uniform spectrum than the halogen) or single super-luminescent LEDs (with spectral bandwidth of up to 100nm).

2.7. Comparative Analysis

A comparative analysis is developed between the proposed sensors and other intensity fiber-optic temperature sensors reported in the literature. From Table 2.2, it can be seen that the different sensor parameters are similar, apart from the sensitivity. The sensitivity of the proposed sensor is similar to that obtained with singlemode [13, 15, 20] or multimode [21, 76] glass fiber, but they are also more fragile and usually need more expensive equipment. The thermal sensibility of the singlemode or multimode glass sensors is improved combining singlemode and multimode glass fibers [19]. The cost and complexity of the fusion spliced limit the use of these structures in low-cost applications. The other sensors based on fluorescence techniques, measure the attenuation of the luminescence signal caused by the presence of a convenient indicator, such as glue or ink [76, 77]; they can obtain a higher sensitivity but making them also more complex approaches.

Intensity sensor	**Fiber**	**Range**	**Sensitivity** (2)	**Resolution**	**Linear Regression Coefficient**
Macro-bend loss [20]	Singlemode glass fiber	0 to 75°C	R=12.5mm: $1.2 \cdot 10^{-2}$dB/°C	<1°C	(3)
Macro-bend loss [13]	Singlemode glass fiber	0 to 74ºC	R=11.5mm: $4.6 \cdot 10^{-2}$dB/ºC R=12.5mm: $1.2 \cdot 10^{-2}$dB/ºC	(3)	R=11.5mm >96% R=12.5mm >98%

Intensity sensor	**Fiber**	**Range**	**Sensitivity** (2)	**Resolution**	**Linear Regression Coefficient**
Macro-bend loss [15]	Singlemode glass fiber	0 to 80ºC	≈$3.1\cdot10^{-2}$ dB/ºC	(3)	(3)
Macro-bend loss and absorbed coated [13]	Singlemode glass fiber	Indian ink: 0 to 50ºC Permanent ink: 20 to 55ºC Black paint: 5 to 35ºC 35 to 75ºC	Indian ink: ≈$9\cdot10^{-3}$dB/°C Permanent ink: ≈$2.2\cdot10^{-2}$dB/°C Black paint: ≈$1\cdot10^{-2}$ dB/°C ≈$2.5\cdot10^{-3}$dB/°C	(3)	(3)
Macro-bend loss [19]	Singlemode and multimode glass fiber	45 to 80ºC	≈$1\cdot10^{-1}$dB/ºC	0.1ºC	(3)
Macro-bend loss and absorbed coated [21]	Multimode polymer-clad-glass fiber	Olives oil: 55 to 85°C Gasoline: 25 to 55°C	Olive oil: $1.5\cdot10^{-2}$dB/°C Gasoline: $2.3\cdot10^{-2}$dB/°C	0.1°C	(3)
Fluorescence and absorbed coated [76]	Multimode glass fiber	25 to 100°C	≈$1.0\cdot10^{-2}$ dB/°C	2°C	>99%
Fluorescence and absorbed coated [77]	Multimode POF	22 to 73°C	≈$8.4\cdot10^{-2}$dB/°C	(3)	>99%
Macro-bend & Dummy sensor [52] (This work)	Multimode POF	27.2 to 50.2ºC (1)	R=2mm: $1.29\cdot10^{-2}$dB/°C (4)	0.3°C	>99%
Macro-bend & Dual-Wavelength [78] (This work)	Multimode POF	26.9 to 65.1°C (1)	R=2mm: $3.82\cdot10^{-3}$dB/°C (4)	(3)	>99%

Notes: 1. Range on the reported measurements. For example, in our prototype the real temperature range for this sensor is from -55 to +70ºC; 2. Approximate values obtained from the graphs of the articles; 3. This value is not shown in the article; 4. Self-reference system sensitivity.

Table 2.2. Comparative table with other intensity fiber-optic temperature sensors.

On the other hand, the experimental results show the effect of the external environment on the temperature measurement. As described previously, changes in the refractive index of the surrounding media in contact with the cladding, especially metals, produce a reduction in a factor of more than two in the sensor sensitivity. For the proper operation of the proposed temperature sensor, it is very important to carry out a characterization of the sensor under real working conditions. This property can also be used to improve the system but at the expense of increasing its complexity. As shown in Table 2.2, different sensors use absorbed coatings [13, 21, 76, 77] that modify the refractive index of the fiber increasing or reducing the sensitivity of the sensor and thereby improving the sensor parameters. This behaviour can also be used to develop other type of sensors, as for example a detector of different metal materials in industrial processes.

An important advance of this work is the use of a simple macro-bend loop on a flexible and easy to handle fiber to perform a cost-competitive fiber-optic temperature sensor. Against other proposals that use GOFs [13, 15, 19-21, 76], this temperature sensor tries to take advantage of the benefits of the POF-based technology. POF-based sensors have intrinsic advantages of any optical fiber and, in addition, they have a larger core diameter and good mechanical properties, making them less fragile and more robust: reducing development and maintenance cost associated with the glass-based systems. POF dimensions allow the use of low precision connectors and lenses. Despite of using low-cost fiber-optic technology, the designed temperature sensor offers good performance in terms of sensitivity and resolution. A competitive advantage in terms of sensitivity is not clearly shown when glass-based technology is used to manufacture the macro-bend sensor. Only the use of a combination of different GOFs lead to high sensitivity sensing solutions but at the cost of very complex and expensive schemes [19].

In terms of reproducibility, as in any intensity sensor it is essential to have a self-reference configuration to avoid the influence of external loss variations of the whole set-up. A comparative analysis is developed between the proposed techniques and other implementations of WDM self-referencing techniques reported on the literature, see Table 2.3.

Self-referencing techniques based on glass [79, 80] require more expensive and accurate equipment than those based on POF. This is due to the small size and low NA of the glass fibers. Some self-referencing techniques [79, 81] use a modulated optical signal at a low frequency for improving the resolution but at the expense of increasing the cost and the complexity of the system.

Self-Reference Technique	**Fiber**	**Light Source**	**Modulated**	**Wavelength demultiplexing**	**Detector**	**Self-Reference parameter** (1)
WDM Technique [80]	GI glass fiber	White light source	Non-modulated	Two bandpass filters and a beam splitter	Two detectors	~5% after inducing 3dB
WDM Technique [79]	SI glass fiber	GaAlAs LED	Square 1kHz	Two optical filters and a beam splitter	Two PIN photodiodes	~1% after coiling the fiber into 5 loops of 1cm
WDM Technique [81]	SI PMMA POF	Multicolor (blue and red) LED	ASK 1kHz (Note 4)	Synchronous detection algorithm	One detector	~1.5% after inducing 0.42dB
Dummy sensor [52] (This work)	SI PMMA POF	Red LED	Non-modulated	Two different paths	Two Si detectors	(2)
WDM Technique [78] (This work)	SI PMMA POF	Halogen bulb and blue LED	Non-modulated	Spectrometer (3)	Spectrometer (3)	0.2% after inducing 3.5dB

Notes: 1. Approximate values obtained from the graphs of the articles; 2. This value is not shown in the article; 3. The proposed self-reference technique can be developed using a POF-based demultiplexer [82] and two Si photodiodes to reduce its cost; 4. ASK: Amplitude-shift keying.

Table 2.3. Self-reference properties in some intensity based sensors.

Part of the cost advantage of the POF sensor reported in [52] is due to the use of a dummy fiber-optic sensor for referencing purposes. But the main drawback is the fact that the reference and the sensing signal follow different paths and the need for an additional sensors. The optical power at those two paths could be affected by different short or long term power perturbations, changing the output power ratio and hence the reading temperature. On the other hand, the tolerance of the sensor manufacturing process can make difficult to manufacture two identical sensors in a repetitive way. To overcome these problems, a second self-referencing configuration is developed using a WDM topology based on a single macro-bend loop [78]. This configuration uses a spectrometer to demultiplexer and measure the optical power at both sensing wavelengths travelling along the macro-bend loop. This technique has smaller fluctuations of the self-referencing parameter in comparison with other WDM implementations, see Table 2.3. The cost

increment for the use of a spectrometer to demultiplexer and measure the transmittance at each wavelength can be easily improved replacing the spectrometer by a demultiplexer and two photodetectors as that reported in [82]. With this cost improvement, the POF macro-bend temperature sensor with the WDM self-referencing technique can be a cost-competitive solution against other proposals.

One potential application field of the proposed temperature sensor is in the biomedical sector. Minimally invasive tools and sensors have become essential for medical diagnosis and surgery with the desire of not only serving at the same time to sense physiological parameters, but also being able to overcome biocompatibility concerns. Nowadays, there are different medical areas where fiber-optic temperature sensors hold enormous potential; particularly if in vivo applications are pursued [83], as here there is a need to develop sensors for minimally invasive surgery procedures. The minimum and maximum temperature that a human body can stand without dying are ~20ºC [84] and ~41.1ºC [85]. According to this temperature range, the proposed sensor can be used in medical applications.

On the other hand, the proposed FOS can be used in temperature measurements in power transformer applications where the presence of EMI limit the use of traditional sensors [86]. The current energy demand overloads power transformers causing overheating. The coolant aging increases the risk of in-service failure, being potentially dangerous through explosions and fire, is costly to repair or replace, and may result in significant loss of revenue [87]. The working temperature range of a transformer oil is from ~20 to ~45ºC [86]. For this reason, the proposed POF temperature sensor can be a good solution.

2.8. Conclusions

Macro-bending loss, caused by the different TO coefficients of the cladding and core of an POF has been shown to be an usable technique for temperature sensing. The sensor has been tested in the temperature range from 27 to 70ºC. Two different self-referencing topologies are analysed in order to avoid false reading caused by fluctuations of the light source, optical fiber attenuation and other undesired losses.

The first configuration uses a dummy fiber-optic sensor for referencing purposes. The sensor sensitivity for a bend radius of 2mm is $1.29 \cdot 10^{-3}$ ºC^{-1}. The sensitivity increases as the radius of curvature increases. In addition, sensor sensitivity measurements are in good agreement with simulations. The automated self-reference sensor system shows a resolution below 0.3 °C and a 3.9% non-linearity full scale error. The influence of external media in contact with the sensors has been analysed.

The second self-referencing configuration uses the optical power ratio between two wavelengths traveling along a single macro-bend loop. A WDM self-referencing technique has shown to provide a robust temperature sensors development independent on the repeatability of the manufacturing process and the different physical path loss evolution of the other self-referencing techniques. The sensitivity increases as the wavelengths used to calculate the self-reference transmittance ratio decreases. Moreover, larger wavelengths induce a lower temperature error and higher linearity. The self-reference sensor based on the transmittance ratio at λ_1=707nm and λ_2=779nm has a sensitivity of $8.95 \cdot 10^{-4}$ $^{o}C^{-1}$. The linear regression coefficient is >99%. It shows a 6% full-scale temperature error due to the spectrometer used in the experiments.

In conclusion, a simple macro-bend loop is designed to perform a cost-competitive fiber-optic temperature sensor. Against other proposals that use GOFs, this temperature sensor tries to take advantage of the benefits of the POF-based technology: reducing the development and costs associated with glass-based systems. Despite of using low-cost fiber-optic technology, the designed temperature sensor offers similar performance in terms of sensitivity and resolution than glass-based macro-bend loops. Only sophisticated combinations of GOFs lead to higher sensitivity sensing solutions but at the cost of more complex and expensive schemes. On the other hand, part of the economy advantage of the designed temperature sensors is due to the use of dummy fiber-optic sensors for referencing purposes. The main drawback to use a dummy sensor is the higher fluctuations of the self-referencing parameters in comparison with other proposals that use WDM topologies. For this reason, a second self-referencing configuration has been developed using a spectrometer to demultiplexer and measure the transmittance at each sensing wavelength. This technique demonstrates that the self-referencing parameter only changes 0.2% when the optical power changes by 3.5dB which is much lower than the same parameter in all similar systems reported in the literature. To reduce the cost of the system, the spectrometer can be replaced by a demultiplexer and two photodetectors. With this cost improvement, the proposed temperature sensors can be a cost-competitive solution against other proposals previously reported.

The sensor can be used in a large range of applications, for instance: power transformers, biomedical applications, instrumentation process, automotive industry, air-conditioning control and chemical industry.

2.9. References

[1] Anonymous, "Temperature Sensor Market, A Study of Major Sensor Types & Applications, Global Forecast & Analysis (2011 – 2016)," 2012.

[2] T. Sudo, H. Sasaki, N. Masuda, and J. L. Drewniak, "Electromagnetic interference (EMI) of system-on-package (SOP)," *IEEE Transactions on Advanced Packaging,* vol. 27, pp. 304-314, 2004.

[3] F. Taffoni, D. Formica, P. Saccomandi, G. D. Pino, and E. Schena, "Optical fiber-based MR-compatible sensors for medical applications: an overview," *Sensors,* vol. 13, pp. 14105-14120, 2013.

[4] G. Murtaza and J. Senior, "Referencing strategies for intensity modulated optical fibre sensors: a review," *Optics & Laser Technology,* vol. 25, pp. 235-246, 1993.

[5] C. Vázquez, J. Montalvo, and P. C. Lallana, "Radio-frequency ring resonators for self-referencing fiber-optic intensity sensors," *Optical Engineering,* vol. 44, pp. 040502-040502, 2005.

[6] C. Vazquez, J. Montalvo, D. S. Montero, and J. M. S. Pena, "Self-Referencing Fiber-Optic Intensity Sensors Using Ring Resonators and Fiber Bragg Gratings," *IEEE Photonics Technology Letters,* vol. 18, pp. 2374-2376, 2006.

[7] J. Montalvo, F. M. Araujo, L. A. Ferreira, C. Vazquez, and J. M. Baptista, "Electrical FIR Filter With Optical Coefficients for Self-Referencing WDM Intensity Sensors," *IEEE Photonics Technology Letters,* vol. 20, pp. 45-47, 2008.

[8] C. Sánchez-Pérez, A. García-Valenzuela, G. E. Sandoval-Romero, J. Villatoro, and J. Hernández-Cordero, "Technique for referencing of fiber-optic intensity-modulated sensorsby use of counterpropagating signals," *Optics Letters,* vol. 29, pp. 1467-1469, 2004.

[9] T. Chang-Da, H. Hui-Hsun, T. Shyh-Lin, C. Hsiao-Lung, and W. Chien-Ping, "Error reduction of referenced intensity-based optical fibre sensor by adaptive noise canceller," *Electronics Letters,* vol. 33, pp. 982-983, 1997.

[10] W. Anbo, H. Xiao, J. Wang, Z. Wang, W. Zhao, and R. G. May, "Self-calibrated interferometric-intensity-based optical fiber sensors," *Journal of Lightwave Technology,* vol. 19, pp. 1495-1501, 2001.

[11] D. S. Montero, C. Vázquez, J. Baptista, J. Santos, and J. Montalvo, "Coarse WDM networking of self-referenced fiber-optic intensity sensors with reconfigurable characteristics," *Optics Express,* vol. 18, pp. 4396-4410, 2010.

[12] A. Moraleda, D. Montero, D. Webb, and C. García, "A Self-Referenced Optical Intensity Sensor Network Using POFBGs for Biomedical Applications," *Sensors,* vol. 14, pp. 24029-24045, 2014.

[13] G. Rajan, Y. Semenova, J. Mathew, and G. Farrell, "Experimental analysis and demonstration of a low cost fibre optic temperature sensor system for engineering applications," *Sensors and Actuators A: Physical,* vol. 163, pp. 88-95, 2010.

[14] J. Senosiain, I. Diaz, A. Gaston, and J. Sevilla, "High sensitivity temperature sensor based on side-polished optical fiber," *IEEE Transactions on Instrumentation and Measurement,* vol. 50, pp. 1656-1660, 2001.

[15] P. Wang, G. Rajan, Y. Semenova, and G. Farrell, "Temperature dependence of a macrobending edge filter based on a high-bend loss fiber," *Optics Letters,* vol. 33, pp. 2470-2472, 2008.

[16] U. S. Raikar, A. S. Lalasangi, V. K. Kulkarni, and I. I. Pattanashetti, "Temperature dependence of bending loss in single mode communication fiber: Effect of fiber buffer coating," *Optics Communications,* vol. 273, pp. 402-406, 2007.

[17] P. Wang, Y. Semenova, and G. Farrell, "Temperature dependence of macrobending loss in all-fiber bend loss edge filter," *Optics Communications,* vol. 281, pp. 4312-4316, 2008.

[18] G. Rajan, Y. Semenova, P. Wang, and G. Farrell, "Temperature-Induced Instabilities in Macro-Bend Fiber Based Wavelength Measurement Systems," *Journal of Lightwave Technology,* vol. 27, pp. 1355-1361, 2009.

[19] Q. Wu, Y. Semenova, A. Hatta, P. Wang, and G. Farrell, "Bent SMS fibre structure for temperature measurement," *Electronics letters,* vol. 46, pp. 1129-1130, 2010.

[20] G. Rajan, Y. Semenova, and G. Farrell, "All-fibre temperature sensor based on macro-bend singlemode fibre loop," *Electronics Letters,* vol. 44, pp. 1123-1124, 2008.

[21] G. Betta and A. Pietrosanto, "An intrinsic fiber optic temperature sensor," *IEEE Transactions on Instrumentation and Measurement,* vol. 49, pp. 25-29, 2000.

[22] H. Ahmad, M. Zulkifli, F. Muhammad, J. Samangun, H. Abdul-Rashid, and S. Harun, "Temperature-Insensitive Bend Sensor Using Entirely Centered Erbium Doping in the Fiber Core," *Sensors,* vol. 13, pp. 9536-9546, 2013.

[23] O. Ziemann, J. Krauser, P. E. Zamzow, and W. Daum, *POF handbook: optical short range transmission systems*: Springer, 2008.

[24] D. S. Montero, C. Vazquez, I. Mollers, J. Arrue, and D. Jager, "A self-referencing intensity based polymer optical fiber sensor for liquid detection," *Sensors,* vol. 9, pp. 6446-55, 2009.

[25] M. L. Casalicchio, M. Olivero, G. Perrone, and A. Vallan, "Plastic optical fiber sensor for displacement monitoring with dual-wavelength compensation of power fluctuations," in *IEEE Instrumentation and Measurement Technology Conference (I2MTC)*, Binjiang (China), 2011, pp. 1-5.

[26] J. Arrue, J. Zubia, G. Fuster, and D. Kalymnios, "Light power behaviour when bending plastic optical fibres," *IEE Proceedings - Optoelectronics,* vol. 145, pp. 313-318, 1998.

[27] S. Minami, "The Development and Applications of POF: Review and Forecast," in *Proceedings of The Third International Conference on Plastic Optical Fibres and Applications*, Yokohama (Japan), 1994, pp. 27-31.

[28] N. Saitoh and K. Shimada, "Optical Fibres and their application to passive components and various digital data links," in *Proceedings of The First International Conference on Plastic Optical Fibres and Applications*, Paris (France), 1992, pp. 10-14.

[29] T. Kaino, M. Fujiki, S. Oikawa, and S. Nara, "Low-loss plastic optical fibers," *Applied Optics,* vol. 20, pp. 2886-2888, 1981.

[30] T. Kaino, "Plastic optical fibers for near-infrared transmission," *Applied Physics Letters,* vol. 48, pp. 757-758, 1986.

[31] Y. Koike and M. Asai, "The future of plastic optical fiber," *NPG Asia Mater,* vol. 1, pp. 22-28, 2009.

[32] Y. Koike, T. Ishigure, and E. Nihei, "High-bandwidth graded-index polymer optical fiber," *Jornal of Lightwave Technology,* vol. 13, pp. 1475-1489, 1995.

[33] D. X. Yang, J. Yu, X. Tao, and H. Tam, "Structural and mechanical properties of polymeric optical fiber," *Materials Science and Engineering: A,* vol. 364, pp. 256-259, 2004.

[34] F. Pigeon, S. Pelissier, A. Mure-Ravaud, H. Gagnaire, and C. Veillas, "Optical fibre Young modulus measurement using an optical method," *Electronics Letters,* vol. 28, pp. 1034-1035, 1992.

[35] A. Nespola, S. Straullu, P. Savio, D. Zeolla, S. Abrate, D. Cardenas*, et al.*, "First demonstration of real-time LED-based Gigabit Ethernet transmission on 50m of A4a.2 SI-POF with significant system margin," in *36th European Conference and Exhibition on Optical Communication (ECOC)*, Turin (Italy), 2010, pp. 1-3.

[36] M. Hattori, M. Nishiguchi, and S. Takagi, "Plastic Optical Fiber and Optical Link Module for Short Haul High-Speed Transmission," in *Proceedings of The International Wire and Cable Symposium (IWCS)*, Philadelphia (USA), 1998, pp. 257-263.

[37] S. Irie and M. Nishiguchi, "Development of the resistant plastic optical fiber," in *Proceedings of The Third International Conference on Plastic Optical Fibers*, Yokohama (Japan), 1994.

[38] M. Ishiharada, H. Kaneda, T. Chikaraishi, S. Tomita, I. Tanuma, and K. Naito, "Properties of flexible ligh guide made of silicone elastomer," in *Proceedings of The First International Conference on Plastic Optical Fibers and Applications*, Paris (France), 1992, pp. 38-42.

[39] J. Zubia and J. Arrue, "Plastic Optical Fibers: An Introduction to Their Technological Processes and Applications," *Optical Fiber Technology,* vol. 7, pp. 101-140, 2001.

[40] W. Yuan, L. Khan, D. J. Webb, K. Kalli, H. K. Rasmussen, A. Stefani*, et al.*, "Humidity insensitive TOPAS polymer fiber Bragg grating sensor," *Optics express,* vol. 19, pp. 19731-19739, 2011.

[41] I. C. Society, "IEEE Standard for Ethernet 802.3," ed, 2012.

[42] J. Berwanger, M. Peller, and R. Griessbach, "Byteflight -A New Protocol for Safety Critical Applications," in *Proceedings of the 28th FISITA World Automotive Congress*, Seoul (Korea), 2000.

[43] K. Schunk, "IEEE 1394 Multimedia - Bus," in *Meeting of the ITG-SC*, Postdam (Germany), 2000.

[44] M. Cooperation. (2010). *Media Oriented Systems Transport. Multimedia and Control Networking Technology. MOST Specification Rev. 3.0*. Available: http://www.mostcooperation.com

[45] D. J. Halski, "FLASH fly-by-light flight control demonstration results overview," in *Proceedings of Fly-by-Light III*, Denver (United States), 1996, pp. 58-70.

[46] J. R. Todd, "Fly-by-light flight control system development for transport aircraft," in *Digital Avionics Systems Conference*, Atlanta (United States), 1996, pp. 153-158.

[47] S. Cherian, H. Spangenberg, and R. Caspary, "Investigation on harsh environmental effects on polymer fiber optic link for aircraft systems," in *Proceedings of Phtonics Applications for Aviation, Aerospace, Commercial, and Harsh Environments V*, San Diego (United States), 2014, pp. 92020I-92020I-11.

[48] J. R. Todd, J. A. Hay, and T. Dinh, "Integrating fly-by-light/power-by-wire flight control systems on transport aircraft," in *Digital Avionics Systems Conference, 1993. 12th DASC., AIAA/IEEE*, 1993, pp. 457-462.

[49] E. Suaste-Gómez, D. Hernández-Rivera, A. S. Sánchez-Sánchez, and E. Villarreal-Calva, "Electrically Insulated Sensing of Respiratory Rate and Heartbeat Using Optical Fibers," *Sensors,* vol. 14, pp. 21523-21534, 2014.

[50] M. Rothmaier, M. P. Luong, and F. Clemens, "Textile pressure sensor made of flexible plastic optical fibers," *Sensors,* vol. 8, pp. 4318-4329, 2008.

[51] S. Muto, O. Suzuki, T. Amano, and M. Morisawa, "A plastic optical fibre sensor for real-time humidity monitoring," *Measurement Science and Technology,* vol. 14, p. 746, 2003.

[52] A. Moraleda, C. García, J. Zaballa, and J. Arrue, "A Temperature Sensor Based on a Polymer Optical Fiber Macro-Bend," *Sensors,* vol. 13, pp. 13076-13089, 2013.

[53] J. Zubia, O. Aresti, J. Arrue, and M. Lopez-Amo, "Barrier sensor based on plastic optical fiber to determine the wind speed at a wind generator," *IEEE Journal of Selected Topics in Quantum Electronics,* vol. 6, pp. 773-779, 2000.

[54] D. S. Montero, P. C. Lallana, and C. Vázquez, "A Polymer Optical Fiber Fuel Level Sensor: Application to Paramotoring and Powered Paragliding," *Sensors,* vol. 12, pp. 6186-6197, 2012.

[55] M. Remouche, F. Georges, and P. Meyrueis, "Flexible Optical Waveguide Bent Loss Attenuation Effects Analysis and Modeling Application to an Intrinsic Optical Fiber Temperature Sensor," *Optics and Photonics Journal,* vol. 2, pp. 1-7, 2012.

[56] M. Remouche, R. Mokdad, A. Chakari, and P. Meyrueis, "Intrinsic integrated optical temperature sensor based on waveguide bend loss," *Optics & Laser Technology,* vol. 39, pp. 1454-1460, 2007.

[57] M. Rayon. (8th January 2015). *Specification Sheet High-Performance Plastic Optical Fiber Eska SH-4001*. Available: http://www.pofeska.com

[58] M. Kovacevic and A. Djordjevich, "Temperature dependence analysis of mode dispersion in step-index polymer optical fibers," *Acta Physica Polonica,* vol. 116, 2009.

[59] M. Oka, (Personal communication) Mitsubishi Rayon Co. Ltd. (Opto-Device Department. Fiber Optics Section) January 15, 2013.

[60] J. W. Fleming, "Material dispersion in lightguide glasses," *Electronics Letters,* vol. 14, pp. 326-328, 1978.

[61] T. Ishigure, E. Nihei, and Y. Koike, "Optimum refractive-index profile of the graded-index polymer optical fiber, toward gigabit data links," *Applied Optics,* vol. 35, pp. 2048-2053, 1996.

[62] A. E.-N. A. Mohammed, M. M. El-Halawany, A. N. Z. Rashed, and S. Hanafy, "High performance of plastic optical fibers within conventional amplification technique in advanced local area optical communication networks," *International Journal of Multidisciplinary Sciences and Engineering (IJMSE),* vol. 2, pp. 34-42, 2011.

[63] Y. Tsukamoto, (Personal communication) Mitsubishi Rayon Co. Ltd. (Plastic Molding Department. Fiber Optics Section)April 4, 2013.

[64] Ratioplast-optoelectronics. (4th February 2015). *Signal-Generator MS100HU*. Available: http://www.ratioplast.com

[65] Linkam. (4th February 2015). *LTS350 Temperature Controlled Stage User Guide*. Available: http://www.linkam.co.uk

[66] Linkam. (4th February 2015). *Linkam Temperature Controllers. TP94. Brochure*. Available: http://www.aps.anl.gov

[67] T. Instruments. (4th February 2015). *LM35 Precision Centigrade Temperature Sensors*. Available: http://www.ti.com

[68] H. M. Shabana, "Determination of film thickness and refractive index by interferometry," *Polymer Testing,* vol. 23, pp. 695-702, 2004.

[69] L. G. Schulz and F. R. Tangherlini, "Optical Constants of Silver, Gold, Copper, and Aluminum. II. The Index of Refraction n," *The Journal of the Optical Society of America (JOSA),* vol. 44, pp. 362-367, 1954.

[70] M. Gottlieb and G. B. Brandt, "Temperature sensing in optical fibers using cladding and jacket loss effects," *Applied Optics,* vol. 20, pp. 3867-3873, 1981.

[71] N. Instruments. (4th February 2015). *National Instruments USB-6009 DAQ*. Available: http://sine.ni.com

[72] Thorlabs. (4th February 2015). *Throlabs PDA100A Si Switchable Gain Detector User Guide*. Available: http://www.thorlabs.de

[73] Avantes. (31st January 2015). *AvaLight-HAL Tungsten Halogen Light Source*. Available: http://www.avantes.com

[74] I. F. Optic. (31st January 2015). *Plastic Fiber Optic Blue LEDs IF-E92*. Available: http://i-fiberoptics.com/

[75] Avantes. (11st January 2015). *AvaSpec-128 StarLine Ultrafast Fiber-optic Spectrometer*. Available: http://www.avantes.com

[76] S. Tao and A. Jayaprakash, "A fiber optic temperature sensor with an epoxy-glue membrane as a temperature indicator," *Sensors and Actuators B: Chemical,* vol. 119, pp. 615-620, 2006.

[77] C.-S. Chu and Y.-L. Lo, "A plastic optical fiber sensor for the dual sensing of temperature and oxygen," *IEEE Photonics Technology Letters,* vol. 20, pp. 63-65, 2008.

[78] A. Tapetado Moraleda, P. Pinzon Castillo, J. Zubia, and C. Vazquez, "Polymer Optical Fiber Temperature Sensor with Dual-Wavelength Compensation of Power Fluctuations," *Journal of Lightwave Technology,* vol. PP, 2015.

[79] J. M. Senior, G. Murtaza, A. I. Stirling, and G. H. Wainwright, "Single LED based dual wavelength referenced optical fibre sensor system using intensity modulation," *Optics & Laser Technology,* vol. 24, pp. 187-192, 1992.

[80] A. Wang, G. Z. Wang, K. A. Murphy, and R. O. Claus, "Fiber-optic temperature sensors based on differential spectral transmittance/reflectivity and multiplexed sensing systems," *Applied Optics,* vol. 34, pp. 2295-2300, 1995.

[81] A. Vallan, M. L. Casalicchio, M. Olivero, and G. Perrone, "Assessment of a Dual-Wavelength Compensation Technique for Displacement Sensors Using Plastic Optical Fibers," *IEEE Transactions on Instrumentation and Measurement,* vol. 61, pp. 1377-1383, 2012.

[82] J. Mizusawa, "Advantages of POF WDM System Design," in *Proceedings of The Eighth International Conference on Plastic Optical Fiber and Applications*, Chiva (Japan), 1999, pp. 31-35.

[83] D. J. Webb, S. Jones, L. Zhang, I. Bennion, M. Hathaway, and D. Jackson, "First in-vivo trials of a fiber Bragg grating based temperature profiling system," *Journal of biomedical optics,* vol. 5, pp. 45-50, 2000.

[84] B. W. Trautner, A. C. Caviness, G. R. Gerlacher, G. Demmler, and C. G. Macias, "Prospective evaluation of the risk of serious bacterial infection in children who present to the emergency department with hyperpyrexia (temperature of 106ºF or higher)," *Pediatrics,* vol. 118, pp. 34-40, 2006.

[85] D. F. Danzl and R. S. Pozos, "Accidental Hypothermia," *New England Journal of Medicine,* vol. 331, pp. 1756-1760, 1994.

[86] B. C. Lesieutre, W. H. Hagman, and J. L. Kirtley, Jr., "An improved transformer top oil temperature model for use in an on-line monitoring and diagnostic system," *IEEE Transactions on Power Delivery,* vol. 12, pp. 249-256, 1997.

[87] M. Wang, A. J. Vandermaar, and K. D. Srivastava, "Review of condition assessment of power transformers in service," *IEEE Electrical Insulation Magazine,* vol. 18, pp. 12-25, 2002.

Chapter 3.

Chapter 3

Self-Reference Optical Intensity Sensor Network using POFBGs for Biomedical Applications

In this chapter, the development of a novel hybrid sensor network combining both glass fiber Bragg gratings (GFBGs) and polymer fiber Bragg gratings (POFBGs) is presented. The proposed schematic bridges the gap between the remote interrogation of multiple optical sensors and the advantages of using inherently biocompatible low-cost polymer optical fiber (POF) based photonics sensing. The topology is compatible with wavelength division multiplexing (WDM) networks so multiple remote sensors can be addressed providing high scalability. A central monitoring unit with virtual data processing is implemented, which could be remotely located up to units of kilometres. The feasibility of the proposed solution for medical environments and biomedical applications is shown.

3.1. Introduction

Minimally invasive tools and sensors have become essential for medical diagnosis and surgery with the desire of not only serving at the same time to sense physiological parameters but also being able to overcome biocompatibility concerns. Nowadays, there are different medical areas where fiber-optic sensors hold enormous potential such as in clinical biomechanics, mainly if in-vivo applications are pursued [1, 2], as here there is a need to develop sensors for minimally invasive surgery procedures. Other important features include small size, light weight, geometrical flexibility, chemical inertness, electric and thermal insulation, and immunity to electromagnetic interference. Measurement principles mainly include the use of optical interferometers in multiple configurations (Sagnac, Michelson, Mach-Zehnder or Fabry-Perot), intensity-based fiber-optic sensors (FOS) and fiber Bragg gratings (FBGs). The first approach usually leads to extremely high sensitivity sensing solutions but at the cost of very complex signal processing schemes whereas the latter can also be a costly post-processing solution. In contrast,

potentially low-cost intensity-based optical sensors modulate the power loss in response to changes in the desired measurand. Those type of sensors have been successfully developed for use in magnetic resonance imaging environments [3-5]. However, the main drawback of the intensity-based approach is the need for a self-referencing scheme in order to avoid undesirable perturbations in the optical power loss (due, for example, to changes in the source power) that can distort the measurement. Intensity-based FOS have been described for monitoring the intravascular blood pressure [6] and intracranial pressure (ICP) [7, 8]. In these solutions, the self-reference property was achieved by a dual-beam technique, using a secondary optical fiber path, and then computing the ratio of both signals. Interesting applications of intensity-based FOS based on a bend optical fiber have also been developed to measure respiratory chest circumference changes [9] and the limb circumference change during occlusion plethysmography [10], respectively. Both sensors utilize the leakage of light from a fiber under mechanical perturbation. However, no self-referencing technique was applied leading to noisy measurements which limited the range and resolution.

Although POF are generally seen as a lower cost alternative solution to glass-based short-distance optical links, they are also very attractive for exploitation in in-vivo sensing applications because they are inherently more biocompatible than to their glass counterparts [11]. Moreover, the use of glass fiber is sometimes inappropriate due to the risks from breakages. No matter the case, the most common problem with these fiber-optic sensing solutions is the need for a fiber link between the point of detection which is in the vicinity of the patient and the read out unit which gives the required information. Areas most distant, considered as "remote", from hospitals do not exceed 50km and distances more than 10km from a general practice service are extremely rare situations [12]. When continuous monitoring of critical parameters in day-to-day activities is required wireless portable interrogators can be cumbersome for both medical practitioners and patients [13] and a smart central monitoring unit for remote interrogation seems to be a good choice.

The application of GFBGs in medicine has already been described in detail in different reviews [14, 15], and their introduction in clinical practice is just at the beginning [16]. There are also initial studies on biomedical applications focused on fiber-optic intensity-based sensors [17, 18], the latter work focused on tapered fiber-optic biosensors, being capable nowadays to monitor a huge amount of measurands and still under development. In [19] a POF-based intensity fiber-optic sensor is reported, which is designed to monitor the human spine motions providing sensitivities around 1.3dB/mm (optical power loss vs. fiber gap) and 0.24dB/º (optical power loss vs. fiber tilt angle). Further development of a spine bending sensor [20] introduces a single sensor self-referenced technique by adding more fibers and allowing a maximum sensitivity of 1.24dB/º.

An angular fiber-optic sensor with possible application in detecting the human extension's articulation is investigated in [21] providing sensitivities of 3mV/º per angle of curvature. The detection of toluene dispersed in water was reported in [22] by swelling the POF cladding with a high density polyethylene (HDPE) to enhance the output light intensity change. It turned out that a sensitivity of 2.3dB/% with respect to the toluene concentration was obtainable. Several authors propose monitoring the heartbeat [23, 24] and respiratory rate [23] measuring the attenuation of a POF according to the heart and respiration cycle, respectively. The majority of the designed devices limit the mobility of the patients. For this reason a huge effort is pursued for the development of wearable monitoring systems able to measure vital physiological parameters. In [25] a POF sensor embedded into textile fabrics for the monitoring of respiratory movement is presented. The elastic textile belt contains an optical fiber in a half-a-loop or "U" shape. When stretching the belt, the curvature radius will increase, thus reducing the bend loss in the fiber. The main disadvantage of these sensor is the non-use of a self-referencing technique that avoids false reading caused by the fluctuation of the light source or other undesired disturbances.

Nowadays, the possibility of inscribing FBGs in POF is developed by using a special type of POF, the microstructured polymer optical fiber (MPOF) [26]. Those POFBGs try to take advantage of polymer benefits such as larger elastic limit, higher maximum strain limit and larger temperature and humidity responses compared to glass while maintaining the benefits of FBG-based sensors. Nevertheless, limited effort has been directed towards synergizing biocompatible POF-based photonic sensing with the WDM interrogation method that allows multiplexing FBGs, with just a few exceptions [27]. The main underlying reason behind this lack of development is the mismatch between the optimum operating wavelength regions of POFs and the optical devices exploited for telecommunications purposes. The latter are developed for a wavelength region (C- and L-bands) totally unsuitable for POF-based transmission over medium-distances (hundreds of meters or greater) due to the high attenuation of polymethylmethacrylate (PMMA) based POF of around 0.35dB/cm at 1,550nm [28]. Such high losses limit the practical length that POF can be used at this wavelength to typically less than tens of cm. Moreover, pigtailed sources, detectors, circulators and mux/demux devices are available off-the-shelf on glass fiber related technology. Consequently the fact that only a short length of POF can be used in the C- and L-bands requires a glass connecting lead to be used unless the sensor is mounted right next to the measurement unit, thus resulting in a very restricted sensing solution design criteria. This glass-POF combination has already been tested in [29] for a single sensor, where a short POFBG sensor section was glued to a glass fiber on a POFBG accelerometer. Another approach is the use of POFBG devices near the optimum operating wavelength of the POF if longer fiber leads are going

to be used, which can be more convenient for certain practical biomedical applications although preventing the use of relatively cheap optical devices designed and manufactured for glass fibers.

In this chapter, the feasibility of a hybrid glass-POF WDM network topology for addressing multiple self-referenced FOS is analysed. The intention is to bridge the gap between the remote interrogation of multiple optical sensors and the advantages of using biocompatible POF-based sensors with low manufacturing cost, including those based on POFBGs. Another important attribute that will be discussed is the power budget analysis of the proposed topology as the POFBG needs to be integrated at some point with glass fiber related technology to make it useful.

3.2. Microstructured Polymer Optical Fibers

3.2.1. Historical Development

In the past few decades POF technology has advanced rapidly due to the expectation that POF will form an integral part of communication networks. POF is advantageously replacing copper cables in low-reach communications links by offering the advantages intrinsic to any optical fiber in relation to transmission capacity, immunity of interference and small weight. In addition, POF serves as a complement for glass fibers in low-reach communications links because they are easy to handle, flexible and economical.

Despite these advantages, POF has not yet achieved widespread deployment in telecommunication networks. The main reason is clear, large core multimode step-index POF offers a large modal dispersion and lower bandwidth, limiting the length of the telecommunication networks. On the other hand, singlemode POF [30], ideal for telecommunication purposes, has proved to be a manufacturing challenge, and the associated small mode area limits the applications. The technology used to improve the transmission of the current POFs is the graded-index polymer optical fiber (GI-POF) [31]. The technology associated to this fiber relies on a complex polymerization process to obtain a particular graded refractive index profile across the diameter of the fiber. The choice of the materials that will form the fiber is extremely limited. However, even in the case of using these materials, the use of conventional POF is limited to a few hundred of meters.

MPOF tries to take advantage of the benefits of POF and photonics crystal fibers (PCF), addressing all the disadvantages of conventional POF. The light guiding mechanism in MPOF is different form conventional POF. It arises from a pattern of microscopic air channels that runs along the length of the fiber rather than from variations in the refractive index of the fiber material. The application of this guiding mechanism to POF offers a range of unique new properties and

benefits. These include the possibility to combine singlemode behaviour with large mode areas, which is the ideal combination for easy-to-install transmission fiber. The lower processing temperature of polymers and the controllability of the polymerization process allows the possibility to use a single polymer or doped polymer for modifying the properties of the fiber. On the other hand, the manufacturing process of MPOF avoids the use of a complex polymerization process as required for conventional GI-POF. As a result, a much larger range of polymer is available for MPOF. This provides great potential for reducing the absorption losses in the fiber material, thereby extending the useful range of POF. In addition, there is potentially an exceptionally low cost associated with the production of MPOF. Since the fiber are fabricated from a single polymeric material, no complex chemistry is required, allowing low-cost and large-volume production.

3.2.2. Materials

Step-index and some graded-index POFs are based on PMMA. This material is widely available, inexpensive and has a low loss in the visible range. The minimum attenuation of PMMA is 0.05dB/m at 570nm [28]. The typical applications of POF products are short distance data transmission, illumination and sensing. The extensive use of PMMA as the base material in POFs resulted that the first MPOF was also made from PMMA and still remains in extensive use. But other commercially available polymers also began to be used so as to take advantage of their specific properties. CYTOP is a perfluorinated polymer that increases the transparency in the visible and near infrared [49]. This allows CYTOP fibers to operate at the 850 and 1,300nm telecommunications windows, and thus be compatible with components developed for glass-based systems. Other important materials used in MPOFs are the cyclo-olefin co-polymer (COC) TOPAS which displays lower water absorption than PMMA [32]. Polystyrene with a higher refractive index, cellulose which is biodegradable and polycarbonate with a higher glass-transition temperature are other possible materials used in MPOFs.

3.2.3. Singlemode Microstructured Polymer Optical Fiber

Although POF technology has focused almost exclusively on large-core and graded-index multimode fibers, singlemode MPOF has also been fabricated [33, 34] – a difficult problem using conventional POF technology due to the small core size and the high contrast refractive index required. The singlemode MPOF core sizes vary from 1 to 15μm depending on the wavelength to be guided, see Figure 3.1. The chromatic dispersion of the singlemode MPOF reported in [35] is measured to be 100ps/(nm·km) at a wavelength of 855nm, with a zero-dispersion wavelength of 1.35μm [36]. As with conventional microstructural glass optical fiber (MGOF), high dispersion

singlemode MPOF can be fabricated for dispersion compensation applications. Singlemode MPOF is of no interest for communications, given the high attenuation of PMMA and the resulting short-reach data communication networks. Singlemode MPOF has important outcomes, however, including the possibility of inscribing gratings for sensing applications. One important use of singlemode MPOF is to inscribe long period gratings (LPG). The simple inscribing process and the resonance features in the 500 to 750nm range, where PMMA-based MPOF is the most transparent [28], allow up to some meters of fiber to be used. LPGs based on singlemode MPOF are used in temperature [32] and strain [37] sensing applications. On the other hand, several authors proposed the use of singlemode MPOF to inscribe FBGs operating around 1.55μm [38] to be compatible with optical communications devices. The material absorption of PMMA exceed 50dB/m at 1,550nm [28], limiting the application of FBGs inscribed in this band. For this reason, singlemode microstructured polymer optical fiber Bragg gratings (MPOFBG) operating at shorter wavelengths [39] are also developed and implemented in many sensing applications [40].

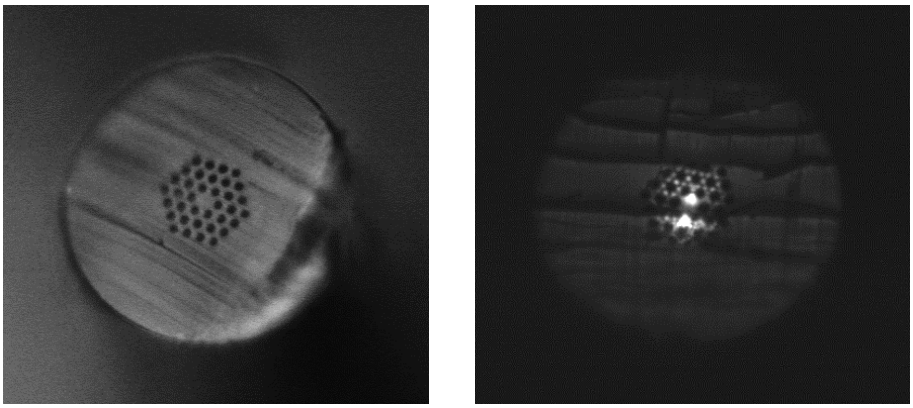

(a) **(b)**

Figure 3.1. Microscope image of a singlemode MPOF based on PMMA. (a) Cross-section (b) Visible guiding light in the fiber core.

3.2.4. Multimode Graded-index Microstructured Polymer Optical Fiber

GI-POF has been developed for high bandwidth short-reach data communication applications, providing flexible fibers and large spot size for easy configurable Local Area Networks (LANs). The technology behind conventional GI-POF is very complex and costly. MPOF technology allows a cost-effective alternative to produce gradual index optical fibers. The gradual-index microstructured polymer optical fiber (GI-MPOF) is fabricated using multiple depressed-index rings. The hole diameter increases with distance from the centre, so that the azimuthal average provides an approximation to the ideal parabolic graded-index profile to

compensate for modal dispersion. GI-MPOF has a minimum loss of 0.8dB/m at 760nm [41] and provides a high bandwidth data transmission capacity in excess of 2.5Gbit/s in 100m [41]. Both parameters are in good agreement with the current requirements used in the short-reach data communications networks.

3.2.5. Few-mode Step-index Microstructured Polymer Optical Fiber

Large core, large diameter, flexible multimode fiber operating in the visible is desirable as that could facilitate low-cost connectors and user installation. Several few-mode or multimode MPOF have been reported with losses in the state-of-art of the commercial PMMA-based POF standard. Multimode MPOF has been used in a very few applications, as the large number of modes and their leaky nature complicates its behaviour. An important feature of multimode MPOF is its high bandwidth. Experimental characterization shows bandwidth around 10Gbit/s at 636nm for lengths between 40 and 75m [42] but the use of multimode MPOF for short-reach communication networks is limited by the non-constant bandwidth-length product. An important advantage of multimode MPOF is the possibility to fabricate Bragg gratings for low cost sensing applications. Multimode MPOF compared to glass fiber is easier to fabricate and the chemical composition of PMMA offers the possibility of chemical modification using organic techniques. On the other hand, the technology behind the fabrication of multimode MPOF is less complex than the singlemode MPOF due to the small core size and the refractive index contrast that imply an exhaustive and accurate control of the manufacturing parameters (e.g. temperature). The multimode MPOF gives possibilities of using ferrule connectors, where slight misalignment in connecting fiber would be insignificant compared to the impracticalities of using singlemode fiber. Using multimode MPOF also lends itself nicely to cheaper light sources, especially when comparing the cost of a broad area emitter to a single transverse mode light source.

3.3. Fiber Bragg Grating in Few-moded Microstructured Polymer Optical Fiber

3.3.1. Inscription Process

The fiber used in this work is a few-moded MPOF and is acquired from Kiriama Pty. Ltd. Sydney, Australia, a detailed description of the manufacturing process is documented in [26]. This fiber is made from a purely PMMA primary preform, into which the desired pattern of holes is frilled. The primary preform is drawn to form a secondary preform, and the secondary preform is drawn to fiber directly. The fiber has a core diameter of 50μm and a cladding diameter of 150μm. The core is surrounded by 72 air holes arranged in three concentric rings. The optical

fiber may present dimensional irregularities due to the novelty of the manufacture technique. The holes provide a lower effective index cladding surrounding a solid higher index core, with the light therefore confined, see Figure 3.2. The corresponding effective refractive index (n_{eff}) is 1.479 [43].

The POFBGs used in this chapter were fabricated by Alberto Tapetado Moraleda during a five month research stay in the Institute of Photonics Technologies at Aston University[2], Birmingham, United Kingdom, under the supervision of Prof. Dr. David J. Webb.

The POFBG manufactured process starts cutting the ends of the fiber with a hot razor blade. The optimum cleaving parameters depend significantly on the material properties of the drawn fiber, and thus also on the specific drawing conditions and the final hole structure. In PMMA MPOF the optimum cleaving temperature is just above the brittle-to-ductile phase transition. For MPOF with an hexagonal hole structure based on standard polymer PMMA, the optimum temperature for both blade and fiber is 77.5ºC. A complete analysis of different parameters on the cleaving process is carried out in [44, 45].

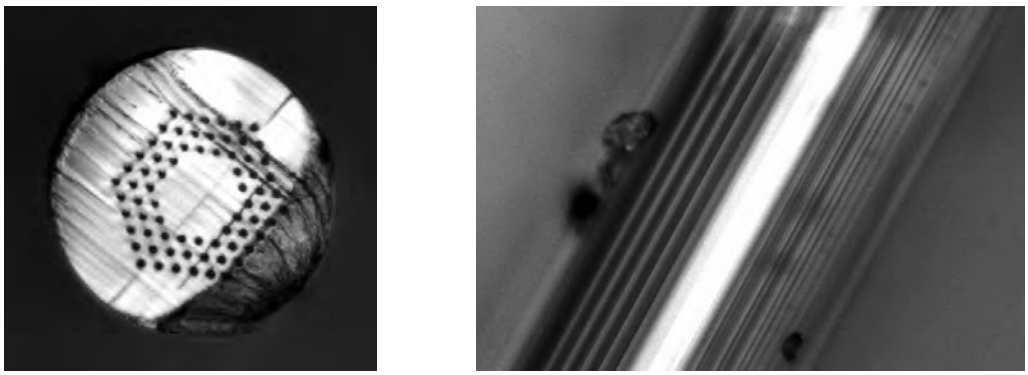

(a) **(b)**

Figure 3.2. Microscope image of a few-moded MPOF based on PMMA. (a) Cross-section (b) Longitudinal-section.

Around 10cm length of MPOF is mounted in a V-Groove, which is attached to a pair of X-Y-Z micropositioning stages, allowing for the adjustment of the fiber position. Inscribing process takes long and hence the MPOF needs to be immobilised to provide a good mechanical stabilization and to minimize the effects of air currents during the inscribing process.

The gratings in the optical fiber are the result of the fabrication of periodic perturbations within the core of the waveguide. The perturbations are created by exposing the core of the fiber

[2] Institute of Photonics Technologies. Aston University. Birmingham. United Kingdom.

to an interference pattern, which modifies the refractive index of the core at the point of exposure. In a FBG inscription process, the interference patterns are perpendicular to the longitudinal axis of the fiber and have a constant period, as shown in Figure 3.3.

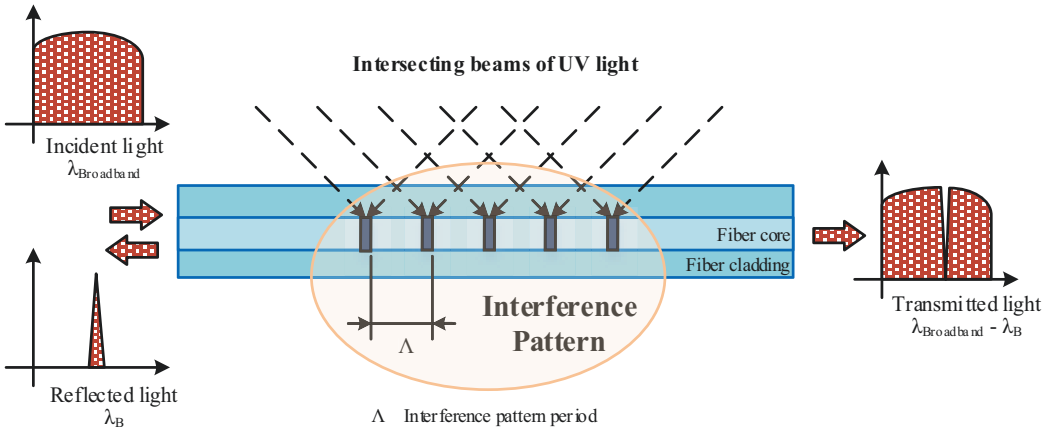

Figure 3.3. Schematic of uniform Bragg grating in an optical fiber.

A narrow band of the incident optical field within the fiber is reflected by successive, coherent scattering form the periodic refractive index variation. The strongest interactions or mode-couplings occur at the Bragg wavelength (λ_B) given by [46]:

$$\lambda_B = 2 \cdot n_{eff} \cdot \Lambda \qquad (3.1)$$

where n_{eff} is the effective refractive index and Λ is the interference pattern period. Each reflection from a crest in the index perturbation is in phase with the next one at λ_B. The grating changes the spectrum of an incident signal by coupling energy to other fiber modes.

Many techniques have been developed for the fabrication of FBG, e.g. the transverse holographic technique [47], the phase mask technique [48, 49] and the point-by-point technique [50]. The phase mask technique greatly simplifies the manufacturing process and its low coherence requirement on the ultraviolet (UV) beam permits the use of a conventional excimer laser. The phase mask technique not only yields high-performance devices, but it is also very flexible, i.e. apodization and chirping techniques are easily introduced to control the spectral response characteristics of the FBGs [51].

The phase mask is plate of a flat silica-glass slab with a periodic structure etched using photolithography techniques, as shown in Figure 3.4.

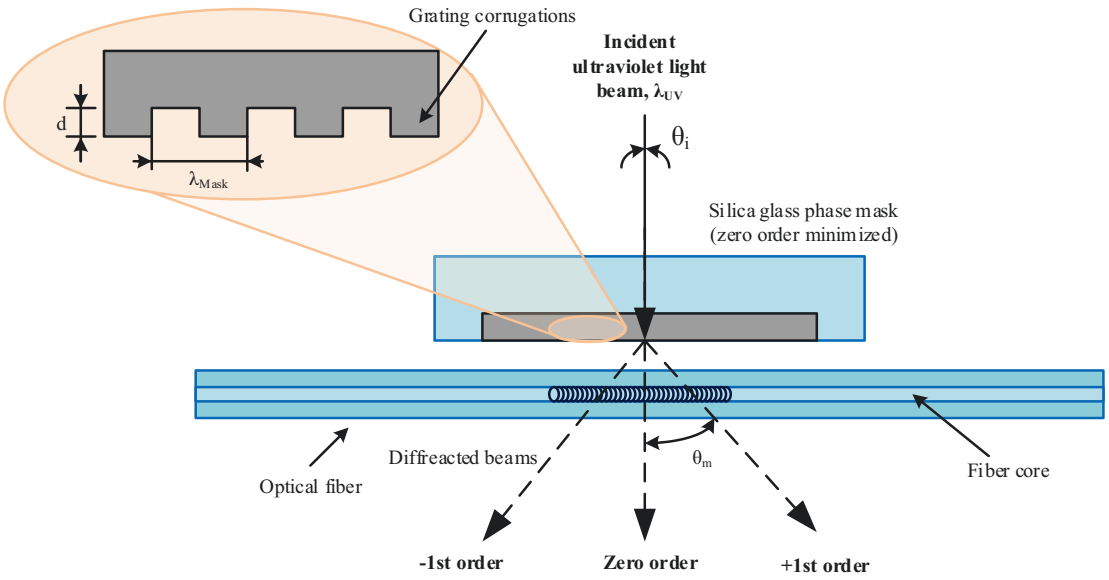

Figure 3.4. Incident UV beam passing through a phase mask.

UV light which is incident normal to the phase mask passes through and is diffracted by the periodic corrugations of the phase mask in different directions, known as orders. The angle of diffraction for each order (θ_m) can be calculated using the following equation:

$$m \cdot \lambda_{UV} = \lambda_{Mask} \cdot \left(\sin\left(\theta_m\right) + \sin\left(\theta_i\right)\right) \qquad (3.2)$$

where m is the diffracted order, λ_{UV} is the wavelength of the UV light, λ_{Mask} is the period of the pattern and θ_i is the angle of incidence of the UV inscription beam. When the angle of incidence of the UV laser beam is normal to the surface of the phase mask, as shown in Figure 3.4, the Equation (3.2) can be simplified as follows:

$$m \cdot \lambda_{UV} = \lambda_{Mask} \cdot \sin\left(\theta_m\right) \qquad (3.3)$$

Most diffracted light is contained in the 0, +1 and -1 diffracted order. However the phase mask is designed to suppress the diffraction into the zero order by controlling the depth of the corrugations in the phase mask. In practice the amount of light in the zero order can be reduced to less than 5% with approximately 40% of the total light intensity divided equally in the ±1 orders [46].

The two ±1 diffracted order beams interfere to produce a periodic pattern that photoimprints a corresponding grating in the optical fiber as shown in Figure 3.5.

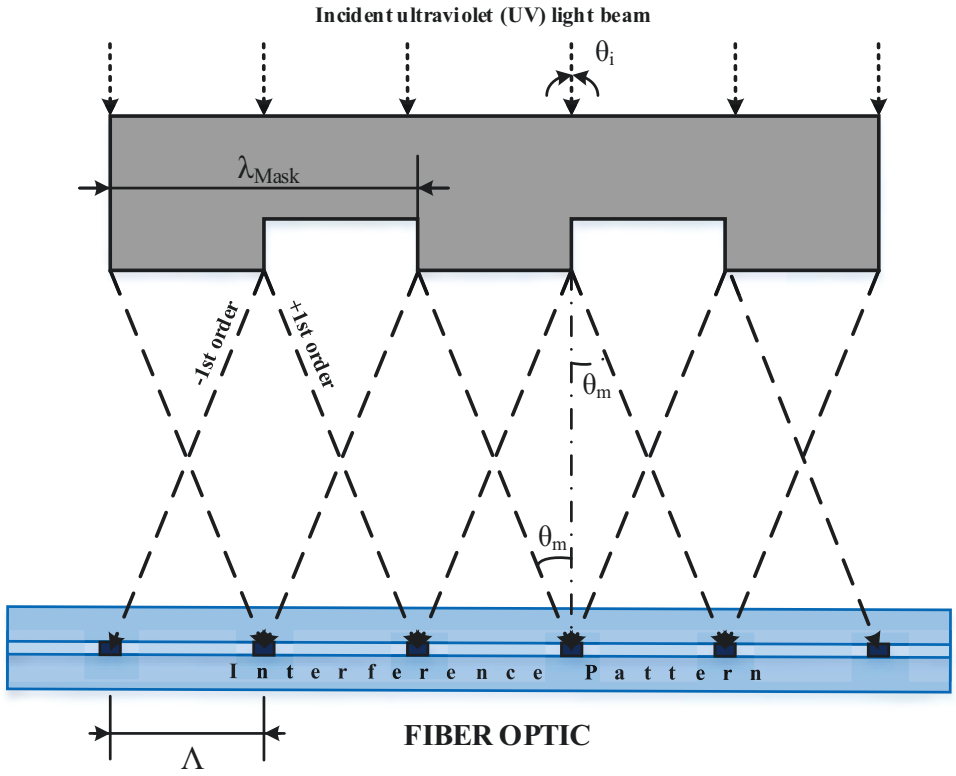

Figure 3.5. UV interference pattern generated from ±1 diffraction orders of the phase mask.

If the period of the phase mask grating is λ_{Mask}, the period of the photoimprinted index is geometrically calculated from the intersection of two beams [46]. The resulting expression is defined as follow:

$$\Lambda = \frac{\lambda_{Mask}}{2} \tag{3.4}$$

Note that this period is independent of the wavelength of UV light irradiating the phase mask; however, the corrugation depth required to obtain reduced zero order light is a function of the wavelength and the optical dispersion. The Bragg wavelength of the FBG response can be calculated using Equation (3.1) and (3.4) as follow:

$$\lambda_B = n_{eff} \cdot \lambda_{Mask} \tag{3.5}$$

FBG inscription is carried out using a phase mask designed for 325nm illumination wavelength [52], see Figure 3.6. Phase masks with different periods are used to produce FBGs with different resonance wavelengths. The phase masks are capable of grating fabrication up to 5mm long and 3mm wide. The manufacturer guaranteed zero order reduction to less than 4% [52].

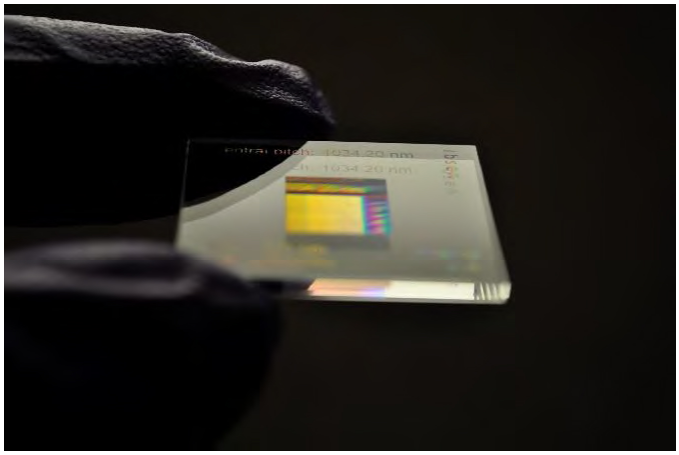

Figure 3.6. Top side of a phase mask used to inscribe MPOFBGs.

The grating is inscribed using a helium-cadmium (He-Cd) laser with a continuous wave (CW) UV output of 30mW at a wavelength of 325nm. The reflection mirror stands by the laser and is controlled by a motorised linear stage and a motion controller, enabling the static inscription of the gratings, see Figure 3.7. The UV beam is vertically focused to the core fiber using a cylindrical lens of focal length 10cm. The focused beam passes down through a phase mask, which is mounted above the fiber at a distance of approximately 200μm from the fiber surface. The laser intensity irradiated on the fiber is approximately 200mW/mm^2 [53]. The length of the grating is controlled by the width of the UV beam. In this case, the grating length, L, is 1.8mm [43]. Alignment of the beam to the fiber core is accomplished by monitoring sideways and backwards scattering from the fiber.

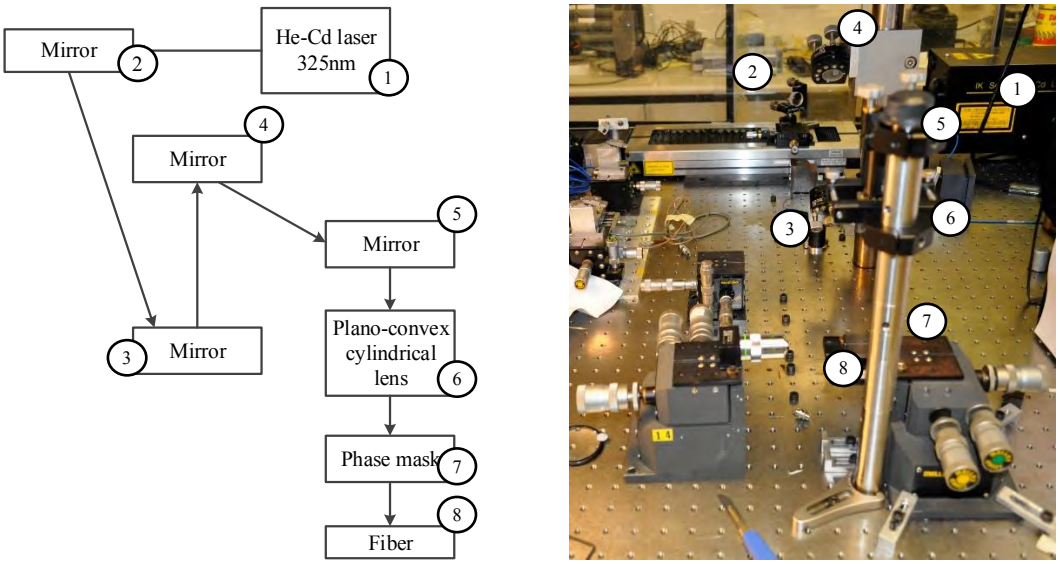

Figure 3.7. (a) Schematic and (b) real picture of the experimental arrangement.

The Bragg grating is interrogated during and after inscription to characterise the grating growth and final response. A broadband light source (BLS) is launched into a multimode 50/125μm fiber coupler with a 50:50 split ratio to enable the monitoring of the reflected power from the inscribed Bragg grating using an optical spectrum analyser (OSA). The glass arm of the coupler connected to the MPOF is equipped with a ferrule contact/angle physical contact (FC/APC) connector. Then a 50/125μm glass fiber pigtail with a FC/APC connector only on one end is connected to the coupler using an adaptor. The fiber end without connector is butt-coupled to the MPOF using a small amount of polymer index matching gel to reduce Fresnel reflections from the glass end face.

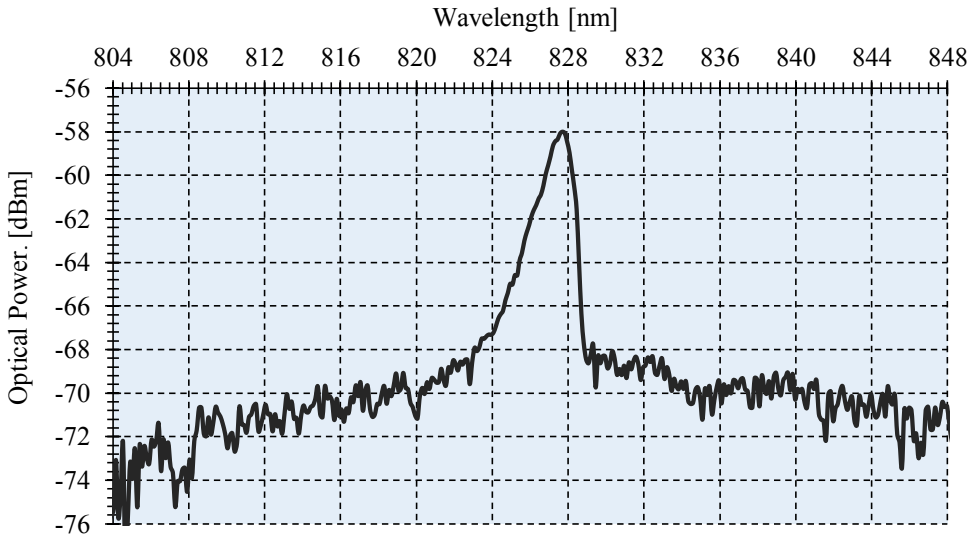

Figure 3.8. Reflection profile of FBG fabricated in a few-moded MPOFBG at 827.6nm.

The reflected spectrum of a FBG inscribed in a few-moded MPOF is shown in Figure 3.8. The FBG takes advantage of the lower attenuation at the 800nm spectral region as documented in [54]. The FBG is fabricated into PMMA microstructured optical fiber (MOF) in 49min using a phase mask with a period of 557.5nm. The resulting reflected Bragg grating response has a central wavelength of 826.6nm and a full width at half-maximum (FWHM) of 1.9nm when using an OSA with a 0.5nm bandwidth resolution. From Equation (3.5), using the fiber effective refractive index and the phase mask period, the theoretical Bragg wavelength is 824.5nm. This value is in concordance with the experimental value obtained from the manufactured FBGs. The deviation between the theoretical and experimental value is due to multiples factors such as the weak connexion between the glass and polymer fiber that modifies the FBG output spectrum, the dimensional irregularity of the optical fiber core and cladding, the exposure time during the inscription process, and the OSA resolution. The signal-to-noise ratio (SNR) is 9.85dB.

The possibility of using FBG reflecting longer wavelength has also been realised using few-moded MPOF. This possibility allows for a wider range of FBG applications in sensor networks operating in the third communication window. As an example, several fabricated FBGs are shown in Figure 3.9. First grating is inscribed for 56min with a central wavelength of 1,530.1nm. The phase mask utilized to inscribe the grating has a period of 1,034.2nm. The FWHM and the SNR are around 2.1nm and 15dB, respectively. The theoretical Bragg wavelength is 1,529.6nm. Second grating is fabricated with a 1,057.2nm phase mask. After 48min inscribing process, the central wavelength, the FWHM and the SNR are 1,563.3nm, 1.8nm and 16dB, respectively. The theoretical Bragg wavelength is 1,563.6nm. Finally, the third grating is fabricated with a phase mask with a period of 1,061.18nm during 40min. The central wavelength is 1,570.3nm. The FWHM and the SNR are 1.2nm and 15.5dB, respectively. The theoretical Bragg wavelength is 1,569.5nm.

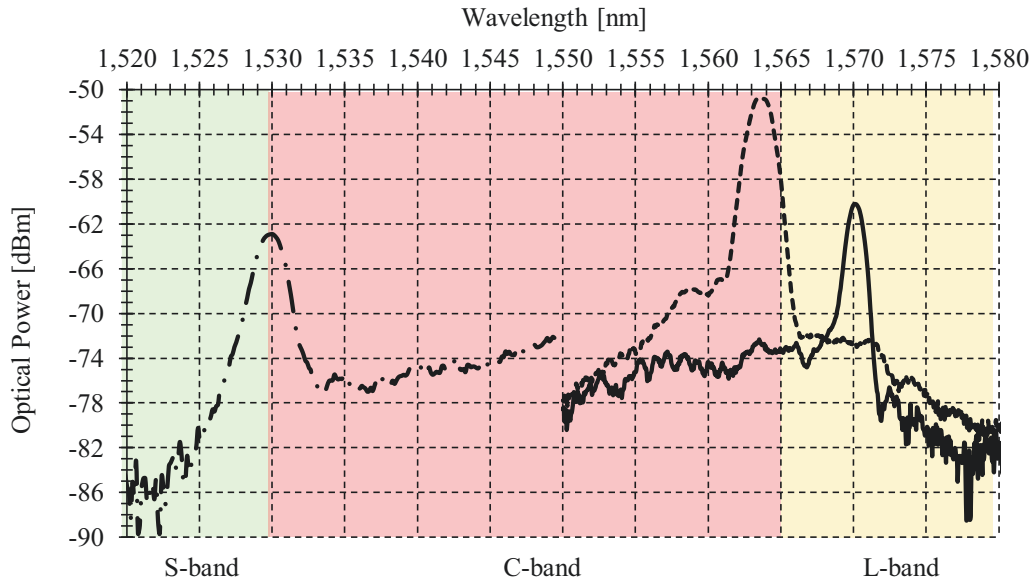

Figure 3.9. Reflection profile of FBGs fabricated in few-moded POFBG in the third fiber optic communication window: ─ · ─ First MPOFBG (λ_c=1,530.1nm), ─ ─ Second MPOFBG (λ_c=1,563.9nm), ── Third MPOFBG (λ_c=1,570.3nm)

It has been demonstrated that FBG can be consistently fabricated in PMMA MPOF within the third communication window. Moreover FBG can also be fabricated in few-moded PMMA MPOF within the first communication window with lower attenuation than at longer wavelengths.

3.3.2. Connectors

As discussed previously, FBGs in few-moded MPOF have an enormous potential in low-cost sensing applications but this technology needs to progress out of the laboratory and into the real world. The lack of singlemode POF components means that connection to glass fiber is

necessary to interrogate the POFBG. Initially, the connection to glass fiber was done by using butt coupling on an optical table [55] but the necessity to implement it in a real scenario limited its use. An important breakthrough was the development of a stable glue union between the glass and MPOF, enabling POFBG to be used with other devices [56]. The investigated technique permits to splice POF to step index glass fiber using a UV curing optical adhesive. The optical adhesive used has a high viscosity, excellent flexibility and durability to moisture exposure. The refractive index of uncured and cured material is 1.48 and 1.51, respectively [57]. The glass transition temperature is 43ºC [57].

The ends of the fiber are cut using a hot razor blade. The temperature of the fiber and the blade is 77.5ºC. In this case, no glass fiber pigtail with FC/APC connector is used, but rather a bare multimode glass fiber cleaved at 8º to reduce the Fresnel reflections from the end face. The core and the cladding of the multimode glass fiber are 50 and 125μm, respectively. The glass fiber has similar core and cladding diameter to the POF to facilitate the alignment process and to reduce the losses. The polymer and glass fibers are placed on separate V-Grooves and aligned on an X-Y-Z micropositioning stage. Alignment is achieved by launching visible light into the POF and monitoring the guidance by projecting the end face profile onto a screen using a microscope objective. After the alignment process, a small amount of adhesive is applied to the joint. Minor adjustments on the X-Y-Z micropositioning stage are required to optimize the Bragg reflection spectrum when the grating is interrogated using a multimode 50/125μm fiber coupler with a 50:50 split ratio, as described in the inscribed process. Then, the adhesive is cured using a curing light source, exposing the glued joint for 1min. The light source output power is 60mW at 365nm with a 2% iris coverage. A second and a third gluing process may be necessary to guarantee a solid union. The second and third exposure time are 5 and 10min, respectively. The result of the gluing process is shown in Figure 3.10.

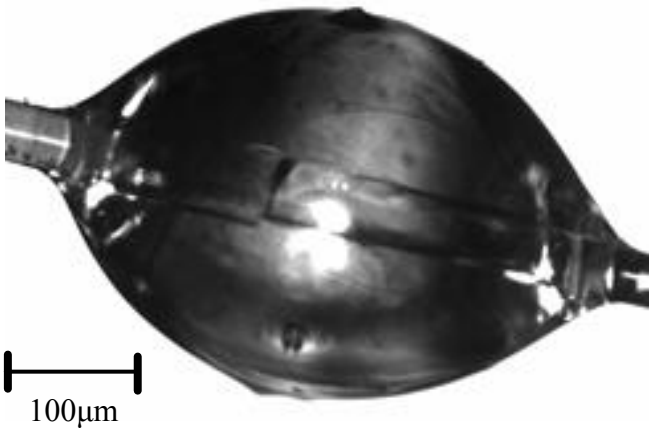

Figure 3.10. Microscope image of the glue union between polymer (left) and a glass (right) fiber.

The principal problem of such connections are the non-permanent union that needs to be realigned regularly. Other important problem occurs during the gluing process. If the gluing process is not quick, the adhesive may possibly travel along the ring of holes of the MPOF. This results in an interruption of the guidance at the glued joint, therefore as the fiber is bent there is modal redistribution and a loss of light at the joint, as described in [29, 56]. To overcome these problems, different alternatives based on polishing [58, 59] and cleaving processes [59] have been developed to make connections with MPOF. The main drawback of the polishing technique is the low clarity of the surface after the polishing cycle, due to the accumulation of polishing debris in the holes. On the other hand, the cleaving technique has the disadvantage of the non-use of adhesive to fix the fiber in the ferrule. The consequence of this is a possible interruption in the guidance due to movements of the fiber in the ferrule. It is clear that the cleaving method is simpler, quicker and more effective than the polishing approach. For these reasons, an improvement on the cleaving technique has been developed to minimize the movement of the polymer fiber in the ferrule. The procedure to cleave the MPOF is shown in Figure 3.11.

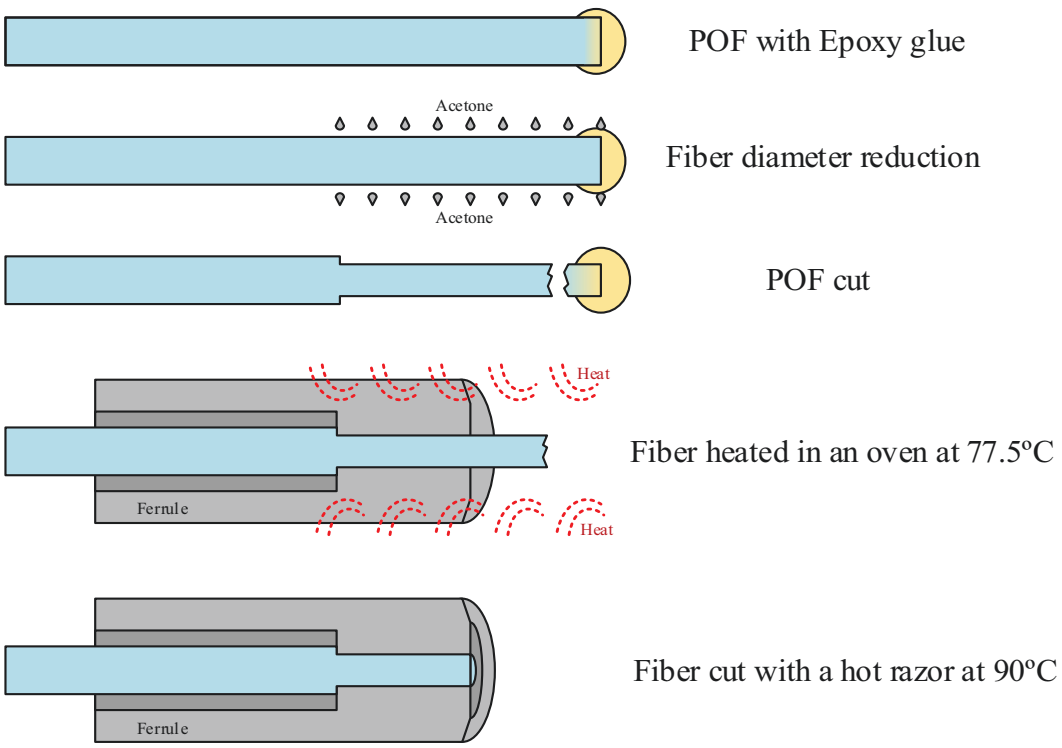

Figure 3.11. Surface preparation by means of an oven.

As in the cleaving technique, acetone is applied to one end of the 150µm diameter few-moded MPOF for 2min to reduce the fiber diameter for fitting it into the 140µm ceramic ferrule connector. A bi-component epoxy adhesive is applied to the fiber. Immediately afterwards, the fiber is inserted into the ferrule of the contact/physical contact (FC/PC) connector but pulled out

five millimetres from the end of the ceramic ferrule, as shown in Figure 3.12.(a). The epoxy adhesive is cured with ambient light for one hour and a half.

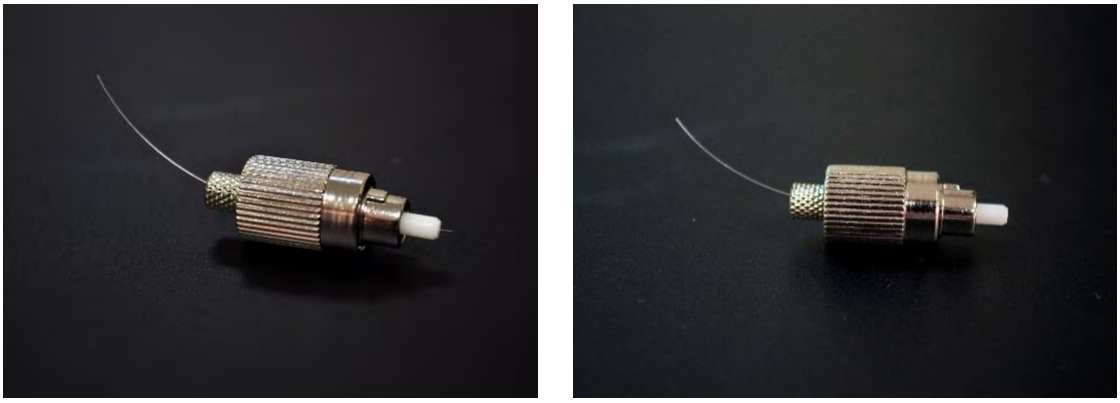

(a) **(b)**

Figure 3.12. MPOF in FC/PC connector (a) before and (b) after the cleaving process.

Finally, the excess fiber in the end of the connector is cleaved with a razor blade, see Figure 3.12.(b). The temperature of the blade is fixed at 90ºC using a high conductivity metal hot plate. The polymer fiber is heated at 77.5ºC using a cure oven which allows a uniform temperature around the connector. The result of the cleaving process in the end of the connector is shown in Figure 3.13.

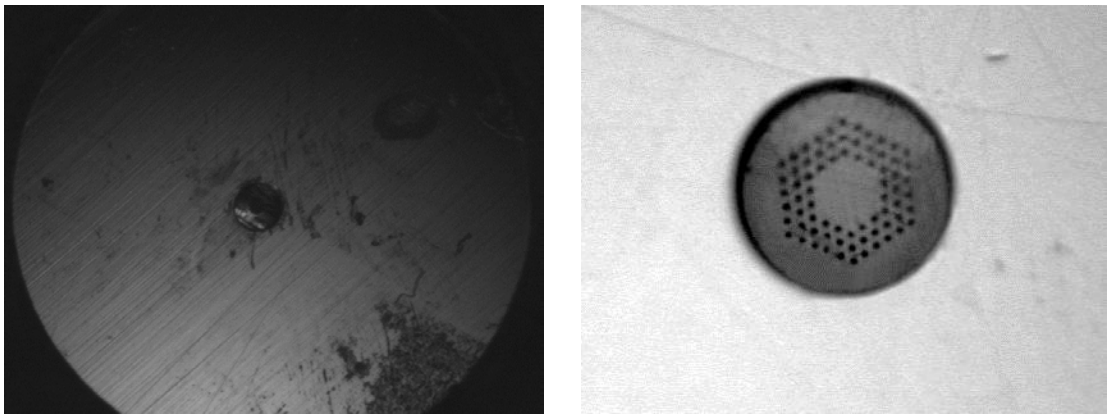

(a) **(b)**

Figure 3.13. (a) Microscope image of the MPOF and ferrule. (b) Fiber cut in the connector.

In summary, the possibility to put a connector in multi-mode or few-mode MPOF has been demonstrated, eliminating the limitations of UV glued connections and increasing the ease with which the devices can be applied in real-world sensing.

3.4. Operation Principle of the Self-referencing Technique

The proposed topology, depicted in Figure 3.14.(a), follows the frequency-based self-referencing technique for remotely addressing fiber-optic intensity sensors, as it is one of the most popular strategies for self-referencing in the last decade. The use of resonant structures as basis of a self-referencing intensity type sensor has been widely identified in literature in an approach that is known as the amplitude-phase conversion technique [60]. In this approach, a broadband light is sine-wave-modulated and launched into the system. In the sensing head, a fraction of that light is not affected by the measured parameter, constituting a reference signal. The other fraction is intensity-modulated by the measured parameter and constitutes the sensing signal. Then, both fractions are combined and delayed at the reception stage, resulting the modulated output signal. First approaches used the delayed signal in the optical domain and a long fiber delay line was required [60], more recently electrical [61] and virtual delays [62] have been considered. The phase of this signal, relative to the phase of the electrical signal that modulates the optical power emitted by the optical source, depends only on the optical loss induced in the sensor head by the measurand, including a constant factor determined by the length of the lead/return fiber. The evaluation of the phase allows information to be obtained about the measurand status; independently of the optical power fluctuations that can occur outside the sensor head thus performing a self-referenced measurement. The improvement of this configuration [62] in comparison with other self-reference solutions [61, 63, 64] is the combination of glass and polymer FBGs for addressing multiple sensors at the remote points with a reduced number of FBGs. In order to get a biocompatible system for medical applications, the usage of a single reference glass FBG and an improved remote reconfigurable virtual lock-in amplifier able to detect low signal variations provide extra features allowing the sensor interrogation.

A BLS is externally modulated at a single frequency (f) by an acousto-optic modulator (AOM). The modulated broadband signal is launched into the remote sensing points via a broadband circulator and a CWDM demultiplexer (demux). Each remote sensing point consists of a sensing few-moded MPOFBG placed after the fiber optic sensor (FOS). The proposed topology is compatible with any kind of POF-based intensity sensor as a FOS_i (see Figure 3.14) whereas the MPOFBGs employed provide the reflected back sensing channel to the central monitoring unit (which can be remotely located far away from the patient if necessary). The MPOFBGs are supposed to be located at the patient's vicinity, or even inside him/her if an invasive or in-vivo biomedical sensing application is considered. There is a glass-polymer glued connection in the FOS vicinity. Single glass FBG is located before the CWDM demux for reference purposes. The central wavelengths of the reference and sensing FBGs are λ_{Si} and λ_{MPOF}, respectively. The broadband optical circulator receives the reflected multiplexing signals from

the reference and the sensor channels, in which the sensor information is encoded. At the remote monitoring unit, the optical signal is demultiplexed by a CWDM device and distributed to an array of photodetectors (PD) by means of a data acquisition board (DAQ) which is used to convert the electrical signals from the PD to digital signals together with a band-pass filter (BPF), used to eliminate noise from all signals at frequencies outside the system frequency. A phase-shift is applied to the reference and sensor digital signals. Finally, a virtual lock-in amplifier is used to interrogate all available sensor channels.

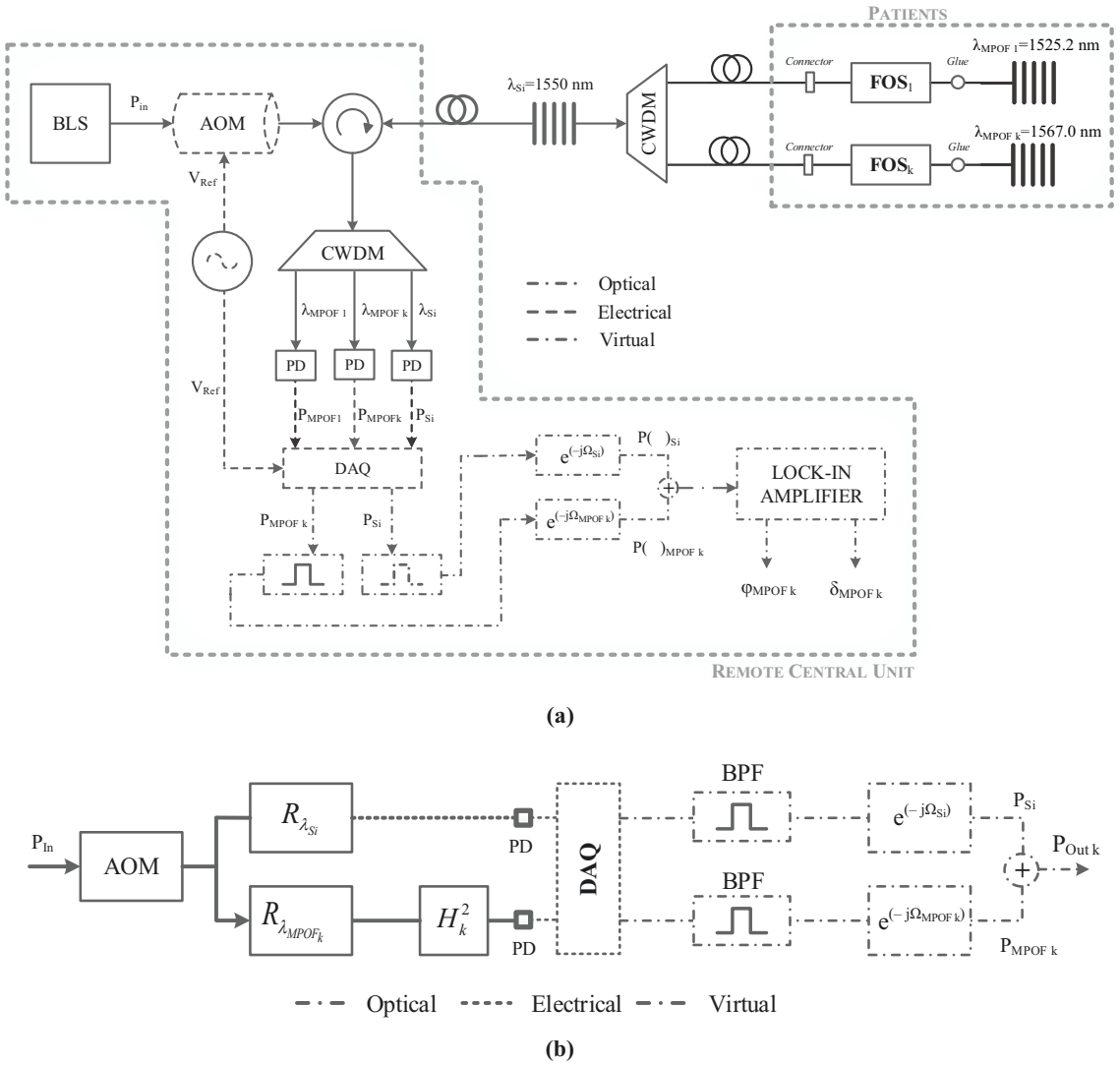

Figure 3.14. (a) Point-to-point self-referenced topology for generic remote sensing points. (b) Filter model of the configuration for a single remote sensing point including DAQ, bandpass filters (BPF) and virtual phase-shifts.

The block diagram for a single remote sensing point is shown in Figure 3.14.(b). The transfer function is derived using the notation and procedure described in [61, 64] and can be expressed as follows:

$$H_o = \frac{P_{Out\,k}}{P_{In}} = \alpha \cdot e^{(-j\cdot\Omega_{Si})} \cdot \left[1 + \beta_k \cdot e^{\left(-j\cdot\left(\Omega_{MPOF_k} - \Omega_{Si}\right)\right)}\right] \quad (3.6)$$

with

$$\alpha = m_{Si} \cdot d_{\lambda_{Si}} \cdot R_{\lambda_{Si}} \quad (3.7)$$

$$\beta_k = \frac{m_{MPOF_k} \cdot d_{\lambda_{MPOF_k}} \cdot R_{\lambda_{MPOF_k}} \cdot L_{CWDM} \cdot L_{MPOFBG-Si}}{m_{Si} \cdot d_{\lambda_{Si}} \cdot R_{\lambda_{Si}}} \cdot H_k^2 \quad (3.8)$$

where Ω_{Si} and Ω_{MPOFk} are the phase shifts for the reference and each sensor signal, respectively. Parameters m_{Si}, $R_{\lambda Si}$ and $d_{\lambda Si}$ are the modulation index, the reflectivity of the glass FBG and the PD responsivity, respectively, at the reference wavelength, whereas m_{MPOF}, $R_{\lambda MPOFk}$ and $d_{\lambda MPOFk}$ are similar but for each sensor wavelength. H_k is the sensor power loss modulation and appears two times due to the reflective operation of the sensing structure. L_{CWDM} is the insertion loss for the CWDM mux/demux. Finally, $L_{MPOFBG-Si}$ are the MPOFBG insertion losses related to the reflectivity of the gratings, attenuation of the MPOF, multimode/singlemode glass fiber connection and glass-polymer glued connection.

The expression of the system transfer function (H_0), see Equation (3.6) to (3.8), in the Z-Transform domain can be identified with that of a digital Finite Impulse Response (FIR) filter as follows:

$$H_o(z) = \frac{P_{Out\,k}}{P_{In}} = \alpha' \cdot \left(1 + \beta_k \cdot z^{-1}\right) \quad (3.9)$$

with

$$\alpha' = m_{Si} \cdot d_{\lambda_{Si}} \cdot R_{\lambda_{Si}} \cdot e^{(-j\cdot\Omega_{Si})} \quad (3.10)$$

$$z^{-1} = e^{(-j\cdot\Omega_k)} \quad (3.11)$$

The transfer function in the Z-Transform domain permits an easy study of the system frequency response in terms of generic design parameters [61]. In this approach, the phase shift difference $\Omega_k=\Omega_{MPOFk}-\Omega_{Si}$ between the time domain reference and sensor signals represents, at the same time, the angular frequency of the digital filter.

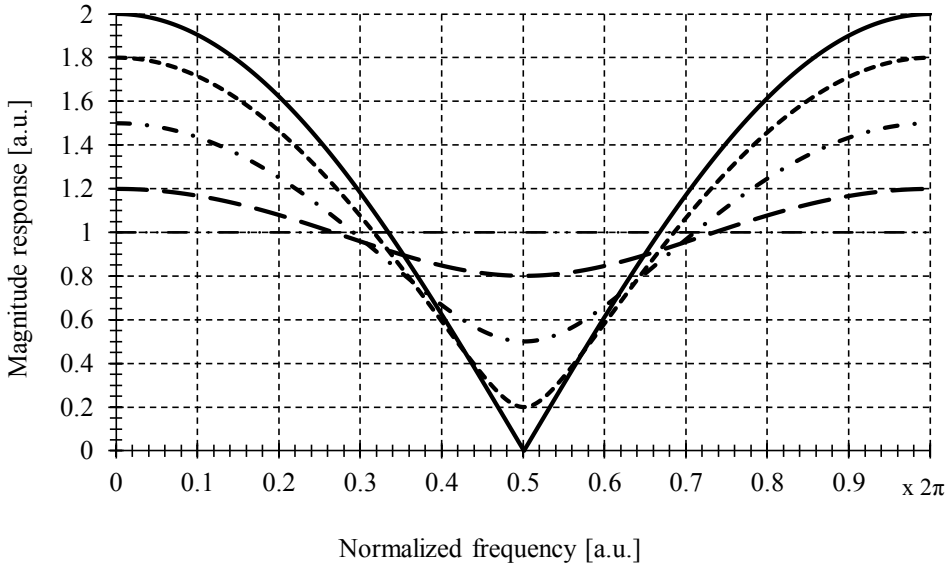

Figure 3.15. Magnitude response of the transfer function of the self-referencing configuration versus normalized frequency: — · · — β_k=0, — — β_k=0.2, — · — β_k=0.5, – – β_k=0.8, —— β_k=1

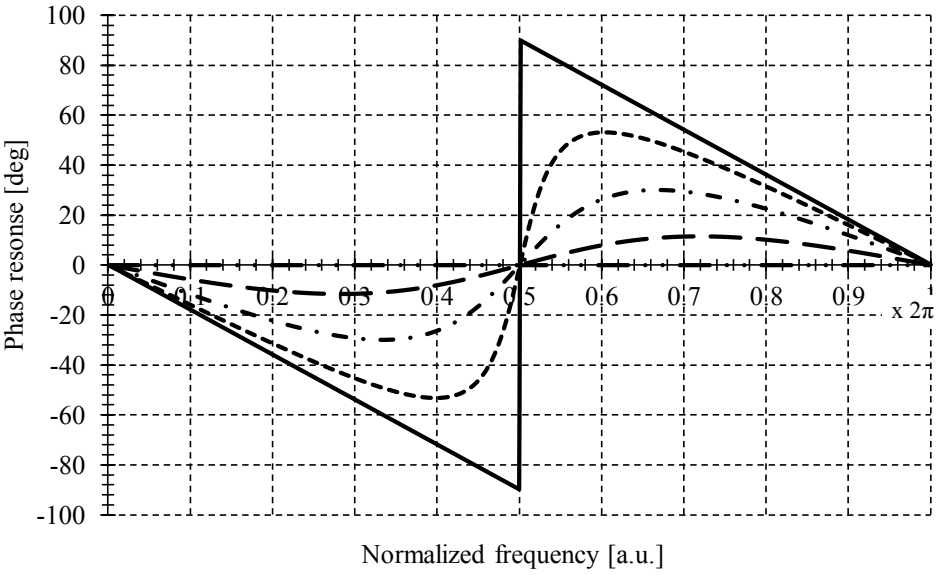

Figure 3.16. Phase response of the transfer function of the self-referencing configuration versus normalized frequency: — · · — β_k=0, — — β_k=0.2, — · — β_k=0.5, – – β_k=0.8, —— β_k=1

The magnitude and phase response versus the normalized frequency (Ω) of the digital filter model is derived from Equation (3.9) and is shown in Figure 3.15 and Figure 3.16, respectively, for different values of β_k. The normalized frequency is calculated as the ratio of the system and sampling frequency. It is shown how the amplitude modulation is converted to phase variations. A symmetrical magnitude shape and an antisymmetrical phase shape can be seen with regards to Ω=π. A zero transmission takes place at condition Ω=π for β_k=1.

If $\beta_k<1$, the phase response increases from zero to positive values as β_k takes greater values, being $\Omega>\pi$, and the maximum value occur at angular frequencies tending to $\Omega=\pi^+$. For angular frequencies lower than $\Omega=\pi$ the phase response decreases from zero to negative values as β_k tends to one, and the peak value takes place around angular frequencies tending to π, being $\Omega=\pi^-$ the frequency of the zero.

Two measurement parameters can be defined for each remote sensing point, as reported in [63], on one hand the parameter output amplitude (δ_k), which is defined as the ratio between the voltage values at the reception stage for different phase-shifts and is given by:

$$\delta_k = \frac{V_o\left(f,\Omega_{MPOF_k}\right)\Big|_{\Omega_{Si}=0}}{V_o\left(f,\Omega_{Si}\right)\Big|_{\Omega_{MPOFk}=0}} = \frac{\left[1+\frac{2\cdot\beta_k}{1+\beta_k^2}\cos\left(\Omega_{MPOF_k}\right)\right]^{1/2}}{\left[1+\frac{2\cdot\beta_k}{1+\beta_k^2}\cos\left(-\Omega_{Si}\right)\right]^{1/2}} \qquad (3.12)$$

On the other hand the output phase (φ_k) of the signal for different phase-shifts at the reception stage is defined and it is given by:

$$\varphi_k = \text{arctg}\left[\frac{-\left(\sin\left(\Omega_{Si}\right)+\beta_k\cdot\sin\left(\Omega_{MPOF_k}\right)\right)}{\left(\cos\left(\Omega_{Si}\right)+\beta_k\cdot\cos\left(\Omega_{MPOF_k}\right)\right)}\right] \qquad (3.13)$$

where β_k is the parameter in which the sensor loss modulation (H_k) is encoded in the transfer function of the self-referencing configuration. Ω_{Si} and Ω_{MPOFk} are the phase shifts for the reference and each sensor signal, respectively. The parameter φ_k is insensitive to power fluctuations except for the sensor modulation (H_k), thus providing a self-referenced measurement approach. A specific example of φ_k versus the parameter dependent on the loss β_k for different external power attenuations is shown in Figure 3.17. $\Omega_{Si}=0.83\pi$ and $\Omega_{MPOF}=0.33\pi$ are the reference and sensor phase-shifts signals, respectively.

For a phase-shift fixed pair of values, the theoretical parameter (φ_k) of the remote sensing point depends only on β_k, which is insensitive to external power fluctuations that might take place in the optical link between the sensing point and the transmission stage. Moreover, the self-referencing parameter can be determined for any pair of phase-shift values providing flexibility to the measurement technique at the remote sensing network for any desired operation point.

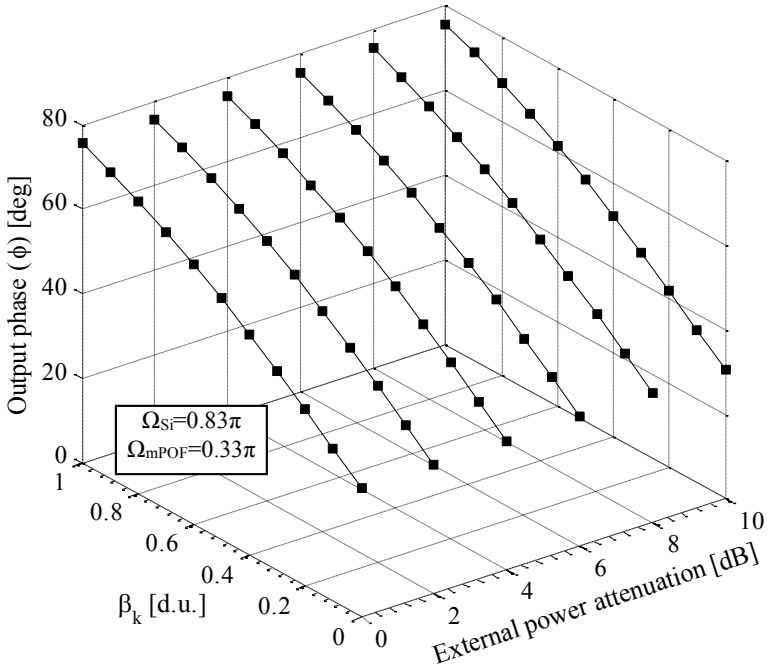

Figure 3.17. Theoretical curves of the output phase φ_k versus β_k for different external power fluctuations at the reception stage.

3.5. Virtual Processing System

In previous works [61, 63, 64] an analog electronic delay by means of an electronic circuit was used to get phase-shifts at the reception stage. In this work, computer software based on a visual programming language is designed to acquire and process the signals for the two sensing points. The software provides to the user a friendly environment and the ability to easily change the control parameters remotely. The block diagram of the computer software is shown in

Figure 3.18. Four stages have been defined in the code: acquisition, filtering, phase shifter and lock-in amplifier.

The first stage uses a DAQ to convert the optical signals from the PDs and the lock-in reference signal to digital signals. The acquisition rate and the number of samples per channel was set to 16kS/s and 8,000samples, respectively. The maximum and minimum signal input range was set to ±1V in order to reduce the noise from the acquisition card.

The second stage uses a digital bandpass filter to eliminate noise from all acquired signals at frequencies outside the system frequency (f=1kHz). The designed filter uses a fifth order Butterworth topology. The low and high cut-off frequencies are fixed at 950 and 1,050Hz, respectively. These parameters can be changed using the graphical interface provided by the software.

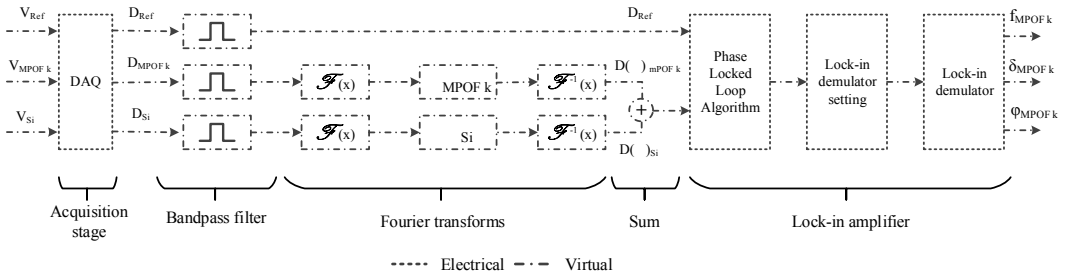

Figure 3.18. Block diagram of the computer software used to acquire and process the electrical signals.

After conditioning the signals, a phase shifter based on Fourier transforms is used to apply an independent delay to the digital reference and sensing signals. Then, both signals are added and introduced into the lock-in amplifier along with the digital lock-in reference signal.

Finally, a lock-in amplifier based on a graphical code [65, 66] is used to obtain the frequency, phase and amplitude of the added signal. The lock-in amplifier consists of three functions. The first function is a phase locked loop algorithm to measure the frequency and phase of the lock-in reference signal. The second function is used to internally calculate the setting for the mixer and the low-pass filter in the demodulator function. Then a lock-in demodulator function extracts the frequency component from the added signal that uses the lock-in reference signal to specify the frequency and phase. In order to calculate the self-referencing parameter (φ_k) one lock-in amplifier is necessary.

3.6. Experimental validation of the Self-Referencing Technique.

The network configuration shown in Figure 3.14.(a) is implemented using single mode glass fiber in order to experimentally validate the phase self-referencing parameter for two remote sensing points. A BLS modulated at f=1kHz by an AOM is employed to launch optical power into the configuration via a broadband circulator. One glass FBG is used for reference purpose, being placed after the broadband circulator and before the CWDM mux/demux. Its central wavelength and reflectivity are λ_{Si}=1,550nm and 49%, respectively. A few-moded MPOFBG is used for each remote sensing point [26, 38, 53] located at the patient's vicinity. Their central wavelengths are λ_{MPOF1}=1,525.2nm for FOS_1 and λ_{MPOF2}=1,567.0nm for FOS_2, and their reflectivities are 27% and 36%, respectively. The attenuation of the MPOF is around 70dB/m at 1,550nm [28]. The MPOF core and cladding diameter are 50 and 150μm, respectively. Being made of three rings of holes on PMMA material. The optical spectrum of the 2-sensor network implemented is shown in Figure 3.19.

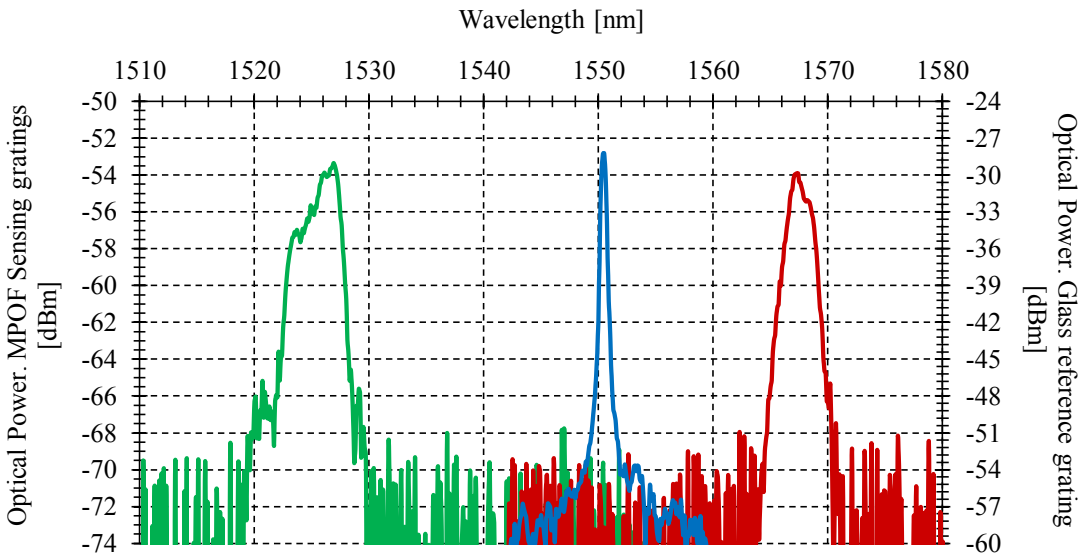

Figure 3.19. Optical spectrum in reflective operation of the MPOFBGs: ─ (green) λ_{MPOF1}=1,525nm (sensing), ─ (red) λ_{MPOF2}=1,567nm (sensing), ─ (blue) λ_{Si}=1,550nm (reference).

A singlemode Variable Optical Attenuator (VOA) is used to emulate the FOS response and for calibration purposes. The VOA used in this experiment allows the user to manually vary the attenuation of the signal in the fiber as it is transmitted through the device. Each attenuator has a lens to collimate the light from the input fiber. A blocking device or windows can be manually adjusted by a screw, see Figure 3.20. Then, a second lens is used to couple light into the output fiber. Thus, the coupling efficiency is changed until the desired attenuation is obtained. One example of the sensor loss modulation used to calibrate the configuration is shown in Figure 3.21.

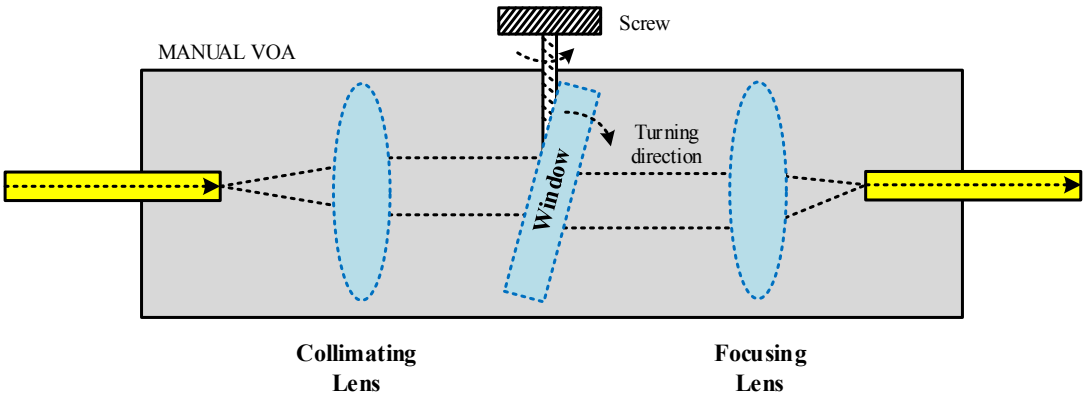

Figure 3.20. Manual VOAs schematic.

The three reflected signals, a reference signal and two sensing signals, are demultiplexed by a CWDM demux and detected by three amplified InGaAs detectors. The amplifier gain is fixed at 70dB for all measurements. A 14-bit low-cost DAQ is used to convert the electrical signals

from the PDs to digital signals. Computer software is used to implement the bandpass filter, the phase-shifts and the lock-in amplifiers at the reception stage. One virtual lock-in amplifier per sensor was used to obtain the self-referencing parameter φ_k, with i=1,2.

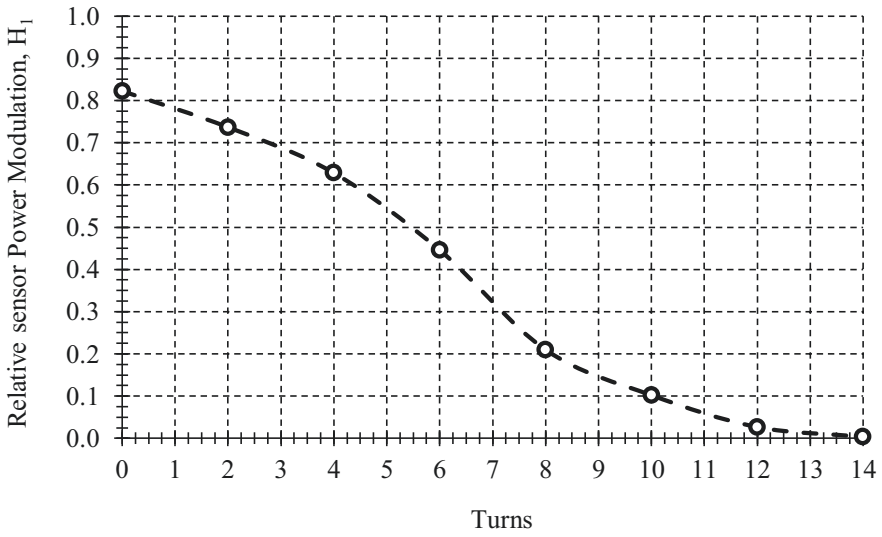

Figure 3.21. Calibration curve of the manual VOA used to emulate the sensor loss modulation H_1.

3.6.1. Self-Reference Measurements

The self-reference property is tested by inducing power fluctuations in the modulated optical source through a VOA, as shown in Figure 3.22.

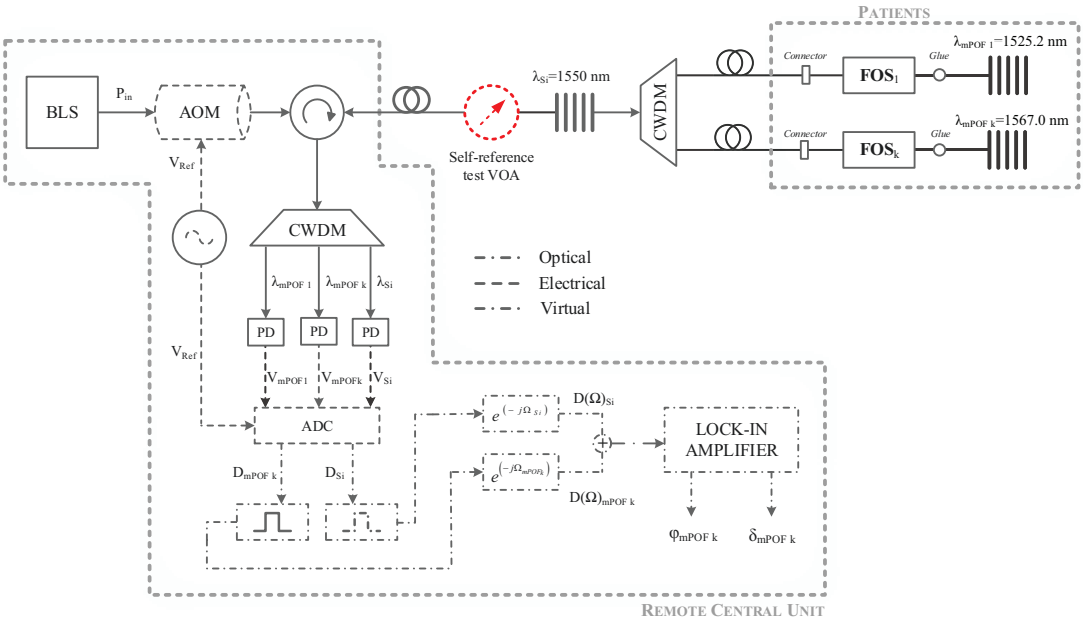

Figure 3.22. Self-referencing scheme to measure the self-reference property.

From Figure 3.23, it is demonstrated that the self-reference system is able to regulate at 0.46% output phase after inducing 10dB of power fluctuations. A normalization procedure has been used to span β_k from Equation (3.8) to a normalized range with a maximum value of 1, and the output phase is scaled proportionally. This procedure applies to all reported measurements.

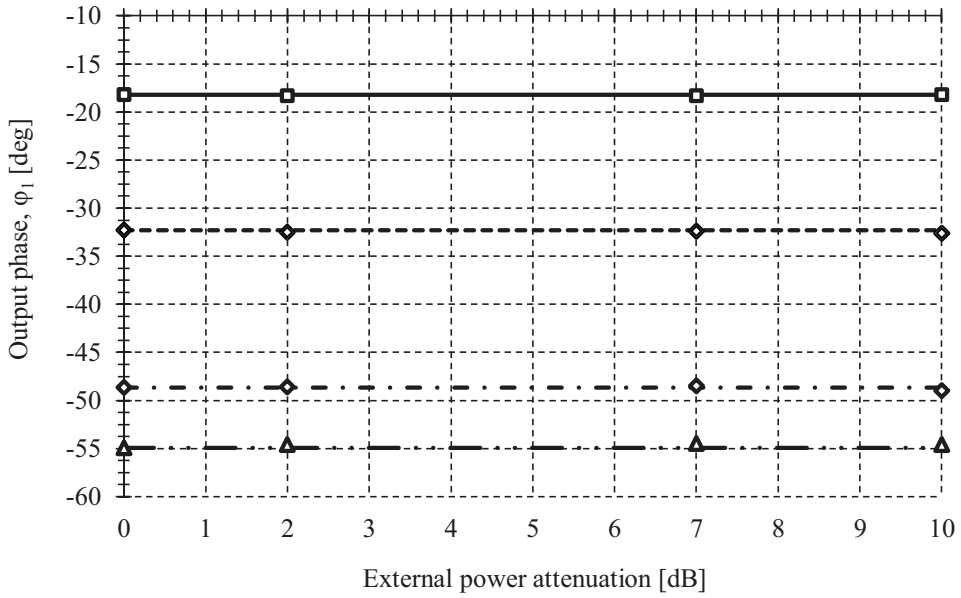

Figure 3.23. Output phase φ_1 self-reference test versus external power fluctuations for different values of sensor losses at the remote sensing point addressed by λ_{MPOF1}: ── β_1=0.32, – – β_1=0.54, ─ · ─ β_1=0.79, ─ · · ─ β_1=0.92

3.6.2. Crosstalk Analysis

Crosstalk analysis is carried out to measure the possible interference between adjacent channels during the measuring process. Several measurements of the self-referencing parameter φ_1 (FOS_1) at wavelength λ_{MPOF1} are taken for different values of the parameter dependent on the sensor loss modulation β_2 (FOS_2) at wavelength λ_{MPOF2}. Both virtual delays, Ω_{Si} and Ω_{MPOFk}, are selected to achieve positive and negative incremental system responses. The negative responses also show the best performance in terms of linearity corresponding to the phase-shift values of $\Omega_{Si}=0\pi$ and $\Omega_{MPOF1}=0.67\pi$ [64]. Experimental results are shown in Figure 3.24. Similar results are obtained when monitoring φ_2 (FOS_2) at wavelength λ_{MPOF2} are taken for different values of the parameter dependent on the sensor loss modulation β_1 (FOS_1) at wavelength λ_{MPOF1}, see Figure 3.25. In this case, one of the responses show the best performance in terms of sensitivity corresponding to the phase-shift values of $\Omega_{Si}=0.05\pi$ and $\Omega_{MPOF2}=0.89\pi$ [64]. In both cases no crosstalk is noticed, so both sensors can be interrogated simultaneously without mutual interference because of the high channel isolation of the CWDM demultiplexer.

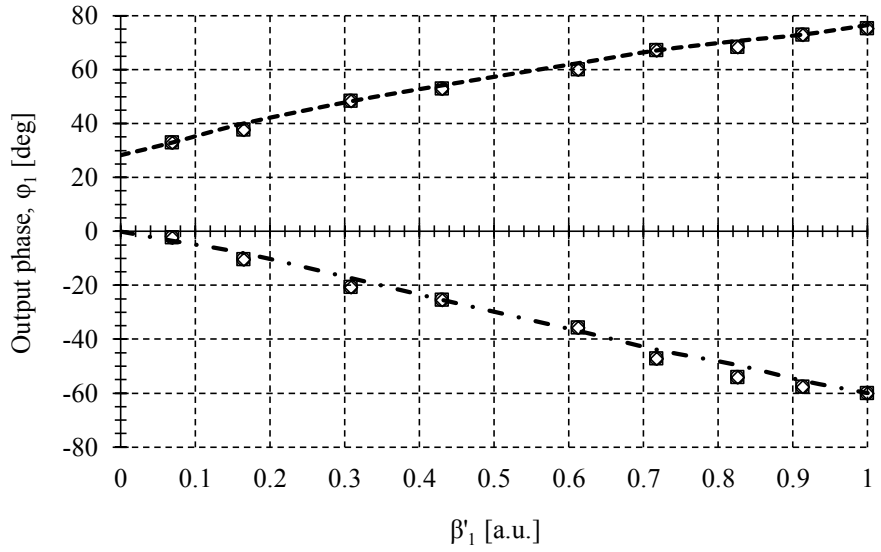

Figure 3.24. Output phase parameter versus sensor loss at channel λ_{MPOF1} (FOS_1) for different values of sensor loss at channel λ_{MPOF2} (FOS_2): ◊ β'2=0.99, □ β'2=0.19, ○ β'2=0.01 Measurements (points) and simulations for different phase-shift configurations: – – Ω_{Si} = 0.83π, Ω_{MPOF1} = 0.33π; — · — Ω_{Si}= 0π, Ω_{MPOF1}=0.67π.

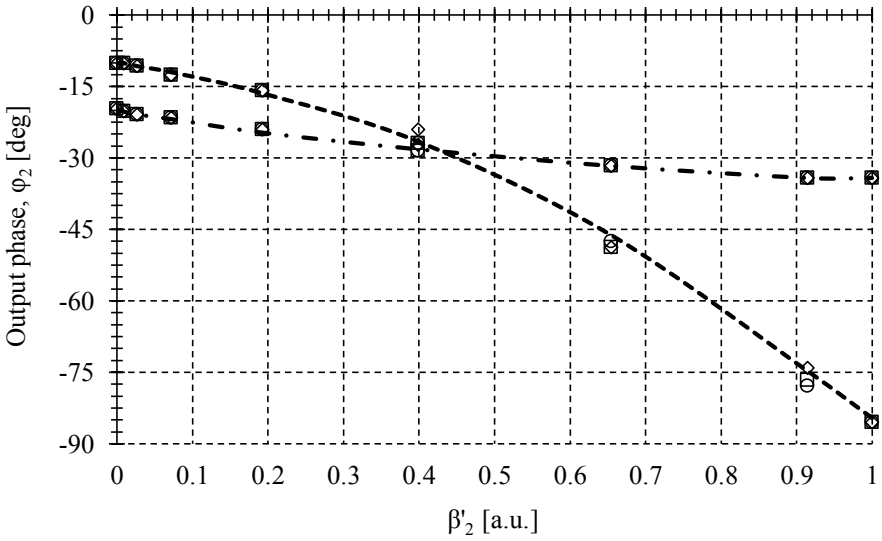

Figure 3.25. Output phase parameter versus sensor loss at channel λ_{MPOF2} (FOS_2) for different values of sensor loss at channel λ_{MPOF1} (FOS_1): ◊ β'_1=0.99, □ β'_1=0.61, ○ β'_1=0.06. Measurements (points) and simulations for different phase-shift configurations: – – Ω_{Si} = 0.05π, Ω_{MPOF2} = 0.89π; — · — Ω_{Si}= 0.11π, Ω_{MPOF2}=0.28π.

3.6.3. Optical Resolution and Electrical Signal-to-Noise Ratio.

In this section, an analysis of the sensing resolution of the output phase parameter is presented. It is clear that the most limiting components in the system's resolution are the active detectors. The InGaAs detector used in the experiment has a spectral response at 700~1,800nm

wavelength range. An eight-position rotary switch allows the user to vary the gain from 0 to 70dB in 10dB steps. In order to overcome the optical power losses of the system, a maximum gain of 70dB is selected. The noise value of the photodetector depends on the selected gain. The photodetector noise at the minimum (0dB) and the maximum (70dB) gain changes from 600μV_{RMS} to 1.5mV_{RMS}, respectively. These values correspond to a bandwidth of 17MHz and 12kHz, respectively. With the noise and bandwidth value at the maximum gain, the theoretical system resolution, considering the detected output power is $3.5 \cdot 10^{-2}$dB. No uncertainty factors are taken into account for this analysis such as stability of the POFBGs. For this reason, a set of measures are carried out to obtain the experimental resolution of the system. The schematic of the experimental set-up is shown in Figure 3.26. The self-referenced output phase is measured replacing the FOS for a programmable VOA which induces controllable power changes in the modulated optical signal.

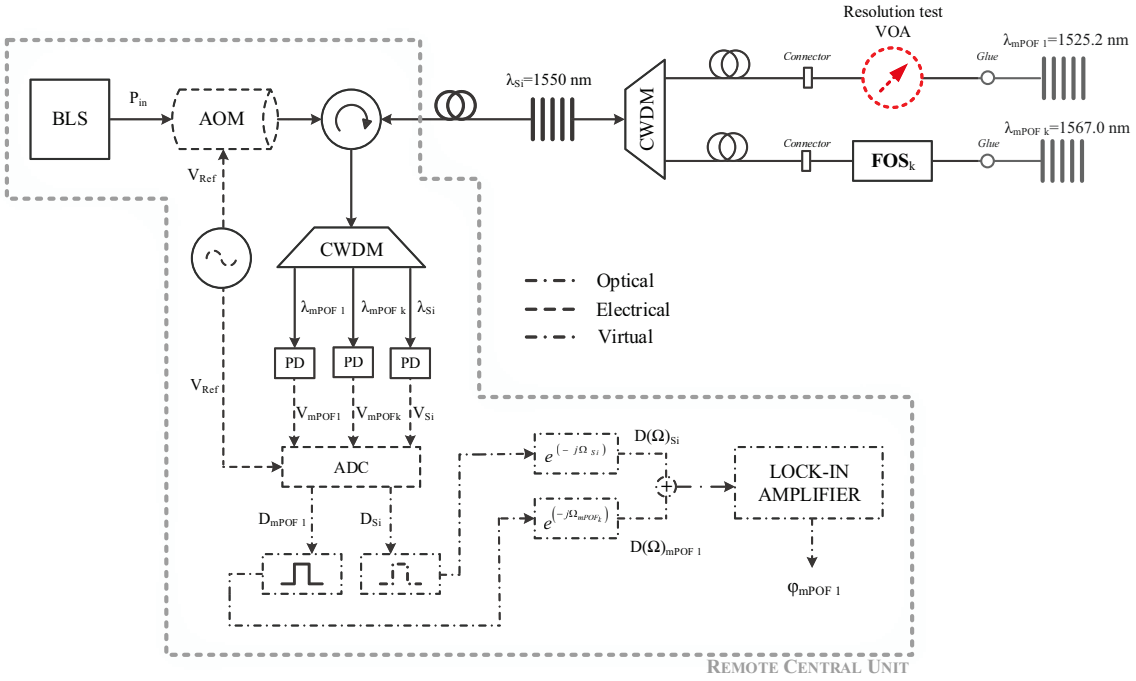

Figure 3.26. Self-referencing scheme to measure the system resolution

Both virtual delays, Ω_{Si} and Ω_{MPOF1} are selected to achieve high sensitivity. These values are 0.05π and 0.89π for Ω_{Si} and Ω_{MPOF1}, respectively. In the experiment, the self-reference output phase is measured from 0 to 0.5dB at 0.01dB intervals. A total of five sets of measurements for the calibration curve are carried out to perform a statistical analysis of the resolution parameter. Software based on a graphical code is developed to acquire the self-reference parameters, to control the programmable VOA and post process the data.

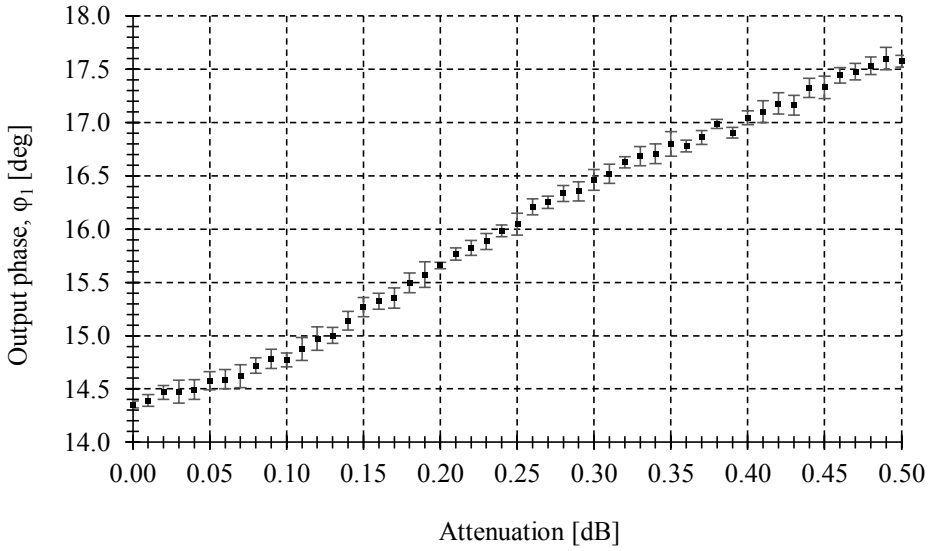

Figure 3.27. Resolution related measurements. Output phase φ_1 versus VOA attenuation for the first sensing channel.

Figure 3.27 shows the measured curve for the first sensing channel. For each attenuation, the mean and the maximum and minimum deviation value of the output phase is represented. The system resolution is obtained calculating the minimum attenuation step that avoids overlap between deviation values. A resolution of $4 \cdot 10^{-2}$dB is obtained. It is clear that using another amplifier detector with a lower noise-equivalent power (NEP), the system resolution would be limited by the DAQ noise ($0.5mV_{RMS}$) to a value of $6.5 \cdot 10^{-3}$dB. These resolution values are far below those provided by most of the POF intensity-based sensing solutions reported in literature, and particularly for biomedical applications.

On the other hand, as commented in Section 3.5, the virtual processing system is based on a lock-in amplifier code. This code can extract a signal with a known carrier wave from an extremely noisy environment. Depending on the dynamic range of the system, signals as small as system noise and fairly close in frequency can still be reliably detected. In order to define the maximum attenuation of the electrical sensing signal a study of the electrical signal-to-noise ratio (ESNR) has been carried out. Again, the most limiting component in the system ESNR is the amplifier detector noise. Considering the maximum input range of the DAQ sensing channel of $\pm 1V_{PP}$ and an amplifier detector gain of 70dB, the ESNR of the system is 59.4dB. This value limits the maximum electrical attenuation of the sensing signal able to be detected by the PD and DAQ.

3.6.4. Power Budget Analysis

Optical Power budget analysis is carried out to calculate the maximum length of the optical fiber network that the remote sensing topology can support. Table 3.1 shows a detailed description

of the main parameters involved in power budget evolution of each system device. P_m is the optical power launched into the system by the BLS, $L_{Devices}$ is the total power loss of light travelling forward or backward (due to the reflective topology) including the loss of the following devices: AOM, optical circulator, glass FBG, mux/demux CDWMs, adaptors and FOS. The maximum power variation of the FOS is fixed at 6dB, high enough to cover any biomedical input magnitude span. P_{Out} is derived from the photodiode NEP figure of merit and the value provided in Table 3.1 refers to the minimum measurable optical power, in terms of both NEP and bandwidth. L_{CWDM} is the CWDM mux/demux insertion loss. $L_{MPOFBG\text{-}Si}$ are the MPOFBG insertion losses related to the reflectivity of the gratings ($R_{\lambda MPOFk}$), attenuation of the MPOF fiber (α_{MPOF}=0.82dB/cm [67], multimode/singlemode glass fiber connection ($L_{(SM\text{-}MM)Si}$=1.56dB) and glass-polymer glue union ($L_{Si\text{-}mPOF}$≈5 dB) [53].

MPOFBG Central Wavelength, nm	**BLS Output Power**, dBm P_{In}	**Devices Insertion Losses**, dB $L_{Devices}$	**CWDM Insertion Loss**, dB L_{CWDM}	**MPOFBG Insertion Losses,** dB $L_{MPOFBG\text{-}Si}$ (Note 1)	**Photodetector Sensitivity**, dBm P_{Out} (Note 2)
λ_1 = 1,525	-17.3	30.2	1.8	15.1	-66.6
λ_2 = 1,567	-15.8	30.2	1.8	14.6	-66.6

Notes: 1. Including $R_{\lambda MPOFk}$; 2. Considering the amplified gain of 70dB, the noise-equivalent power (NEP) and the bandwidth of the amplified InGaAs detector are $2 \cdot 10^{-12}$ W/√Hz and 12kHz, respectively.

Table 3.1. Optical power budget analysis of the proposed hybrid glass-POF WDM remote sensing scheme.

Computing the power budget at the most restrictive sensing wavelength in terms of distance reachable, a maximum length of 11km could be obtained. However, the latter can be easily improved and extended to the access network domain (up to 20km) by launching more optical power into the system, using optical devices with lower insertion losses or using a more efficient technique to connect MPOFBGs. In comparison to other configurations that use splitters [68], a power budget improvement in more than 15dB for a 16-sensor network can be achieved.

3.7. Discussion

In this chapter, a hybrid glass-POF WDM network topology for addressing multiple self-referenced fiber-optic POF-based sensors is proposed. Its performance in terms of crosstalk between sensors and its self-referencing property is validated. However, system factors such as the sensitivity, the resolution, the remote interrogation distance reachable or the maximum sensor insertion losses, and some applications are further investigated.

From Equation (3.8), if the modulation index and the PD responsivity are considered to be similar at reference and sensor wavelength the new sensor sensitivity is given by:

$$\frac{\partial \beta_k}{\partial A} = 2 \cdot H \cdot \frac{R_{\lambda MPOFk}}{R_{\lambda Si}} \cdot L_{CWDM} \cdot L_{MPOFBG-Si} \cdot \frac{\partial H}{\partial A} \qquad (3.14)$$

where A is the magnitude to be measured and $\partial H/\partial A$ is the sensor sensitivity without self-reference and is implemented in the experiments using a VOA. From Equation (3.14), we see that the different losses are the dominant factor altering the sensitivity and they should be kept as low as possible.

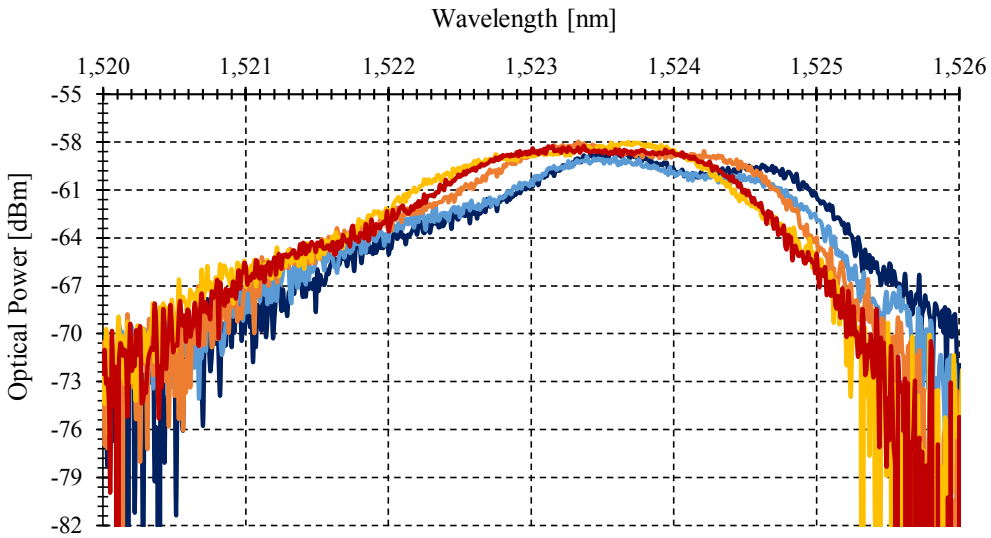

Figure 3.28. Optical spectrum in reflective operation for the MPOFBGs versus temperature: (dark blue line) 25ºC, (light blue line) 29ºC, (orange line) 34ºC, (yellow line) 38ºC and (red line) 42ºC.

By additionally monitoring each central MPOFBG wavelength shift within the range of each CWDM channel, temperature can be measured, apart from the parameter under test. Temperature characterization of one sensing point can be seen in Figure 3.28; showing a temperature sensitivity of -60pm/ºC.

One of the disadvantages of using PMMA-based FBGs is their aptitude for water absorption, and PMMA FBG sensors have a significant cross-sensitivity to humidity. This problem might be reduced by using FBGs based on TOPAS fiber [69]. The humidity sensitivity of a TOPAS-based FBG is ~64 times smaller than for an equivalent FBG manufactured in PMMA fiber at 1,565 nm [32]. FBGs fabricated in TOPAS display a temperature sensitivity of -37pm/ºC for a grating at 1,568nm [32]. On the other hand, TOPAS fiber has the same high attenuation as

its PMMA counterpart in the 1,550nm spectral region and also needs to be glued at the end of a singlemode glass fiber lead for being connected to other optical devices.

But this temperature sensitivity can also be an important issue with POFBGs is terms of cross-sensitivity. The self-referenced technique uses a POFBG placed at the vicinity of the patients, which is affected by the patient's temperature. The displacement of the Bragg wavelength with temperature must be compatible with the bandwidth spacing of the CWDM mux/demux channels. The two channels used in the measurements have a central wavelength of 1,571.3 for FOS_1 and 1,531.1 for FOS_2, with passband widths of 15.9 and 16.4nm, respectively. The MPOF Bragg wavelength variation with temperature is -60pm/°C. The Full Width at Half Maximum (FWHM) of the gratings are 5.8 for FOS_1 and 4.8nm for FOS_2. The minimum and maximum temperature that a human body can stand without dying are ~20ºC [70] and ~41.1°C [71], respectively. Considering the sensitivity and the human body temperature range, the wavelength shift ($\Delta\lambda_{MPOFShift}$) is ~1nm well within the CWDM mux/demux pass-band width. In a general design, to overcome the cross-sensitivity of the sensing gratings, the central wavelength of the MPOFBGs used should fulfil the following condition:

$$\lambda_{\mathrm{MPOFk}} + \Delta\lambda_{\mathrm{MPOFShift}} + \frac{\mathrm{FWHM}_{\mathrm{MPOFk}}}{2} < \lambda_{\mathrm{CWDMk}} + \frac{\mathrm{BW}_{\mathrm{CWDMk}}}{2} \qquad (3.15)$$

where λ_{CWDMk} and BW_{CWDMk} are the central wavelength and the pass-band width of a specific k mux/demux channel, respectively. $FWHM_{MPOFk}$ is the FWHM parameter of the grating used in channel k. The above estimation of the wavelength shift can be considered to have a negligible impact on the parameters previously defined in Equation (3.8) for a real-case scenario thus allowing simple sensor interrogation.

Considering the results of the optical power budget described in the previous section, the proposed method could provide a remote monitoring service unit fully compliant for short-reach networks (typically less than 1km), i.e., LANs and in-building/in-hospital networks. Indeed it is suitable for medium reach-distances (typically up to 10km) with application in inter-hospital networks or to provide a convergent all-optical and straightforward connection between patient's homes and a general practice service for telemedicine purposes. However, the latter can also be easily provided by including a wireless transmission at any point of the optical fiber link beyond the remote monitoring unit. Nevertheless, the above distances are unbeatable if an all-POF-based optical network is intended to be deployed and a hybrid approach should be considered.

Finally, the proposed self-referenced sensor network has been evaluated with an intensity-based optical sensor for the measurement of bend angles in the spines of human physiotherapy

patients. The received light intensity decreases as the gap between emitting and receiving fibers and /or the bending angle between them increases. The output power measurements versus the applied tilt angle is extracted from [19] and shown in Figure 3.29.(a). Using Equations (3.8) and (3.13), the output phase parameter versus tilt angle at channel λ_{MPOF1} (FOS_1) has been calculated for a specific set of virtual delays, as shown in Figure 3.29.(b).

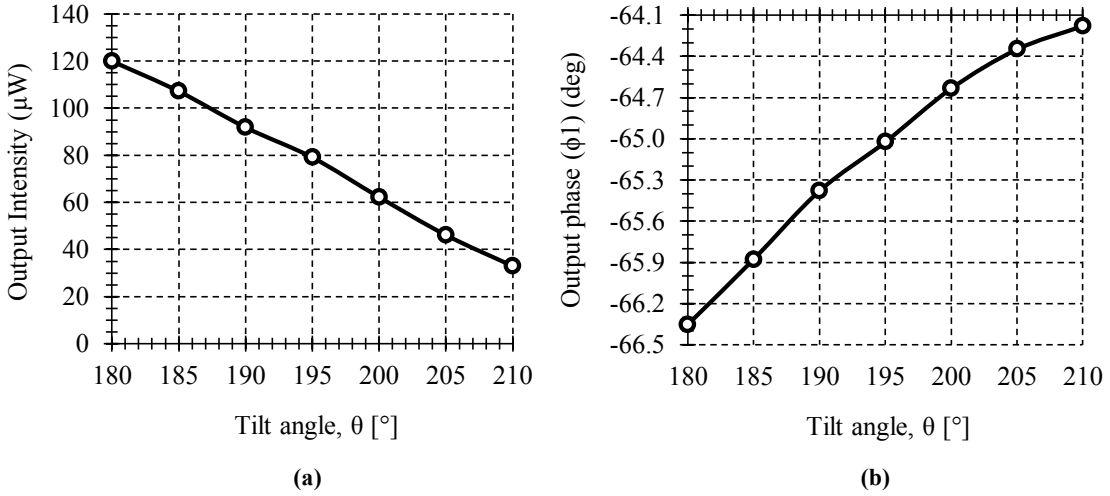

Figure 3.29. (a) Light intensity versus fiber tilt angle [19]. (b) Output phase parameter versus fiber tilt angle at channel λ_{MPOF1} (FOS_1).

The propose topology for self-reference multiple intensity fiber optic sensors is able to regulate at 0.46% output phase after inducing 10dB of power fluctuations. Further development of a spine bending sensor [20] introduces a single sensor self-referenced technique by adding more fibers and allowing 0.55% output signal fluctuations after inducing only ~1.4dB. Another important feature of the proposed technique in this work is the possibility to address multiple self-referenced intensity optical fiber sensors providing great flexibility and easy reconfiguration.

3.8. Conclusions

The need for an optical fiber link between the remote sensing area at the vicinity of the patient and the measuring unit may be the most important concern when employing inherently biocompatible POF intensity-based optical sensors. The feasibility of a hybrid glass-POF WDM network topology for addressing multiple self-referenced fiber-optic POF-based sensors is demonstrated. The intention is to bridge the gap between the remote interrogation of multiple optical sensors and the advantages of using biocompatible POF, including those based on MPOFBGs. One self-reference parameter has been tested to be robust to 10dB power fluctuations. Proper selection of both virtual delays can lead to linear responses and high sensitivities.

The proposed topology has high scalability and power budget enhancement in comparison with all POF-based solutions as it uses off-the shelf WDM-based devices with low insertion losses and a lock-in detection scheme. It also provides great flexibility and easy reconfigurability due to the use of virtual instrumentation solutions. By additionally monitoring each central POFBG wavelength shift within the range of each CWDM channel, temperature changes can also be tracked.

The self-referenced solution uses a low-cost 14-bit DAQ board which offers a resolution of $1.7 \cdot 10^{-2}$dB. The resolution and the number of sensors to be interrogated are limited by the number of analog channels and the resolution provided by the DAQ board, but easily improved. The proposed topology provides a central remote monitoring unit that can be located several km away from the patient's location, where the sensors are placed. It is shown the potential of the proposed technique to be useful in self-referencing multiple intensity optical sensors for measuring bend angles in the spines of human physiotherapy patients.

3.9. References

[1] J. Arkwright, N. Blenman, I. Underhill, S. Maunder, M. Szczesniak, P. Dinning*, et al.*, "In-vivo demonstration of a high resolution optical fiber manometry catheter for diagnosis of gastrointestinal motility disorders," *Optics express,* vol. 17, pp. 4500-4508, 2009.

[2] D. J. Webb, S. Jones, L. Zhang, I. Bennion, M. Hathaway, and D. Jackson, "First in-vivo trials of a fiber Bragg grating based temperature profiling system," *Journal of biomedical optics,* vol. 5, pp. 45-50, 2000.

[3] P. Polygerios, P. Puangmali, T. Schaeffer, R. Razavi, L. D. Seneviratne, and K. Althoefer, "Novel miniature MRI-compatible fiber-optic force sensor for cardiac characterization procedures," in *IEEE International Conference on Robotics and Automation*, Ancorage (USA), 2010, pp. 2598-2503.

[4] F. Taffoni, D. Formica, P. Saccomandi, G. D. Pino, and E. Schena, "Optical fiber-based MR-compatible sensors for medical applications: an overview," *Sensors,* vol. 13, pp. 14105-14120, 2013.

[5] A. Lau, Z. Chen, J. T. Teo, S. H. Ng, H. Rumpel, Y. Lian*, et al.*, "Intensity-modulated microbend fiber optic sensor for respiratory monitoring and gating during MRI," *IEEE Transactions on Biomedical Engineering,* vol. 60, pp. 2655-2662, 2013.

[6] A. Lekholm and L. Lindström, "Optoelectronic transducer for intravascular measurements of pressure variations," *Medical and biological engineering,* vol. 7, pp. 333-335, 1969.

[7] P. Hollingsworth-Fridlund, H. Vos, and E. Daily, "Use of fiber-optic pressure transducer for intracranial pressure measurements: a preliminary report," *Heart & lung: The Journal of Critical Care,* vol. 17, pp. 111-120, 1988.

[8] A. Wald, K. Post, J. Ransohoff, W. Hass, and F. Epstein, "A new technique for monitoring epidural intracranial pressure," *Medical instrumentation,* vol. 11, p. 352, 1977.

[9] A. Babchenko, B. Khanokh, Y. Shomer, and M. Nitzan, "Fiber optic sensor for the measurement of respiratory chest circumference changes," *Journal of biomedical optics,* vol. 4, pp. 224-229, 1999.

[10] E. N. Stenow and P. Oberg, "Venous occlusion plethysmography using a fiber-optic sensor," *IEEE Transactions on Biomedical Engineering,* vol. 40, pp. 284-289, 1993.

[11] D. J. Webb, "Polymer photonic crystal fibre sensor applications," in *Optical Sensing and Detection*, Brussels (Belgium), 2010, p. 77260Q.

[12] H. Jordan, P. Roderick, D. Martin, and S. Barnett, "Distance, rurality and the need for care: access to health services in South West England," *International journal of health geographics,* vol. 3, pp. 1-9, 2004.

[13] J. Witt, F. Narbonneau, M. Schukar, K. Krebber, J. De Jonckheere, M. Jeanne*, et al.*, "Medical textiles with embedded fiber optic sensors for monitoring of respiratory movement," *IEEE Sensors Journal,* vol. 12, pp. 246-254, 2012.

[14] V. Mishra, N. Singh, U. Tiwari, and P. Kapur, "Fiber grating sensors in medicine: Current and emerging applications," *Sensors and Actuators A: Physical,* vol. 167, pp. 279-290, 2011.

[15] H. J. Kalinowski, "Fiber Bragg grating applications in biomechanics," in *19th International Conference on Optical Fibre Sensors*, Perth (Australia), 2008, pp. 700430-700430-4.

[16] S. C. M. Ho, M. Razavi, A. Nazeri, and G. Song, "FBG sensor for contact level monitoring and prediction of perforation in cardiac ablation," *Sensors,* vol. 12, pp. 1002-1013, 2012.

[17] P. Roriz, A. Ramos, J. L. Santos, and J. A. Simões, "Fiber optic intensity-modulated sensors: a review in biomechanics," *Photonic Sensors,* vol. 2, pp. 315-330, 2012.

[18] A. Leung, P. M. Shankar, and R. Mutharasan, "A review of fiber-optic biosensors," *Sensors and Actuators B: Chemical,* vol. 125, pp. 688-703, 2007.

[19] M. Zawawi, S. O'Keeffe, and E. Lewis, "Plastic optical fibre sensor for spine bending monitoring," in *Journal of Physics: Conference Series*, 2013, p. 012004.

[20] M. A. Zawawi, S. O'Keeffe, and E. Lewis, "Plastic Optical Fibre Sensor for Spine Bending Monitoring with Power Fluctuation Compensation," *Sensors,* vol. 13, pp. 14466-14483, 2013.

[21] L. Cherbi, M. Mehenni, and R. Aksas, "Conception and realization of an angular optical sensor," *Microwave and optical technology letters,* vol. 40, pp. 500-503, 2004.

[22] Y. Fujii, S. Honma, M. Morisawa, and S. Muto, "Development of new optical fiber toluene sensor," in *Advanced Materials and Devices for Sensing and Imaging III*, Beijing (China), 2007, p. 68291Z.

[23] M. Krehel, M. Schmid, R. M. Rossi, L. F. Boesel, G.-L. Bona, and L. J. Scherer, "An optical fibre-based sensor for respiratory monitoring," *Sensors,* vol. 14, pp. 13088-13101, 2014.

[24] E. Suaste-Gómez, D. Hernández-Rivera, A. S. Sánchez-Sánchez, and E. Villarreal-Calva, "Electrically Insulated Sensing of Respiratory Rate and Heartbeat Using Optical Fibers," *Sensors,* vol. 14, pp. 21523-21534, 2014.

[25] A. Grillet, D. Kinet, J. Witt, M. Schukar, K. Krebber, F. Pirotte*, et al.*, "Optical fiber sensors embedded into medical textiles for healthcare monitoring," *IEEE Sensors Journal,* vol. 8, pp. 1215-1222, 2008.

[26] G. Barton, M. A. van Eijkelenborg, G. Henry, M. C. Large, and J. Zagari, "Fabrication of microstructured polymer optical fibres," *Optical Fiber Technology,* vol. 10, pp. 325-335, 2004.

[27] F. Berghmans, T. Geernaert, S. Sulejmani, H. Thienpont, G. V. Steenberge, B. V. Hoe*, et al.*, "Photonic crystal fiber Bragg grating based sensors—opportunities for applications in healthcare," in *Asia Communications and Photonics Conference and Exhibition*, Shanghai (China), 2011, p. 831102.

[28] O. Ziemann, J. Krauser, P. E. Zamzow, and W. Daum, *POF handbook: optical short range transmission systems*: Springer, 2008.

[29] A. Stefani, S. Andresen, W. Yuan, N. Herholdt-Rasmussen, and O. Bang, "High sensitivity polymer optical fiber-Bragg-grating-based accelerometer," *IEEE Photonics Technology Letters,* vol. 24, pp. 763-765, 2012.

[30] Y. Koike, "High bandwidth and low-loss polymer optical fibre," in *The First International Conference on Plastic Optical Fibers and Applications*, Paris (France), 1992.

[31] Y. Koike, T. Ishigure, and E. Nihei, "High-bandwidth graded-index polymer optical fiber," *Journal of Lightwave Technology,* vol. 13, pp. 1475-1489, 1995.

[32] W. Yuan, L. Khan, D. J. Webb, K. Kalli, H. K. Rasmussen, A. Stefani*, et al.*, "Humidity insensitive TOPAS polymer fiber Bragg grating sensor," *Optics express,* vol. 19, pp. 19731-19739, 2011.

[33] Y. Koike, "Novel miniature MRI-compatible fiber-optic force sensor for cardiac characterization procedures," in *The First International Conference on Plastic Optical Fibres and Applications*, Paris (France), 1992, pp. 15-19.

[34] D. Bosc and C. Toinen, "Full polymer single-mode optical fiber," *IEEE Photonics Technology Letters,* vol. 4, pp. 749-750, 1992.

[35] M. van Eijkelenborg, M. Large, A. Argyros, J. Zagari, S. Manos, N. Issa*, et al.*, "Microstructured polymer optical fibre," *Optics Express,* vol. 9, pp. 319-327, 2001.

[36] Y. Zhao, M. van Eijkelenborg, M. Large, and S. Fleming, "Interferometric chromatic dispersion measurement of short length of MPOF," in *Australian Conference on Fibre Optic Technology (ACOFT)*, Sydney (Australia), 2002.

[37] G. Durana, J. Gomez, G. Aldabaldetreku, J. Zubia, A. Montero, and I. S. de Ocariz, "Assessment of an LPG mPOF for Strain Sensing," *IEEE Sensors Journal,* vol. 12, pp. 2668-2673, 2012.

[38] H. Dobb, D. J. Webb, K. Kalli, A. Argyros, M. C. Large, and M. A. van Eijkelenborg, "Continuous wave ultraviolet light-induced fiber Bragg gratings in few-and single-mode microstructured polymer optical fibers," *Optics letters,* vol. 30, pp. 3296-3298, 2005.

[39] I. Bundalo, K. Nielsen, C. Markos, and O. Bang, "Bragg grating writing in PMMA microstructured polymer optical fibers in less than 7 minutes," *Optics express,* vol. 22, pp. 5270-5276, 2014.

[40] W. Yuan, D. J. Webb, K. Kalli, K. Nielsen, A. Stefani, H. K. Rasmussen*, et al.*, "870nm Bragg grating in single mode TOPAS microstructured polymer optical fibre," in *21st International Conference on Optical Fibre Sensors*, Ottawa (Canada), 2011, pp. 77538X-77538X-4.

[41] M. Van Eijkelenborg, A. Argyros, A. Bachmann, G. Barton, M. Large, G. Henry*, et al.*, "Bandwidth and loss measurements of graded-index microstructured polymer optical fibre," *Electronics Letters,* vol. 40, pp. 592-593, 2004.

[42] R. Provo, S. G. Murdoch, J. D. Harvey, R. Lwin, S. G. Leon-Saval, and A. Argyros, "Error free 9.5 Gb/s transmission over 50 m of multimode microstructured polymer optical fibre," in *Quantum Electronics Conference & Lasers and Electro-Optics*, 2011, pp. 784-786.

[43] I. Johnson, "Grating Deices in polymer optical fibre," Engineering and Applied Science, Aston University, Birmingham, 2012.

[44] S. Law, J. Harvey, R. Kruhlak, M. Song, E. Wu, G. Barton*, et al.*, "Cleaving of microstructured polymer optical fibres," *Optics communications,* vol. 258, pp. 193-202, 2006.

[45] A. Stefani, K. Nielsen, H. K. Rasmussen, and O. Bang, "Cleaving of TOPAS and PMMA microstructured polymer optical fibers: Core-shift and statistical quality optimization," *Optics Communications,* vol. 285, pp. 1825-1833, 2012.

[46] K. O. Hill and G. Meltz, "Fiber Bragg grating technology fundamentals and overview," *Lightwave Technology, Journal of,* vol. 15, pp. 1263-1276, 1997.

[47] G. Meltz, W. W. Morey, and W. H. Glenn, "Formation of Bragg gratings in optical fibers by a transverse holographic method," *Optics Letters,* vol. 14, pp. 823-825, 1989.

[48] D. Z. Anderson, V. Mizrahi, T. Erdogan, and A. E. White, "Phase-Mask Method for Volume Manufacturing of Fiber Phase Gratings," in *Conference on Optical Fiber Communication/International Conference on Integrated Optics and Optical Fiber Communication*, San Jose (California), 1993, p. PD16.

[49] K. O. Hill, B. Malo, F. Bilodeau, D. C. Johnson, and J. Albert, "Bragg gratings fabricated in monomode photosensitive optical fiber by UV exposure through a phase mask," *Applied Physics Letters,* vol. 62, pp. 1035-1037, 1993.

[50] K. O. Hill, B. Malo, K. A. Vineberg, F. Bilodeau, D. C. Johnson, and I. Skinner, *Efficient mode conversion in telecommunication fibre using externally written gratings* vol. 26: Institution of Engineering and Technology, 1990.

[51] B. Malo, S. Thériault, D. C. Johnson, F. Bilodeau, J. Albert, and K. O. Hill, *Apodised in-fibre Bragg grating reflectors photoimprinted using a phase mask* vol. 31: Institution of Engineering and Technology, 1995.

[52] I. Photonics. (25st March 2015). *FBG Phase masks. Plus first and minus first order principle*. Available: http://www.ibsenphotonics.com

[53] C. Zhang, "Fibre Bragg Grating in Polymer Optical Fibre for Applications in Sensing," Engineering and Applied Science, Aston University, Birmingham, 2011.

[54] I. P. Johnson, K. Kalli, and D. J. Webb, "827 nm Bragg grating sensor in multimode microstructured polymer optical fibre," *Electronics letters,* vol. 46, pp. 1217-1218, 2010.

[55] R. Lwin and A. Argyros, "Connecting microstructured polymer optical fibres to the world," in *The 18th International Conference on Plastic Optical Fibers*, Sydney (Australia), 2009.

[56] I. P. Johnson, D. J. Webb, K. Kalli, M. C. J. Large, and A. Argyros, "Multiplexed FBG sensor recorded in multimode microstructured polymer optical fibre," in *Photonic Crystal Fibers IV*, Brussels, Belgium, 2010, pp. 77140D-77140D-10.

[57] Henkel. (2008). *Technical Data Sheet Loctite 3525*. Available: https://tds.us.henkel.com

[58] A. Abang and D. J. Webb, "Demountable connection for polymer optical fiber grating sensors," *Optical Engineering,* vol. 51, pp. 080503-1-080503-3, 2012.

[59] A. Abang, D. Saez-Rodriguez, K. Nielsen, O. Bang, and D. Webb, "Connectorisation of fibre Bragg grating sensors recorded in microstructured polymer optical fibre," in *Fifth European Workshop on Optical Fibre Sensors*, Krakow (Poland), 2013, pp. 87943Q-87943Q-5.

[60] S. Abad, F. M. Araújo, L. A. Ferreira, J. L. Santos, and M. López-Amo, "Interrogation of Wavelength Multiplexed Fiber Bragg Gratings Using Spectral Filtering and Amplitude-to-Phase Optical Conversion," *Journal of Lightwave Technology,* vol. 21, p. 127, 2003.

[61] J. Montalvo, F. Araújo, L. Ferreira, C. Vázquez, and J. M. Baptista, "Electrical FIR filter with optical coefficients for self-referencing WDM intensity sensors," *IEEE Photonics Technology Letters,* vol. 20, pp. 45-47, 2008.

[62] A. Moraleda, D. S. Montero, D. Webb, and C. García, "A Self-Referenced Optical Intensity Sensor Network Using POFBGs for Biomedical Applications," *Sensors,* vol. 14, pp. 24029-24045, 2014.

[63] J. Montalvo, O. Frazão, J. L. Santos, C. Vázquez, and J. M. Baptista, "Radio-frequency self-referencing technique with enhanced sensitivity for coarse WDM fiber optic intensity sensors," *Journal of Lightwave Technology,* vol. 27, pp. 475-482, 2009.

[64] D. Montero, C. Vázquez, J. Baptista, J. Santos, and J. Montalvo, "Coarse WDM networking of self-referenced fiber-optic intensity sensors with reconfigurable characteristics," *Optics express,* vol. 18, pp. 4396-4410, 2010.

[65] N. Instruments. (2013). *How to Measure Small Signals Buried in Noise Using LabVIEW and Lock-In Amplifier Techniques*. Available: http://www.ni.com

[66] N. Instruments. (2013). *Multi Channel Count Lock-In Amplifier with Simulated Data or NI-4472 and DAQmx*. Available: http://www.ni.com

[67] K. E. Carroll, C. Zhang, D. J. Webb, K. Kalli, A. Argyros, and M. C. Large, "Thermal response of Bragg gratings in PMMA microstructured optical fibers," *Optics Express,* vol. 15, pp. 8844-8850, 2007.

[68] J. Montalvo, C. Vázquez, and D. S. Montero, "CWDM self-referencing sensor network based on ring resonators in reflective configuration," *Optics Express,* vol. 14, pp. 4601-4610, 2006.

[69] I. P. Johnson, W. Yuan, A. Stefani, K. Nielsen, H. K. Rasmussen, L. Khan*, et al.*, "Optical fibre Bragg grating recorded in TOPAS cyclic olefin copolymer," *Electronics letters,* vol. 47, pp. 271-272, 2011.

[70] B. W. Trautner, A. C. Caviness, G. R. Gerlacher, G. Demmler, and C. G. Macias, "Prospective evaluation of the risk of serious bacterial infection in children who present to the emergency department with hyperpyrexia (temperature of 106 F or higher)," *Pediatrics,* vol. 118, pp. 34-40, 2006.

[71] D. F. Danzl and R. S. Pozos, "Accidental Hypothermia," *New England Journal of Medicine,* vol. 331, pp. 1756-1760, 1994.

Chapter 4

Chapter 4

Two-colour Pyrometer: Error Analysis by Numerical Simulations

A numerical simulation is developed to evaluate measurement errors for one-colour and two-colour-pyrometers as a function of temperature and emissivity. The pyrometer is simulated by a computer algorithm, which can be used to explore the behaviour of different configurations such as different photodetectors, different filtering wavelengths, among other. General conclusions can be drawn about what makes a good pyrometer, and an existing pyrometer is evaluated, to predict its behaviour as a function of temperature. With those predictions, a validation of the simulations is carried out. The results show which combination of two filtering channels give the best performance for lower errors.

4.1. Introduction

Temperature measurement is especially important in adaptive control for automatic machine tools wherein the more sophisticated adaptive control not only improve the productivity of the machine, but also improves the quality of the part being machined thereby. An uncontrolled temperature generated by the cutting tool is the main cause of surface degradation such as subsurface deformation, metallurgical structural alterations in the machined surface residual stresses in the finished part [1]. Tool wear not only reduces the tool life, but also increases the forces and tensile residual stresses, affects surface finish and causes white layer surface damages [2]. In order to prevent these effects, these adaptive controls require continuous temperature measurement at a fast response time in order to allow the machine to adapt itself to the changes for which it is programmed.

The maximum temperature in a machining process, in general, occurs at the interface between the cutting edge and the workpiece [3]. Measurement of the interface between the cutting tool and the workpiece, however, is often difficult since such small area is generally inaccessible

to conventional temperature-measuring apparatus and radiation type detectors are often hampered by poor optical path due to the interference of chips and cutting fluids, among others.

The conventional method for measuring the cutting edge temperature of a machine tool employs a thermoelectric couple [4-8]. Their basic working principle is that thermocouples produce an output voltage which depends on the temperature difference between the junctions of two different metal wires. The thermocouples are used as embedded part in the workpiece [6] or the insert [9] in order to measure localized areas. They are inexpensive and easy to operate transducers, and under controlled conditions, this method is relatively accurate for single point cutting tools. But it is inaccurate for multiple point tools because the temperature measured tends to be the average over the total contact region and thus local areas cannot be measured. Additional disadvantages of the thermocouple technique are that the output signal is small and noisy during the cutting due to the presence of electromagnetics disturbances, the thermocouples can interfere with the flow of heat, have limited transient response, and the temperature gradient is hard to estimate.

In addition to thermocouples, infrared (IR) radiation thermography [10-13] is developed to overcome the thermocouples problems. This technique is based on measuring the surface temperature using the thermal energy emitted by the surface. This measurement is made using cameras with films or chips sensitive to IR radiation.

The use of IR cameras have many advantages over the thermocouple technique. Thermography is a non-intrusive technique, i.e. no physical contact with the heat source is attained so there is no adverse effect on the temperature and materials. Other important characteristic is the fast response, making it a very useful instrumentation in temperature measurement because the high cutting speeds used in machining process made the response of the experimental system a very important condition. On the other hand, the disadvantage of the radiation technique is that the exact surface emissivity should be known in order to make an accurate measurement. Knowing the exact surface emissivity during cutting is extremely difficult because the surface emissivity is a function of surface temperature, surface roughness [14]. Chip obstruction is another disadvantage in this techniques. There is limited optical access to interesting measurement positions, limiting the measurement of small hot spots.

Fiber-optic pyrometers can be a possible solution to overcome these difficulties. In these sensors, the radiation emitted from the target are accepted by an optical fiber and transmitted to the IR detector and then converted to an electric signal. Using the power ratio of two sensors detecting signals at different wavelength ranges to avoid the influence of the temperature and

material dependent emissivity as reported by Müller et al. [15-17], and Ueda et al. [18-21] among others [22-27]. This non-invasive technique presents several advantages when compared with the other methods, previously described. Optical fibers can be placed to measure localized temperature on machined surfaces and can be embedded on different sections. On the other hand, this technique avoids false readings that can be caused by electromagnetic disturbances.

The advantage of the two-colour pyrometer is that the measured temperature is independent of emissivity variations with temperature. Therefore, the main source of error for the measured absolute temperature is that the gray-body behaviour is not fulfilled [28]. Different authors have been analysed theoretically the influence of the working wavelength selection on the temperature error [29, 30]. Their results show that the measurement errors are least when the channels are widely separated in wavelength and located at lower wavelengths. In parallel with these studies, different researchers propose the use of pyrometers with a large number of channels. Some studies show that increasing the number of wavelengths does not necessarily imply a better accuracy on the temperature and they need and adequate emissivity model to avoid a possible divergence of the temperature evaluation [22]. For this reason, different works show that the spectral response of the entire system including all optical elements must be accounted for reducing the two-colour pyrometer temperature error [30].

In this chapter, it is to develop a computer code based on a mathematical algorithm to evaluate the measurement errors for a two-colour pyrometer as a function of temperature. The calculations allow an examination of the predicted performance as a function of temperature and wavelength for any proposed choice of components for the development of the pyrometer such as photodetector responsivity, fiber attenuation, filter insertion losses, coupling light losses, among others. General conclusions can be drawn about what make a good pyrometer in terms of improving temperature errors. In order to validate the algorithm predictions, the computer code is compared with experimental results reported in the literature.

4.2. Theoretical Background

The spectral radiance of a blackbody (L_B) is given by Planck's law [31]:

$$L_B(\lambda, T) = \frac{C_1}{\lambda^5 \cdot \left(e^{\frac{C_2}{\lambda \cdot T}} - 1 \right)} \qquad 4.1$$

where C_1 and C_2 are Planck's radiation constants, whose values are $1.191 \cdot 10^8$ W·Sr^{-1}·μm^4·m^{-2} and $1.439 \cdot 10^4$ μm·K, respectively, λ is the wavelength, and T the absolute temperature of the body.

It is of interest to look at the asymptotic behaviour of Planck's law for small wavelengths. For large values of $C_2 \cdot \lambda^{-1} \cdot T^{-1}$ the term "-1" in the denominator of Equation 4.1 may be neglected, leading to Wien's distribution law [31]:

$$L_B(\lambda, T) \simeq \frac{C_1}{\lambda^5 \cdot \left(e^{\frac{C_2}{\lambda \cdot T}} \right)} \qquad 4.2$$

with

$$\frac{C_2}{\lambda \cdot T} \gg 1 \qquad 4.3$$

Figure 4.1 represents the spectral radiance variation versus wavelength for different temperatures using the Planck's law and the Wien's distribution. Examination of this figure shows that Wien approximation it is very accurate over most of the spectrum, with a total energy content of the entire spectrum approximately 8% lower than the total energy using Plank's law [32]. Most of this energy divergence is related to longer wavelengths. For this reason, the Wien's distribution law is frequently utilized in theoretical analysis in order to simplify the calculations.

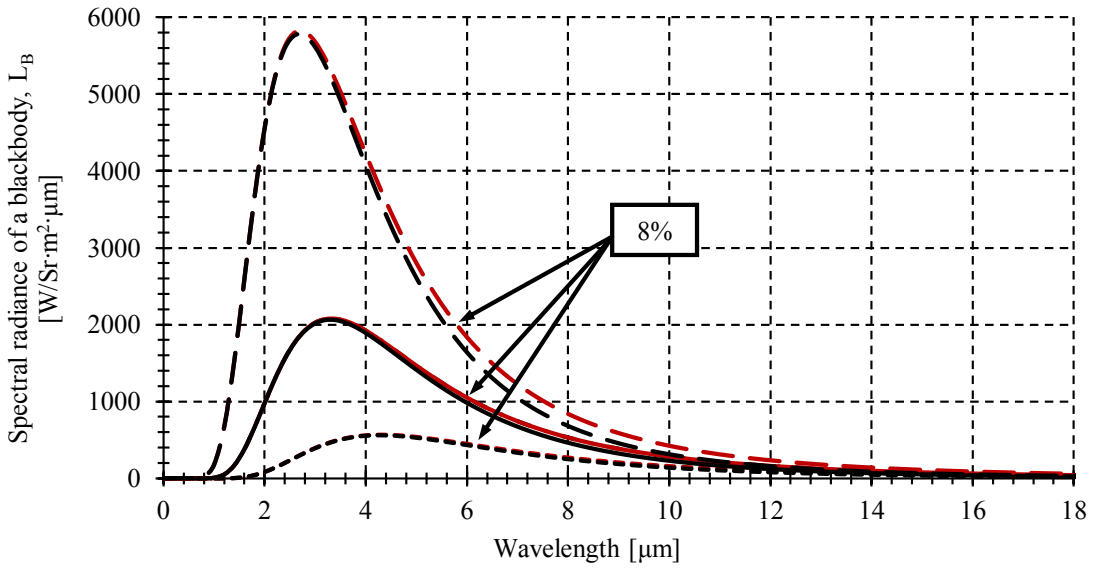

Figure 4.1. Planck's (red lines) and Wien's (black lines) blackbody emissive power spectrum for different temperatures: - -400ºC — 600ºC, – – 800ºC.

Most materials encountered in practice are not a perfect emitter of radiation. The majority of them emit radiation at a specific proportion. The emissivity (ε) is a parameter which represents

the ratio of the radiation emitted by a body at a given temperature to the radiation emitted by a blackbody at the same temperature.

The emissivity of a real surface is not a constant. Rather, it varies with the temperature of the surface as well as the wavelength, among others. It can be defined as:

$$\varepsilon(\lambda,T)=\frac{L(\lambda,T)}{L_B(\lambda,T)} \qquad 4.4$$

Considering the emissivity of a real body, the spectral radiance (L) given by Equation 4.2 can be expressed as:

$$L(\lambda,T)=\frac{C_1\cdot\varepsilon(\lambda,T)}{\lambda^5\cdot\left(e^{\frac{C_2}{\lambda\cdot T}}\right)} \qquad 4.5$$

The radiation emitted by a body is propagated in all directions.

4.3. Fiber-optic Pyrometer

The basic schematic of a fiber-optic pyrometer is shown in Figure 4.2.

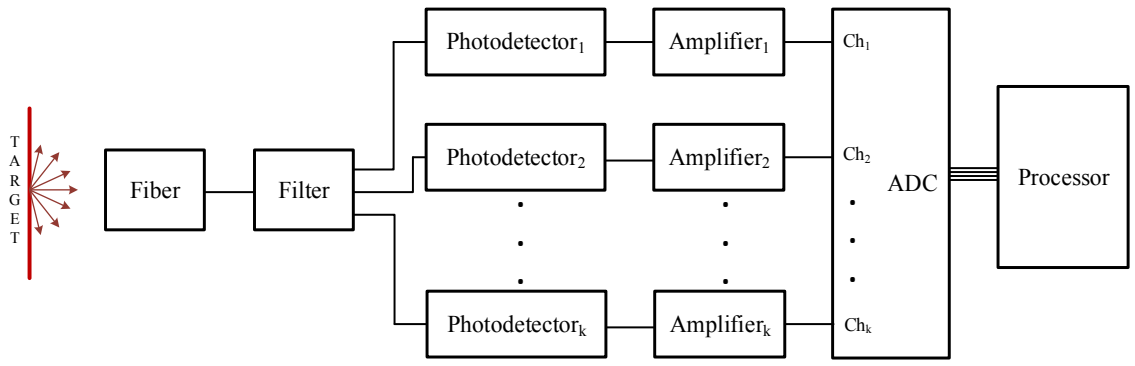

Figure 4.2. Basic schematic of fiber-optic pyrometer with multiple channels.

The IR rays radiated form the object are accepted by an optical fiber. The gathered radiation can be divided into two or more channels (k) using a filter. Filtering channels are linked to photodetectors in order to measure the optical power at different wavelength bands. The photo-generated currents are amplified and converted into voltage and then acquired by an analog-to-digital converter (ADC). The resulted digital signals are filtered and processed by a computer in order to estimate and display the temperature.

As commented in the previous section, every physical body at a specific temperature emits radiation in all directions. Only rays which are inside the acceptance angle (θ_{Max}) of the optical fiber can be transmitted, owing to total internal reflection at the core and cladding interface. The acceptance angle depends on the fiber optic numerical aperture (NA) which varies as a function of the refractive index of the core and cladding. Therefore the target area and the acceptable energy are influenced by the location of the optical fiber and the physical characteristics of the optical fiber.

The influence of the setting location of the fiber on the energy accepted and transmitted by the fiber is analysed by Ueda et all in [19, 21]. In this analysis, the cutting area of an abrasive grain is assumed as a circular plane.

As shown in Figure 4.3, the optical fiber is place vertically at a distance (t) from the target and the center of the target (O_T) is on the center axis of the optical fiber (O_F). The assumption that the target area is a blackbody surface at a uniform temperature and there are no losses at all is supposed in this theoretical development.

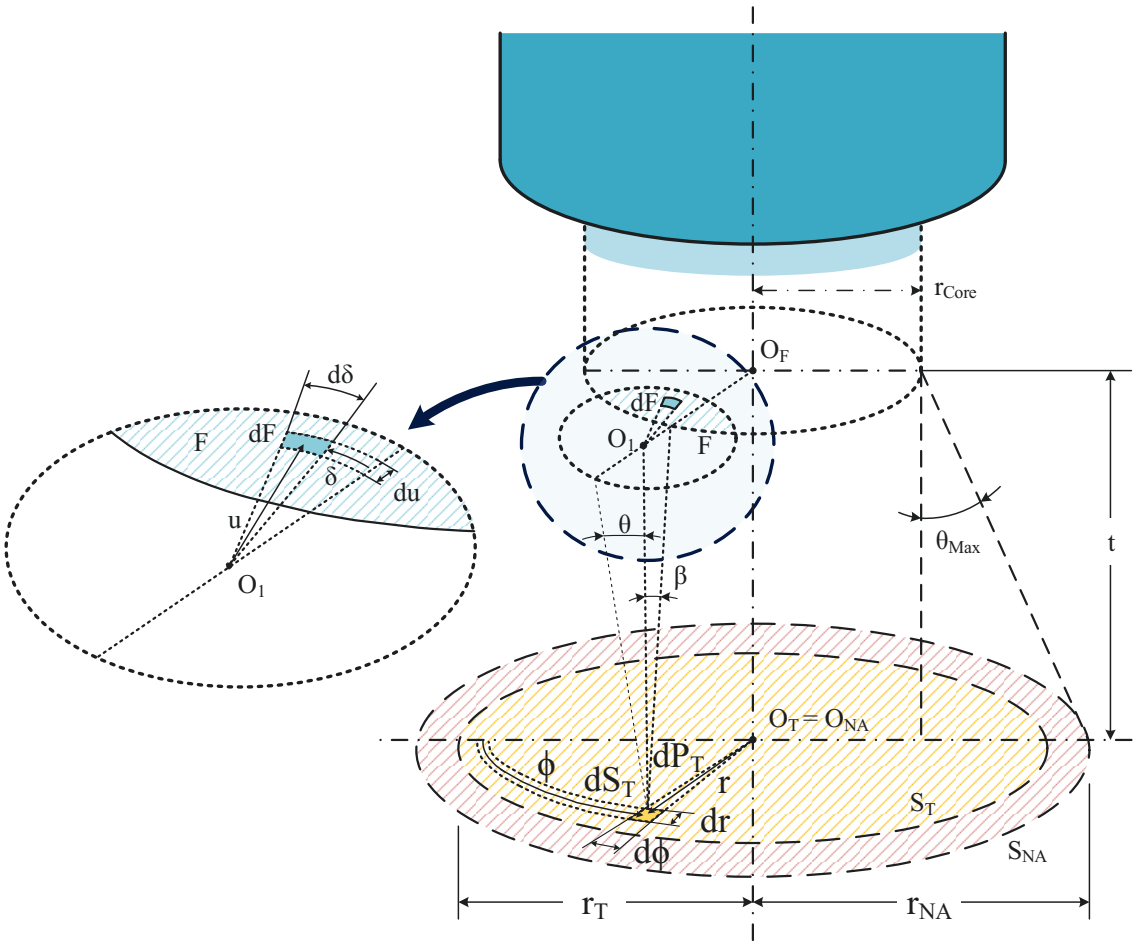

Figure 4.3. Schematic of the optical fiber pyrometer measurement surface area.

S_T with radius r_T and S_{NA} with radius r_{NA} represent the target area and the area covered by the fiber optic NA, respectively.

Two elements, dS_T and dF, are defined as differential elements of an area in the target surface (S_T) and the fiber face (F), respectively. From these elements and according to Ueda et all in [21], the light power of an element (dP_T) from dS_T incident on dF is expressed by the following equation:

$$dP_T(\lambda) = L(\lambda) \cdot d\lambda \cdot dS_T \cdot \frac{\cos^4(\beta)}{t^2} \cdot dF \qquad 4.6$$

where L is the spectral radiance and β is the angle of incidence. Therefore the light power (P_F) from dS_T accepted by the core is obtained by integrating Equation 4.6 over the area F as shown in Figure 4.3.

$$P_F(\lambda, r) = \iint_F L(\lambda) \cdot d\lambda \cdot dS_T \cdot \frac{\cos^4(\beta)}{t^2} \cdot dF \qquad 4.7$$

with

$$dF = u \cdot du \cdot d\delta \qquad 4.8$$

$$\tan(\beta) = \frac{u}{t} \qquad 4.9$$

The resulted equation can be expressed as:

$$P_F(\lambda, T, r) = \iint_F L(\lambda, T) \cdot d\lambda \cdot dS_T \cdot \frac{t^2 \cdot u \cdot du \cdot d\delta}{\left(t^2 + u^2\right)^2} = L_\lambda \cdot d\lambda \cdot g(r) \cdot dS_T \qquad 4.10$$

with

$$g(\lambda, r) = \iint_{F(\lambda)} \frac{t^2 \cdot u}{\left(t^2 + u^2\right)^2} \cdot du \cdot d\delta \qquad 4.11$$

Thus, the total power accepted by the fiber core (P_F) is obtained by integrating Equation 4.10 over the measuring area, S_T.

$$P_F(\lambda, T, r) = \iint_{S_T} L(\lambda, T) \cdot g(\lambda, r) \cdot dS_T \cdot d\lambda \qquad 4.12$$

This equation can be rewritten as a function of the relative position of the optical fiber to the target.

If the target center is on center axis of the fiber and the radii of the target (r_T) is smaller than the radii of the spot (r_{NA}) projected by the fiber NA on the target surface, Equation 4.12 can be expresses as [21]:

$$P_F(\lambda,T)=\int_0^{r_T}\int_0^{2\pi}L(\lambda,T)\cdot r\cdot g(\lambda,r)\cdot d\delta\cdot dr\cdot d\lambda \qquad 4.13$$

On the other hand, if $O_T = O_{NA}$ and $r_T > r_{NA}$, Equation 4.12 can be expresses as [21]:

$$P_F(\lambda,T)=\int_0^{r_{NA}}\int_0^{2\pi}L(\lambda,T)\cdot d\lambda\cdot g(\lambda,r)\cdot d\phi\cdot dr=L(\lambda,T)\cdot\kappa(\lambda)\cdot d\lambda \qquad 4.14$$

with

$$\kappa(\lambda)=\frac{\pi^2\cdot d_{Core}^2}{8}\cdot\left[1-\cos\left(2\cdot\theta_{Max}(\lambda)\right)\right] \qquad 4.15$$

where κ represents the amount of emitted light coupled into the fiber. d_{Core} is the diameter of the fiber core. This expression suggests that the setting location of the fiber is independent of the light power accepted when $r_T > r_{NA}$.

From Equations 4.5, 4.13 and 4.14, the light power measured by the pyrometer (P_D) is calculated for the two cases under study:

For $r_T < r_{NA}$:

$$P_D(T,\lambda)=\int_{\lambda_A}^{\lambda_B}\int_0^{r_T}\int_0^{2\pi}\frac{C_1\cdot L_{Filter}(\lambda)\cdot\alpha(\lambda)\cdot\varepsilon(\lambda,T)}{\lambda^5\cdot\left(e^{\frac{C_2}{\lambda\cdot T}}\right)}\cdot r\cdot g(\lambda,r)\cdot d\delta\cdot dr\cdot d\lambda \qquad 4.16$$

For $r_T > r_{NA}$:

$$P_D(T,\lambda)=\int_{\lambda_A}^{\lambda_B}\frac{C_1\cdot L_{Filter}(\lambda)\cdot\alpha(\lambda)\cdot\varepsilon(\lambda,T)}{\lambda^5\cdot\left(e^{\frac{C_2}{\lambda\cdot T}}\right)}\cdot\kappa(\lambda)\cdot d\lambda \qquad 4.17$$

where λ_A and λ_B are the shortest and longest wavelength on the filter wavelength band, respectively. L_{Filter} is the insertion losses of the filter. α is the loss factor corresponding to the fiber attenuation.

The mathematical model for calculating the optical power measured by the pyrometer is compared with an experimental pyrometer reported in the literature. The aim of this comparison is to evaluate the simulation robustness for different temperatures.

Figure 4.4 shows the experimental pyrometer calibration curves given by Mincent et all in [23]. This figure shows the normalized output power versus temperature at two wavelengths, 1.31 and 1.5µm. The sensor uses a multimode glass fiber with a core and cladding diameter of 400 and 440µm, respectively. Two interference filters are used to separate the light power emitted by a blackbody in two spectral bands centered at 1.31 and 1.5µm with a bandwidth of 60nm. An optical power meter based on a Germanium (Ge) photodiode is used to measure the power through interference filters. No data about the wavelength dependence loss are shown in the article. It is supposed that the surface area is infinitely larger than the area covered by the fiber NA. Using Equation 4.17 and the pyrometer design parameters, the normalized output light power is calculated from a temperature of 750 to 900ºC, as also shown in Figure 4.4.

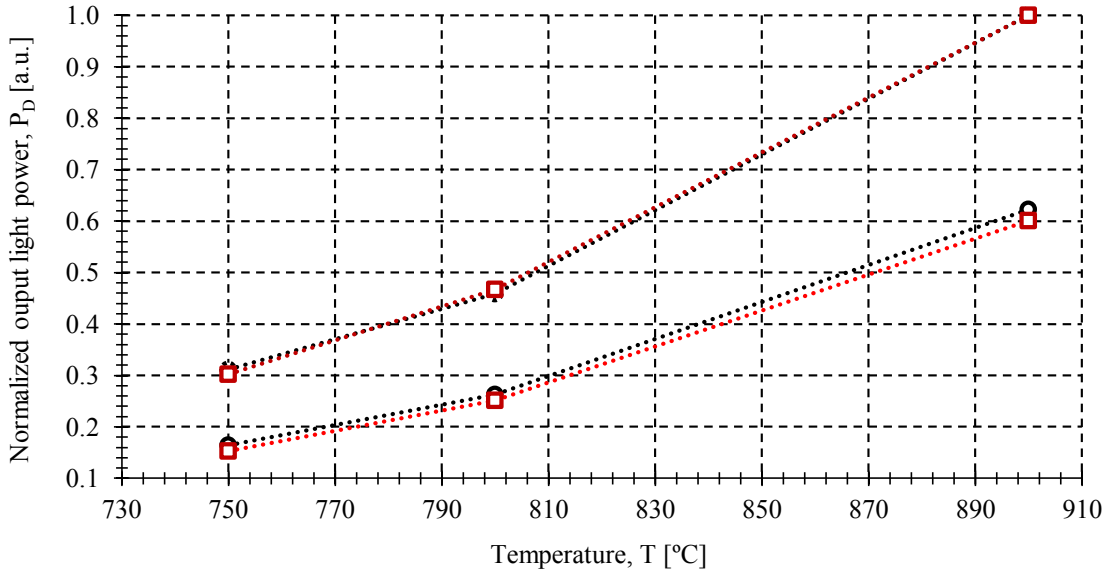

Figure 4.4. Normalized output power versus temperature using experimental [23] (red line) and theoretical curves (black line) for different filtering wavelengths: ○ 1.31µm, □ 1.5µm.

The measured and simulated light power is higher at the longest wavelength. According to the Wien's distribution law shown in Figure 4.1, in the wavelength range from 1.31 to 1.55µm the light power increases when the wavelength of the light increases. On the other hand, the

measured light power increases as temperature increases, showing an exponential trend as in Figure 4.1.

From Figure 4.4, a maximum difference between the experimental and theoretical output power ratio of 0.25dB is obtained at a temperature of 750ºC. The experimental output power ratio is fitted with a lineal regression. Using the resulted lineal equation and the maximum output power ratio difference expressed in linear units, a temperature error of 6% is obtained. The low temperature error demonstrates that the mathematical model is able to predict the pyrometer behaviour at each wavelength. The difference between theoretical and experimental curves can be due to avoiding the wavelength dependence loss in the simulations.

In order to simplify the expressions of the pyrometer behaviour, it is supposed that the target radius is smaller than the radius of the spot projected by the fiber NA on the target surface. This assumption will be the most common in a practical situation of interest in this work, due to the reduced size of the spot. Using a multimode optical fiber with 62.5/125µm core and cladding diameters and a distance between the fiber end and the target of 0.3mm, the diameter of the spot projected by the fiber NA on the surface is ~160µm. Under this assumption, the expression of the current signal generated in a photodetector (I_D) is derived from Equation Equation 4.17:

$$I_D(T,\lambda) = \int_{\lambda_A}^{\lambda_B} \frac{C_1 \cdot R(\lambda) \cdot L_{Filter}(\lambda) \cdot \alpha(\lambda) \cdot \varepsilon(\lambda, T)}{\lambda^5 \cdot \left(e^{\frac{C_2}{\lambda \cdot T}} \right)} \cdot \kappa(\lambda) \cdot d\lambda \qquad 4.18$$

where R is the photodetector responsivity. The photodetector responsivity is the ratio between the generated photocurrent and the input optical power in photoconductive mode. Responsivity is a function of the wavelength of the incident light, and sensor material, among others.

If a single wavelength is considered by an idealization of a monochromatic pyrometer, a relation between the measured surface temperature (T_R) and the calibration temperature (T) can be deduced from Equation 4.18 by setting the measured photocurrent of the pyrometer equal to the photocurrent during the calibration. The resulted equation can be expresses as [15]:

$$T_R = \left(\frac{1}{T} + \frac{\lambda}{C_2} \cdot \left[\ln\left(\frac{\varepsilon(\lambda)}{\varepsilon_c(\lambda)} \right) \right] \right)^{-1} \qquad 4.19$$

where ε and ε_c are the measure and calibration emissivity, respectively, and ε_s is defined as the emissivity ratio between them. The temperature error (E_T) is defined as:

$$E_T = \frac{(T_R - T)}{T} \cdot 100 \quad [\%] \qquad 4.20$$

If the pyrometer is calibrated with a blackbody, the calibration emissivity is equal to 1. If the surface emissivity is the same as the one of the calibration process, the second term on the right-hand of Equation 4.19 is zero and thus the measured temperature correspond to the surface temperature. On the contrary, if the conditions of the measurement surface cannot be measured in the calibration setup and the emissivity of the surface is unknown, an exact determination of the temperature is not possible.

4.4. Two-colour Pyrometer

The two-colour pyrometer has the advantage that a correct measurement of the absolute temperature is possible without knowing the surface emissivity. The two-colour pyrometer technique uses the ratio of two signals obtained from different wavelength bands, and then a lineal or polynomial approximation is used to convert the two-signal ratio into temperature. If the wavelength bands are not sufficiently narrow, an error will only arise if the surface emissivity are not equal at the two operating bands of the pyrometer. From Equation 4.18 the output signal ratio, γ, of the two-colour pyrometer is given by:

$$\gamma = \frac{I_{D,\lambda_1}}{I_{D,\lambda_2}} = \frac{\int_{\lambda_{1,A}}^{\lambda_{1,B}} \frac{C_1 \cdot L(\lambda_1) \cdot R(\lambda_1) \cdot \alpha(\lambda_1) \cdot \varepsilon(\lambda_1) \cdot \tau(\lambda_1)}{\lambda_1^5 \cdot \left(e^{\frac{C_2}{\lambda_1 \cdot T}} \right)} \cdot d\lambda_1}{\int_{\lambda_{2,A}}^{\lambda_{2,B}} \frac{C_1 \cdot L(\lambda_2) \cdot R(\lambda_2) \cdot \alpha(\lambda_2) \cdot \varepsilon(\lambda_2) \cdot \tau(\lambda_2)}{\lambda_2^5 \cdot \left(e^{\frac{C_2}{\lambda_2 \cdot T}} \right)} \cdot d\lambda_2} \qquad 4.21$$

where λ_A and λ_B are the shortest and longest wavelength of each wavelength bands centered at λ_1 and λ_2, respectively.

If two single wavelengths are considered by ideally filtering both channels, a relationship between the measured surface temperature (T_R) and the true temperature (T) can be deduced from the ratio of the signals of both pyrometer channels based on Equation 4.21 [33]:

$$T_R = \left(\frac{1}{T} + \frac{\ln\left(\varepsilon_r \cdot \delta_r\right)}{C_2 \cdot \left(\frac{-4 \cdot \Delta\lambda}{4 \cdot \lambda_c^2 - \left(\Delta\lambda\right)^2} \right)} \right)^{-1} \qquad 4.22$$

with

$$\lambda_c = \frac{\lambda_2 + \lambda_1}{2} \qquad 4.23$$

$$\Delta\lambda = \lambda_2 - \lambda_1 \qquad 4.24$$

$$\delta_r = \frac{\delta_{\lambda_1}}{\delta_{\lambda_2}} = \frac{R_{\lambda_1}}{R_{\lambda_2}} \cdot \frac{\alpha_{\lambda_1}}{\alpha_{\lambda_2}} \cdot \frac{L_{\lambda_1}}{L_{\lambda_2}} \cdot \frac{\tau_{\lambda_1}}{\tau_{\lambda_2}} \qquad 4.25$$

$$\varepsilon_r = \frac{\varepsilon_{\lambda_1}}{\varepsilon_{\lambda_2}} \qquad 4.26$$

where λ_c and $\Delta\lambda$ are the average central wavelength and the wavelength spacing of the ideally filtering channels, respectively. ε_r and δ_r are the measured surface emissivity ratio and the wavelength dependence loss ratio, both at the two selected wavelengths.

A similar process can be carried out to obtain the pyrometer expressions of the current signal, temperature error and output signal ratio when the target area is smaller than the spot area.

4.5. Pyrometer Wavelength Bands Selection

The designed pyrometer should be capable of measuring the absolute temperature of multiple surfaces with a high accuracy. The use of a one-colour pyrometer is a very common solution due to its simple setup. However, to determine the true surface temperature it is necessary to know the emissivity of the surface at the measurement wavelength or to calibrate the pyrometer at the measurement surface as previously described.

At first the accuracy of the one-colour pyrometer is analysed in this section. The error of the measured absolute temperature, depending on the surface emissivity, is calculated using Equation 4.19 and 4.20. If the one-colour pyrometer is calibrated with a blackbody, the emissivity ratio (ε_r) can be supposed to be equal to 1. In this case, the maximum measurement error is

obtained. In practice, calibrating the pyrometer with the real measurement surface is often tried. If the surface conditions can be approximated well in a calibration setup the temperature error are smaller. The temperature error which is caused by a difference between measured and calibrated surface emissivity is shown in Figure 4.5 for a pyrometer operating at a wavelength of 1.55µm.

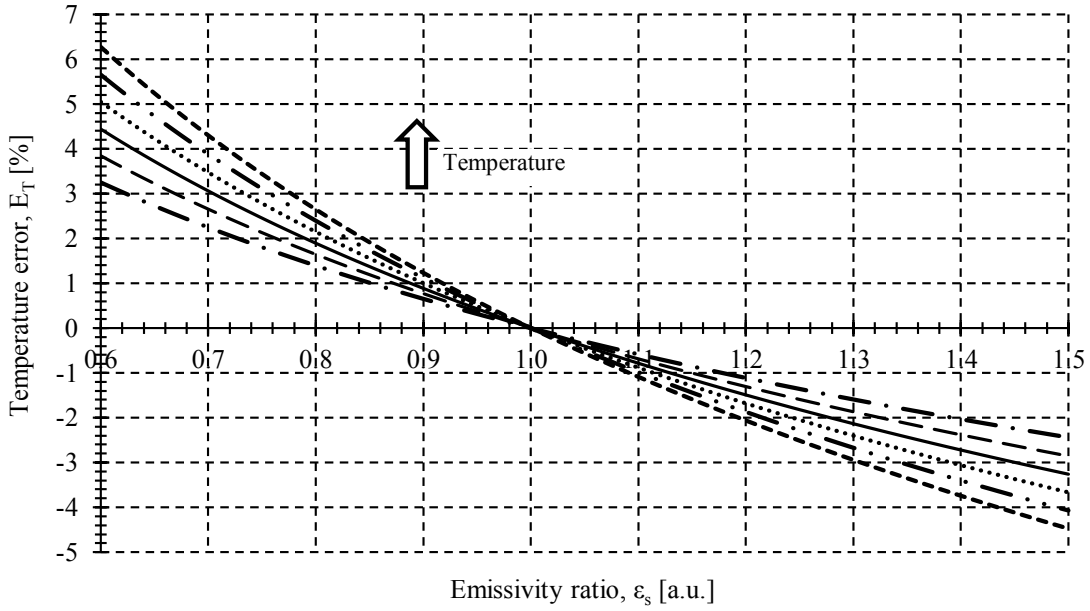

Figure 4.5. Temperature error as a function of emissivity ratio at a wavelength of 1.55µm for different temperatures: –·– 300ºC, – – 400ºC, — 500ºC, · · 600ºC, –··– 700ºC, - -800ºC.

A deviation between the emissivities of -20% causes an error of ~2.5% at a temperature of 800ºC which means a measured temperature of ~828ºC. The main problem of the one-colour pyrometer is that the emissivity can change dramatically if surface conditions changes slightly. Figure 4.6 shows the total hemispherical emissivity variation with temperature for several metallic materials in the temperature range from 0 to 1,000ºC. From this figure, it is clear that the emissivity of metals increases with temperature [34].

Figure 4.6 also shows that oxidation causes significant increment in the emissivity of metals. Heavily oxidized metals can have emissivities comparable to non-metals and the blackbody. If the pyrometer is calibrated at the surface of Inconel 718 and the surface oxidizes during the measurement, the temperature error will be ~8% at a temperature of 500ºC. Even higher values can be reached for surfaces with low emissivities such as Al-alloy 7075 as pointed by Muller et al in [15]. So, if the surface emissivity is unknown and changes during the measurement it is not possible to determine the absolute temperature of the surface accurately.

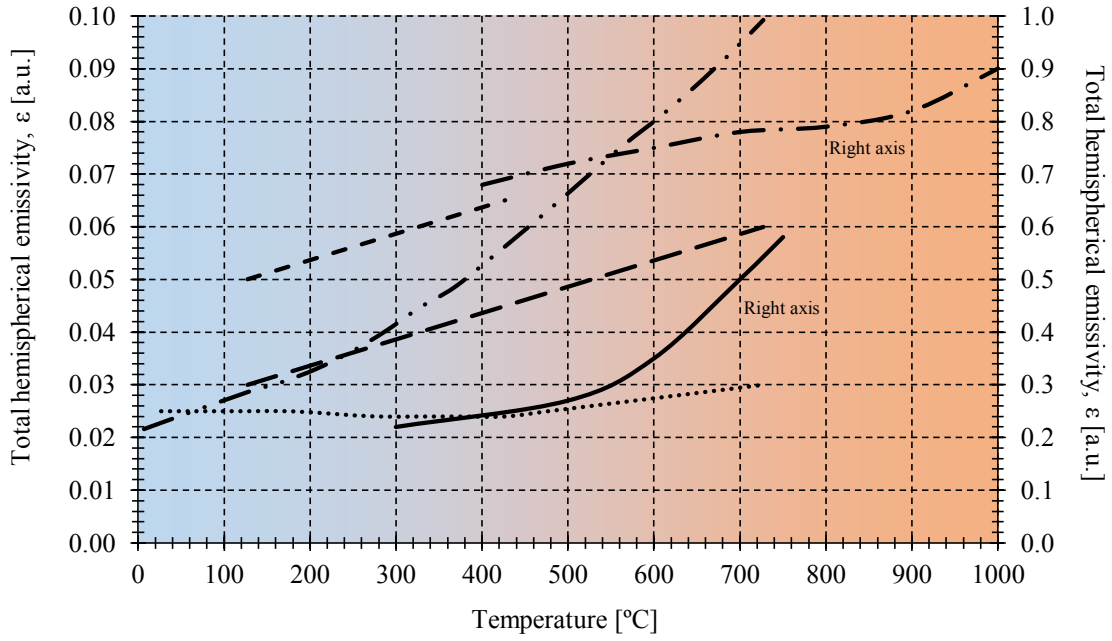

Figure 4.6. Total hemispherical emissivity for selected metals: · · Copper, – – Gold, - - Aluminium, –·– Tungsten, — Inconel 718, –·– Inconel 718 previously oxidized at 815ºC, from [33, 35, 36].

For these reasons, two-colour pyrometers have the advantage of measuring the absolute surface temperature without the knowledge of the surface emissivity if the emissivities at the two wavelengths are equal. It means that the surface fulfilled the grey body behaviour. Different authors have investigated the temperature errors arising for different number of pyrometer channels, e. g. Khan et al in [37], and have come to the conclusion that there is not any advantage in using more than two-colours if a good selection of the operated wavelength are carried out in the two-colour pyrometer.

According to the Wien's distribution law given by Equation 4.2, the spectral radiance depends on wavelength and temperature, as shown in Figure 4.7. In this figure, the evaluated wavelength range corresponds to a commonly used sub-division scheme of the Near-infrared (NIR), Short-wavelength infrared (SWIR) and the Mid-wavelength infrared (MWIR).

The maximum of this curve can be obtained by differentiating Equation 4.1 with respect to wavelength (λ) while holding temperature (T) constant and setting the results equal to zero, leading to an equation that can be solved as [31]:

$$\lambda_{L_{Max}} \cdot T = 2897.8 \quad [\mu m \cdot K] \qquad 4.27$$

Equation 4.27 is known as Wien's displacement law and represents the wavelength at the maximum spectral radiance (λ_{Lmax}) that a blackbody can emitted at a specific temperature. For low

temperatures, the radiation energy is small and thus the measurement wavelengths should be located close to the wavelength at the peak of maximum radiation energy. For a temperature range between 300 and 800ºC, Wien's displacement law gives the maximum spectral radiance between 5.1 and 2.7μm. For higher temperatures closely to the sun temperature, the maximum spectral radiance is located at 1.9μm. For this reason, to measure higher power signals, the pyrometer wavelengths should be located between 1.9 and 5.1μm.

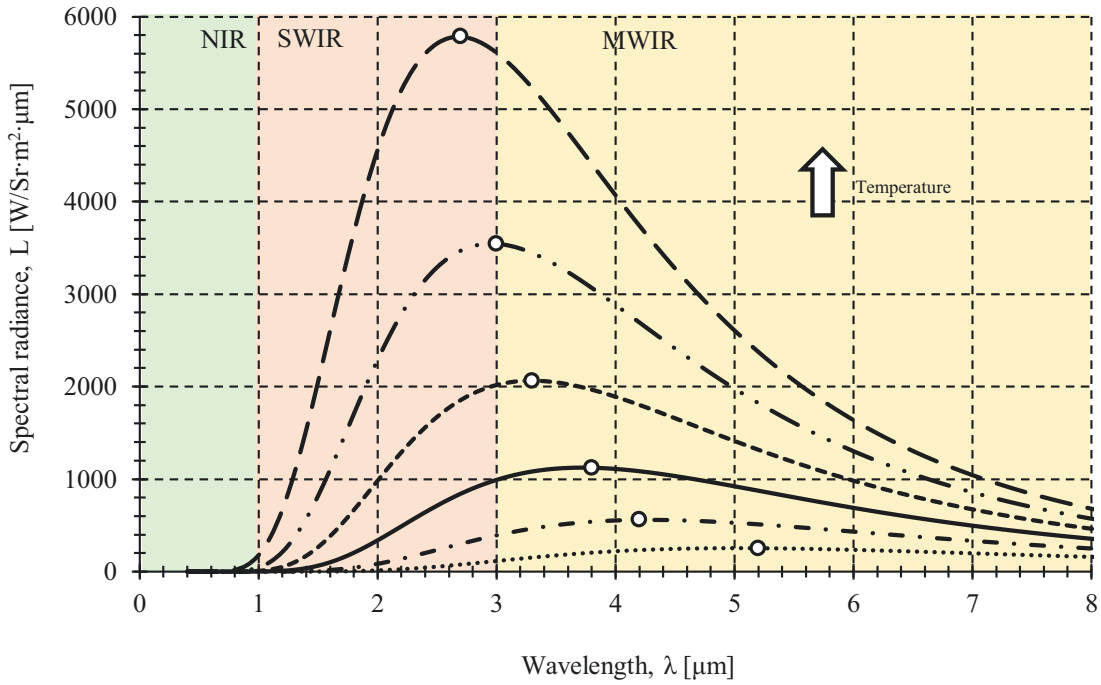

Figure 4.7. Blackbody spectral radiance spectrum for different temperatures: · · 300ºC, –·– 400ºC, — 500ºC, - -600ºC, –··– 700ºC, – – 800ºC.

The primary source of error for the measured absolute temperature is that the grey-body behaviour is not fulfilled. Typical spectral behaviour of surface emissivities is shown in Figure 4.8 for few metals [38]. It can be shown the values for directional emittances in the direction normal to the surface versus wavelength. However, the spectral behaviour is similar to hemispherical emissivities [32].

In general, non-metal have relatively high emissivity, which may vary erratically across the spectrum, and metals behave similarly for short wavelengths but tend to have lower emissivities with more regular spectral dependence in the IR spectrum [39]. Especially in the wavelength range of visible light and NIR many metals like copper, nickel and aluminium show very strong changes in the emissivity.

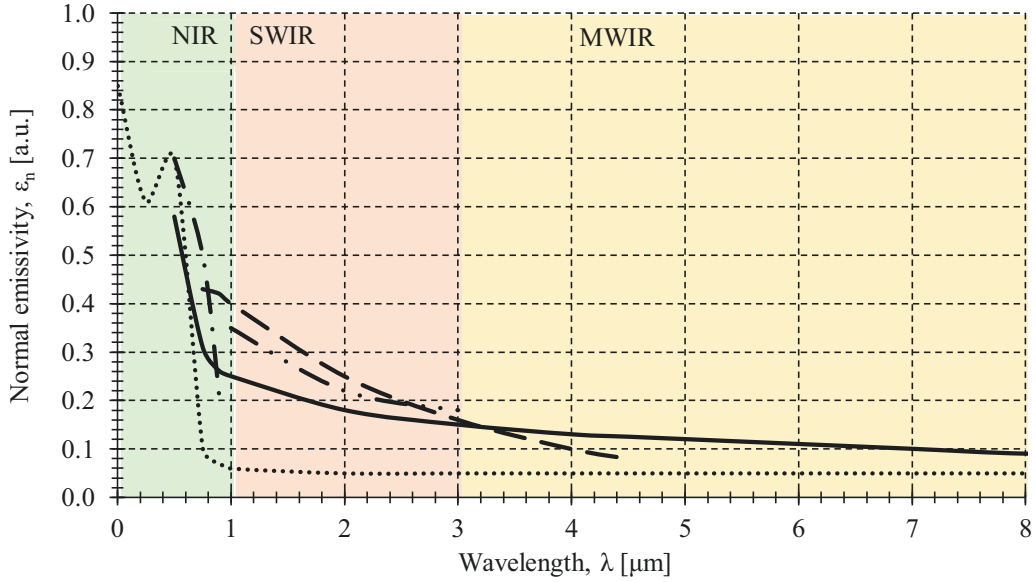

Figure 4.8. Normal spectral emissivities for selected metals: · · Copper, −·− Gold, — Aluminium, −··− Nickel, − − Tungsten, from [38].

The temperature error caused by this behaviour is analysed using Equations 4.22 to 4.26 for different wavelengths and operating at 500ºC, as shown in Figure 4.9. The wavelength dependence loss ratio is considered constant in this analysis. These errors are compared to those analysed in [15-17] using a central wavelength and a wavelength shift of 1.85 and 0.3μm, respectively.

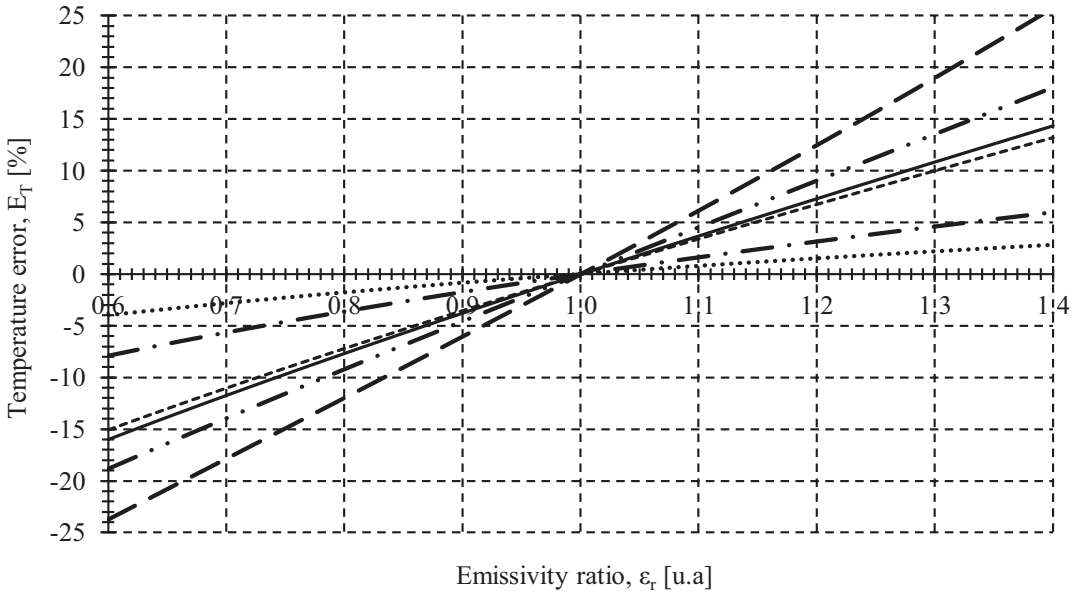

Figure 4.9. Temperature error as a function of emissivity ratio at a temperature of 500ºC for different filtering channels: · · $\Delta\lambda$=0.9μm & λ_c=1.25μm,- -$\Delta\lambda$=0.3μm & λ_c=1.4μm, — $\Delta\lambda$=0.3μm & λ_c=1.45μm, − · − $\Delta\lambda$=0.6μm & λ_c=1.4μm, − · · − $\Delta\lambda$=0.24μm & λ_c=1.43μm, − − $\Delta\lambda$=0.2μm & λ_c=1.6μm.

From Figure 4.9, it can be seen that the temperature error decreases if the channel spacing increases. The distance between wavelengths has to be long enough to minimize the temperature error and filter both channels without overlapping, but close enough to ensure a constant emissivity across the filtering channels. Figure 4.9 also shown that the temperature error is smaller for shorter central wavelengths, as pointed out by Müller et all in [15].

The error calculations for the two-colour pyrometer show that a general statement concerning the temperature accuracy is not possible. A major advantage of the two-colour pyrometer is that it does not need to be calibrated for each measurement surface which make it more suitable for a multipurpose measurement device. Another important advantage of the two-colour pyrometer is that the surface temperature is not affected by any signal attenuation caused for example by dirt, changes of distance between the fiber and the surface, among others, but only if the signals of both channels are equally attenuated.

An important factor in the accuracy of the measured absolute temperature is the characteristics of the devices used in the pyrometer set-up at the two filtering wavelengths.

The wavelength of light to which the photodetector responds is a critical parameter that is dependent upon the material used in the photodetector. Figure 4.10 shows the responsivity curve for different materials used to produce photodetectors in the NIR and SWIR wavelength range.

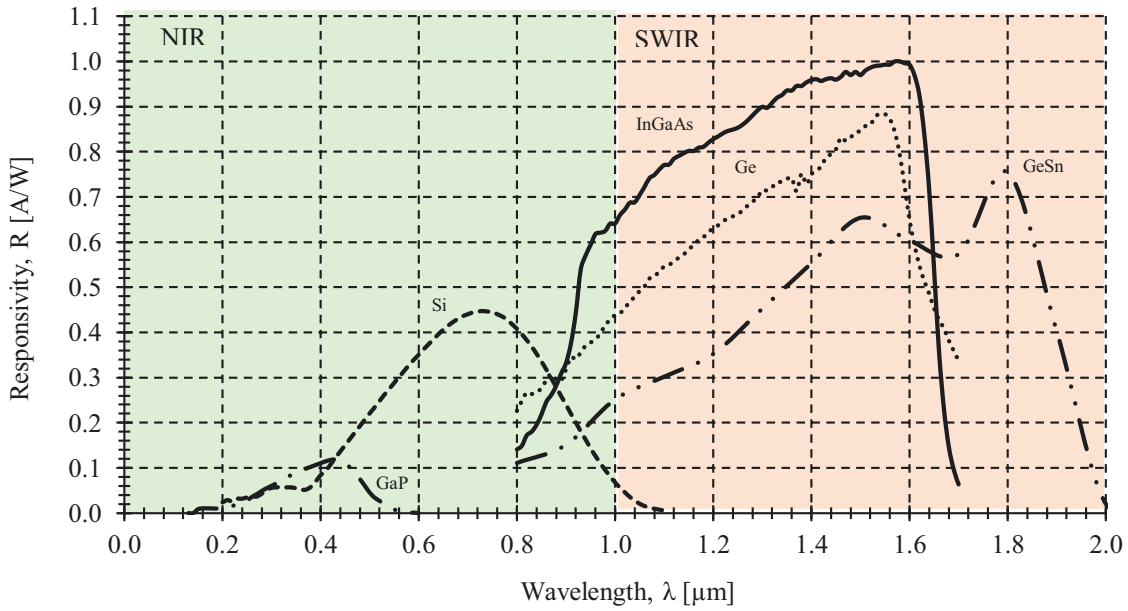

Figure 4.10. Responsivity values versus wavelength for different detector materials: · · Ge, – –Si, —··— GeSn, —·— GaP, — InGaAs.

The benefit of the higher radiation energy at longer wavelength for low temperature is diminished by the lower responsivity of the detector in this wavelength ranges. As evident in Figure 4.10, Silica (Si) detectors are ideal for detection in the NIR and Indium Gallium Arsenide (InGaAs) is the preferred detector in the SWIR. The photodetector's world market offer the possibility to use other materials such as Ge, Gallium Phosphide (GaP) and Germanium Tin (GeSn), as shown in Figure 4.10, although the maximum responsivity is smaller than the responsivity of Ge or InGaAs detectors.

Other important problem to take into account is the different responsivity value at each wavelength. From Equation 4.22 to 4.26, temperature error as a function of the emissivity ratio is calculated for different filtering channels and operating at 500ºC, see Figure 4.11. The wavelength dependence loss ratio of the filter and the optical fiber are considered constant in this analysis. The filtering channels proposed in Figure 4.9 are analysed in order to evaluate the impact of the photodetector responses in the previous wavelength selection. The InGaAs responsivity value corresponding to each channel (see Figure 4.10) is used in the calculations of the temperature error.

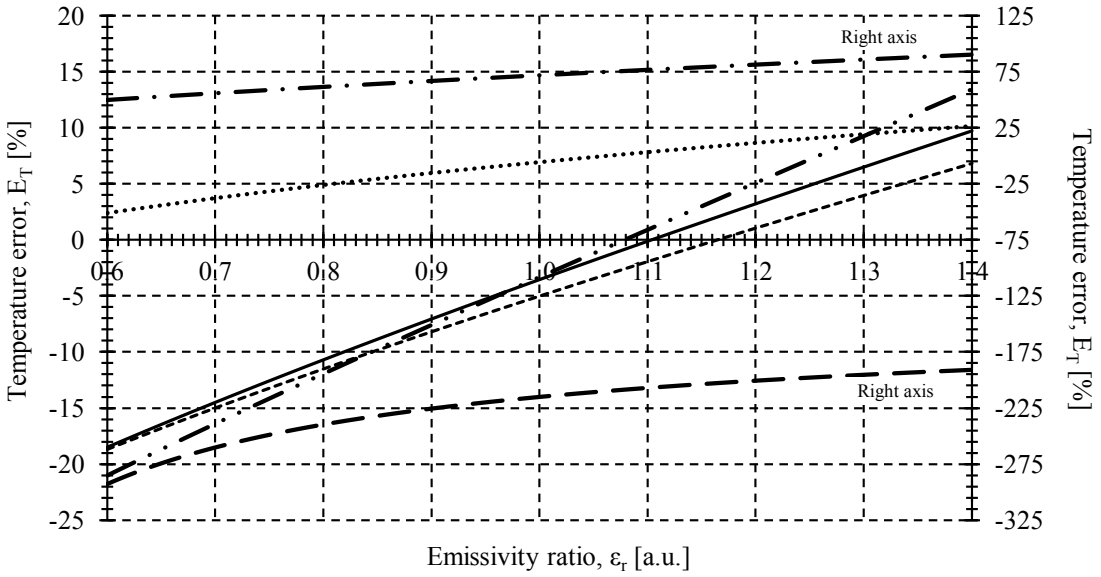

Figure 4.11. Temperature error as a function of emissivity ratio at a temperature of 500ºC considering InGaAs responsivity curve for different filtering channels: · · $\Delta\lambda$=0.9µm & λ_c=1.25µm, - - $\Delta\lambda$=0.3µm & λ_c=1.4µm, — $\Delta\lambda$=0.3µm & λ_c=1.45µm, – · · – $\Delta\lambda$=0.24µm & λ_c=1.43µm, – – $\Delta\lambda$=0.2µm & λ_c=1.6µm (Right axis), – · – $\Delta\lambda$=0.6µm & λ_c=1.4µm (Right axis),

Analysing the result shown in Figure 4.11, it can be seen that the temperature error is not only dependent on the channel spacing and the average central wavelength as shown in Figure 4.9. The photodetector responsivity, among other factors, can change the temperature error. This

statement is demonstrated using the average central wavelength and the wavelength spacing of 1.43 and 0.24μm, respectively. Figure 4.9 shows that the temperature error is zero when changes in the surface emissivity at both filtering channel are not appreciated. This result is only valid when a photodetector with a flat responsivity curve or the same responsivity at both filtering channels is used. In practice, photodetector responsivity curve is not flat and changes with wavelength as shown in Figure 4.10. The use a photodetector with the same responsivity at both channels is often tried. For this reason it is necessary to study the influence of the photodetector responsivity in the temperature error. Figure 4.11 show that using the InGaAs responsivity curve for an average central wavelength and a wavelength spacing of 1.43 and 0.24μm, the temperature error is incremented around 3.3% from the value previously calculated without the effect of the photodetector responsivity. Even higher values can be reached for an average central wavelength of 1.4μm and the wavelength spacing of 0.6μm. These values correspond to two spectral bands centered at 1.1 and 1.7μm. Using these wavelengths and the responsivity of an InGaAs photodetector, the temperature error is incremented around 72% due to the high attenuation of one of the channels.

From this example, it is demonstrated that unequal changes in both channels during the gathering, filtering and measuring process can change the final value of the measured temperature. The influence of the optical fiber and the filter should be taken into account in order to develop a pyrometer capable to measure temperature with low errors in a wide variety of surface materials.

4.6. Conclusions

The influence of the electrical and optical characteristics of the two-colour pyrometer have been analysed in order to develop a sensor capable of measuring temperatures of unknown emissivities surfaces with low temperature error.

Temperature errors for a two-colour pyrometer have been evaluated for different wavelengths. From these values, it can be seen that the temperature error decreases if the channel spacing increases. The distance between wavelengths has to be long enough to minimize the temperature error and to filter both channels without overlapping, but close enough to ensure a constant emissivity across the filtering channels. This analysis also shown that the temperature error is smaller for shorter wavelengths.

On the other hand, it is demonstrated that the pyrometer temperature error is not only dependent on the selected wavelength ranges. The influence of the characteristics of the devices used in the pyrometer set-up at the two filtering channels are an important factor to analyse in order to measure temperatures with low temperature errors. The coupling light loss, fiber

attenuation, filter insertion loss, and photodetector responsivity are parameters to be analysed. It is demonstrated that unequal changes in both channels during the gathering, filtering and measuring process can change the final value of the measured temperature.

Finally, a mathematical model based on thermal radiation equations is developed to predict the pyrometer optical power measurement at each wavelength range. Simulations are compared with pyrometer measurements reported in the literature. A maximum power difference of 0.2dB is obtained. This result demonstrates that the mathematical model is able to predict the pyrometer behaviour at different wavelength ranges.

4.7. References

[1] R. Komanduri and Z. B. Hou, "A review of the experimental techniques for the measurement of heat and temperatures generated in some manufacturing processes and tribology," *Tribology International*, vol. 34, pp. 653-682, 2001.

[2] I. Lazoglu and Y. Altintas, "Prediction of tool and chip temperature in continuous and interrupted machining," *International Journal of Machine Tools and Manufacture*, vol. 42, pp. 1011-1022, 2002.

[3] Z. Y. Wang and K. P. Rajurkar, "Cryogenic machining of hard-to-cut materials," *Wear*, vol. 239, pp. 168-175, 2000.

[4] F. E. Kennedy, D. Frusescu, and J. Li, "Thin film thermocouple arrays for sliding surface temperature measurement," *Wear*, vol. 207, pp. 46-54, 1997.

[5] D. Stephenson, "Tool-work thermocouple temperature measurements - theory and implementation issues," *Journal of Engineering for Industry*, vol. 115, pp. 432-437, 1993.

[6] W. Grzesik, "Experimental investigation of the cutting temperature when turning with coated indexable inserts," *International Journal of Machine Tools and Manufacture*, vol. 39, pp. 355-369, 1999.

[7] K. Trigger, R. Campbell, and B. Chao, "A Tool-Work-Thermocouple Compensating Circuit," *in Transactions of the ASME*, 1956.

[8] T. Kitagawa, A. Kubo, and K. Maekawa, "Temperature and wear of cutting tools in high-speed machining of Inconel 718 and Ti6·Al6V·2Sn," *Wear*, vol. 202, pp. 142-148, 1997.

[9] A. Kus, Y. Isik, M. Cakir, S. Coşkun, and K. Özdemir, "Thermocouple and Infrared Sensor-Based Measurement of Temperature Distribution in Metal Cutting," *Sensors*, vol. 15, pp. 1274-1291, 2015.

[10] C. Dinc, I. Lazoglu, and A. Serpenguzel, "Analysis of thermal fields in orthogonal machining with infrared imaging," *Journal of Materials Processing Technology*, vol. 198, pp. 147-154, 2008.

[11] L. Wang, K. Saito, and I. Jawahir, "Infrared temperature measurement of curled chip formation in metal machining," *Transactions-North American Manufacturing Research Institution of SME*, pp. 87-92, 1996.

[12] T. Fu, H. Zhao, J. Zeng, M. Zhong, and C. Shi, "Two-color optical charge-coupled-device–based pyrometer using a two-peak filter," *Review of Scientific Instruments*, vol. 81, p. 124903, 2010.

[13] J. Pujana, L. d. Campo, R. B. Pérez-Sáez, M. J. Tello, I. Gallego, and P. J. Arrazola, "Radiation thermometry applied to temperature measurement in the cutting process," *Measurement Science and Technology*, vol. 18, p. 3409, 2007.

[14] G. Sutter, L. Faure, A. Molinari, N. Ranc, and V. Pina, "An experimental technique for the measurement of temperature fields for the orthogonal cutting in high speed machining," *International Journal of Machine Tools and Manufacture*, vol. 43, pp. 671-678, 2003.

[15] B. Muller and U. Renz, "Development of a fast fiber-optic two-color pyrometer for the temperature measurement of surfaces with varying emissivities," *Review of Scientific Instruments*, vol. 72, pp. 3366-3374, 2001.

[16] B. Müller and U. Renz, "Time resolved temperature measurements in manufacturing," *Measurement*, vol. 34, pp. 363-370, 2003.

[17] B. Müller and U. Renz, "A Fast Fiber-optic Two-color Pyrometer for Temperature Measurements of Metallic Surfaces with Varying Emissivities," in *Measurement and Control in Science and Industry*, Chicago (United States of America), 2003, pp. 741-746.

[18] T. Ueda, K. Yamada, and T. Sugita, "Measurement of Grinding Temperature of Ceramics Using Infrared Radiation Pyrometer with Optical Fiber," *Journal of Manufacturing Science and Engineering*, vol. 114, pp. 317-322, 1992.

[19] T. Ueda, M. Sato, T. Sugita, and K. Nakayama, "Thermal Behaviour of Cutting Grain in Grinding," *CIRP Annals - Manufacturing Technology*, vol. 44, pp. 325-328, 1995.

[20] T. Ueda, M. Sato, A. Hosokawa, and M. Ozawa, "Development of infrared radiation pyrometer with optical fibers - Two-color pyrometer with non-contact fiber coupler," *CIRP Annals - Manufacturing Technology*, vol. 57, pp. 69-72, 2008.

[21] T. Ueda, A. Hosokawa, and A. Yamamoto, "Studies on Temperature of Abrasive Grains in Grinding—Application of Infrared Radiation Pyrometer," *Journal of Manufacturing Science and Engineering*, vol. 107, pp. 127-133, 1985.

[22] J. Thevenet, M. Siroux, and B. Desmet, "Measurements of brake disc surface temperature and emissivity by two-color pyrometry," *Applied Thermal Engineering*, vol. 30, pp. 753-759, 2010.

[23] E. Milcent, G. Olalde, J. F. Robert, D. Hernandez, and M. Clement, "Influence of high temperatures on a fiber-optic probe for temperature measurement," *Applied Optics*, vol. 33, pp. 5882-5887, 1994.

[24] T. Beno and U. Hulling, "Measurement of Cutting Edge Temperature in Drilling," *Procedia CIRP*, vol. 3, pp. 531-536, 2012.

[25] F. J. Madruga, D. A. G. Fernandez, and J. M. Lopez-Higuera, "Error estimation in a fiber-optic dual waveband ratio pyrometer," *IEEE Sensors Journal*, vol. 4, pp. 288-293, 2004.

[26] F. J. Madruga, D. Gonzalez, V. Alvarez, J. Echevarria, O. M. Conde, and J. M. Lopez-Higuera, "Field test of noncontact high temperature fiber optic transducer in a steel production plant," in *15th International Conference on Optical Fiber Sensors*, Portland (United States of America), 2002, pp. 483-486.

[27] M. Sato, T. Ueda, and H. Tanaka, "An experimental technique for the measurement of temperature on CBN tool face in end milling," *International Journal of Machine Tools and Manufacture*, vol. 47, pp. 2071-2076, 2007.

[28] E. C. Pyatt, "Some consideration of the errors of brightness and two-colour types of spectral radiation pyrometer," *British Journal of Applied Physics*, vol. 5, p. 264, 1954.

[29] Y. Wang, M. Yao, and Y. Liao, "Selection of optimal working wavelengths and bandwidths for dual-wavelength optical fiber pyrometer," in *Self-Calibrated Intelligent Optical Sensors and Systems*, Philadelphia (United States of America), 1995, pp. 75-80.

[30] G. R. Gathers, "Error analysis of a ratio pyrometer by numerical simulation," *International Journal of Thermophysics*, vol. 13, pp. 173-185, 1992.

[31] R. G. Driggers, Encyclopedia of optical engineering vol. 2: CRC press, 2003.

[32] M. F. Modest, Radiative heat transfer, 2nd ed.: Academic Press, 2003.

[33] D. P. DeWitt and G. D. Nutter, Theory and practice of radiation thermometry. New York: Wiley, 1988.

[34] Y. A. Çengel and A. J. Ghajar, Heat and mass transfer: fundamentals & applications: McGraw-Hill, 2011.

[35] G. A. Greene, C. C. Finfrock, and T. F. Irvine Jr, "Total hemispherical emissivity of oxidized Inconel 718 in the temperature range 300-1000°C," *Experimental Thermal and Fluid Science*, vol. 22, pp. 145-153, 2000.

[36] D. P. Verret and K. G. Ramanathan, "Total hemispherical emissivity of tungsten," *Journal of the Optical Society of America*, vol. 68, pp. 1167-1172, 1978.

[37] M. A. Khan, C. Allemand, and T. W. Eagar, "Noncontact temperature measurement. II. Least squares based techniques," *Review of Scientific Instruments*, vol. 62, pp. 403-409, 1991.

[38] F. M. White, Heat transfer: Addison-Wesley Longman, 1984.

[39] Y. S. Touloukian and D. P. DeWitt, Thermal radiative properties: metallic elements and alloys: IFI/Plenum, 1970.

Chapter 5

Chapter 5

Two-colour Pyrometer for in Process Temperature Measurement during Machining

Reducing structural weight is one of the major ways to improve aircraft performance. The superalloys are usually employed in the manufacture of components for aerospace industry due to high strength at elevated temperatures and wear resistance. Energy consumed by these superalloys in a machining operation is largely converted into heat. The control of the temperature during the machining process allows to have more efficient cutting processes. In order to measure the higher temperature of the machining process, the use of the capabilities of the two-colour fiber-optic pyrometer is feasible. The designed pyrometer permits to measure temperature in a range from 300 to 650ºC, with a full-scale temperature error of 4.4%. Pyrometer temperature errors are analysed using numerical simulations in order to improve the minimum detectable temperature while reducing the temperature errors. A study of different influence factors on the temperature measurements is performed to identify the sensor limitations, such as a possible damage on the fiber termination or the distance between the fiber end and the target. Finally, a test on metallic surface has been performed to verify the correct operation of the sensor in a real situation.

5.1. Introduction

There is a strong trend in the aero engine industry towards reducing weight of the engine components and fuselage structure [1, 2] in order to reduce both emission and fuel consumption. On the other hand, the aerospace industry demands of hotter and more powerful engines led to development of new materials. The ability to retain high mechanical and chemical properties at elevated temperature of superalloys make them ideal materials for use in both rotating and stationary components in the hot end of jet engines. Components produced with superalloys are

smaller and lighter than those made of conventional steel with the consequent fuel saving and reduction in pollution. Each kilogram weight reduction typically results in a US$ 150,000 saving in fuel cost over the life of the engine [3].

Nickel-based alloys constitute over 45-50% of the total material required in the manufacture of an aircraft engine [4]. They exhibit unique properties like high strength at elevated temperatures, resistance to chemical degradation and wear resistance. Ability to maintain these properties at elevated temperature severely hinder the machinability of these alloys. These alloys can be economically machined at higher speed conditions. Energy consumed in a machining process is largely converted into heat, reaching temperatures greater than 500ºC [5]. Most problems encountered during machining are due to heat generation, mainly during deformation process and friction at the tool-workpiece interface, and the consequent high temperature associated with it. It is due to the low thermal conductivity of nickel-based allows in comparison to conventional steels or iron, increasing the temperature between the cutting tool and the workpiece [6].

Temperature plays an important role in machined induced damage at the machined surface, commonly surface roughness, imperfections and residual stresses in the finished component [7]. Temperature also increases tool wear rates reducing tool life. Tool wear is one of the limiting factors for productivity in manufacturing. It is due to increase the forces and tensile residual stresses, affect surface finish and cause white layer surface damages [8]. Temperature measurement in exactly defined locations is a key challenge in order to ensure surface integrity and tool wear control.

Reported measurement methods of cutting temperature in some machining processes include thermocouples [9, 10], and infrared (IR) cameras [11, 12], among others [7]. The use of thermocouples and IR cameras have several problems [13], but the difficulty of installation between the cutting tool and the workpiece make them unsuitable for local measurement. As an alternative to thermocouples and IR cameras, two-colour fiber-optic pyrometers have been developed to monitor temperature in harsh environment [14-16].

Two-colour fiber-optic pyrometer is a non-intrusive technique with very fast response, making it a very useful instrumentation in temperature measurements because the high cutting speeds used in Ni-alloys machining made the response a very important parameters. On the other hand, the disadvantage of this method is the temperature error dependence with the spectral response of the entire system. This problem requires preliminary studies on the set-up characteristics in order to measure absolute temperatures with low temperature errors.

The aim of the present work is to develop the concept of two-colour pyrometer for measuring temperature in machining process. The objective is the in-process temperature measurement during turning of Inconel 718, one of the most used Ni-alloys in critical aero engine components. Many of the reported two-colour pyrometers operate at wavelengths outside from the telecommunication wavelength range implying the use of expensive and more complex optoelectronics devices. This work pretends to develop a low-cost two-colour fiber-optic pyrometer integrated in machining process with low temperature errors using fiber-optic components compatible with commercial off-the-shelf optoelectronics well established on Wavelength Division Multiplexing (WDM) based optical communication networks. To achieve the temperature error reduction, an analysis of the characteristics of the electro-optical devices at the selected pair of wavelengths is carried out. This analysis pretends to reduce the wavelength dependence losses that affects to the temperature error. The resulted two-colour pyrometer is applied to measure the temperature in machining process. The optical fiber is embedded in the tool holder and the temperature history of the interface between the cutting tool and workpiece is measured. Due to the reduced number of published data describing the temperature of superalloys in machining process, the measurements are compared with an accurate numerical model based on finite element method. Finally, the influence of the distance and the fiber end termination are carried out in order to perform a complete study of the potential system errors.

5.2. Pyrometer Design and Calibration Set-up

Figure 5.1 shows the set-up schematic to measure the work piece temperature. The sensor is made of standard graded index glass fiber OM1 with 62.5/125 core and cladding diameters in microns [17], the buffer coating is partially removed at the sensing end to withstand higher temperatures. The fiber length is 0.5m. A low insertion loss WDM fiber-optic filter is arranged to split the radiation collected by the optical fiber into two spectral components, that is a first component having a wavelength around 1.3μm and a second component having a wavelength around 1.55μm. An optical power meter with a dual InGaAs photodetector with an almost constant responsivity at both wavelength ranges delimited by the filter is used.

The two-colour pyrometer is calibrated using a dry block calibrator and a blackbody kit [18], as shown in Figure 5.2.(a). The dry block provides an isothermal enclosure in which thermometers and thermostats can be checked against the temperature indicated on the temperature controller. The control unit ensures a maximum temperature stability and uncertainty of ±0.03 and ±0.17ºC, respectively, for a temperature range from 50 to 650ºC. The emissivity of the blackbody is greater than 0.99.

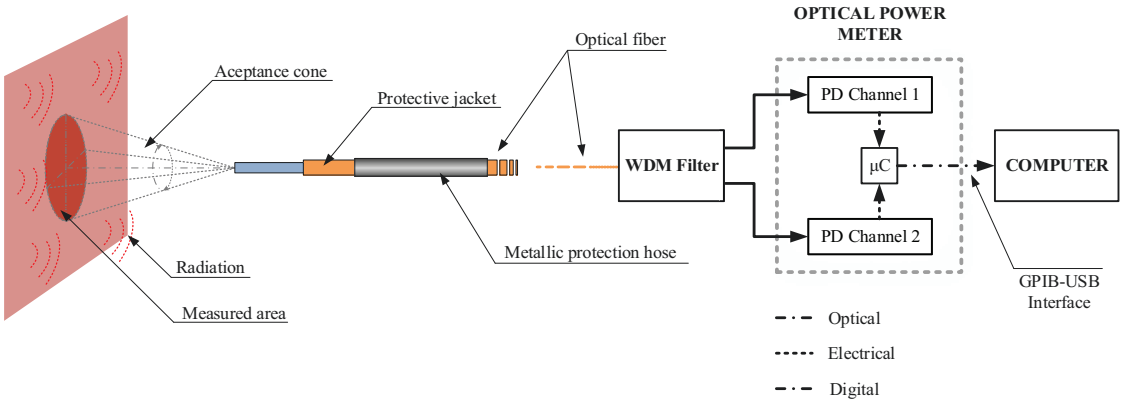

Figure 5.1. Schematic of the experimental set-up for the measurement of the work piece temperature.

The calibrated metallic holder used in this chapter is fabricated by Eng. Ernesto García Ares, at the Technical Department of Carlos III University of Madrid[3].

The fiber sensor is fixed at a distance of 0.3mm from the blackbody using a calibrated metallic holder as shown in Figure 5.2.(b). In order to facilitate the fiber set-up and to avoid the fiber breakage during the positioning of the fiber in the metallic holder, a high temperature protection hose is used to give more rigidity to the fiber end. The protection hose is manufactured using three steel needles with different diameters which are introduced one needle into another. The result is a protection hose with an external and internal diameter of ~1 and 0.14mm, respectively

(a) **(b)**

Figure 5.2. (a) Photograph of the dry block calibrator and the blackbody on top of it. (b) Photograph of the metallic holder used to positioning the fiber at a distance of 3mm to the blackbody surface.

[3] Technical Department. Carlos III University of Madrid. Leganés. Spain.

Software based on graphical code is developed to acquire the optical power at the two selected wavelength ranges and to post-process the statistical data of the calibration curves.

5.3. Experimental Results

5.3.1. Error Analysis

The use of a two-colour pyrometer has the advantage of measuring the absolute temperature without knowledge of the surface emissivity meanwhile the emissivities at both wavelengths are equal. The spectral response of the electro-optical devices must be accounted for in calculating the temperature errors, as derived from Equation 4.22 to 4.26. For this reason, to quantify the temperature error of the proposed sensor, the loss ratio between both filtering channels is analysed for all devices used in the pyrometer set-up. This analysis takes into account the coupling light loss, fiber attenuation, filter insertion losses and photodetector responsivity.

The coupling light loss refers to the power loss that occurs when the radiation emitted by the surface is transferred to the optical fiber. The coupling light loss depends on many factors but the major contribution comes from the relative position between the optical fiber and the hot surface. This case is not considered in this analysis because both wavelengths are attenuated in the same way. As shown in Equation 4.15, the coupling light loss is also dependent on the core diameter and the numerical aperture (NA).

An optical fiber only propagates light that enters the fiber within a certain cone, known as the acceptance cone of the fiber. The half-angle of this cone is called the acceptance angle (θ_{max}). The relation between the acceptance angle, the NA and the refractive index of the core and cladding is given by:

$$\sin\left(\theta_{max}\right) = NA\left(\lambda\right) = \sqrt{n_{Core}^2 - n_{Cladding}^2} \qquad 5.1$$

where n_{Core} and $n_{Cladding}$ are the core and cladding fiber optic refractive index. The optical fiber pyrometer proposed in this work is based on a glass optical fiber. The coupling light losses depends on the NA change with the core and cladding refractive index variations. Those refractive indexes depend on the wavelength. The refractive index of the core and cladding can be fit to a three-term Sellmeier dispersion relation of the form [19] and are shown in Table 5.1.

$$n\left(\lambda\right) = \left[1 + \sum_{i=1}^{3} \frac{A_i \cdot \lambda^2}{\lambda^2 - l_i^2}\right]^{1/2} \qquad 5.2$$

where n is the refractive index of the core and cladding, A_i is the oscillator strength, l_i is the oscillator wavelength, and λ is the wavelength of light. The Sellmeier equation coefficients for a graded-index glass-based multimode optical fiber with a SiO_2 core doped with 6.3mol-% GeO_2 and a SiO_2 cladding are reported in [20].

Coefficient	Units	SiO_2 core doped with 6.3mol-% GeO_2	SiO_2
A_1	a.u.	0.7083952	0.6965325
l_1	μm^2	0.0853842	0.0660932
A_2	a.u.	0.4203993	0.4083099
l_2	μm^2	0.1024838	0.11811007
A_3	a.u.	0.8663412	0.8968766
l_3	μm^2	9.896175	9.8961604

Table 5.1. Coefficients of the Sellmeier equation for a multimode glass optical fiber.

The coupling light coefficient is defined as the ratio between the coupling light loss at both wavelengths. From Equation 4.15, 5.1 and 5.2, and using the Sellmeier coefficients of the core and cladding, the coupling light coefficient for a filtering channel of 1.3 and 1.55μm is $2.41 \cdot 10^{-4}$ $\Omega \cdot m^2$ and $2.416 \cdot 10^{-10}$ $\Omega \cdot m^2$, respectively. Using these values, the coupling loss ratio between both channels is 0.014dB.

The second factor to be analysed is the attenuation of the fiber. The propagation of light through the core of an optical fiber is based on total internal reflection of the light rays. Different factors cause light attenuation such as absorption, scattering, bending losses, among others. The attenuation induced by these mechanisms changes with wavelength. Thus, the attenuation of light can be quantified as a function of wavelength (λ) using the Lambert's law:

$$\frac{P_{Out}}{P_{In}} = \cdot e^{-\alpha(\lambda)\cdot L} \qquad (5.3)$$

where α is the attenuation coefficient (involving all attenuation mechanisms), L is the fiber length, P_{In} is the input light power and P_{Out} is the output light power. This equation is not valid for attenuation predictions in the OH- Absorption peak. Anyhow, the selected wavelengths are selected to avoid the higher attenuation in this spectral region.

The attenuation coefficient for the OM1 Corning optical fiber with 62.5/125μm core and cladding diameters manufactured by Corning and used in the pyrometer developed in this work is shown in Figure 5.3.

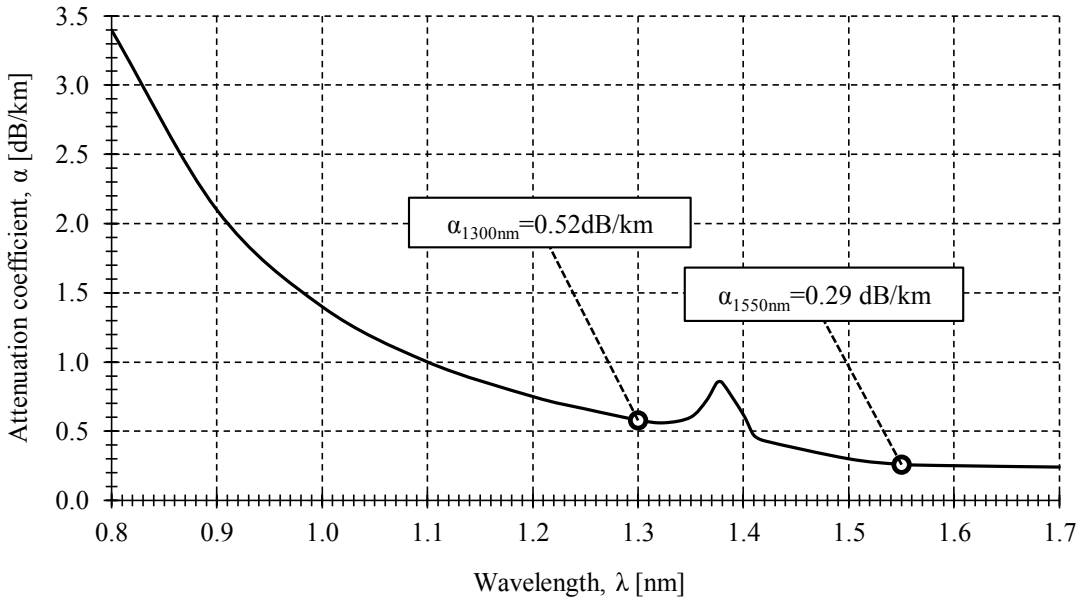

Figure 5.3. Attenuation coefficient for a Corning manufactured optical fiber [21].

Figure 5.3 shows that transmitted power decreases exponentially with propagation distance through the optical fiber. The attenuation coefficient at 1.3 and 1.55μm is 0.52 and 0.29dB/km [21]. Using Equation (5.3) and the attenuation coefficients shown in Figure 5.3, the fiber attenuation for a probe length of 0.5m is $2.9 \cdot 10^{-4}$ and $1.38 \cdot 10^{-4}$dB, respectively. These values represent a power difference between filtering channels of $1.53 \cdot 10^{-4}$dB. This result shows that the effect of the fiber attenuation is practically negligible for short lengths. This effect could be considered if the fiber probe has a length of hundreds of meters.

The filter insertion losses at each filtering channel is another factor to be considered in this analysis. A filter with low and constant insertion losses along the measuring wavelengths is necessary in order to reduce temperature errors. The majority of the filters have an irregular response along wavelength. A high difference between insertion losses at each filtering channel increases the temperature error. The insertion loss is determined by the ratio of the input power, P_{In}, to the output power, P_{Out}, from one branch of the coupler, k. It can be generally written as:

$$L_k = 10 * \log\left(\frac{P_{In}}{P_{Out,k}}\right) \qquad (5.4)$$

Figure 5.4 shows the output spectrum of the WDM filter at each filtering channel. This figure also represents the output spectrum of the broadband light source used to characterize the WDM filter. From this figure, the filter insertion loss at a wavelength of 1.3 and 1.55μm is 0.21 and 0.06dB, respectively. The power different between both filtering channels is 0.14dB. So the filter insertion loss is an important parameter in order to obtain a compensated system insertion losses.

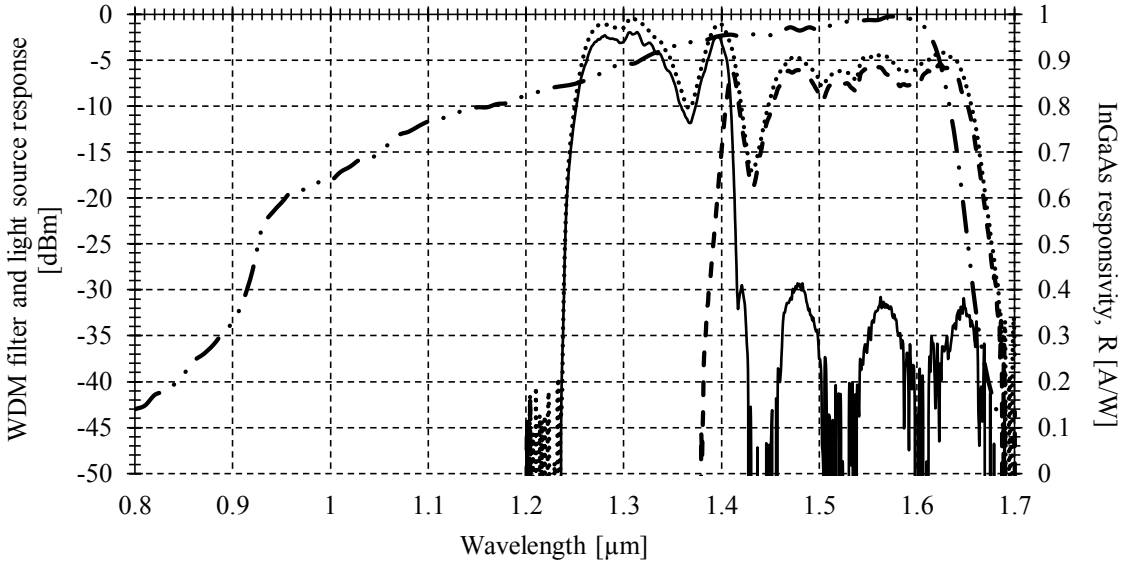

Figure 5.4. (Left axis) WDM filter spectrum: — 1.3μm, – – 1.55μm, · · Input light source, —··— InGaAs responsivity. (Right axis) InGaAs responsivity curve.

The light power emitted by the surface and collected by the optical fiber is separated in two wavelength ranges by the WDM filter. Each wavelength ranges are measured by two identical photodetectors. The factor that quantifies the conversion between the optical and electrical domain is the responsivity. As occur with other devices, the photodetector responsivity changes with wavelength. Figure 5.4 shows the InGaAs photodetector responsivity versus wavelength. It is clear that the maximum responsivity is reached around 1.5μm and its value is close to 1A/W. Depending on the measured wavelength, there is a different responsivity to convert the input light power to an electrical signal. From Figure 5.4, the photodetector responsivity is 0.89 and 0.98A/W for a wavelength of 1.3 and 1.55μm, respectively. These results show that to measure the same photocurrent at both wavelengths, a light power difference of 0.22dB should be desirable to have between 1.3 and 1.55μm filtering channels.

From the previous analysis of the power difference between each filtering channel in all devices used in the pyrometer set-up, it is clear that the photodetector responsivity and the filter insertion loss are the main factors in the pyrometer temperature error. Temperature errors caused

by the wavelength dependence loss at each device are quantified using Equation 4.22 to 4.26. The temperature error is calculated as a function of the emissivity ratio and operating at 500ºC. Fiber attenuation and filter insertion losses are previously converted to a linear scale to calculate the wavelength dependence loss ratio (δ_r) in Equation 4.22.

Temperature errors caused by the wavelength dependence losses of the pyrometer are plotted together in Figure 5.5. Those errors are obtained adding simultaneously the different effects: coupling light, fiber attenuation, filter insertion loss and photodetector responsivity.

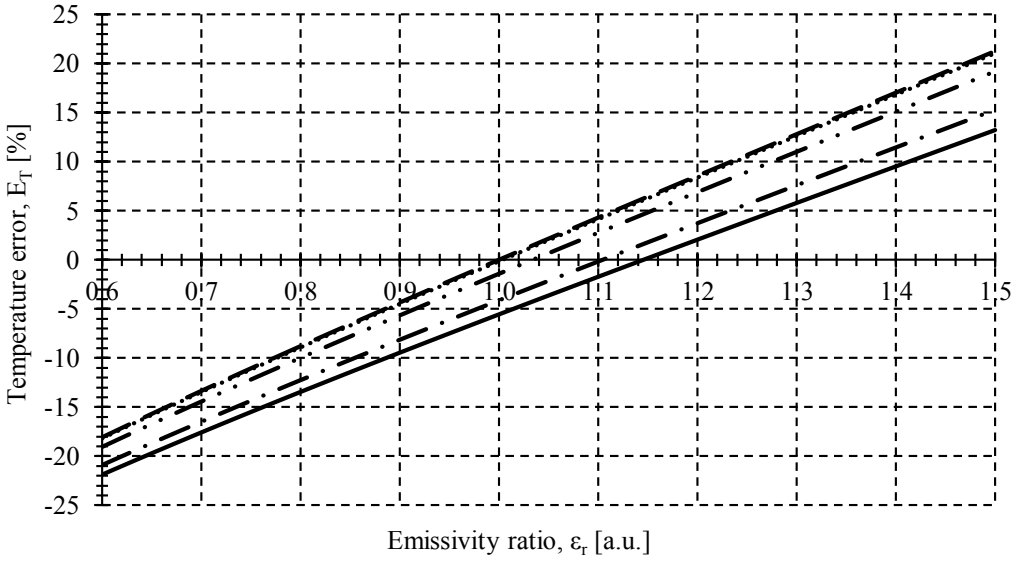

(a)

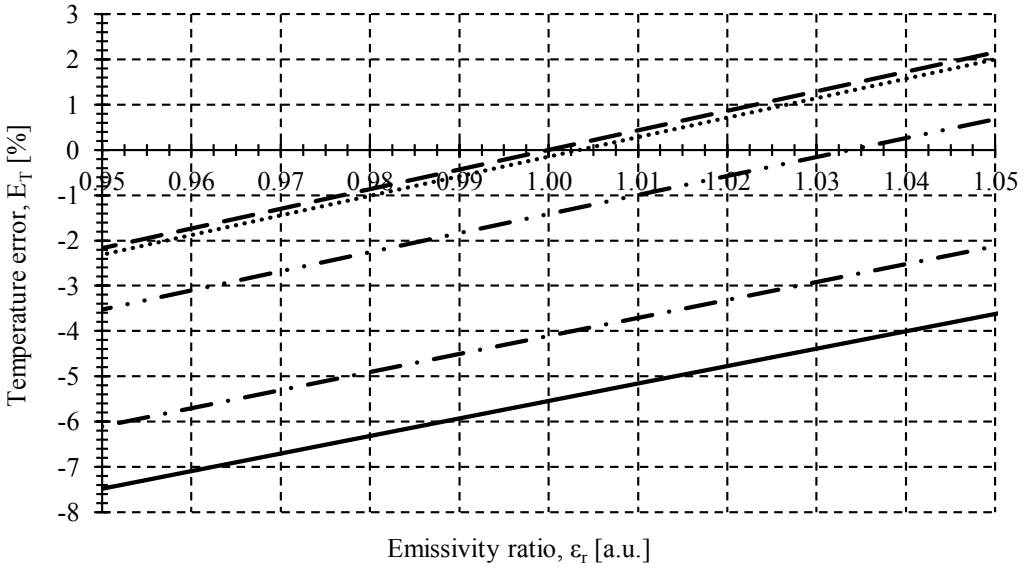

(b)

Figure 5.5. (a) Enlarge scale and (b) Reduced scale for the temperature error versus emissivity ratio at a temperature of 500ºC considering different wavelength dependence losses: − · · − WDM filter insertion loss, · · Coupling light loss, − · − Photodetector responsivity, − − Fiber attenuation, — Pyrometer setup.

Analysing the temperature error for each curve, it can be seen that the responsivity difference between both wavelengths induces a high percentage of the overall temperature error. The temperature error associated with the photodetector responsivity is 4.1% at 500ºC for an emissivity ratio equal to 1. On the other hand, the filtering quality is also a key element in order to reduce the temperature error. In this case, the low-loss WDM filter used in the calibration setup can reduce the temperature error up to 1.4%. The contribution of the coupling light loss and the fiber attenuation in the temperature error is also shown in Figure 5.5. The temperature error attributed to these factors is practically negligible as commented in the power analysis. Finally, computing all wavelength dependence loss factors, the pyrometer temperature error is 5.5% at 500ºC for an emissivity ratio equal to 1. In general terms, different photodetector responsivities at both wavelength ranges can be equalized by the filter insertion losses.

5.3.2. Calibration Curves

Calibration curves at each wavelength range are shown in Figure 5.6. Radiant flux emitted by the blackbody is measured at 1.3 and 1.55μm wavelength range, meanwhile the temperature of the micropyramidal surface changes from 300 to 650ºC at 10ºC intervals. The calibration curve is measured considering the warming up and cooling down process. The maximum temperature was limited by the capabilities of the dry block calibrator. The photodetector noise at the shorter wavelength range delimits the minimum temperature that the system can measure. A time interval of 45min has been set, between each temperature measurement, to ensure the stabilization of the optical power values. The sample rate and the number of samples at each temperature have been fixed at 1kHz and 10 samples, respectively.

The ratio between the measure light power at 1.3 and 1.55μm for each temperature is calculated from the mean of the samples during the process cycle. The results are shown in Figure 5.6. The advantage of using the output power ratio is that the reading temperature is not affected by any signal attenuation caused for example by the emissivity variations, the distance between the fiber and the surface, dirt, among others, if the signals of both channels are equally attenuated. The output power ratio is fitted with a lineal regression. The sensitivity obtained is $6.98 \cdot 10^{-4}$ ºC^{-1}. A statistical analysis of the calibration curve shows a non-linearity full-scale temperature error and lineal regression coefficient of 2.5% and 99%, respectively. The full-scale temperature error is 4.4%. The output power ratio accuracy is calculated using the standard deviation of the 20 samples for the warming and cooling calibration curve at each temperature. The result is a full-scale output power ratio accuracy of 1.8%. Hysteresis is not appreciated in the experimental calibration curves in a temperature range from 300 to 650ºC. Comparing the full-scale

temperature error with the value calculated from the theoretical analysis reported in the previous section, it can be shown that the experimental and theoretical errors are in good agreement.

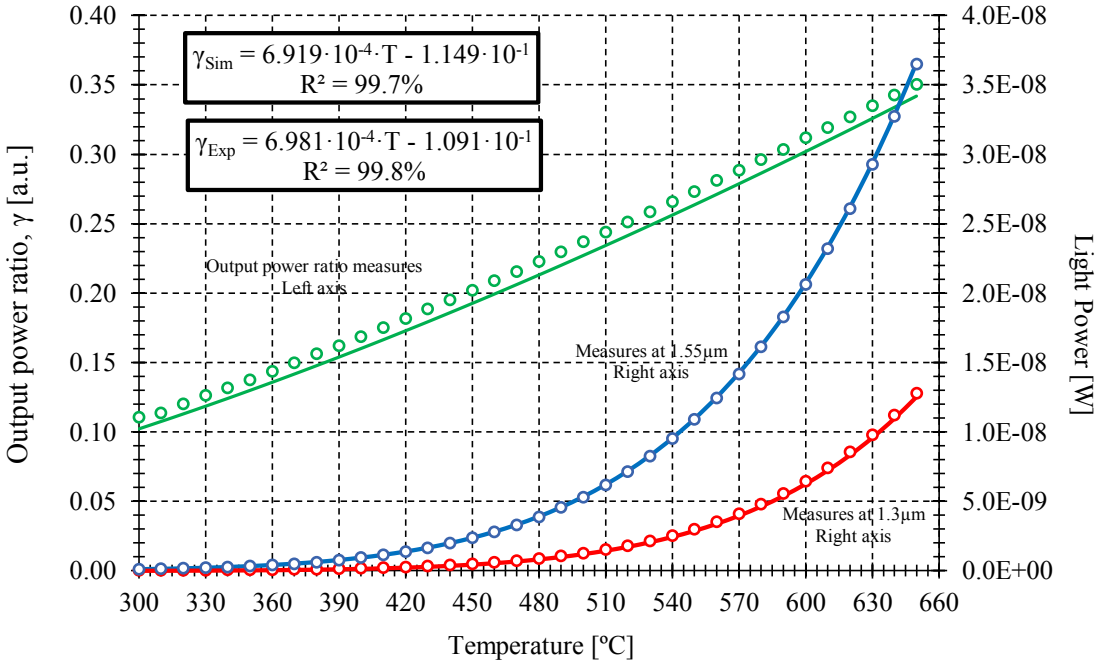

Figure 5.6. Theoretical (—) and experimental (○) calibration curves for: (Red) 1.3µm, (Blue) 1.55µm, (Green) 1.3/1.55µm.

Using Equation 4.17, the light power measured by each photodetector is simulated from 300 to 650ºC at 10ºC intervals. The blackbody target has a diameter of ~3.5cm. On the other hand, the spot area projected on the blackbody surface has a diameter of ~160µm. The difference between both diameters induces to assume that the blackbody surface is infinitely bigger than the fiber spot. Using this assumption, the light power is not dependent on the distance between the fiber end and the measured surface as demonstrated in Equation 4.15. For the first filtering channel, the longest and shortest wavelength limits are 1.43 and 0.8µm, respectively. On the other hand, the second filtering channel contains signals from 1.38 to 1.7 µm. The longest and shortest limits for the first and second filtering channel, respectively, are limited by the wavelength range of the InGaAs responsivity curve (see Figure 5.4). The emissivity of a blackbody is used in the simulation. A filter insertion loss of 0.21 and 0.06dB are considered at 1.3 and 1.55µm, respectively.

The measured output light power is strongly conditioned by the optical fiber core diameter. The optical fiber is made of glass and manufactured using a drawing tower that fixes the core and cladding diameter. The smaller diameter of the fiber the more difficult the drawing process, fixing a tolerance in the nominal core diameter of ±3µm [21]. For this reason, the simulation of the

output light power at each filtering channel is carried out by varying the nominal core diameter between the upper and lower limit, see Figure 5.7.

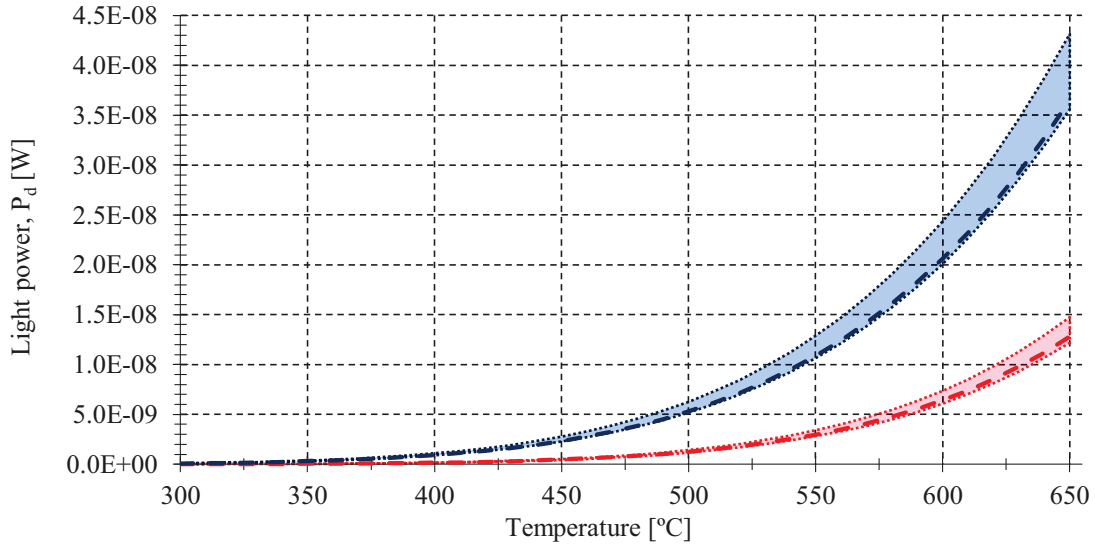

Figure 5.7. Output power variation versus temperature for the theoretical (filled areas) and experimental (dashed lines) calibration curves at different filtering channels: --- 1.3µm, --- 1.55µm.

It is clear that the experimental calibration curves are within the diameter tolerance given by the manufacturer. The diameter that provides a good agreement between the theoretical and experimental curves is 62.5-1.1µm, as shown in Figure 5.6 where this diameter has been considered in the simulations.

The output power ratio between the theoretical light power at each filtering channel is also represented in Figure 5.6. The slope of the linear regression shows that the output power ratio increases with temperature as occurs with the experimental measures. The theoretical sensitivity and the linear regression coefficient are $6.935 \cdot 10^{-4}$ ºC^{-1} and 99%, respectively. These values confirm that the experimental calibration curve is in good agreement with the theoretical curve.

5.3.3. Influence of Distance from Fiber-optic to Cutting Surface.

An important problem using optical fiber in machining processes is the accurate position of the optical fiber below the major cutting edge. Commercial systems usually position the fiber some distance away and use lenses to achieve good light collection. The distance from cutting surface is within few hundred microns in a very difficult to access area in the machine under operating conditions avoiding the potential to use dedicated optics to improve light collimation, see Figure 5.8.

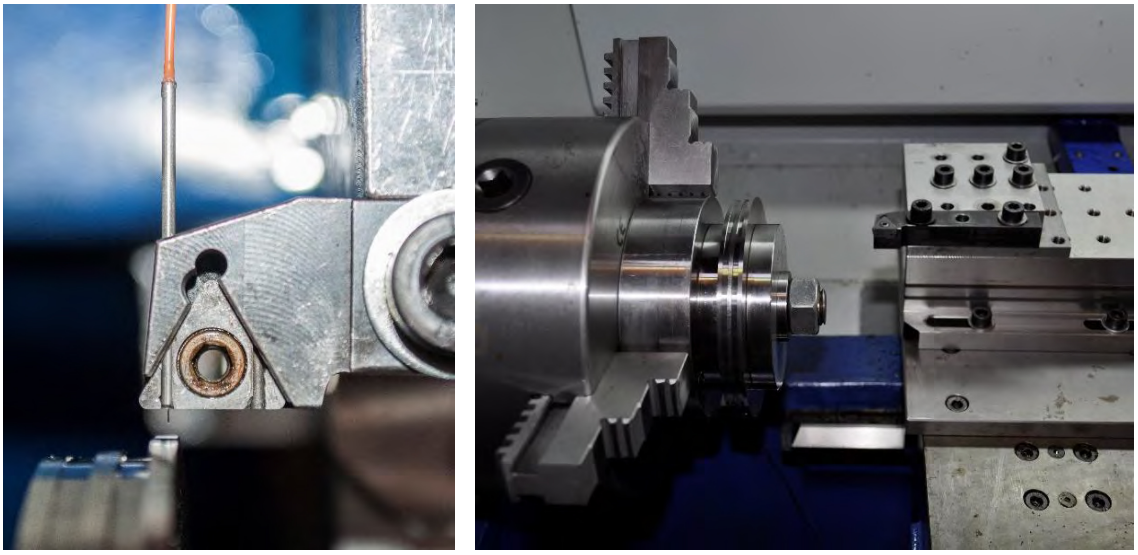

(a) **(b)**

Figure 5.8. (a) Visualization of the distance between the optical fiber and the workpiece (tool insert is removed). (b) Photograph of the lathe with the machining tool.

The system achieves good spatial resolution, while avoiding the use of lenses, by situating the fiber very close to the target (the fresh machined surface) and below the tool insert. The fiber can be adjusted to the desired measurement position and fixed in a notch of the shim with a nut. Since the fiber is located below the tool insert, the maximum distance between fiber and machined surface is 2mm.

A set of measures are carried out to evaluate the effect of the distance between the fiber end and the target during the machining process, as shown in Figure 5.9. The measurements are done using the same set-up as the one used for measuring the calibration curves. Radiance emitted by the blackbody is measured at a wavelength of 1.3 and 1.55µm. The temperature of the blackbody is fixed at 650ºC to ensure sufficient light power to avoid the photodetector noise at low temperatures. Using calibrated washers, the distance between the black body and the fiber end is changed from 0.2 to 2mm at different intervals. A total of ten set of measurements for each distance have been carried out to perform a statistical analysis.

The experimental results are compared with simulations to validate the coherence of the measurements, see Figure 5.9. Using Equations 4.16 and 4.17, the light power measured by each photodetector is calculated from a distance of 0 to 2mm at 0.5mm intervals. The temperature is fixed at 650ºC. The pyrometer design parameters are considered equal than those used to simulate the pyrometer calibration curves.

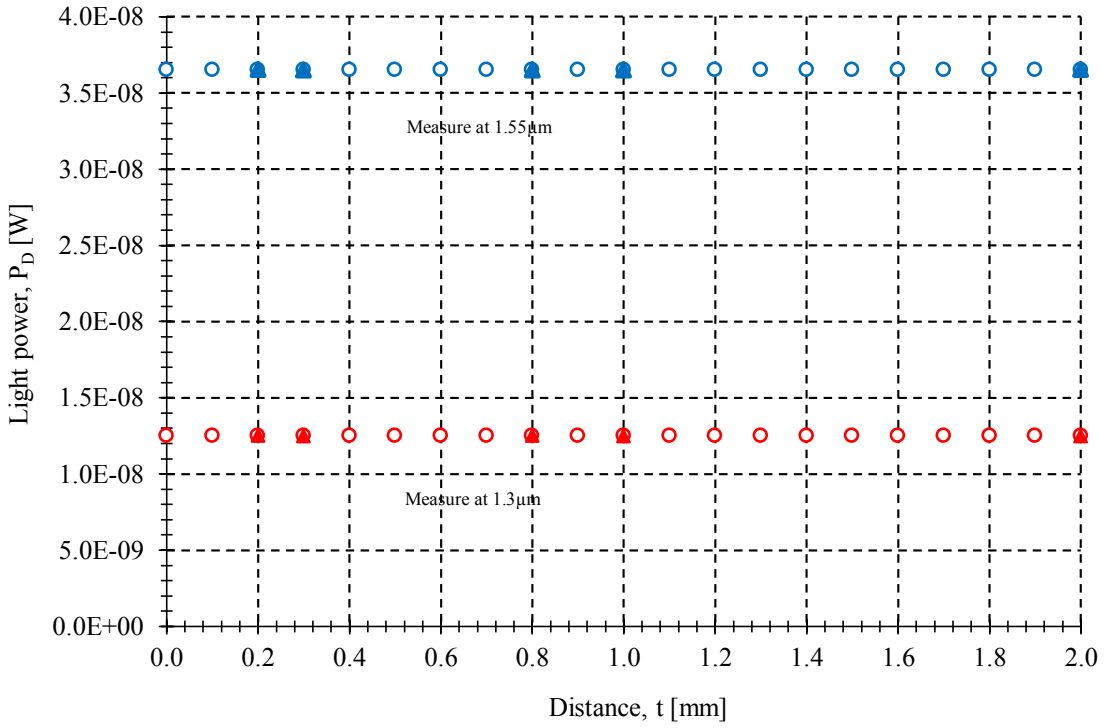

Figure 5.9. Light power measured by the photodetector versus distance for a wavelength of (red) 1.3µm and (blue) 1.55µm: ○ Simulation, ▲ Measures.

Figure 5.9 shows a deviation between the theoretical and experimental curves of 9.5 and 7.5pW for a filtering channel of 1.3 and 1.55µm, respectively. Thus, considering a sensor power accuracy of 1.1 and 3.4pW, respectively, the power deviations are within photodetector power accuracy. The measured power accuracy is within the specification given by the manufacturer [22]. These results demonstrate that the experimental and theoretical values are in good agreement.

5.3.4. Influence of Fiber-optic Non-perfect End

Other potential problem using optical fibers in industrial machining environment, not previously considered in the literature, is the possible damage of the sensing fiber termination. Measuring conditions are very hard in terms of accessibility and dirt. During the machining process, from the interface between the cutting tool and the work piece, metal chips tend to detach, see Figure 5.10. These metal chips can sometimes cause serious damage to the surface of the fiber termination which can affect the power collected by the optical fiber increasing the sensor temperature error.

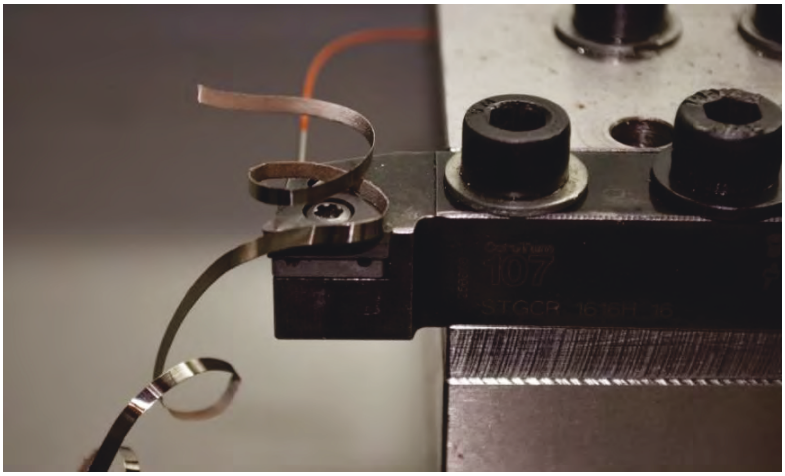

Figure 5.10. Detached metal chirp during the machining process.

An example of a no-damage and damage sensing optical fiber end can be seen on Figure 5.11.(a) and (b), respectively.

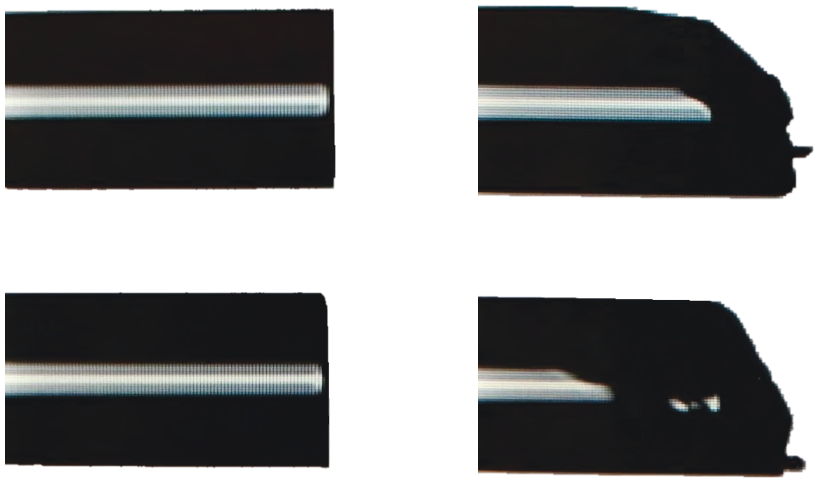

(a) **(b)**

Figure 5.11. Top and side views of the longitudinal profile of the glass optical fiber. (b) No damage (b) Damage.

To evaluate the effect on the measurements of the optical fiber termination, a total of twenty-five set of measures of output power ratio have been carried out. The temperature of the dry block calibrator is fixed at 650ºC. The distance between the blackbody and the fiber is fixed at 0.3mm. No changes in the measured light power are appreciated. It is due to the damage on an optical fiber can be approximated by a small distance increment between the fiber end and the surface. For a hot surface infinitively larger than the area covered by the fiber NA, the light power measured by the photodetector is not dependent on the distance, see Equation 4.17. These results prove the capability of the damage fiber end to still be able to measure the temperature in those conditions.

5.3.5. Temperature Measurements in Metal Cutting

The system developed is applied to the measurement of temperature during orthogonal turning of Nickel (Ni) alloy. Ni alloys are low machinability materials exhibiting elevated mechanical properties maintained up to high temperatures combined with low thermal conductivity. The control of temperature during cutting of Ni alloys is crucial to avoid surface damage in terms of residual stresses or hardened layer [23, 24]. On the other hand, temperature provides relevant information since this parameter governs phenomena influencing chip morphology and wear patterns in metal cutting [25, 26].

The temperature measurements of the two-colour fiber-optic pyrometer in the machining processes are done in collaboration with the Manufacturing Department and Mechanics and Biomechanics Components Group[4] of the Mechanical Engineering Department at Carlos III University of Madrid leaded by Prof. Dr. María Henar Miguélez Garrido.

Orthogonal cutting tests are developed in a Pinacho Smart turn 6/125 lathe and cutting forces are measured with a Kistler 9257B dynamometer to estimate of the machining behaviour, see Figure 5.12.(a). The workpiece is Inconel Alloy 718 annealed at 968ºC held for 50min [27], water cooled, shaped as a disc with diameter (D) of 120mm and thickness (e) of 2mm. Several rings were previously machined in the disc in order to allow performing orthogonal cutting, as shown in Figure 5.12.(b).

(a) **(b)**

Figure 5.12. (a) Photograph of the machining tool and the dynamometer. (b) Photograph of the Inconel Alloy workpiece.

[4] Manufacturing Department and Mechanics and Biomechanics Components Group. Mechanical Engineering Department. Carlos III University of Madrid. Leganés. Spain

The cutting tool holder is modified with the aim of attaching the optical fiber located inside the capillary tube. Tool insert is provided with one or several small holes which are formed through the rear surface of insert and terminate in close proximity to the lead surface, see Figure 5.13.

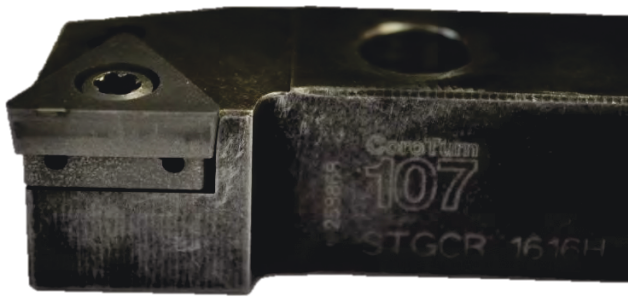

Figure 5.13. Photograph of the machine tool configuration.

Schematic of the cutting operation is illustrated in Figure 5.14 wherein a chip is being removed from a work piece by a cutting edge of the tool insert due to relative motion between the cutting edge and the work piece. As it is well known, removal of material from a work piece occurs due to shearing action as the material deforms by shear along a narrow zone extending from the cutting edge called the primary shear zone. The material lying ahead of the tool as it reaches the shear plane is displaced by shear to form the chip which then slides along the face of the tool and away from the cutting area. Main sources of heat generation in the process are the plastic deformation of the material at the primary shear zone and frictional heat along the tool-chip interface, called the secondary zone. Friction also results in heat generation at the tertiary zone, because of the contact between the tool inset and the fresh machined surface.

The amount of heat generated depends on cutting speed and feed rate, generally increasing with both parameters. During the process, heat is continually removed from the cutting zone, part with the chip and part is transmitted to the tool. The tool-workpiece interface temperature is not uniform along the surface. The hole for fiber location was drilled on the clearance surface, in a region close to the cutting zone: the temperature is measured at the fresh machined surface. The distance between the cutting edge and the fiber end is 4mm. The hole has a diameter of ~1.3mm and can be extended in order to give the possibility to introduce a fiber bundle to collect more radiation. The distance between the cutting edge and the hole is limited by the capability of the drilling process to machine small diameter holes in hard materials such as carbide inserts. With a conventional electrical discharge machining processes this distance can be reduced to few millimetres. The hole for fiber location guaranteed a distance between the fiber and the target (t) of 0.3mm.

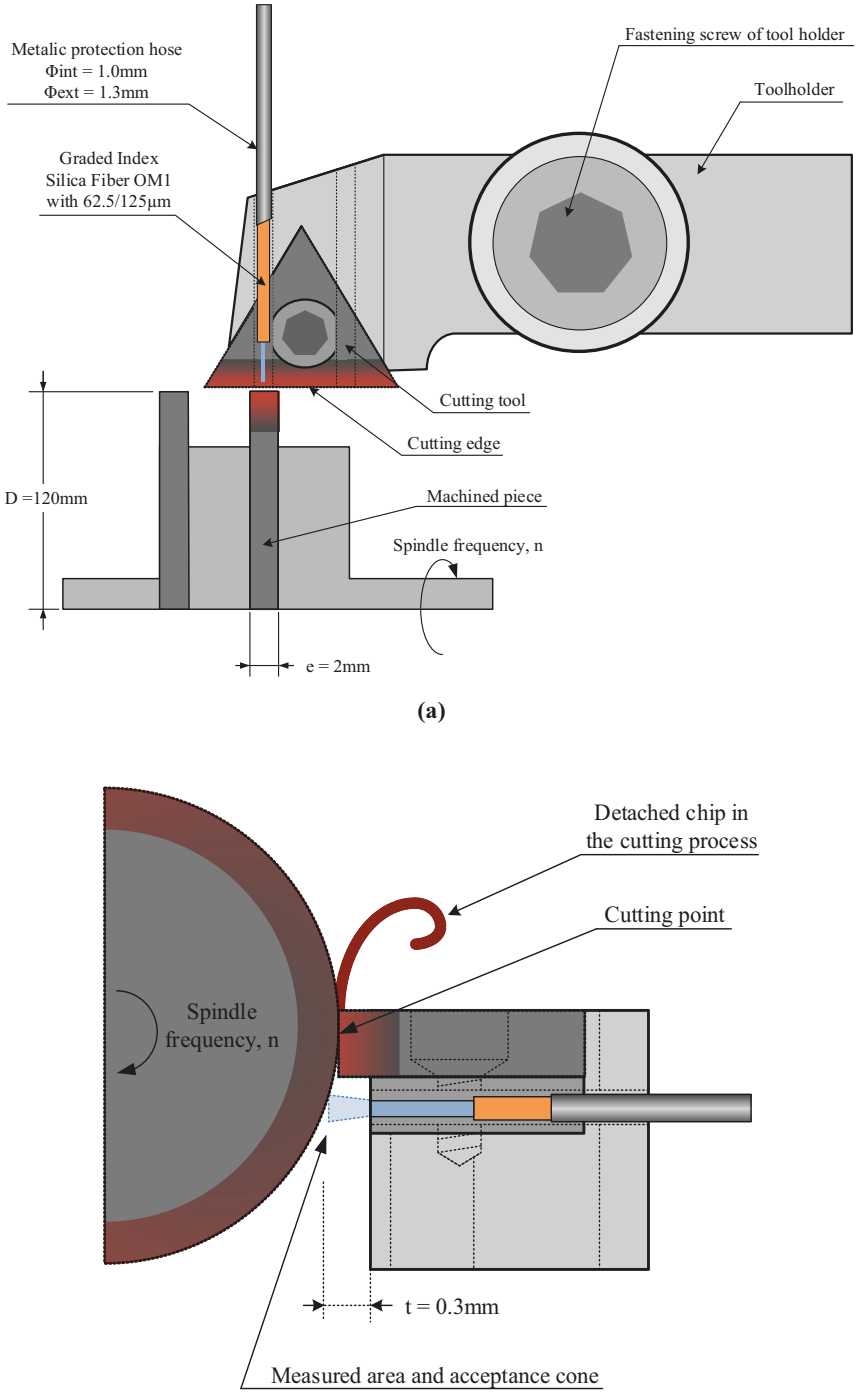

Figure 5.14. Schematic of the tool member with the optical fiber during the machining process. (a) Top view; b) Side view.

The cutting tool is a commercial carbide triangular shaped cutting insert for finishing operation. The cutting edge radius is equal to 20µm, and the rake angle and clearance angle are 0 and 7º, respectively [28].

A computer software based on a visual programming language is designed to acquire and post-process the signals for the two sensing channels. The software provides to the user a friendly environment and the ability to easily change the control parameters remotely. Three stages are defined in the core: acquisition, filtering and computing (see Figure 5.15).

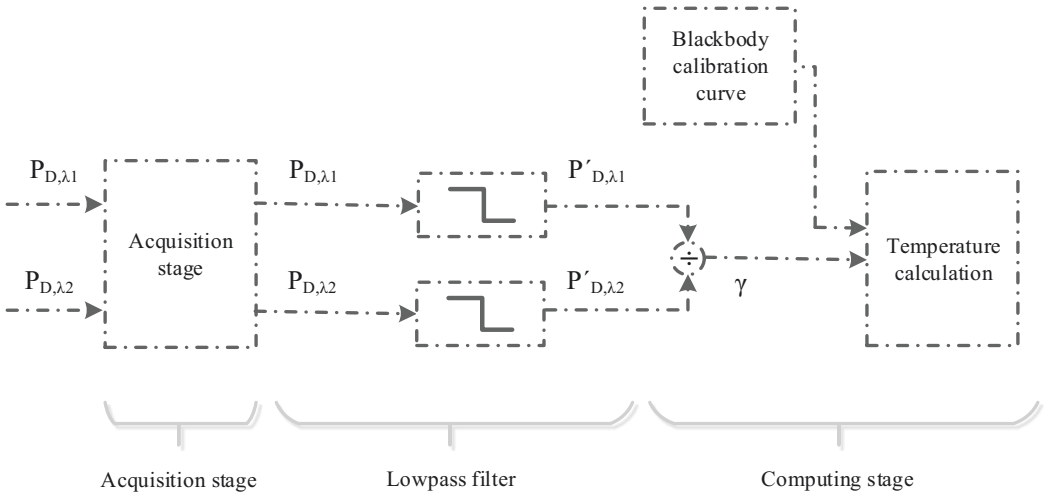

Figure 5.15. Block diagram of the computer software used to acquire and process the signals

The first stage uses communication control unit to configure and start the acquisition process in the optical power meter. The acquisition rate and the number of samples per channel is set to 1kS/s and 10,000 samples, respectively. These values are selected to assure a minimum acquisition time of 10s. The synchronism mode in the optical power meter is activated in order to acquire samples at the same time.

The second stage uses a digital low-pass filter to eliminate noise from the acquired signals ($P_{D,\lambda1}$, $P_{D,\lambda2}$) at the spindle frequency of the lathe. The spindle frequency is calculated using the cutting speed and the disc diameter. Using these values, the spindle frequency (n) of the lathe is 318rpm. This value can be expressed as 5.3Hz. The digital filter is designed using a equiripple finite impulse response (FIR) method. The pass and stop frequency is fixed at 1 and 4Hz. These parameters can be changed using the graphical interface provided by the software.

Finally, a computing stage is implemented to internally calculate the estimated temperature. This stage calculates the output power ratio (γ) of both filtered signals and then, using the calibration curve of the blackbody, estimates the cutting temperature. The software permits to show a complete statistical analysis after the measuring process is completed.

Using the computer software and the pyrometer set-up, a set of three measurements are carried out to perform a complete statistical analysis of the temperature sensor in a real scenario,

see Figure 5.16. The measurements are performed in dry conditions, meaning that no coolant is used in the machining process. The linear cutting speed (V_c), the depth of cut (d) and the feed rate (f) are equal to 120m/min, 2mm and 0.05mm/rev, respectively. These values represent the speed difference between the cutting tool and the workpiece surface, the thickness of workpiece material that can be removed per time unit and the relative velocity at which the cutting tool is advanced along the workpiece.

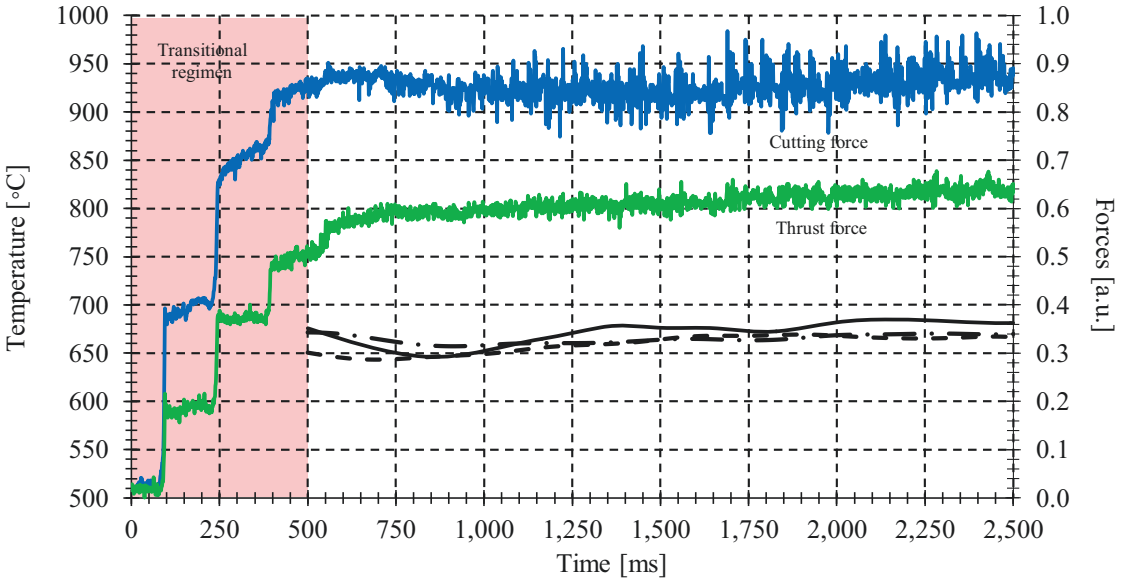

Figure 5.16. Temperature measurements (black lines), and cutting (blue line) and thrust (green line) force evolution when machining Inconel 718 with a carbide cutting tool: V_c=120m/min, d=2mm, f=0.05mm

As can be observed in Figure 5.16, two different regions can be differentiated during the temperature measurement. The first region occurs when the cutting tool starts to remove material from the workpiece. In that region, false temperature readings from the pyrometer are obtained as they are higher than the melting temperature of Inconel 718. The melting temperature depends on the alloy composition but can be changed from 1,260 to 1,336ºC. The possible reason for those false readings is the low temperature of the workpiece at the beginning of the cutting process. Real readings are obtained by measuring signals of optical powers higher than 1.6pW. This effect is also shown in the forces curves. Forces increase quickly at the beginning of the cutting process, the maximum force is reached after 1s, and then it stabilizes during after seconds. During the stationary regime, a maximum temperature of around 650ºC is obtained for a few seconds.

Finally, using the three sets of measurements, the repetitivity in the stationary regime is observed. These results show that the two-colour pyrometer is able to measure the absolute temperature of 650ºC with an error of 14ºC.

Analysing the tendency of the cutting forces and the temperature distribution, different conclusions can be obtained in order to predict futures behaviours. An example of anomalous temperature behaviour during a cutting test is shown in Figure 5.17.

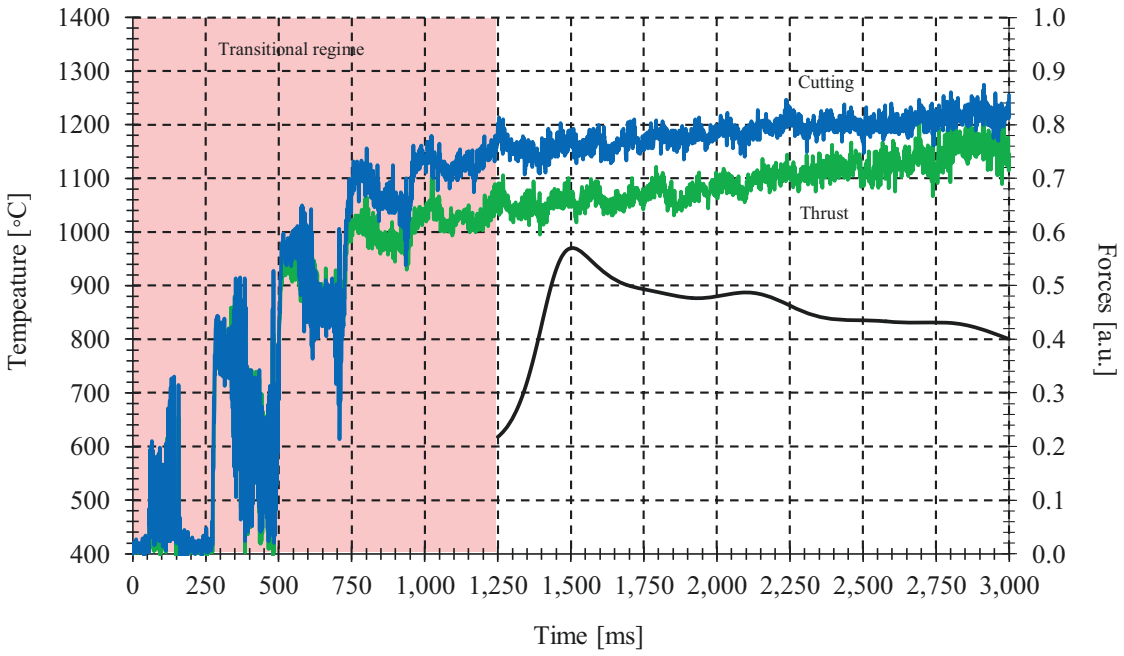

Figure 5.17. Temperature (black lines), and cutting (blue line) and thrust (green line) force evolution when machining Inconel 718 with a damage carbide cutting tool: V_c=60m/min, d=2mm, f=0.05mm

Figure 5.17 shows the temperature evolution when the cutting edge breaks down during a machining process. As it occurs in Figure 5.16, false temperature readings at the beginning of the cutting process are obtained. In a machining process without damage in the cutting tool, lower cutting speed induces lower machining temperatures. For this reason, lower temperatures than in the previous experiment should be expected. In this situation, after the transitional regime, temperature increases reaching a maximum temperature of 919ºC and then, decreases slowly to a temperature of 800ºC. The higher temperatures during this machining process can be due to different mechanisms such as micro-breakages along the cutting edge, a blunt edge of the cutting tool, or a premature wear of the cutting tool, among others. Any of these problems can change rapidly the cutting forces and thus, can increment the machining temperature" instead of "The higher temperatures during this machining process can be due to different mechanisms such as micro-breakages along the cutting edge, a blunt edge of the cutting tool, premature wear of the cutting tool, among others. These problems can change rapidly the cutting forces and thus, increment the machining temperature.

5.4. Discussion

The proposed temperature sensor uses the ratio of output light power at two different wavelengths to provide a robust WDM self-referencing technique in order to avoid the emissivity variation of the measure surface. The sensor uses a standard graded index glass fiber OM1 to gather the emitted radiation from the target. A low insertion loss WDM filter separates the input beam into two spectral components. Their central wavelengths are 1.3 and 1.55µm. An optical power meter with dual InGaAs photodetector is used to measure the light power at each filtering channel. The sensor can operate in a temperature range from 300 to 650ºC. The upper limit is delimited by the capabilities of the dry block calibrator. The real upper temperature is only delimited by the melting point of the glass fiber [29]. This value is around 1,414ºC and depends on the fiber optic composition. The measure calibration curve shows a sensitivity and linear regression coefficient of $6.98 \cdot 10^{-4}$ $ºC^{-1}$ and >99%, respectively. The output power ratio accuracy and full-scale temperature error are 2.6 and 5%, respectively.

The most limiting component in order to measure lower temperatures is the photodetector. The InGaAs photodetector used in this experiment has a total uncertainty of 1.3 and 0.5pW for a wavelength of 1.3 and 1.55µm, respectively. From these values, it is clear that the most limiting channel correspond to the 1.3µm filtering channel. From the Planck's law, it is clear that shorter wavelengths emit less radiation than longer wavelengths in the SWIR spectrum. Despite of this disadvantage, the output light power at the selected as the minimum measurable temperature is ten times higher than the photodetector noise. By using another optical power meter with lower uncertainty and higher responsivity, the minimum measured temperature can be reduced. Other possibility is the use of a chopper and a phase-sensitive detector [30, 31] in order to reduce the system noise, and thus be able to measure lower temperatures. Other types of optical fibers can also be used to measure lower temperatures but if the localized target area is not a restriction.

Finally, the proposed temperature sensor is evaluated with a real surface in order to measure the emissivity variation as a function of temperature and the filtering wavelengths. Calibration curves at each filtering channels are measured from a piece of Inconel 718 using the calibration set-up described in this chapter. The measurement is made for a surface in the as-rolled condition. The output light power at each filtering channel is measured from 300 to 400ºC at 10ºC intervals. The maximum temperature is limited by the oxidation process that occurs when the piece of Inconel 718 is subjected at higher temperatures for a long time, as shown in Figure 5.18.

(a) (b)

Figure 5.18. Piece of Inconel 718 (a) as-rolled and –received (b) as-received and oxidized for 2hours at 650ºC.

Oxidation of metal components, as the result of a thermal transient in an oxidizing environment, increase the emissivity of the surfaces, thus improving the heat rejection capability of the system by thermal radiation to nearby heat sinks, as pointed by Greene et al in [32]. The resulted emissivity value is similar to the emissivity of a blackbody at both wavelengths. Taking into account this problem and using the calibration curves, the emissivity of the Inconel 718 as a function of the temperature is calculated using the output power between the Inconel and blackbody for each filtering channel, see Figure 5.19.

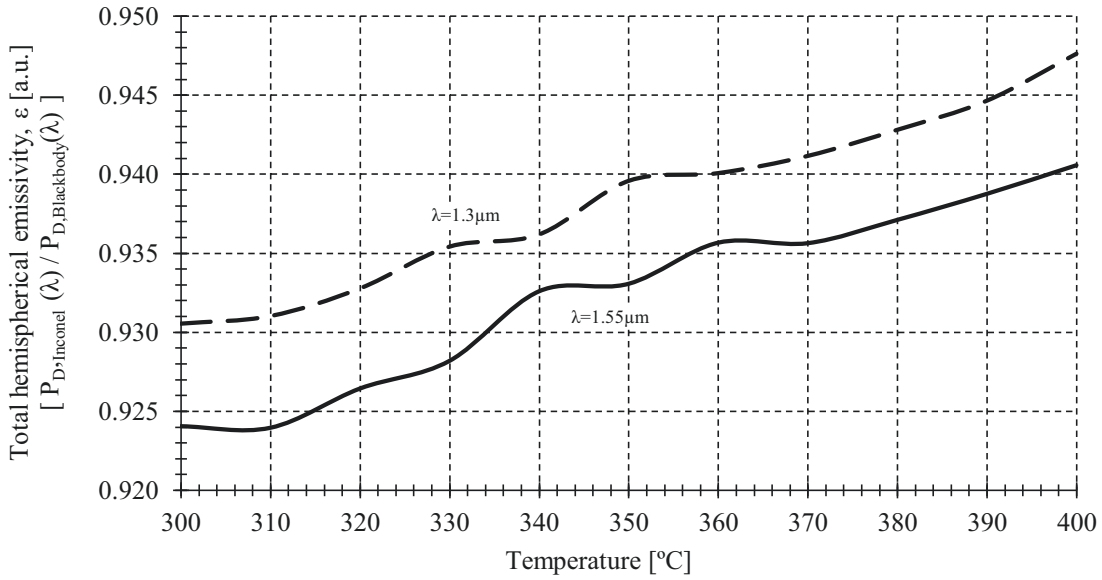

Figure 5.19. Variation of total hemispherical emissivity of Inconel with temperature for an unoxidized Inconel 718 and different wavelengths: – – λ=1.3µm, —λ=1.55µm.

It is evident from Figure 5.19 that the emissivity of Inconel 718 increases when the temperature increases as shown in Figure 4.6. The oxide layer on the surface changes its dimensions with temperature and thus, the emissivity of Inconel tends to the emissivity of a black body. On the other hand, the emissivity decreases as the wavelength of the light increases, as shown in Figure 4.7. These results show the importance of using a two-colour pyrometer to avoid the influence of the emissivity change with temperature and wavelength.

5.5. Comparative Analysis

A comparative analysis is developed between the proposed sensor and other pyrometers reported in the literature, as shown in Table 5.2.

Ref.	Fiber	Lens-head	Filter (1)	Photodetectors
[33]	Single glass or Quartz optical fiber	No	Two bulk optical filters λ_1=1.3~1.8μm λ_2=1.8~2.1μm	One GaAs or CdS photodetector
[34]	Two glass optical fiber	Yes	Two optical fibers with different transmittances λ_1=0~1.5μm, λ_2=0~2.5μm	Two PbS photodetectors
[35]	Single optical fiber with single or multiple cores ϕ_{Core}=100~300μm	Yes	One Thin film wavelength modulator filter	Several photodetectors (2)
[36]	Glass optical fiber	No	Two optical lenses and beam splitters λ_1>0.8μm, λ_2<0.8μm	Two photodetectors (2)
[37]	Glass optical fiber (2)	Yes	Two different optical filters. Overlapping wavelengths	Two photodetectors (2)
[38]	Glass optical fiber (2)	No (3)	Two thin film filters. λ_1=0.6μm, λ_2=0.8μm	Two identical photodetectors (2)
[39]	Multiple glass optical fibers	Yes	One optical filter λ_1=0.4~0.85μm	Two Si photodetector
[40]	Multiple glass or Quartz optical fibers	No (3)	One optical filter λ_1<0.8μm	Three Si and InGaAs photodetectors
This work [41]	Single multimode Glass optical fiber ϕ_{Core}=62.5μm $\phi_{Cladding}$=125μm	No	One WDM Filter λ_1=1.3μm λ_2=1.55μm	Two InGaAs photodetectors

Notes: 1. λ_1 and λ_2 represent the lower and upper filtering channel for the two-colour pyrometer, 2.More specifications are not shown in the patent; 3. Optional plug-in with lens-head is available.

Table 5.2. Optical specifications in some two-colour fiber-optic pyrometers patents.

The present sensor [41] differs from other proposals in that they use lenses at the end of the fiber [34, 35, 37, 39], fiber bundles [34, 39, 40] and fibers with larger diameters [35] to enhance the probe's light gathering and focusing capabilities. A large measuring area permits to enhance the temperature resolution and the minimum measured temperature as the fiber is able to gathered more energy and thus to improve the signal to noise ratio. Other important characteristic of the present sensor is the non-use of fiber lens. In most applications, the space between the rotating work piece and the cutting tool is very close so that the use of a single glass fiber without lens permits a closer placement of the fiber to the machined surface. The use of fibers with a smaller diameter also permits sensing localized areas such as the interface between the cutting tool and the workpiece.

Another feature of the proposed sensor is the use of a low-loss filter to separate the input beam into two wavelength ranges. The filter has a low insertion loss and shows an output spectrum with high uniformity at both filtering channels. Other proposals uses two different materials [34], having different spectral transmittance properties, in a bifurcated or trifurcated optical fibers to achieve the same effect as optical filter. Moreover, the use of fibers to perform the filtering function permits a closer placement of the fiber end faces to their respective detectors. This would not be the case if filtered lenses [33, 35-40] and beam splitters [36-38] are interposed between the fiber ends and the photodetectors. The close placement avoids the spreading loss of radiation which would occur in the intervening space if filters are used. On the other hand, the use of a WDM filter permits high isolation between filtered optical channels.

Other important feature of the proposed sensor is the use of two identical photodetectors in the separate branches of the WDM filter. The use of identical detectors is desirable on the basic that their physical and electrical properties can be matched. Problems are thereby avoided concerning unequal detectors size, sensitivities, response times, temperature characteristics and aging properties that produces the use of different photodetectors [40].

The proposed method to sense temperature offers the advantage that there are no moving mechanical parts in comparison with other methods [33].

In order to compare the different experimental configurations reported in the literature, temperature errors for different two-colour pyrometer are shown in Table 5.3.

Ref.	Fiber	Range	Filter and Splitter	Detector	Temperature error
[14]	Quartz optical fiber ϕ_{Core}=1mm	200 to 1,200ºC	Beam splitter and filters. λ_1=1.69µm, $\Delta\lambda_1$=92nm λ_2=2.02µm, $\Delta\lambda_2$=117nm	Two InGaAs detectors	Non-Linearity: 10ºC Resolution: 12ºC at 400ºC ~50ºC at 320ºC
[42]	Fluoride glass optical fiber ϕ_{Core}=450µm ϕ_{Clad}=500µm	200 to 800ºC	Bandwidth filters λ_1=.5µm, λ_2=3.9µm	HgCdTe detector	Accuracy: ~40ºC at 200ºC ~18ºC at 300ºC 14ºC at 550ºC
[43]	Quartz optical fiber. ϕ_{Core}=50µm ϕ_{Clad}=75µm	700 to 1,100ºC	No filters are used. Signals are separated by a coupler.	Ge and InSb detectors	(2)
[44]	Bundle of glass optical fibers ϕ_{Core}=100µm ϕ_{Clad}=140µm	700 to 1,450ºC	No filters are used	Sandwich Si and Ge detector	Resolution: 1ºC Accuracy: 5ºC Precision: 17ºC
[45] (3)	Doped glass optical fiber. ϕ_{Clad}=280µm	500 to 2,500ºC	Beamsplitter, collimation lenses and filters. λ_1=1.3µm, λ_2=1.55µm	Two InGaAs detectors	10ºC for a temperature from 400 to 1,400ºC
[30] (4)	Silver halide (AgClBr) fiber	42 to 77ºC	Elliptical mirror and 6 Hollow glass waveguides working as 12 filters. λ=[2~14µm], ϕ_{Core}=1mm	Sandwich HgCdTe and InSb detector	~1.7ºC
This Work [41]	OM1 glass optical fiber ϕ_{Core}=62.5µm ϕ_{Clad}=125µm	300 to 650ºC (5)	WDM Filter λ_1=1.3µm λ_2=1.55µm	Two InGaAs detectors	Non-linearity: 9ºC Precision: 8.5ºC Precision at 250ºC: 21ºC

Notes: 1. Different fibers with diameter up to 1mm are used such as: quartz, sapphire, amount others. 2. More specifications are not shown in the article. 3. Absorption/emission technique. 4. Chopper and phase-sensitive detector are used. 5. Range on the reported measurements. For example, in our prototype the potential temperature range for this sensors is from 300 to 1,414ºC (melting point of the glass fiber).

Table 5.3. Optical specifications in some two-colour fiber-optic pyrometers published in scientific journal articles.

The majority of the sensors reported in the literature use optical fibers made of materials with high melting temperature. Glass is a material commonly used in applications of IR radiation pyrometer [44] due to its low-cost, low attenuation in the NIR and the high melting temperature, generally around 1,414ºC [46]. Different authors proposes the use of quartz [14, 43] to measure temperature in extreme temperature processes due to its higher melting point close to 1,713ºC [47]. On the other hand, disadvantages are the higher cost, the smaller NA and the high attenuation [48] in comparison with the OM1 glass fiber [17] proposed in this work. Other authors propose the use of doped optical fibers [42, 45] and halogens fibers [30] to reach higher temperatures, but the high requirements during the manufacturing processes increase its costs, doing them unsuitable for machining applications where the fiber can frequently be broken by chips.

Many authors advocate the use of fibers with larger diameters [14, 42, 45] or fiber bundles [44] in order to enhance the measuring area and thus the minimum measured temperature [14, 42] and temperature resolution [44]. As commented previously, the main disadvantage of using larger gathering areas is the limitation when localized areas should be measured. To overcome this problem, different authors propose the use of reflectometry [45] or phase-sensitive [30] techniques to improve the measurement process while using smaller diameters. Disadvantages of these techniques are the need for an effective control of the geometric configuration, and the use of expensive and complex schemes, suitable only for critical or laboratory measurements.

An important advance of this work is the use of a low-loss two-colour fiber-optic pyrometer for localized temperature measurements in machining processes. An analysis of the measuring mechanism permits identify which factors are related to the system temperature error and the minimum detectable temperature. From this analysis, it is clear that the characteristics of the opto-electronic devices used in the pyrometer set-up are an important factor to be taken into account in order to reduce the system temperature error. Low insertion losses and low wavelength dependence loss ratio are basic requirements in order to measure lower temperature errors at low temperatures.

Many proposals try to reduce temperature errors using fibers with large diameters [42], fiber bundles [44] or lenses [37] to enhance the probe's light gathering and thus, compensate the high insertion losses and the high wavelength dependence loss ratio of the devices used in the pyrometer set-up. These high losses are related to the use of photodetectors with a different responsivity at each sensing wavelength [33, 43]. The use of an identical responsivity at each sensing wavelength is desirable on the basis that their physical and electrical properties can be matched. In the same way, filters and splitters with high uniformity output spectrum at both sensing channels are necessary in order to minimize the changes of the measured optical power.

In this sense, the proposed temperature sensor tries to take advantage of the benefits of commercial off-the-shelf optoelectronic devices well stablished on WDM-based optical communication networks [41]. These devices are optimized to operate in the optical telecommunication bands, reducing the insertion losses and enhancing the wavelength dependence loss ratio, respectively. A good selection of the sensing wavelengths permits to compensate the low losses of each device and to enhance the pyrometer temperature error. The use of these devices also permits to reduce the complexity and system cost.

On the other hand, an important characteristic of the proposed sensor is the lack of need of fiber lenses or fibers with large diameters. In most applications, the space between the rotating work piece and the cutting tool is very close so that the use of a standard single glass fiber without a lens permits a closer location of the fiber to the machined surface. The use of a fiber with a smaller diameter also permits sensing localized areas such as the interface between the cutting tool and the workpiece.

5.6. Conclusions

Temperature plays an important role in machined induced damage at the machined surface, leading to imperfections and residual stress in the finished component. Temperature also increases tool wear rates reducing tool life and limiting the productivity in the machining industry. Temperature measurement in exact locations is a key challenge in order to ensure surface integrity and tool wear control. For this reason, a two-colour pyrometer has been developed to measure the temperature of metallic surfaces in the machining process.

The proposed two-colour fiber-optic pyrometer is optimized for temperature measurements during Inconel 718 machining operations, reaching temperatures greater than 500ºC. The pyrometer uses low-loss fiber optic components designed for telecommunications purposes in order to reduce temperature errors. The pyrometer consists of a multimode glass optical fiber, a WDM filter, a dual InGaAs photodetector and a computer. The output power ratio at λ_1=1.3μm and λ_2=1.55μm has a sensitivity of $6.981 \cdot 10^{-4}$ ºC^{-1}, in a temperature range from 300 to 600ºC. The linear regression coefficient is greater than 99%. The sensor shows a 4.4% full-scale temperature error. Hysteresis is not present in the calibration curves. Simulations of the optical power measured by the photodetectors at both wavelength ranges are carried out to analyse the tendency and the absolute values of the calibration curves. The simulations show that the theoretical and experimental curves are in good agreement

Error analysis is carried out in order to identify the influence of the coupling light loss, fiber attenuation, filter insertion losses and photodetector responsivity at both wavelength ranges

on the absolute measurement error. This study has shown that the photodetector responsivity and filter insertion losses are the main parameters to be taken into account in order to have lower temperature errors and to reduce the minimum detectable temperature.

On the other hand, it is demonstrated that the measured absolute temperature is independent of the distance between the fiber end and the target. This assumption is only valid for target areas higher than the area projected by the fiber NA on the target surface. The influence of possible damage to the sensing fiber termination during the cutting process is also analysed. The result shows that metal chips can damage the surface of the fiber termination without influencing the temperatures readings. These results make the proposed two-colour pyrometer a good solution when temperature is required to measure in harsh industrial environments.

Temperature measurements are carried out on a real scenario using a lathe. The optical fiber which is fixed in a tool holder collects the IR rays radiated from the workpiece and the temperature history is measured. In machining of Inconel 718, the workpiece temperature is 650ºC at a cutting speed, cut depth and feed rate of 120m/min, 2mm and 0.05mm, respectively. Three sets of measurements are performed during the machining test in order to measure the repetitivity error. A maximum temperature deviation of 14ºC is obtained. The temperature evolution also permits to identify future damage or other incidents during the cutting process, reducing the tool wear and cost while increasing the productivity.

In summary, an important advance of this work is the use of a low-loss two-colour fiber-optic pyrometer for localized temperature measurements in machining processes. Low insertion losses and low wavelength dependence loss ratio are basic requirements in order to measure lower temperature errors at low temperatures. Many proposals try to reduce temperature errors using fiber with large diameters, fiber bundles or lenses to enhance the probe's light gathering and thus, compensate the high insertion losses and the high wavelength dependence loss ratio of the devices used in the pyrometer set-up. In this sense, the proposed temperature sensor tries to take advantage of the benefits of the commercial off-the-shelf opto-electronic devices well stablished on WDM-based optical communication networks. These devices are optimized to operate in the optical telecommunication bands, reducing the insertion losses and enhancing the wavelength dependence loss ratio, respectively. A good selection of the sensing wavelengths permits to compensate the low losses of each device and to enhance the pyrometer temperature error. The use of these devices also permits to reduce the complexity and system cost. Finally, an important characteristic of the proposed sensor is the use of a single standard optical fiber which permits sensing localized areas such as the interface between the cutting tool and the workpiece.

5.7. References

[1] J. P. Immarigeon, R. T. Holt, A. K. Koul, L. Zhao, W. Wallace, and J. C. Beddoes, "Lightweight materials for aircraft applications," *Materials Characterization*, vol. 35, pp. 41-67, 1995.

[2] J. C. Williams and E. A. Starke Jr, "Progress in structural materials for aerospace systems1," *Acta Materialia*, vol. 51, pp. 5775-5799, 2003.

[3] E. O. Ezugwu, "Key improvements in the machining of difficult-to-cut aerospace superalloys," *International Journal of Machine Tools and Manufacture*, vol. 45, pp. 1353-1367, 2005.

[4] E. O. Ezugwu, Z. M. Wang, and A. R. Machado, "The machinability of nickel-based alloys: a review," *Journal of Materials Processing Technology*, vol. 86, pp. 1-16, 2/15/ 1999.

[5] D. Dudzinski, A. Devillez, A. Moufki, D. Larrouquère, V. Zerrouki, and J. Vigneau, "A review of developments towards dry and high speed machining of Inconel 718 alloy," *International Journal of Machine Tools and Manufacture*, vol. 44, pp. 439-456, 2004.

[6] Z. Y. Wang and K. P. Rajurkar, "Cryogenic machining of hard-to-cut materials," *Wear*, vol. 239, pp. 168-175, 2000.

[7] R. Komanduri and Z. B. Hou, "A review of the experimental techniques for the measurement of heat and temperatures generated in some manufacturing processes and tribology," *Tribology International*, vol. 34, pp. 653-682, 2001.

[8] I. Lazoglu and Y. Altintas, "Prediction of tool and chip temperature in continuous and interrupted machining," *International Journal of Machine Tools and Manufacture*, vol. 42, pp. 1011-1022, 2002.

[9] B. Alvelid, "Cutting temperature thermo-electrical measurements," *Ann. CIRP*, vol. 18, pp. 547-554, 1970.

[10] A. Kus, Y. Isik, M. Cakir, S. Coşkun, and K. Özdemir, "Thermocouple and Infrared Sensor-Based Measurement of Temperature Distribution in Metal Cutting," *Sensors*, vol. 15, pp. 1274-1291, 2015.

[11] C. Dinc, I. Lazoglu, and A. Serpenguzel, "Analysis of thermal fields in orthogonal machining with infrared imaging," *Journal of Materials Processing Technology*, vol. 198, pp. 147-154, 2008.

[12] W. F. Kosonocky, M. B. Kaplinsky, N. J. McCaffrey, E. S. H. Hou, C. N. Manikopoulos, N. M. Ravindra, et al., "Multiwavelength imaging pyrometer," in *Infrared Detectors and Focal Plane Arrays III*, Orlando (United States of America), 1994, pp. 26-43.

[13] A. Goyal, S. Dhiman, S. Kumar, and R. Sharma, "A Study of Experimental Temperature Measuring Techniques used in Metal Cutting," *Jordan Journal of Mechanical & Industrial Engineering*, vol. 8, 2014.

[14] B. Muller and U. Renz, "Development of a fast fiber-optic two-color pyrometer for the temperature measurement of surfaces with varying emissivities," *Review of Scientific Instruments*, vol. 72, pp. 3366-3374, 2001.

[15] T. Ueda, A. Hosokawa, and A. Yamamoto, "Studies on Temperature of Abrasive Grains in Grinding—Application of Infrared Radiation Pyrometer," *Journal of Manufacturing Science and Engineering*, vol. 107, pp. 127-133, 1985.

[16] A. Tapetado, C. Vázquez, X. Soldani, H. Miguélez, and D. S. Montero, "Temperature sensor based on fiber optic pyrometer in material removal processes," in *22nd International Conference on Optical Fiber Sensors*, Beijing (China), 2012, pp. 84212V-84212V-4.

[17] ISO/IEC, "IEEE Standard. Information technology. Generic cabling for customer premises. ISO/IEC 11801:2002," ed, 2002.

[18] Isotech. (7st July 2015). Dry Block Calibrator. Jupiter. Available: http://www.isotech.co.uk

[19] J. W. Fleming, "Material dispersion in lightguide glasses," *Electronics Letters*, vol. 14, pp. 326-328, 1978.

[20] D. S. Montero, "Multimode Fibre Broadband Access and Self-Referencing Sensor Networks," Electronics Technlogy Department, Universidad Carlos III de Madrid, Leganés (Spain), 2011.

[21] Corning. (2015, 17th May 2015). Corning 62.5/125 Optical Fiber. Product Information. Available: http://www.corning.com

[22] Keysight. (2014, 7th Jul 2015). Keysight Technologies Power Sensor ModulesOptical Heads Return Loss Modules. Available: http://literature.cdn.keysight.com

[23] J. L. Cantero, J. Díaz-Álvarez, M. H. Miguélez, and N. C. Marín, "Analysis of tool wear patterns in finishing turning of Inconel 718," *Wear*, vol. 297, pp. 885-894, 2013.

[24] J. Díaz-Álvarez, J. L. Cantero, H. Miguélez, and X. Soldani, "Numerical analysis of thermomechanical phenomena influencing tool wear in finishing turning of Inconel 718," *International Journal of Mechanical Sciences*, vol. 82, pp. 161-169, 2014.

[25] M. H. Miguélez, X. Soldani, and A. Molinari, "Analysis of adiabatic shear banding in orthogonal cutting of Ti alloy," *International Journal of Mechanical Sciences*, vol. 75, pp. 212-222, 2013.

[26] A. Molinari, R. Cheriguene, and H. Miguelez, "Contact variables and thermal effects at the tool–chip interface in orthogonal cutting," *International Journal of Solids and Structures*, vol. 49, pp. 3774-3796, 2012.

[27] S. Metals. (2007, 9th April 2015). Inconel alloy 718. Available: http://www.specialmetals.com

[28] Sandvik. (2012, 9th April 2015). TCMW 16 T3 08 H13A CoroTurn 107 Insert for turning. Available: http://sandvik.ecbook.se

[29] J. Ballato, T. Hawkins, P. Foy, R. Stolen, B. Kokuoz, M. Ellison, et al., "Silicon optical Fiber," *Optics Express*, vol. 16, pp. 18675-18683, 2008.

[30] I. Uman, S. Sade, V. Gopal, J. A. Harrington, and A. Katzir, "All-fiber-optic infrared multispectral radiometer for measurements of temperature and emissivity of graybodies at near-room temperature," *Applied Optics*, vol. 43, pp. 2039-2045, 2004.

[31] M. Saito, T. Nishikawa, and M. Shishido, "Background-noise reduction in the infrared fiber optic thermometry," in *15th International Conference on Optical Fiber Sensors*, Portland (United States of America), 2002, pp. 511-514.

[32] G. A. Greene, C. C. Finfrock, and T. F. Irvine Jr, "Total hemispherical emissivity of oxidized Inconel 718 in the temperature range 300-1000°C," *Experimental Thermal and Fluid Science*, vol. 22, pp. 145-153, 2000.

[33] G. J. Carlson, "Tool surface temperature measuring apparatus," US 3579775, 1971.

[34] A. S. Dostoomian and J. S. Lord, "Band-ratio radiometer," US 4225230, 1980.

[35] Y. Chen, R. O. Claus, and Y. Liu, "Multiwavelength pyrometer for measurement in hostile environments," US 6357910 B1, 2002.

[36] D. A. Kahn, "Pyrometer system using separated spectral components from a heat source," US 4326798, 1982.

[37] S. C. Jensen, "Temperature detecting pyrometer," 0216458B1, 1990.

[38] R. R. Dils and A. K. Winslow, "Method and apparatus for determining temperature in a blackbody radiation sensing system," US 4845647, 1989.

[39] J. R. Gebhart, B. E. Kinchen, and R. R. Strange, "Optical pyrometer and technique for temperature measurement," US 4222663, 1980.

[40] E. Suarez-Gonzalez and R. L. Oqlukian, "Triple spectral area pyrometer," US 3579775, 1992.

[41] C. Vázquez, A. Tapetado, J. Díaz-Álvarez, and H. Miguélez, "Pirómetro de fibra óptica a dos colores," ES P201530546, 2015.

[42] J. Thevenet, M. Siroux, and B. Desmet, "Measurements of brake disc surface temperature and emissivity by two-color pyrometry," *Applied Thermal Engineering*, vol. 30, pp. 753-759, 2010.

[43] T. Ueda, M. Sato, T. Sugita, and K. Nakayama, "Thermal Behaviour of Cutting Grain in Grinding," *CIRP Annals - Manufacturing Technology*, vol. 44, pp. 325-328, 1995.

[44] F. J. Madruga, D. A. G. Fernandez, and J. M. Lopez-Higuera, "Error estimation in a fiber-optic dual waveband ratio pyrometer," *IEEE Sensors Journal*, vol. 4, pp. 288-293, 2004.

[45] D. Hernandez, G. Olalde, A. Beck, and E. Milcent, "Bicolor pyroreflectometer using an optical fiber probe," *Review of Scientific Instruments*, vol. 66, pp. 5548-5551, 1995.

[46] C. J. Glassbrenner and G. A. Slack, "Thermal Conductivity of Silicon and Germanium from 3K to the Melting Point," *Physical Review*, vol. 134, pp. A1058-A1069, 1964.

[47] W. A. Deer, R. A. Howie, and J. Zussman, An Introduction to the Rock-Froming Minerals, 2nd Edition ed.: Pearson, 1992.

[48] T. Ueda, K. Yamada, and T. Sugita, "Measurement of Grinding Temperature of Ceramics Using Infrared Radiation Pyrometer with Optical Fiber," *Journal of Manufacturing Science and Engineering*, vol. 114, pp. 317-322, 1992.

Chapter 6

Conclusions and Future Work

6.1. Conclusions

The demand for temperature sensors is growing. The growth is driven by the different applications in which the temperature sensors can be applied. Traditional temperature sensor schemes are not well suited for use whenever specific needs are required. This is the case of temperature measures in industrial processes in harsh environment or biomedical applications in the presence of electromagnetic interferences generated, for example, by electrical power transformers or magnetic resonance imaging machines. In this sense, a new type of temperature sensors based on optical fibers is buoyed by an expanding demand for industrial applications with sophisticated functionalities. The fast-paced technological advancement in fiber optic telecommunication field has introduced highly power-efficient and miniaturized fiber optic sensors. These trends have brought about positive growth in the market for fiber optic sensors. However, they are still sometimes not regarded as being affordable. But intensity fiber-optic sensors can provide very attractive characteristics in the industrial temperature measuring field such as the simplicity of the implementation using relative low-cost devices and the possibility to use multiplexing schemes. The intensity fiber-optic sensors also take advantage of the inherent characteristics of the optical fiber sensors such as flexibility, resistance to hostile environment, immunity of electromagnetic disturbances, and geometric versatility, among other.

In this field, some contributions are reported in this work and are summarized as follows:

- A polymer optical fiber (POF) macro-bend temperature sensor for low-cost temperature measurements was developed. Two self-reference techniques were demonstrated in order to avoid false readings caused by unwanted optical power fluctuations. The first configuration used a dummy fiber-optic sensor. The sensor sensitivity for a bend radius of 2mm is $1.29 \cdot 10^{-3}$ ºC^{-1}. The self-reference sensor system showed a resolution below 0.3ºC and a 3.9% non-linearity full scale error. The second self-reference configuration used a robust WDM self-referencing technique with a sensitivity of $8.95 \cdot 10^{-4}$ ºC^{-1}. The self-reference transmission ratio

accuracy and full-scale temperature error are 0.1% and 2.6%, respectively. The experimental results were also theoretically demonstrated using a mathematical model based on geometric approaches.

- It was experimentally verified the effect of the external environment on the temperature measurements. The sensor sensitivity changed when the macro-bend loop was in contact with other materials.

- The use of two-colour fiber-optic pyrometer for temperature measurement in machining process was demonstrated. The pyrometer was made of low-cost fiber-optic components compatible with commercial off-the-shelf optoelectronics well established on Wavelength Division Multiplexing (WDM) based optical communication networks in order to improve temperature errors of others pyrometers reported in the literature. The output power ratio at λ_1=1.3μm and λ_2=1.55μm was used in order to implement a self-reference technique to avoid false readings caused by fluctuations of the light source, optical fiber attenuation and the effect of the emissivity of the measure surface. The pyrometer showed a sensitivity of $6.98 \cdot 10^{-4}$ ºC^{-1} in a temperature range from 300 to 650ºC. The linear regression coefficient is greater than 99%. The sensor shows a 4.4% full-scale temperature error. It was theoretically demonstrated that the proposed pyrometer enables high-accuracy temperature measurements in machining process.

- The two-colour pyrometer was tested in a real scenario using a lathe. In machining of Inconel 718, the workpiece temperature was demonstrated to be around 650ºC at a cutting speed, cut depth and feed rate of 120m/min, 2mm, and 0.05mm, respectively. A maximum deviation of 14ºC was achieved between three set of measurements at the same conditions. The temperature monitoring was used to identify incidents during the cutting process.

- Error analyses were studied and experimentally verified using the proposed two-colour fiber optic pyrometer. From this study, photodetector responsivity and filter insertion losses at both wavelengths were identified as the main parameters to be taken into account in order to achieve lower temperature errors.

As demonstrated, intensity-based optical sensors is a potentially solution for industrial applications due to its low-cost and simplicity. However, the main drawbacks of the intensity-based approach in the need for a self-referencing scheme in order to avoid undesirable perturbations in the optical power loss. In this sense, reflective fiber Bragg grating based

configuration have been demonstrated to be effective approaches for addressing any optical intensity sensor, as well as opening up wavelength-division multiplexing capabilities. The recent advances on fiber Bragg grating (FBG) manufactured in polymer optical fiber bridge the gap between the remote interrogation of multiple sensors and the advantages of using biocompatible POF, including those based on microstructured polymer optical fiber Bragg grating (MPOFBGs).

Within this research field, some original contributions to the state-of-the art of self-referencing technique based on POFBGs are reported.

- The digital filter theory was applied to the analysis of the proposed self-referencing technique. Closed-form formulas for the description of the transfer function versus sensor-induced power modulation were reported.

- The feasibility of a hybrid glass-POF WDM network topology for addressing multiple self-referenced fiber-optic POF-based sensors was proposed and analysed. One self-reference phase parameter was studied and experimentally verified using few-moded MPOFBGs to address each optical intensity sensor. A glass fiber Bragg grating was located in a common branch before the fiber optic sensors for reference purposes. Such configuration provided arbitrary modulation frequencies, compact sensing heads and flexibility of operation through virtual computer software designed to remotely reconfigure the system, and acquire and process the signals. The self-referenced solution used a low-cost 14-bit data acquisition (DAQ) board which offers a resolution of $1.7 \cdot 10^{-2}$dB. The self-reference topology was able to regulate at 0.46% output phase after inducing 10dB of power fluctuations. It was also demonstrated that no crosstalk was induced when two sensors operating in adjacent Coarse WDM (CWDM) channels are simultaneously interrogated.

- The proposed method was developed to provide a remote monitoring service unit fully compliant for short-reach networks (typically less than 1km), and medium reach-distances (typically up to 10km). It was developed to have high scalability and power budget enhancement in comparison with all POF based solutions as it used off-the shelf WDM-based devices with low insertion losses. It also provided great flexibility and easy reconfigurability due to the use of virtual instrumentation solutions. By additionally monitoring each central MPOFBG wavelength shift within the range of each CWDM channel, temperature changes were also tracked.

- In addition, the reported self-reference technique was successfully improved and adapted for its use in a new low-cost in-service preventive monitoring system for

dense wavelength division multiplexing - passive optical networks (DWDM-PONs). In this sense, with this new topology, an attenuation measurement accuracy of 0.27dB with a maximum power penalty of 0.37dB in a 12.5Gb/s transmission was demonstrated. The computer software was capable of measuring the attenuation of 32 channels in 8 seconds.

6.2. Future Work

Several issues related to the development of intensity-based fiber-optics temperature sensors can be considered in further detail as possible future research. Some of them are described below.

- The temperature dependence of the macrobending loss caused by the different thermo-optic coefficients of the cladding and core could be tested for other types of POF such as singlemode MPOF, few-moded MPOF or graded-index POF.

- The power budget of the self-reference scheme for addressing multiple polymer optical fiber sensors could be improved using low-loss standard connectors.

- In order to accurately evaluate the workpiece temperature close to the interface between the cutting tool and the workpiece, the optical fiber end should be positioned at a closer distance to the cutting edge. In this sense, a new adapted tool holder should be designed.

- The proposed two-colour fiber-optic temperature sensor can be experimentally and theoretically validated using different materials under different cutting conditions, for example changing the cutting speed, feed rate and depth of cut. Temperature simulation can be developed with commercial finite element software to reproduce the orthogonal turning test using the same tool geometry and cutting parameters involved in the turning test. The objective would be to find the better geometrical tool configuration and the optimal cutting conditions in order to obtain more acceptable surface integrity and longer tool life, making the machining process more efficient and economic.

- The proposed two-color fiber-optic pyrometer can be improved by developing a portable detection unit and by using phase sensitive techniques. In this sense, the virtual lock-in amplifier developed in this work could be a simple and a low-cost

solution to measure lower temperatures as those expected when machining composite materials or in medical applications.

- Some of the concepts developed in this work can be translated to photonic integrated circuits adding sensing functionalities to them.

6.3. Publications Related with this Work

6.3.1. International Papers

A. Tapetado, P. J. Pinzon, J. Zubia, and C. Vázquez, "**Polymer Optical Fiber Temperature Sensor With Dual-Wavelength Compensation of Power Fluctuations**," *Journal of Lightwave Technology*, vol. 33, pp. 2716-2723, 2015.

A. Tapetado, D. S. Montero, D. J. Webb, and C. Vázquez, "**A self-referenced optical intensity sensor network using POFBGs for biomedical applications**," *Sensors*, vol. 14, pp. 24029-45, 2014.

A. Tapetado, C. Vázquez, J. Zubia, and J. Arrue, "**A temperature sensor based on a polymer optical fiber macro-bend**," *Sensors*, vol. 13, pp. 13076-89, 2013.

6.3.2. Patents

C. Vázquez, A. Tapetado, M. H. Miguélez, and J. Díaz-Álvarez, "**Pirómetro de fibra óptica a dos colores**," Spanish National Patent, Ref. P201530546, 2015. (under revision)

C. Vázquez, A. Tapetado, D. S. Montero, and J. Montalvo, "**Método y sistema de monitorización de redes de fibras ópticas**," Spanish National Patent, Ref. P201530018, 2015. (under revision)

6.3.3. International Conferences

D. S. Montero, P. J. Pinzón, A. Tapetado Moraleda, C. Vázquez, and J. Zubia, "**Performance evaluation of short-range PF-GIPOF links: on discrete multi-tone transmission and WDM enhancement**," The *23rd International Conference on Plastic Optical Fibers*, Yokohama (Japan), 2014.

A. Tapetado, D. S. Montero, C. Vázquez, and D. J. Webb, "**WDM sensor network approach: Bridging the gap towards POF-based photonic sensing**," *IEEE Sensors*, Valencia (Spain), 2014, pp. 746-749.

A. Tapetado, P. J. Pinzón, J. Zubia, I. Pérez, and C. Vázquez, "**Self-referenced temperature sensor based on a polymer optical fiber macro-bend**," 23rd *International Conference on Optical Fibre Sensors*, Santander (Spain), 2014, pp. 915716-915716-4.

C. Vázquez, A. Tapetado, J. Orcutt, H. C. Meng, and R. Ram, "**Tolerance analysis for efficient MMI devices in silicon photonics**," *Silicon Photonics IX*, San Francisco (USA), 2014, pp. 89900A-89900A-7.

A. Tapetado, C. Vázquez, J. Zubia, D. S. Montero, and P.C. Lallana, "**Experimental test of Polymer Optical Fiber Temperature sensor on different surrounding media**," The 22rd *International Conference on Plastic Optical Fibers*, Armação dos Buzios (Brazil), 2013.

A. Tapetado, C. Vázquez, X. Soldani, H. Miguélez, and D. S. Montero, "**Temperature sensor based on fiber optic pyrometer in material removal processes**," 22nd *International Conference on Optical Fiber Sensors*, Beijing (China), 2012, pp. 84212V-84212V-4.

A. Tapetado, C. Vázquez, J. Zubia, "**Temperature sensor based on Polymer Optical Fiber macro-bends**," The 20rd International *Conference on Plastic Optical Fibers*, Bilbao (Spain), 2011.

6.3.4. National Conferences

A. Tapetado, D. S. Montero, J. Montalvo, P. J. Pinzón, C. Vázquez, "**Sistema permanente de supervisión de detección y localización de fallos de fibra óptica en PONs**", *IX Reunión Española de Optoelectrónica, OPTOEL*, Salamanca (Spain), 2015.

6.3.5. Book Chapters

D. S. Montero, I. Pérez, C. Vázquez, P. C. Lallana, A. Tapetado, and P. Pinzón, "**Recent Advances in Wavelength-Division-Multiplexing Plastic Optical Fiber Technologies,**" InTech Open Science, ISBN: 978-953-51-4134-1, 2015.
Link: http://cdn.intechopen.com/pdfs-wm/48153.pdf

6.3.6. Other Publications

C. Vázquez, A. Tapetado, H. Miguélez, "**Monitoring machining temperature using optical fibers**," SPIE Newsroom, DOI: 10.1117/2.1201406.005510, 2014.
Link: http://spie.org/x108710.xml

C. Vázquez, A. Tapetado, H. Miguélez, J. Díaz-Alvarez, "**Optic Fiber for Recording the Temperature in Extreme Industrial Environments**," General news, 2015.
Link: http://portal.uc3m.es/portal/page/portal/actualidad_cientifica/noticias/fiber_temperature

6.3.7. Other Related Works

To date, Alberto Tapetado Moraleda, as a researcher of the Electronic Technology Department at Carlos III University of Madrid, has performed as the supervisor of the following Bachelor's Degree Final Project:

- Estefanía Crespo Bardera, "**Fuente de Luz Multilambda para Aplicaciones de Sensado y Comunicaciones Ópticas**", Mark: 9.5/10, Bachelor's Degree in Communication System Engineering, Carlos III University of Madrid, October 2014.

To date, Alberto Tapetado Moraleda, as a researcher of the Electronic Technology Department at Carlos III University of Madrid, has performed as a member of the evaluation committee of the following Master's Degree Final Project and Bachelor's Degree Final Projects:

- Cristina Lianes García, "**Sistema de Caracterización de Fibras Ópticas de Plástico Microestructurada y Aplicaciones**", Master in Industrial Engineering, July 2015.

- Tomás Rodríguez Sánchez-Miguel, "**Evaluación de Rendimiento de Sensores Biométricos en Dispositivos Móviles**", Bachelor's Degree in Security Engineering, Centro Universitario de la Guardia Civil – Carlos III University of Madrid, June 2015.

- Andrés Marmolejo Doña, "**Sistemas de Reconocimiento de Huella Dactilar a Gran Escala**", Bachelor's Degree in Security Engineering, Centro Universitario de la Guardia Civil – Carlos III University of Madrid, June 2015.

Chapter 7.

Chapter 7

Resumen del Trabajo Realizado

7.1. Motivación de este Trabajo

Durante los últimos años, el interés por el desarrollo de redes de comunicaciones de alta velocidad se ha visto incrementado por la fuerte demanda de la sociedad actual de un acceso a la información de forma rápida y fiable desde sus hogares. Este incremento de la demanda se ha visto potenciado por el auge de la televisión en alta definición (HDTV, High Definition Television), las redes de intercambio de archivos (P2P, Peer-to Peer), el almacenamiento en la nube (Cloud storage) y el vídeo bajo demanda (VOD, Video on Demand), entre muchas otras aplicaciones. Estos servicios requieren de redes de acceso con una mayor capacidad que las que actualmente se disponen. Para solventar este problema, el creciente número de proveedores de acceso a internet está adoptando soluciones capaces de aprovechar las ventajas que ofrecen las redes de comunicaciones basadas en fibra óptica. Estos proveedores están sustituyendo los tradicionales cables de cobre por líneas de transmisión basadas en cables de fibra óptica.

El gran auge de la tecnología de fibra óptica ha permitido una reducción de costes en los dispositivos de uso en comunicaciones ópticas, este factor junto con la demanda creciente en diferentes sectores como la automatización y el control de procesos, ha estimulado el desarrollo de nuevas aplicaciones de la fibra óptica. Entre ellas destaca el desarrollo de sensores para la medida de diversas magnitudes físicas y químicas, como son la temperatura, la presión, la humedad, la deformación, la concentración de sustancias químicas, entre otras.

Actualmente, el campo de los sensores de temperatura cubre un alto porcentaje del mercado debido al gran número de aplicaciones en las cuales es necesario controlar la temperatura, por ejemplo: en el sector aeroespacial, eléctrico y de la automoción, en la industria química, en biomedicina, en la industria alimentaria, entre muchas otras. Estos sectores demandan en ocasiones sensores capaces de hacer frente a necesidades que los sensores tradiciones no son capaces de satisfacer.

Un caso práctico es la medida de la temperatura de los transformadores de potencia en el sector eléctrico. El incremento de la demanda de energía en los hogares obliga a la fabricación de

transformadores eléctricos cada vez más potentes y de mayor tamaño . Los costes de sustitución por rotura de un transformador eléctrico pueden alcanzar la cifra del orden del millón de dólares. Además del daño económico que puede provocar la rotura de un transformador eléctrico, hay que sumarle el riesgo para el personal que trabaja en las instalaciones. Para prevenir fallos durante el servicio y mantener los transformadores en un correcto estado de funcionamiento, es importante controlar la temperatura del líquido refrigerante que baña al transformador. El uso de sensores de temperatura tradicionales no resulta una opción viable debido a la fuerte presencia de interferencias electromagnéticas generadas por los circuitos inductivos en el interior del transformador. Además, al tratarse de un ambiente de trabajo con líquidos inflamables, el uso de sensores eléctricos no resulta apropiado por el riesgo de incendios o explosiones. Por otra parte, los sensores instalados en la cuba del transformador deben de poder ser monitorizados y controlados remotamente desde el centro de control, ubicado a decenas de kilómetros de la subestación. Una posible solución es el uso de dispositivos que interroguen los sensores de forma inalámbrica, pero la alta tasa de fallos en la conexión de estos sistemas puede propiciar la pérdida del control del estado del transformador. En este sentido, sensores compatibles con sistemas de comunicaciones que permitan una comunicación estable y segura es un requisito indispensable.

Otro de los campos donde los sensores tradicionales no ofrecen una clara ventaja competitiva frente a las nuevas alternativas es el campo de la instrumentación biomédica para el diagnóstico, monitorización y tratamiento eficiente de las enfermedades de las personas. En este contexto, las aplicaciones de sensado biomédico están cobrando relativa importancia para desarrollar sensores que se puedan utilizar en procedimientos quirúrgicos. Estos sensores deben de ofrecer una compatibilidad absoluta con la vida humana. Además de esta importante característica, los sensores deben de ser seguros, rentables, fiables, y ofrecer la posibilidad de ser esterilizados. Por otra parte, estos sensores deben de diseñarse para evitar rechazos durante su uso en operaciones quirúrgicas o el monitorizado permanente del paciente. El tamaño del encapsulado del sensor también resulta determinante a la hora de utilizarse en implantes médicos. Finalmente, uno de los avances que ha supuesto una mejora en el diagnóstico y tratamiento de las enfermedades es el uso de técnicas basadas en imágenes por resonancia magnética. El uso de sensores para monitorizar las constantes vitales del paciente en presencia de fuertes interferencias electromagnéticas resulta cada vez más frecuente en los tratamientos médicos. Un caso práctico son las resonancias magnéticas en casos de hipertermia del paciente. Por este motivo, los sensores de temperatura basado en materiales biocompatibles que no vean perturbada su medida bajo fuertes campos magnéticos resultan cruciales para mantener una correcta diagnosis del paciente.

Otra aplicación importante donde los sensores tradicionales no tienen un campo de aplicación bien definido es la medida de la temperatura en procesos de mecanizado de piezas

propias del sector aeroespacial. El uso de superaleaciones en este sector resulta de especial interés debido a la posibilidad de fabricar aeronaves más resistentes, ligeras y con un menor consumo que la generación de aeronaves actual. La energía consumida durante el mecanizado de estas aleaciones se convierte en su mayor parte en calor durante el proceso de corte. Un aumento excesivo de la temperatura en el filo de la herramienta es la principal causa de la degradación de la superficie de trabajo y el desgaste prematuro de la misma, provocando un aumento considerable de los costes de mecanizado. Por este motivo, la medida de la temperatura en el filo de corte de la herramienta resulta fundamental para prevenir estos problemas. En este sentido, el uso de sensores tradicionales resulta poco aconsejable debido a que requieren un contacto entre el sensor y la superficie de mecanizado. Además, estos sensores requieren tiempos de estabilización prolongados para lograr lecturas de la temperatura estables y fiables, limitando su uso en aplicaciones de mecanizado por la alta variación de la temperatura en periodos de tiempo muy reducidos. Por este motivo, en la década de los años treinta, la termografía infrarroja cobró especial relevancia para la medida de la temperatura en procesos de mecanizado. En general, estas técnicas permiten medir la temperatura en procesos en los que se originan cambios bruscos de temperatura en un corto espacio de tiempo. Si bien estas técnicas requieren una visión directa del punto de medida y por tanto, en procesos de mecanizado donde el espacio entre la herramienta de corte y la superficie de mecanizado es muy reducida, la instalación de este tipo de sensor resulta difícil.

Los recientes avances en la tecnología de fibra óptica ha promovido el desarrollo de sensores capaces de medir la temperatura en aquellos sectores donde los sensores tradicionales no tienen cabida. En particular, los sensores de fibra óptica por modulación en intensidad ofrecen algunas ventajas debido a la gran cantidad de configuraciones posibles. Comparando estas técnicas con topologías basadas en interferometría, los esquemas basados en modulación por intensidad ofrecen configuraciones simples y menos costosas que las técnicas interferométricas. La principal desventaja reside en una considerable reducción de la resolución y sensibilidad de estos sensores. Junto con estas características, los sensores de intensidad poseen las características intrínsecas de los sensores de fibra óptica como son la inmunidad a interferencias electromagnéticas, el reducido tamaño y peso, entre otras.

A pesar de estas ventajas competitivas, el principal problema de los sensores de intensidad es la necesidad de un sistema de autoreferencia que evite fluctuaciones indeseables de la potencia óptica, por ejemplo, por la presencia de suciedad en la medida de la temperatura en procesos de mecanizado o movimientos del paciente durante la medida de la temperatura en operaciones quirúrgicas. El principal beneficio de incorporar sistemas de autoreferencia es la posibilidad de aumentar la resolución y el número de sensores interrogados simultáneamente. Estas mejoras se

consiguen con la utilización de sistemas complejos que incrementan sustancialmente el coste total del sistema.

La motivación por implementar redes de sensores depende mayoritariamente de la aplicación, pero una de las principales razones es la reducción del coste de implementar el sistema de autoreferencia asociado al sensor de intensidad. El uso de sistemas que permitan incrementar el número de sensores interrogados permite reducir el coste por sensor. Además, el uso de sistemas de multiplexado permite reducir el número de tramos de fibra óptica usados, ayudando con ello a la reducción de los costes del sistema.

Existe una amplia variedad de técnicas para implementar esquemas de autoreferencia y multiplexado basadas en sensores de intensidad. La elección de uno u otro esquema de multiplexado depende de los requisitos de la aplicación. La tendencia actual se orienta a desarrollar esquemas de sensado que utilicen topologías ampliamente desarrolladas en sistemas de comunicaciones. Con ello lo que se pretende es reducir los costes de instalación y mantenimiento gracias al uso compartido de la red de comunicaciones y sensado. En este marco, la actual generación de redes de acceso permite el uso de dispositivos basados en multiplexación por longitud de onda (WDM, Wavelength Division Multiplexing) en infraestructuras basadas en redes ópticas pasivas (PON, Passive Optical Networks). Este tipo de esquema ha sido adoptado por una amplia mayoría de los proveedores de acceso a Internet como una solución simple y económica desde el punto de vista del despliegue y mantenimiento de las infraestructuras. Además de estas claras ventajas, la arquitectura WDM-PON destaca por su alta eficiencia y bajo nivel de potencia consumida. El objetivo principal es demostrar la viabilidad de utilizar una infraestructura común de fibra óptica para aplicaciones de sensado y comunicaciones.

7.2. Objetivos de este Trabajo

El objetivo de este trabajo se centra especialmente en el desarrollo de sensores de fibra óptica y técnicas de autoreferencia para la medida de la temperatura en diferentes entornos industriales.

El primer objetivo de este trabajo consiste en el diseño y desarrollo de un sensor de fibra óptica de bajo coste para la medida de la temperatura en transformadores de potencia y aplicaciones biomédicas. En estas aplicaciones, el uso de sensores de temperatura tradicionales resulta inadecuado debido a la presencia de fuertes interferencias electromagnéticas que pueden perturbar la lectura de la temperatura. Uno de los requisitos fundamentales para diseñar un sensor de temperatura que pueda usarse en aplicaciones biomédicas es el uso de materiales biocompatibles en su fabricación. En este sentido, una configuración simple que permite cumplir

con los requisitos mencionados anteriormente es la modulación por intensidad en fibras poliméricas. Este tipo de sensores basan la lectura de la temperatura en medir las variaciones de potencia óptica en función de los cambios de temperatura que se aplican sobre el sensor. En este contexto, el uso de la tecnología asociada con la fibra óptica de plástico ofrece ventajas competitivas frente a otros materiales, como son: el uso de dispositivos opto-electrónicos de bajo coste, la posibilidad de utilizar conectores de baja precisión, la posibilidad de utilizar multiplexores y demultiplexores de muy bajo coste, entre muchas otras ventajas. A pesar de estas ventajas, los sensores de intensidad necesitan de esquemas de autoreferencia que eviten fluctuaciones de potencia que interfieran en la lectura de la temperatura. Estas fluctuaciones pueden provenir de fluctuaciones de potencia a lo largo del tramo de fibra óptica entre la unidad de control y el sensor, fluctuaciones de la fuente de luz por cambios en la corriente de alimentación, pérdidas de potencia por envejecimiento de la instalación, entre otras causas.

El segundo objetivo de este trabajo consiste en promover el estudio y el desarrollo de técnicas de multiplexado y autoreferencia que implementen sensores fabricados en fibra óptica de plástico. Estas topologías deberán de utilizar dispositivos eficientes desde el punto de vista del consumo de potencia para mejorar con ello el balance de potencias del sistema y por tanto, poder utilizar este tipo de esquemas en redes de corto y medio alcance.

Para alcanzar este objetivo, en este trabajo se desarrollan técnicas de autoreferencia y multiplexado de bajo coste basadas en multiplexación por longitud de onda vasta (CWDM, Coarse Wavelength Division Multiplexing). Esta técnica se caracteriza por su amplio desarrollo en el campo de telecomunicaciones como estándar para aplicaciones de corto o medio alcance en redes metropolitanas. Los multiplexores y demultiplexores diseñados para esta topología tienen una rejilla de longitudes de onda con una separación entre canales de 20nm. Este espaciado entre canales dificulta la multiplexación de un elevado número de dispositivos o sensores como podría llevarse a cabo si se usaran dispositivos basados en multiplexación por longitud de onda densa (DWDM, Dense Wavelength Division Multiplexing). Pero presentan una clara ventaja competitiva, los esquemas CWDM requieren bajas tolerancias en la fabricación de fuentes de luz, un control menos exhaustivo de la temperatura de la fuente, filtros ópticos de bajo coste y esquemas de diseño menos complejos. Los menores requisitos técnicos de los dispositivos utilizados con esta tecnología hacen que sea una topología interesante para su uso en redes de sensores de bajo coste.

El tercer objetivo consiste en desarrollar sensores sin contacto basados en pirometría de dos colores para el sensado de la temperatura en procesos de mecanizado industrial. Con esta propuesta lo que se pretende mejorar el posicionamiento del sensor en la zona de corte, reducir el

efecto de la emisividad y evitar que se obtengan falsas lecturas incorporando un robusto sistema de autoreferencia. Este trabajo además se centra en la reducción de los errores de temperatura dependientes de las pérdidas de inserción de los dispositivos. Para ello se pretende realizar un análisis del comportamiento de cada uno de los dispositivos que integran el pirómetro en cada longitud de onda con el fin tener pérdidas de inserción equilibradas en ambos canales de sensado. Para implementar un sensor con bajas pérdidas dependientes de la longitud de onda, se pretende adoptar configuraciones simples y robustas que hayan sido ampliamente desarrolladas en otras aplicaciones. En este sentido, se plantea la utilización de dispositivos diseñados para aplicaciones de comunicaciones ópticas basados en topologías por división en longitud de onda. La estandarización y el profundo conocimiento de estos dispositivos juega a favor a la hora de diseñar un sensor de temperatura con bajas pérdidas de inserción.

Además de los objetivos principales planteados en este documento, se pretende utilizar las técnicas de multiplexación y autoreferencia desarrolladas en este documento para abordar nuevos retos o aplicaciones.

Se pretende adaptar el sistema de autoreferencia para sensores de intensidad al desarrollo de una técnica de monitorizado de fallos en redes de comunicaciones por división en longitud de onda en redes ópticas pasivas. En este escenario, el uso de una técnica de autoreferencia que permita interrogar múltiples suscriptores permitirá reducir el coste de mantenimiento de la red de distribución mientras se garantiza un alto nivel de servicio a los clientes.

Por otra parte, se plantea mejorar la integración de las funciones fotónicas en la siguiente generación de microprocesadores, integrando en una plataforma las funciones de sensado y comunicación. Para ello se plantea el uso de dispositivos basados en interferencia multimodal (MMI, Multimodal Interference) junto con topologías de sensado por división en longitud de onda. Su uso conjunto pretende abrir la posibilidad de desarrollar dispositivos electrónicos que aumentan la potencia y eficiencia de la actual generación de procesadores reduciendo considerablemente su tamaño.

El trabajo se ha desarrollado en el marco de las actividades de investigación llevadas a cabo en el Grupo de Displays y Aplicaciones Fotónicas (GDAF) de la Universidad Carlos III de Madrid.

7.3. Conclusiones de este Trabajo

La demanda de sensores de temperatura crece de forma continuada año tras año. Esta demanda se produce principalmente por la creciente necesidad de controlar la temperatura en

procesos industriales. En este contexto, existen diversas aplicaciones en las cuales los sensores tradicionales no permiten realizar esta medida debido a los altos requisitos técnicos que ciertas aplicaciones necesitan. Este es el caso de la medida de la temperatura en presencia de ambientes inflamables, aplicaciones biomédicas o en presencia de fuertes interferencias electromagnéticas. Ejemplos de estas aplicaciones son la medida de la temperatura del líquido refrigerante en el seno de un trasformador eléctrico, la medida de temperatura en procesos de mecanizado o la medida de la temperatura del cuerpo humano durante el diagnóstico del paciente por medio de imágenes por resonancia magnética. En este contexto, este trabajo ha contribuido a aportar nuevos desarrollos en el estado del arte de los sensores de temperatura de fibra óptica. De entre todas ellas, las que ofrecen mayor relevancia se resumen a continuación:

- En este trabajo se ha diseñado un sensor basado en macrocurvatura en fibra óptica de plástico para el sensado de la temperatura en aplicaciones industriales de bajo coste. Para reducir las fluctuaciones de potencia óptica que causan falsas lecturas de la temperatura, se han implementado dos técnicas de autoreferencia. La primera configuración utiliza un segundo sensor, idéntico al sensor principal, como elemento de referencia. La sensibilidad del sistema para un radio de curvatura del sensor de 2mm es de $1.29 \cdot 10^{-3}$ ºC^{-1}. El sistema de autoreferencia permite medir la temperatura con una resolución y un error de no linealidad de 0.3ºC y 3.9%, respectivamente. La segunda técnica permite aumentar la robustez del sistema gracias al uso de técnicas por división en longitud de onda. Implementado esta topología, el sistema ofrece una sensibilidad de $8.95 \cdot 10^{-4}$ ºC^{-1}. La precisión del parámetro de autoreferencia y el error en temperatura total a fondo de escala es de 0.1% y 2.6%, respectivamente. Para corroborar los resultados obtenidos, los resultados experimentales han sido comparados teóricamente con modelos matemáticos basados en aproximaciones geométricas.

- Durante la toma de las medidas se ha verificado el efecto del ambiente externo sobre la lectura de la temperatura del sensor. Se ha comprobado que la sensibilidad cambia ligeramente cuando el sensor está en contacto con materiales o ambientes diferentes a los cuales se utilizaron para medir la curva de calibración, especialmente en el caso de los metales.

- Se ha demostrado la posibilidad de usar un pirómetro de dos colores para la medida de la temperatura en procesos de mecanizado industrial. El pirómetro se ha fabricado con componentes de fibra óptica de bajo coste compatibles con dispositivos opto-electrónicos diseñados para comunicaciones por fibra óptica usando esquemas de

división por longitud de onda. El cociente de potencias entre λ_1=1.3µm y λ_2=1.55µm se usa como parámetro de autoreferencia para evitar fluctuaciones de potencia, atenuación de la fibra óptica o cambios de la emisividad del objeto que se quiere medir. El pirómetro ofrece una sensibilidad de $6.98 \cdot 10^{-4}$ ºC^{-1} en un rango de temperaturas desde 300ºC hasta 650ºC. El coeficiente de regresión lineal obtenido a partir de la curva de calibración es mayor de 99%. Se han obtenido errores en las medidas bajos en el rango de temperaturas de interés usando elementos de bajo coste. Así, el sensor muestra un error de temperatura a fondo de escala del 4%. Se ha corroborado teóricamente que el sensor permite medir la temperatura en procesos de mecanizado con una alta precisión.

- El análisis de los factores que influyen en el error de temperatura del pirómetro se ha llevado a cabo de forma teórica y experimental con el fin de abrir el camino a posibles mejoras del sistema. Este estudio ha mostrado que la responsividad del fotodetector y las pérdidas de inserción del filtro óptico en ambas longitudes de onda son los parámetros principales a tener en cuenta para minimizar los errores en la medida de temperatura.

- El correcto funcionamiento del pirómetro en el laboratorio se ha comprobado en un entorno real usando una máquina de corte por control numérico. Para realizar esta prueba se ha procedido a mecanizar una pieza de Inconel 718. Se ha programado la herramienta de corte para mantener durante el mecanizado una velocidad de corte, profundidad de pasada y velocidad de avance de 120m/min, 2mm y 0.05mm/rev, respectivamente. Para comprobar la repetitividad del sensor, esta prueba se ha repetido tres veces. La desviación de temperatura entre las tres medidas ha sido de 14ºC. Con estas pruebas se ha demostrado que el sensor de temperatura también permite la detección de anomalías durante el proceso de corte.

- Como se ha demostrado, los sensores de fibra óptica por modulación en intensidad son una solución real para aplicaciones industriales de bajo coste debido a su escasa complejidad. Sin embargo, el principal problema que subyace sobre los sensores de intensidad es la necesidad de incorporar un sistema de autoreferencia que evite falsas lectura de la temperatura a causada de fluctuaciones de potencia óptica en el sistema. En este sentido, se ha desarrollado un sistema de autoreferencia basado en redes de Bragg en fibra óptica (FBG, Fiber Bragg Grating) para el monitorizado de múltiples sensores de intensidad haciendo uso de los avances en técnicas de división por longitud de onda. Los recientes avances en el grabado de redes de Bragg en fibra

óptica de plástico (POFBGs, Polymer Optical Fiber Bragg Gratings), abren el camino al desarrollo de técnicas de autoreferencia y multiplexado de múltiples sensores en aplicaciones biomédicas.

En este campo de investigación, se resumen a continuación las aportaciones más importantes:

- Se ha demostrado la posibilidad de utilizar topologías WDM híbridas usando fibra óptica microestructurada de plástico (MPOF, Microstructured Polymer Optical Fiber) y sílice (GOF, Glass Optical Fiber) para implementar redes de sensores autoreferenciados. El sistema permite utilizar dos parámetros de autoreferencia con cada uno de los sensores.

- Se ha demostrado experimentalmente y teóricamente la validez del uso del parámetro de fase con redes de Bragg grabadas en fibra microestructurada de plástico. El sistema propuesto también usa una red de Bragg grabada sobre fibra óptica de sílice como elemento de referencia común a todas las ramas de sensado. El esquema de autoreferencia permite configurar de forma virtual cada uno de los parámetros del sistema. El sistema de autoreferencia usa una tarjeta de adquisición de bajo coste de 14-bits con la cual se obtienen resoluciones de $1.7 \cdot 10^{-2}$dB y es capaz de regular hasta un 0.46% del parámetro de autoreferencia si se inducen fluctuaciones indeseadas de potencia de 10dB. Durante los experimentos se ha demostrado la ausencia de crosstalk entre canales adyacentes mientras se interrogan dos sensores de forma simultánea.

- El sistema permite monitorizar redes de sensores de corto (típicamente menores de 1km) y medio (típicamente hasta 10km) alcance. El sistema permite ampliar el número de sensores interrogados de forma rápida y sencilla, ofreciendo bajos niveles de pérdidas gracias al uso de dispositivos WDM. El sistema también ofrece una gran flexibilidad gracias a la utilización de un entorno virtual desde el cual se puede configurar y visualizar la respuesta de cada uno de los sensores del sistema.

- El sistema de autoreferencia descrito en este trabajo también se ha utilizado como sistema de monitorización de fallos en redes de comunicaciones ópticas basadas en técnicas por división de longitud de onda densa en redes ópticas pasivas. En este sentido, el sistema permite medir atenuaciones con una precisión de 0.27dB, introduciendo un máximo de pérdidas de potencia en la transmisión de 0.37dB para

una velocidad de transmisión de 12.5Gb/s. El código implementado permite medir la atenuación de 32 sensores en un máximo de 8 segundos.

7.4. Trabajos Futuros

- A partir de las conclusiones obtenidas de los sensores de temperatura y los esquemas de autoreferencia desarrollados en este trabajo, se plantean diversas líneas de investigación futuras.

- La dependencia de las pérdidas por macrocurvatura con la temperatura causadas por cambios del coeficiente termo-óptico de la cubierta y el núcleo de la fibra pueden ser evaluadas usando otros tipos de fibra óptica de plástico. Ejemplos de nuevas propuestas son: el uso de la fibra óptica microestructurada de plástico monomodo o de muy pocos modos y fibra óptica de plástico de índice gradual.

- El balance de potencias del sistema de autoreferencia para el monitorizado de múltiples sensores en aplicaciones biomédicas puede ser mejorado utilizando un sistema de conectorizado de las redes de Bragg que permita reducir las pérdidas de inserción que introduce el actual sistema de pegado.

- Para poder evaluar con una mayor precisión las temperaturas que se originan en la interfaz entre la herramienta de corte y la superficie de mecanizado, resulta conveniente realizar orificios de posicionamiento de la fibra óptica más cercanos al filo de corte de la herramienta.

- El pirómetro de dos colores se puede validar experimentalmente con diversos materiales y realizar medidas de temperatura en condiciones no disponibles actualmente en la literatura. Además, se podría realizar un set de medidas más extenso con el fin de poder comprobar si existen cambios de temperatura cuando se utilizan diferentes condiciones de corte. Con ello se podría estudiar la evolución de las temperatura en las distintas configuraciones que pueden darse en un proceso de mecanizado. Se trataría de medidas preventivas que ayuden a incrementar la productividad y mejorar el acabado de las piezas producidas en el proceso de mecanizado.

- El pirómetro de dos colores puede mejorarse desarrollando una unidad de detección portable de bajo coste que use técnicas basadas en la detección de fase. En este sentido el amplificador de lock-in virtual desarrollado para el sistema de

autoreferencia puede ofrecer una solución simple y de bajo coste para medir temperaturas por debajo de los 300ºC de forma precisa y fiable. La posibilidad de medir temperaturas cercanas a la temperatura del cuerpo humano abre la posibilidad de utilizar el pirómetro de dos colores en aplicaciones biomédicas.

7.5. Publicaciones Obtenidas

7.5.1. Publicaciones en Revistas Internacionales

A. Tapetado, P. J. Pinzon, J. Zubia, and C. Vázquez, "**Polymer Optical Fiber Temperature Sensor With Dual-Wavelength Compensation of Power Fluctuations**," *Journal of Lightwave Technology*, vol. 33, pp. 2716-2723, 2015.

A. Tapetado, D. S. Montero, D. J. Webb, and C. Vázquez, "**A self-referenced optical intensity sensor network using POFBGs for biomedical applications**," *Sensors*, vol. 14, pp. 24029-45, 2014.

A. Tapetado, C. Vázquez, J. Zubia, and J. Arrue, "**A temperature sensor based on a polymer optical fiber macro-bend**," *Sensors*, vol. 13, pp. 13076-89, 2013.

7.5.2. Patentes

C. Vázquez, A. Tapetado, M. H. Miguélez, and J. Díaz-Álvarez, "**Pirómetro de fibra óptica a dos colores**," Sistema de patentes español, Ref. P201530546, 2015. (En revisión)

C. Vázquez, A. Tapetado, D. S. Montero, and J. Montalvo, "**Método y sistema de monitorización de redes de fibras ópticas**," Sistema de patentes español, Ref. P201530018, 2015. (En revisión)

7.5.3. Publicaciones en Congresos Internacionales

D. S. Montero, P. J. Pinzón, A. Tapetado Moraleda, C. Vázquez, and J. Zubia, "**Performance evaluation of short-range PF-GIPOF links: on discrete multi-tone transmission and WDM enhancement**," *The 23rd International Conference on Plastic Optical Fibers*, Yokohama (Japan), 2014.

A. Tapetado, D. S. Montero, C. Vázquez, and D. J. Webb, "**WDM sensor network approach: Bridging the gap towards POF-based photonic sensing**," *IEEE Sensors*, Valencia (Spain), 2014, pp. 746-749.

A. Tapetado, P. J. Pinzón, J. Zubia, I. Pérez, and C. Vázquez, "**Self-referenced temperature sensor based on a polymer optical fiber macro-bend**," *23rd International Conference on Optical Fibre Sensors*, Santander (Spain), 2014, pp. 915716-915716-4.

C. Vázquez, A. Tapetado, J. Orcutt, H. C. Meng, and R. Ram, "**Tolerance analysis for efficient MMI devices in silicon photonics**," *Silicon Photonics IX*, San Francisco (USA), 2014, pp. 89900A-89900A-7.

A. Tapetado, C. Vázquez, J. Zubia, D. S. Montero, and P.C. Lallana, "**Experimental test of Polymer Optical Fiber Temperature sensor on different surrounding media**," *The 22rd International Conference on Plastic Optical Fibers*, Armação dos Buzios (Brazil), 2013.

A. Tapetado, C. Vázquez, X. Soldani, H. Miguélez, and D. S. Montero, "**Temperature sensor based on fiber optic pyrometer in material removal processes**," *22nd International Conference on Optical Fiber Sensors*, Beijing (China), 2012, pp. 84212V-84212V-4.

A. Tapetado, C. Vázquez, J. Zubia, "**Temperature sensor based on Polymer Optical Fiber macro-bends**," *The 20rd International Conference on Plastic Optical Fibers*, Bilbao (Spain), 2011.

7.5.4. Publicaciones en Congresos Nacionales

A. Tapetado, D. S. Montero, J. Montalvo, P. J. Pinzón, C. Vázquez, "**Sistema permanente de supervisión de detección y localización de fallos de fibra óptica en PONs**", *IX Reunión Española de Optoelectrónica, OPTOEL*, Salamanca (Spain), 2015.

7.5.5. Capítulos de Libro

D. S. Montero, I. Pérez, C. Vázquez, P. C. Lallana, A. Tapetado, and P. Pinzón, "**Recent Advances in Wavelength-Division-Multiplexing Plastic Optical Fiber Technologies,**" InTech Open Science, ISBN: 978-953-51-4134-1, 2015.
Link: http://cdn.intechopen.com/pdfs-wm/48153.pdf

7.5.6. Otras Publicaciones

C. Vázquez, A. Tapetado, H. Miguélez, "**Monitoring machining temperature using optical fibers**," SPIE Newsroom, DOI: 10.1117/2.1201406.005510, 2014.
Enlace: http://spie.org/x108710.xml

C. Vázquez, A. Tapetado, H. Miguélez, J. Díaz-Alvarez, "**Optic Fiber for Recording the Temperature in Extreme Industrial Environments**," General news, 2015.
Enlace: http://portal.uc3m.es/portal/page/portal/actualidad_cientifica/noticias/fiber_temperature

7.5.7. Otros Trabajos Relacionados

Hasta la fecha, Alberto Tapetado Moraleda, como investigador en el Departamento de Tecnología Electrónica de la Universidad Carlos III de Madrid, ha actuado como director de los siguientes Trabajos Final de Grado:

- Estefanía Crespo Bardera, "**Fuente de luz multilambda para aplicaciones de sensado y comunicaciones ópticas**", Calificación: 9.5/10, Grado en Ingeniería de Sistemas de Comunicación, Octubre de 2014.

Hasta la fecha, Alberto Tapetado Moraleda, como investigador en el Departamento de Tecnología Electrónica de la Universidad Carlos III de Madrid, ha actuado como tribunal en los siguientes Proyectos Final de Master y Trabajos Final de Grado:

- Cristina Lianes García, "**Sistema de Caracterización de Fibras Ópticas de Plástico Microestructurada y Aplicaciones**", Master en Ingeniería Industrial, Julio de 2015.

- Tomás Rodríguez Sánchez-Miguel, "**Evaluación de Rendimiento de Sensores Biométricos en Dispositivos Móviles**", Grado en Ingeniería de la Seguridad, Centro Universitario de la Guardia Civil – Universidad Carlos III de Madrid, Junio de 2015.

- Andrés Marmolejo Doña, "**Sistemas de Reconocimiento de Huella Dactilar a Gran Escala**", Grado en Ingeniería de la Seguridad, Centro Universitario de la Guardia Civil – Universidad Carlos III de Madrid, Junio de 2015.

Appendix A

Analytical Expressions for the Self-Referencing Parameters in Sensor Networks with POFBG

A.1. Transfer Function of the Digital FIR Filter

The block diagram for a single remote sensing point is shown in Figure A.1.

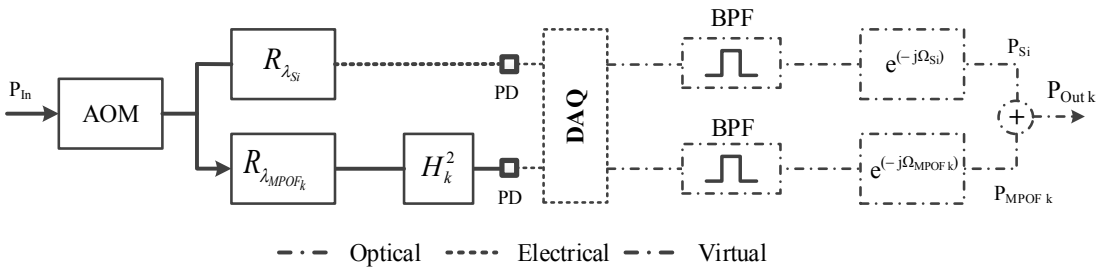

Figure A.1. Filter model of the configuration for a single remote sensing point including AOM, DAQ, bandpass filters (BPF) and virtual phase-shifts.

The temporal dependence of the reference and *k* sensing channel signals in the time domain are given by:

$$p_{Si}(t) = \cos(2\pi \cdot f \cdot t - \Omega_{Si}) \tag{A.1}$$

$$p_{MPOF_k}(t) = \cos(2\pi \cdot f \cdot t - \Omega_{MPOF_k}) \tag{A.2}$$

The reference and sensing channels are modulated at a frequency (*f*) by an acousto-optic modulator (AOM).

Equations (A.1) and (A.2) represent the time domain expression for the reference and sensing channels, respectively, using an electro-optical design. In this work, a data acquisition board (DAQ) is used to convert the electrical signals from the photodetectors to digital signals. Then, a bandpass filter is used to eliminate noise and recover the modulated signal from the

sensing and reference channels. Although the resulting signals are virtual, these signals can be analyzed using the theoretical expressions of the electro-optical design due to the use of a 16-bits DAQ with low quantization error and a filter with a narrow bandpass centered at the modulated frequency (*f*).

The system output voltage in the time domain, $p_{Out}(t)$, is expressed as follows:

$$p_{Out\,k}(t) = \alpha \cdot \left(p_{Si}(t) + \beta_k \cdot p_{MPOFk}(t)\right) \tag{A.3}$$

with

$$\alpha = m_{Si} \cdot d_{\lambda_{Si}} \cdot R_{\lambda_{Si}} \tag{A.4}$$

$$\beta_k = \frac{m_{MPOF_k} \cdot d_{\lambda_{MPOF_k}} \cdot R_{\lambda_{MPOF_k}} \cdot L_{CWDM} \cdot L_{MPOFBG-Si}}{m_{Si} \cdot d_{\lambda_{Si}} \cdot R_{\lambda_{Si}}} \cdot H_k^2 \tag{A.5}$$

where Ω_{Si} and Ω_{MPOFk} are the phase shifts for the reference and each sensor signal, respectively. Parameters m_{Si}, $R_{\lambda Si}$ and $d_{\lambda Si}$ are the modulation index, the reflectivity of the glass fiber Bragg grating (FBG) and the photodetector responsivity, respectively, at the reference wavelength, whereas m_{MPOF}, $R_{\lambda MPOFk}$ and $d_{\lambda MPOFk}$ are similar but for each sensor wavelength. H_k is the sensor power loss modulation and appears two times due to the reflective operation of the sensing structure. L_{CWDM} is the insertion loss for the coarse wavelength division multiplexer (CWDM) mux/demux. Finally, $L_{MPOFBG\text{-}Si}$ are the microstructured polymer optical fiber Bragg grating (MPOFBG) insertion losses related to the reflectivity of the gratings, attenuation of the MPOF, multimode/singlemode glass fiber connection and glass-polymer glued connection.

Using Equation (A.4) and (A.5), the Equation (A.3) is rewritten as follows:

$$p_{Out\,k}(t) = \alpha \cdot \left[\cos\left(2\pi \cdot f \cdot t - \Omega_{Si}\right) + \beta_k \cdot \cos\left(2\pi \cdot f \cdot t - \Omega_{MPOF_k}\right)\right] \tag{A.6}$$

Equation (A.6) is studied using phasor transform of the corresponding sinusoidal signals:

$$P_{Si} = P_{In} \cdot \alpha \cdot e^{(-j \cdot \Omega_{Si})} \tag{A.7}$$

$$P_{MPOF_k} = P_{In} \cdot \alpha \cdot \beta_k \cdot e^{\left(-j \cdot \Omega_{MPOF_k}\right)} \tag{A.8}$$

Adding sinusoidal signals of the same frequency in the timer domain is equivalent to adding their phasor transform in the phasor domain, so phasor $P_{Out\,k}$ is calculated using Equation (A.7) and (A.8) as follows:

$$P_{Out\,k} = \alpha \cdot \left[P_{In} \cdot e^{(-j \cdot \Omega_{Si})} + \beta_k \cdot P_{In} \cdot e^{\left(-j \cdot \Omega_{MPOF_k}\right)} \right] = P_{in} \cdot \alpha \cdot e^{(-j \cdot \Omega_{Si})} \cdot \left[1 + \beta_k \cdot e^{\left(-j \cdot \left(\Omega_{MPOF_k} - \Omega_{Si}\right)\right)} \right] \quad (A.9)$$

Finally, the expression of the system transfer function from input to output is given by:

$$H_o = \frac{P_{Out\,k}}{P_{In}} = \alpha' \cdot \left[1 + \beta_k \cdot e^{\left(-j \cdot \left(\Omega_{MPOF_k} - \Omega_{Si}\right)\right)} \right] \quad (A.10)$$

where

$$\alpha' = \alpha \cdot e^{(-j \cdot \Omega_{Si})} \quad (A.11)$$

The expression of the system transfer function from input to output as a phase can be directly identified with the transfer function of a digital Finite Impulse Response (FIR) filter in the Z-Transform domain as follows:

$$H_o(z) = \frac{P_{Out\,k}}{P_{In}} = \alpha' \cdot \left(1 + \beta_k \cdot z^{-1}\right) \quad (A.12)$$

where

$$z^{-1} = e^{(-j \cdot \Omega_k)}, \quad \Omega_k = \Omega_{MPOF_k} - \Omega_{Si} \quad (A.13)$$

A.2. Self-referencing Parameters

Using the expression of the normalized system output as a phase given by:

$$H_o(z) = \frac{P_{Out\,k}}{P_{In}} = \alpha' \cdot \left(1 + \beta_k \cdot z^{-1}\right) \quad (A.14)$$

where

$$z^{-1} = e^{(-j \cdot \Omega_k)}, \quad \Omega_k = \Omega_{MPOF_k} - \Omega_{Si} \quad (A.15)$$

Using the Euler's identity:

$$e^{(-j\cdot\Omega_k)} = \cos(\Omega_k) - j\cdot\sin(\Omega_k) \tag{A.16}$$

The Equation (A.12) is rewritten as follow:

$$H_o(\Omega_k) = \left\lfloor \alpha\cdot\left(\cos(\Omega_{Si}) + \beta_k\cdot\cos\left(\Omega_{MPOF_k}\right)\right)\right\rfloor - j\cdot\left\lfloor \alpha\cdot\left(\sin(\Omega_{Si}) + \beta_k\cdot\sin\left(\Omega_{MPOF_k}\right)\right)\right\rfloor \tag{A.17}$$

Identifying the real and imaginary terms of the transfer function given in Equation (A.17) in the complex plane:

$$\Re H(\Omega_k) = \alpha'\cdot\left(1+\beta_k\cdot\cos(\Omega_k)\right) = \left\lfloor \alpha\cdot\left(\cos(\Omega_{Si}) + \beta_k\cdot\cos\left(\Omega_{MPOF_k}\right)\right)\right\rfloor \tag{A.18}$$

$$\Im H(\Omega_k) = -\alpha'\cdot\beta_k\cdot\sin(\Omega) = -\left[\alpha\cdot\left(\sin(\Omega_{Si}) + \beta_k\cdot\sin\left(\Omega_{MPOF_k}\right)\right)\right] \tag{A.19}$$

The magnitude response of the filter is defined as:

$$\left|H(\Omega_k)\right| = \left[\left(\Re H(\Omega_k)\right)^2 + \left(\Im H(\Omega_k)\right)^2\right]^{1/2} \tag{A.20}$$

Equation (A.20) can be expressed in terms of the power modulation parameter of the self-referencing configuration. Using the helpful tool of the trigonometric identities defined by:

$$\sin^2(\theta) + \cos^2(\theta) = 1 \tag{A.21}$$

$$\cos(\theta_1 - \theta_2) = \cos(\theta_1)\cdot\cos(\theta_2) + \sin(\theta_1)\cdot\sin(\theta_2) \tag{A.22}$$

Using Equation (A.18) to (A.22), the final expression of the magnitude response can be expressed as:

$$\left|H(\Omega_k)\right| = \alpha'\cdot\left(1+2\cdot\beta_k\cdot\cos(\Omega_k) + \beta_k^2\right)^{1/2} = \alpha'\cdot\left[1+\left(\frac{2\cdot\beta_k}{1+\beta_k^2}\right)\cdot\cos(\Omega_k)\right]^{1/2} \tag{A.23}$$

where

$$\Omega_k = \Omega_{MPOF_k} - \Omega_{Si} \tag{A.24}$$

Defining the self-referencing parameter δ_k as the ratio between voltages at the reception stage (V_o) for different phase-shifts, the expression can be calculated as:

$$\delta_k = \frac{V_o\left(f,\Omega_{MPOF_k}\right)\Big|_{\Omega_{Si}=0}}{V_o\left(f,\Omega_{Si}\right)\Big|_{\Omega_{MPOF_k}=0}} = \frac{\left|H\left(f,\Omega_{MPOF_k}\right)\right|_{\Omega_{Si}=0}}{\left|H\left(f,\Omega_{Si}\right)\right|_{\Omega_{MPOF_k}=0}} = \frac{\left[1+\left(\frac{2\cdot\beta_k}{1+\beta_k^2}\right)\cdot\cos\left(\Omega_{MPOF_k}\right)\right]^{1/2}}{\left[1+\left(\frac{2\cdot\beta_k}{1+\beta_k^2}\right)\cdot\cos\left(-\Omega_{Si}\right)\right]^{1/2}} \qquad (A.25)$$

where f is the modulation frequency of the optical light source and Ω_{Si} and Ω_{MPOFk} are the phase-shift applied to the radio frequency modulating signal at the reference and sensing channel, respectively.

On the other hand, the output phase self-referencing parameter φ_k is given by:

$$\varphi_k = \arctan\left(\frac{\Im H(z)}{\Re H(z)}\right) = \arctan\left(\frac{-\sin\left(\Omega_{Si}\right)+\beta_k\cdot\sin\left(\Omega_{MPOF_k}\right)}{\cos\left(\Omega_{Si}\right)+\beta_k\cdot\cos\left(\Omega_{MPOF_k}\right)}\right) \qquad (A.26)$$

Appendix B

Application of Self-Reference Sensors Technique for Preventing Faults on WDM-PON Networks

B.1. Introduction

During latest years, massive deployments of fiber access networks are taking place worldwide very rapidly, already surpassing 100 million Fiber to the Home (FTTH) subscribers in 2014 [1]. While residential deployments are in their vast majority supported by power splitter based fiber infrastructures and GPON/EPON standards, Wavelength Division Multiplexing Passive Optical Networks (WDM-PONs) based on Wavelength Routed Optical Distribution Networks (WR-ODN) can be a cost-effective solution when logical point-to-point connections are required for higher security and performance, such as aggregation networks, mobile front-hauling or business services. In these scenarios, especial monitoring tools are needed in order to reduce operational costs of the optical distribution network and to guarantee high Service Level Agreement (SLA) requirements.

While remote optical transceiver monitoring [2] using in-band diagnostics can be helpful for remotely checking the optical parameters in the customer premises equipment (CPE), this approach offers a low measurement accuracy (±3dB) and is only available when the device in the customer premises is active and working properly. As a consequence, the remote diagnostic of optical transceivers does not allow preventive ODN monitoring and cannot distinguish between fiber and CPE faults in some situations. Recently, Tunable Optical Time Domain Reflectometers [3] (T-OTDRs) have been proposed overcoming the former restrictions, with the capability of performing in-service fiber monitoring and fault localization in the drop fibers of WDM-PONs independently of CPEs operation.

As an optional complement to OTDR systems, a preventive low cost technique for quick fiber monitoring in Coarse WDM-PONs has also been proposed, but it requires two coloured reflectors at each branch of the PON and cannot be used with the network in service.

In this section, we propose a new low-cost in-service preventive monitoring system for Dense WDM-PONs, using a single colourless reflector at ONU side.

B.2. Architecture of the Measurement Technique

The self-reference scheme shares the reception stage (Optical Monitoring Module) and partially the architecture of the frequency-based self-referencing technique for remotely addressing fiber-optic intensity sensors reported in Chapter 3. This topology is applied to a general scenario where an Access/Aggregation node, typically a WDM-PON Optical Line Termination (OLT), is connected to several remote devices, typically Optical Network Units (ONUs), see Figure B.1.

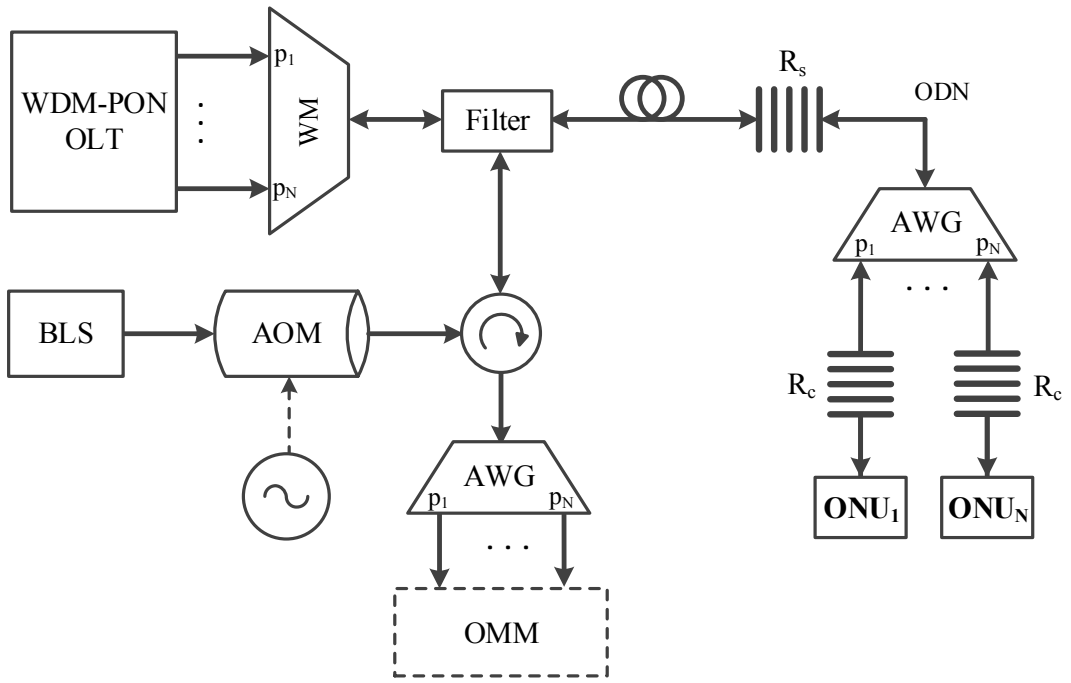

Figure B.1. General architecture of the proposed technique: (BLS) Broadband light source, (AOM) Acousto-optic modulator, (OMM) Optical Monitoring Module, (AWG) Arrayed Waveguide Grating.

A broadband light source (BLS) is externally modulated by and acousto-optic modulator (AOM). The modulated broadband signal is launched into the ODN via a broadband circulator and a fiber-optic filter. The filter also permits a bidirectional communication link between the Access/Aggregation Node and the ONUs, allowing the redirection of sensing signals from the ONUs to a cycled Arrayed Waveguide Grating (AWG) mux/demux with k ports ($p_1 ... p_k$). All sensing signals from the AWG mux/demux are introduced in an OMM to be processed by several virtual lock-in amplifiers. In the ODN side, the technique adds a single reflector (R_s) in the input of a cyclic AWG mux/demux with k ports ($p_1 ... p_k$). Finally, at the end of each branch of the

mux/demux (or optionally inside the remote devices/ONUs), a single colourless optical reflector (R_c) is used. In this case of study, the single and colourless reflectors are implemented using glass fiber Bragg gratings (GFBGs) but other reflector can be used.

B.3. Principle of Operation

The monitoring technique operates simultaneously to data transmission in the ODN . From the BLS a reference optical (λ_0) signal and a monitoring broadband light are delivered to the ODN through the fiber-optic filter. Both reference and monitoring signals are comprised within free wavebands in the ODN not used for data transmission. The reference optical signal is reflected by reflector R_s at the input of the AWG and received back in the OMM.

On the other hand, the monitoring BLS is filtered by the AWG, delivering a different monitoring signal (λ_k, with k=1, 2, … N) to the end of the corresponding AWG output port (p_k, with k=1, 2, … N), where the monitoring signal is reflected by reflector R_c and received back in the OMM. This monitoring waveband covers one cycle of the AWG which is not used by the data signals.

For each remote device, the reflections of the reference signal and the monitoring signals are digitally processed in the OMM, and self-referenced measurement values are obtained. The measurement values obtained depend on the optical losses at the AWG for each port and the fiber attenuation between each AWG port and each colourless reflector of the corresponding remote device.

B.4. Self-Referencing Parameters

For each ODN branch (k, with k=1, 2, … N), the output phase (φ) self-reference parameter is obtained [4] using Equation 3.13. This parameter represents the electrical phase shift between the reflected waves at λ_0 and λ_k received at the OMM. For each branch, the sensitivity to the fiber attenuation and the linearity of the self-referencing parameters can be configured in a flexible way using phase shifting in the reference and monitoring reflected signals.

Because of the self-referencing nature of the signal processing at the OMM, the measured values are resilient to variations of the absolute optical power and sensitivity of the light sources and receivers, respectively. The use of Radio-Frequency (RF) modulation in the monitoring signals allows achieving improved Signal-to-Noise-Ratio (SNR) in the measurements, which are also insensitive to the interference of other electronic signals.

B.5. Experimental Validation

Result analysis and technical support in this work were done in the frame of collaboration with the Fixed Access and Home Network Direction at Telefónica Investigación y Desarrollo[5]. The scientific supervisor of this collaboration in Telefónica was Dr. Julio Montalvo García.

A Bit Error Rate (BER) tester using DWDM SFP+ transceiver is used to emulate OLT ports and ONUs, see Figure B.2.

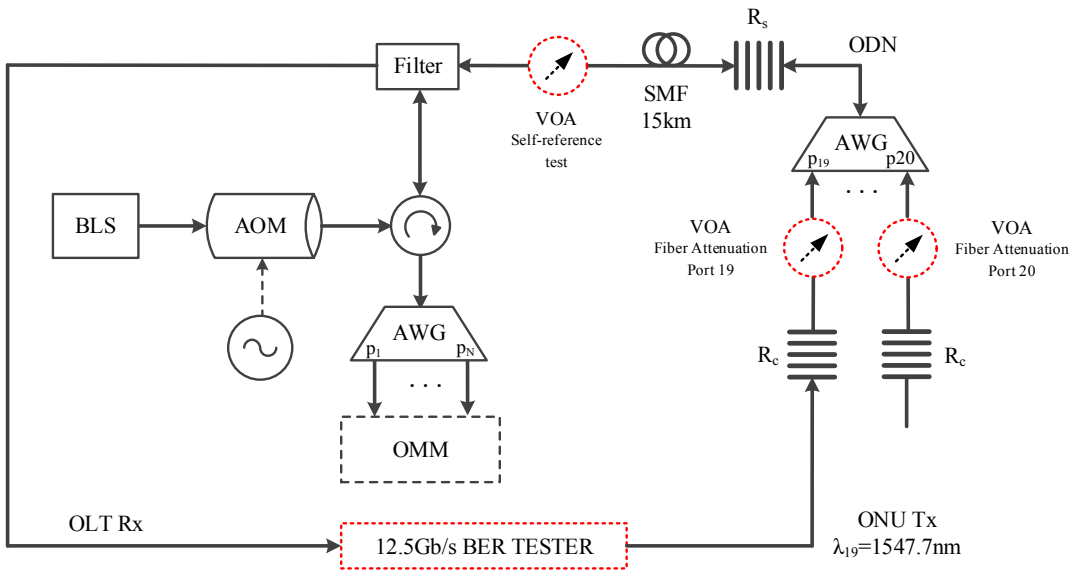

Figure B.2. Experimental set-up for validation of the principle of operation.

The OMM is formed by an array of photodetector (PD) by means of a data acquisition board (DAQ) which is used to convert the electrical signals form the PD to digital signals together with a band-pass filter (BPF), used to eliminate noise from all signals at frequencies outside the system frequency. A phase-shift is applied to the reference (Ω_{Ref}) and sensor (Ω_{Sen}) digital signal. Finally, a virtual lock-in amplifier is used to interrogate all available sensor channels. More details of the OMM structure can be found in Chapter 3. The software takes 8 seconds in acquiring and processing the 32 channels of the AWG.

The ODN consists of a 15-km singlemode fiber (SMF) coil between the fiber-optic filter and a cyclic 32-port AWG with several cycles in the S-, C- and L-bands. The S-band is used as monitoring waveband, while the C- and L-bands are used for data transmission between ONU and OLT.

[5] Fixed Access and Home Network Direction, Telefónica Investigación y Desarrollo. Madrid. Spain.

A FBG with nominal reflectance centered at 1,490nm is used as reference reflector (R_s). Two identical wideband Fiber Bragg Reflectors with nominal reflectance centered at 1,470nm and 5nm bandwidth are used in output ports 19 and 20 of the AWG as colourless reflectors (R_c). Variable optical attenuators (VOA) are employed at each output port to emulate fiber attenuation (α) on the ODN. In the experiments an attenuation range from 0dB to 5.5dB is configured for maximum linearity of the self-referenced parameters.

For each attenuation value at output ports 19 and 20 of the AWG, self-referenced parameters φ_{19} and φ_{20} are obtained in the OMM. The mathematical expression for φ_k, see Equation 3.13, is ruled by the fiber attenuation as well as the phase-shifts for the reference and sensing signals configured at the OMM. The monitoring system provides high-linearity or high-sensitivity monitoring performance, this flexibly is configured as desired.

In order to test the self-reference of the measurement technique, an optical attenuator adding optical losses up to 8dB is used, with negligible variations (0.2dB) of the measurement parameter φ_{19}. A measurement accuracy of fiber attenuation as low as 0.27dB is achieved, meanwhile data transmission is also active. The self-referenced measurements of φ_{19} versus the attenuation of the ODN branch 19 are shown in Figure B.3. A crosstalk test with regards the attenuation of ODN branch 20 can also be seen in the same figure, showing a negligible crosstalk (<0.1dB) between the two self-referenced measurements in both AWG adjacent channels.

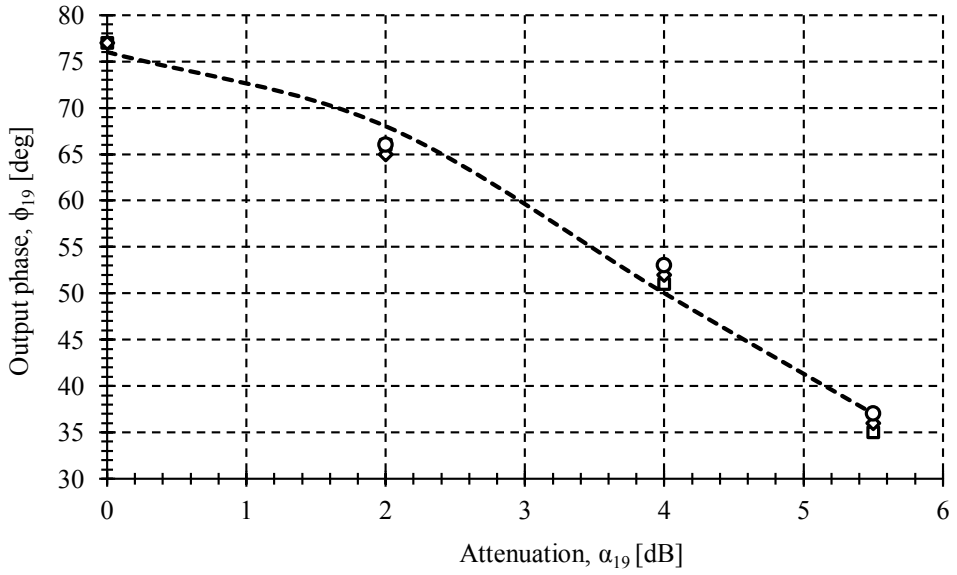

Figure B.3. Output phase parameter versus attenuation at power 19 attenuation for different values of sensor attenuation at port 20: ○ α_{20}=0dB, ◊ α_{20}=4, □ α_{20}=5.5. Measurements (triangle, square and circle dots) and simulations (discontinuous line) at a phase-shift configuration: – – $\Omega_{Ref} = 0.58\pi$, $\Omega_{Sen} = 0.99\pi$

Finally, a maximum power penalty of 0.37dB on data transmission due to the use of the optical monitoring technique has been obtained at 12.5Gb/s (NRZ, PRBS=2^{31}-1), see Figure B.4.

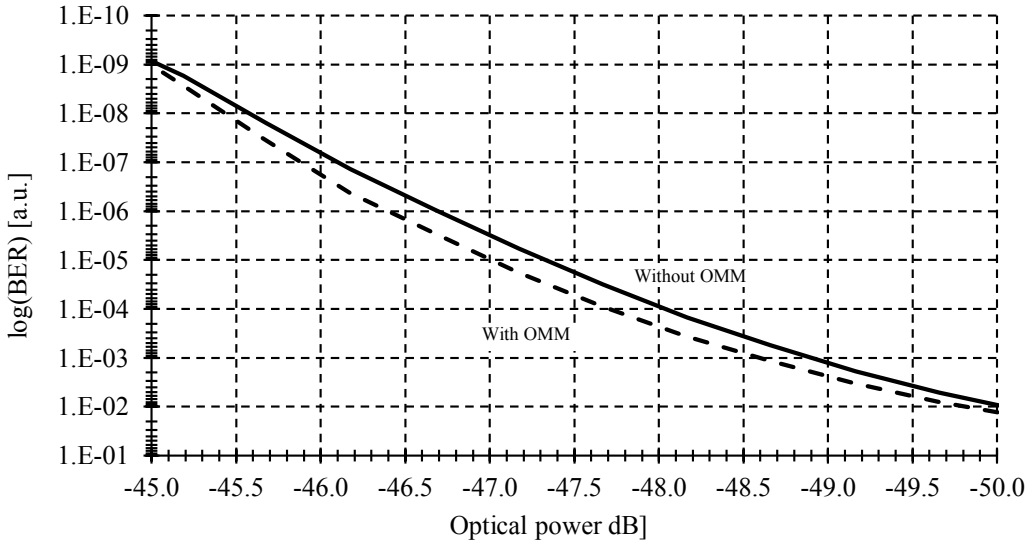

Figure B.4. BER for ONU at 12.5Gb/s transmission in AWG port 19: ── Without OMM, – – With OMM

B.6. Conclusions

A new preventive optical monitoring system for remote self-referenced measurement of the drop fiber attenuation in WDM-PONs is experimentally validated. An attenuation measurement accuracy of 0.27dB with a maximum power penalty of 0.37 dB in a 12.5 Gb/s transmission has been demonstrated using a general purpose platform. The setup is capable of measuring the attenuation of 32 channels in 8 seconds.

B.7. References

[1] "FTTH, DSL, and Cable Subscribers report," Infonetics Research, 2015.

[2] SFF, "Diagnostic Monitoring Interface for Optical Transceivers " SFF-8472 Rev 12.2, 2014.

[3] D. Villafani Caballero, J. P. von der Weid, and P. J. Urban, "Tuneable OTDR measurements for WDM-PON monitoring," in *Microwave & Optoelectronics Conference (IMOC)*, Rio de Janeiro (Brazil), pp. 1-5, 2013

[4] C. Vazquez, A. Tapetado, D. S. Montero, and J. Montalvo, "Método y sistema para la monitorización de redes de fibras ópticas," Spanish Patent, ES P201530018, 2015, (under revision).

Appendix C

Towards Sensors on Silicon Integrated Nanophotonics

C.1. Introduction

Silicon is considered a promising platform for photonics integrated circuits (PIC). PIC can be used in the integration of photonics links between the processing cores on multicore Central Processing Unit (CPU) fabricated in a bulk CMOS process and the main memory chips. The chief metric of this system are energy efficiency and bandwidth density. This technology enables the communication interface to processing elements within future computing systems to fit within the required thermal budget and physical real estate footprint. The required components are those of a typical wavelength division multiplexing (WDM) data link: modulators, receivers, add-drop filters and coupling interfaces. The high resolution photolithography developments enable the precise dimension control that is critical to manufacture a wide variety of photonics devices. An important example of such devices is a multimode interference (MMI) coupler. These devices have the advantages of using relaxed fabrication requirements and smaller footprints compared to other configurations, potentially energy efficient designs. MMI devices have already been used as 1x2 splitters, 2x1 combiners in Quadrature Phase Shift Keying modulators, 3-dB couplers, and cross couplers for switches, among others. This appendix intents to show the characterization process used to verify the functionality of manufactured MMI devices on bulk CMOS. The characterization of 3-dB, butterfly and cross-MMI couplers based on silicon waveguides is presented. The underlying objective of this work is to develop robust devices for communication interfaces which can also be used in sensing applications to improve the energy efficiency of modern microprocessors.

C.2. Calibration set-up

The MMI couplers proposed in this work were fabricated in the frame of collaboration with the Physical Optics and Electronics Group at Massachusetts Institute of Technology[6] leaded by

[6] Physical Optics and Electronics Group, Research Laboratory of Electronics, Massachusetts Institute of Technology, Cambridge. United States of America

Prof. Dr. Rajeev Ram. Alberto Tapetado Moraleda was allowed to use their installations in this work.

A broadband vertically-coupled test platform is used to characterize the MMI devices, see Figure C.1. This platform consists of a two electro-optic X-Y stations that accurately position two fibers at a variable angle to the chip surface. The exact angle of the fiber relative to the normal surface is dependent upon the working angle of the second-order input grating at the test wavelengths. Due to design considerations and fabrication errors, this angle may vary over +/-20 degrees. To accommodate such variability, a fiber positioning arm, with a widely variable coupling angle, is fit at few centimetres on the chip surface. The arm holder allows the positioning arms to be extended any arbitrary length and held in position via a set-screw through the visible hole.

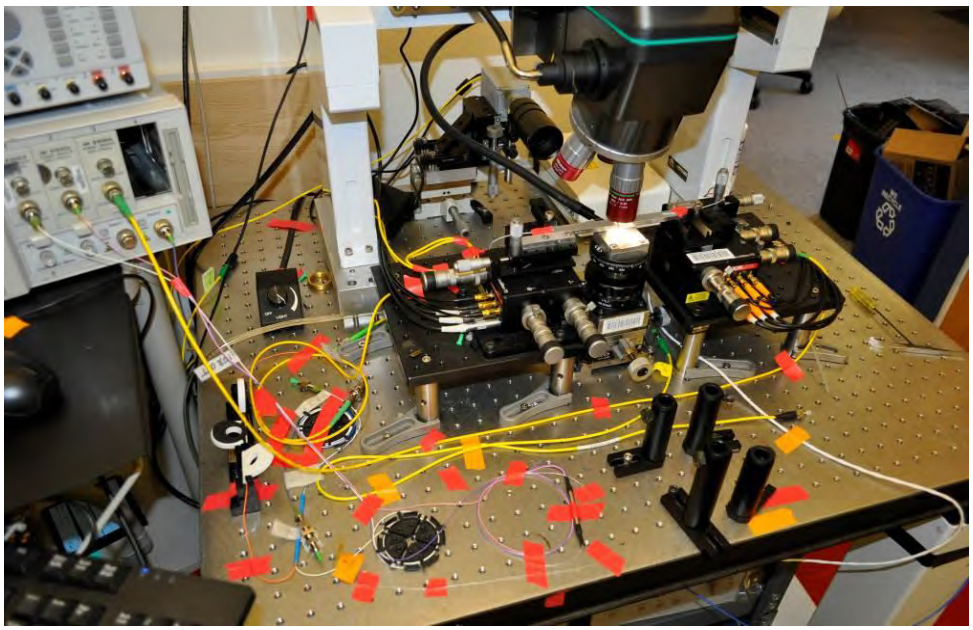

Figure C.1. Photograph of the basic vertical coupling setup. The microscope is visible at the top center of the picture. Under this objective, fixed fiber positioning arms with an angle hold two fibers above the chip surface.

To align the optical fiber, a microscope with an IR camera mounted on a microscope structure is located vertically on the chip surface. The objective used in this imaging setup has a 20x zoom with a 20mm working distance. This objective is chosen to provide sufficient detail of chip features and a 0.4 numeric aperture (NA) to provide an angular acceptance cone of 23.6º to allow viewing of the output coupler light. The fiber arms are machined at fixed angles and adjustable only under the narrow angle range provided by the fiber positioning stage. Two magnets on the end of the positioning arms pull the fiber in a precision cut V-groove for mounting. The distance between the fibers and the chip surface is controlled by a

standard colour camera connected to a 40x zoom macro lens. To provide sufficient light for this camera, a separate illuminator connected to two lightpipe focusers are aimed at the coupling setup from the rear side. The focusers and the macro lens are visible behind the fiber arms at the center of Figure C.2.

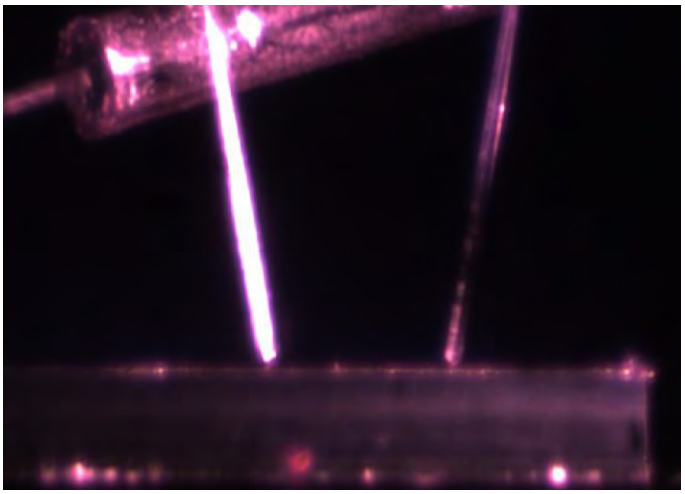

Figure C.2. Photograph of the distance between the fibers and the chip surface through a background colour camera.

The sample under test is held down to the temperature-controlled vacuum-chuck. The custom-machined aluminium chuck has three 1.27mm holes drilled at a 2.55mm spacing. These holes are connected to a vacuum line drilled from the rear of the stage.

The stage is temperature controlled by a PID controller connected to a 500W cartridge heater and 10kΩ thermistor in the front side of the chuck. Under normal test conditions, the stage temperature is maintained at 25±0.02°C and may be swept for thermal tuning. The sample positioning is then coarsely controlled by a three-axis stage. This positioning flexibility allows the relative port spacing of the fibers to be maintained when moving to another test location on the sample.

The MMI devices are tested and calibrated using a tunable laser source for measuring the device response versus wavelength, see Figure C.3. The 10% input power is monitored using a fiber-optic coupler with 10:90 coupling ratio in order to test the source performance, and to take a reference measurement. Then, a vertically-coupled test platform is used to fix the angle relative to the normal surface and to match the mode size of the grating couplers. Finally, an optical power meter is used to measure the optical power at the output of the selected MMI device.

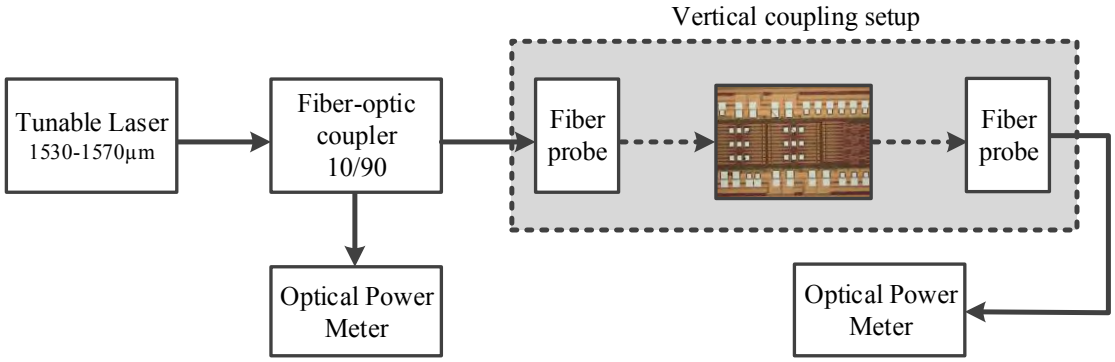

Figure C.3. Optical scheme used to characterise the MMI devices.

C.3. Measurements

A detailed description of the process allowing integrating photonic devices with electronic components can be shown in [1]. The operation design wavelength is 1,550nm. The polysilicon gate is used as the waveguide core, Figure C.4.(a), which is surrounded by a Si_3N_4 conformal layer. The cladding is formed by SiO_2. In this process the thickness of the polysilicon layer is 225nm. The waveguides are designed for a barely single mode operation and minimizing bending loss. In this case the width is 440nm.

Different MMI devices, 3-dB couplers and cross couplers are designed for achieving higher manufacturing tolerances so with the shortest lengths and highest normalized access waveguide widths. A detailed description of the tolerance analysis is carried out in [2]. A minimum separation of 500nm between core access waveguides is considered to avoid crosstalk. 3-dB and cross couplers have a width of 3.6µm. Schematics of the top view of the designed devices are shown in Figure C.4.(b), all dimensions are in microns.

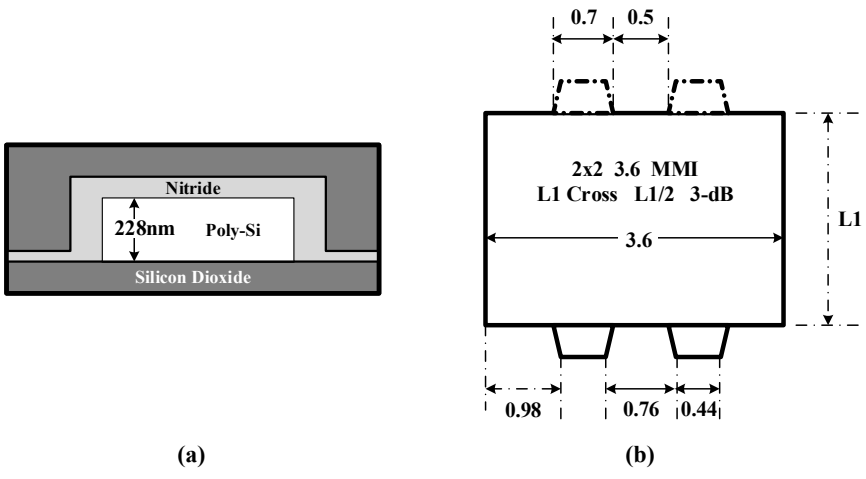

Figure C.4. (a) Schematic of waveguide structure. (b) MMI 3-dB and cross couplers

.The optical test and calibration path in the setup are optimized for a wavelength from 1,460 to 1,570nm. Optimum coupling for specific wavelength range is achieved by using a vertically-coupled test platform with input/output SMF-28e fibers at a fix angle relative to the normal surface to match the mode size of the grating couplers. 10% input power is monitored to test the source performance, and to take a reference measurement. A tunable laser source is used for measuring the output power versus wavelength as a test of the MMI device behaviour.

Output power of MMI devices have been characterized from 1,530 to 1,570nm. In Figure C.5.(a), output optical power measurements of a 3-dB coupler with a footprint of 3.6x14.7mm^2 are reported.

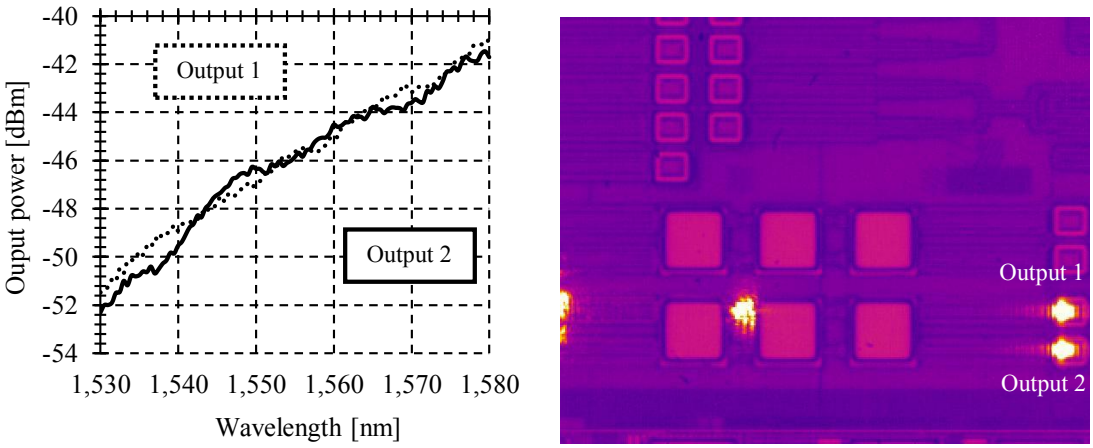

Figure C.5. (a) Power measurements versus wavelength for a 3-dB MMI coupler: (—) First output channel, (· · ·) Second output channel. (b) Infrared photograph of the 3-dB MMI coupler output ports.

It is clear that the input light power injected into the input channel of the 3-dB coupler is divided into two light beams of equal light power. A visual example of the 3-dB coupler operation is shown in Figure C.5.(b). On the other hand, the principle of operation of a cross coupler is also demonstrated. In this case, the light power injected into the input channel of the cross coupler is addressed only to a single output. This output corresponds to the cross output from the input channel, as shown in Figure C.6.

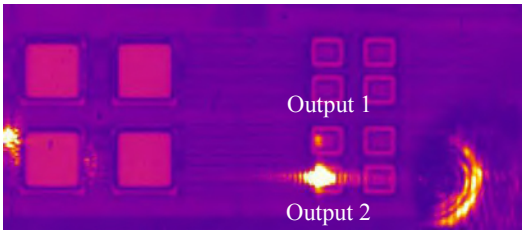

Figure C.6. Infrared photograph of the cross MMI coupler output ports.

C.4. Conclusions

Small footprints MMI couplers based on silicon waveguides are realized on bulk CMOS technology. It has been experimentally demonstrated the operation of 3-dB and cross MMI couplers for communication interfaces which can also be used in sensing applications to improve the energy efficiency of modern microprocessors.

C.5. References

[1] J. Orcutt, "Monolithic Electronic-Photonic Integration in State-of-the-Art CMOS Processes," Department of Electrical Engineering and Computer Science, Massachusetts Institute of Technology, 2012.

[2] C. Vázquez, A. Tapetado, J. Orcutt, H. C. Meng, and R. Ram, "Tolerance analysis for efficient MMI devices in silicon photonics," in *Silicon Photonics IX*, San Francisco (United States of America), 2014, pp. 89900A-89900A-7.